

NOTE TO USERS

This reproduction is the best copy available.

UMI[®]

RICE UNIVERSITY

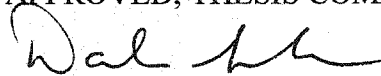
CHARACTERIZING SHALLOW AQUIFERS WITH WAVE-PROPAGATION BASED
GEOPHYSICAL METHODS: IMAGING AND ATTRIBUTE ANALYSIS

by

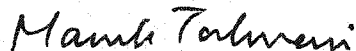
JOHN BRADFORD

A THESIS SUBMITTED
IN PARTIAL FULFILLMENT OF THE
REQUIREMENTS FOR THE DEGREE
DOCTOR OF PHILOSOPHY

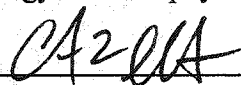
APPROVED, THESIS COMMITTEE



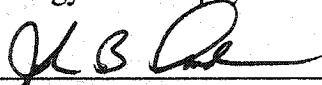
Dale S. Sawyer, Chairman
Geology and Geophysics



Manik Talwani, Co-Chairman
Geology and Geophysics



Colin A. Zelt
Geology and Geophysics



John B. Anderson
Geology and Geophysics



Philip Bedient
Environmental Science and Engineering

Houston, Texas
November, 1998

UMI Number: 3138871

INFORMATION TO USERS

The quality of this reproduction is dependent upon the quality of the copy submitted. Broken or indistinct print, colored or poor quality illustrations and photographs, print bleed-through, substandard margins, and improper alignment can adversely affect reproduction.

In the unlikely event that the author did not send a complete manuscript and there are missing pages, these will be noted. Also, if unauthorized copyright material had to be removed, a note will indicate the deletion.



UMI Microform 3138871

Copyright 2004 by ProQuest Information and Learning Company.

All rights reserved. This microform edition is protected against unauthorized copying under Title 17, United States Code.

ProQuest Information and Learning Company
300 North Zeeb Road
P.O. Box 1346
Ann Arbor, MI 48106-1346

RICE UNIVERSITY

CHARACTERIZING SHALLOW AQUIFERS WITH WAVE-PROPAGATION BASED
GEOPHYSICAL METHODS: IMAGING AND ATTRIBUTE ANALYSIS

by

JOHN BRADFORD

A THESIS SUBMITTED
IN PARTIAL FULFILLMENT OF THE
REQUIREMENTS FOR THE DEGREE
DOCTOR OF PHILOSOPHY

APPROVED, THESIS COMMITTEE

Dale S. Sawyer, Chairman
Geology and Geophysics

Manik Talwani, Co-Chairman
Geology and Geophysics

Colin A. Zelt
Geology and Geophysics

John B. Anderson
Geology and Geophysics

Philip Bedient
Environmental Science and Engineering

Houston, Texas
October, 1998

ABSTRACT

Characterizing Shallow Aquifers with Wave-Propagation Based Geophysical Methods: Imaging and Attribute Analysis

by

John Bradford

As the results of seismic reflection and ground penetrating radar (GPR) studies become more prevalent as input for quantitative groundwater and engineering studies, it is important to evaluate traditional approaches to data processing and analysis. Where conventional methods fail it is necessary to investigate and/or develop non-traditional approaches to data analysis. I present five stand-alone studies that are focused on characterizing shallow aquifers using seismic reflection and GPR data processing and analysis. Each of the projects involves a new approach to data analysis either through alternative processing strategies that are not widely applied in environmental studies or development of new processing methods and/or algorithms.

The first two studies are focused on seismic reflection imaging problems that arise in the shallow environment. I first present a detailed discussion of the errors that can result from conventional normal-moveout (NMO) processing, and the application of pre-stack depth migration (PSDM) to improve image accuracy. Second, I apply dip-moveout (DMO) processing to a data set from the Puget Sound. DMO is rarely applied in environmental studies, but can improve velocity analysis and image quality where there are dipping layers or scattering events.

The final three studies are focused on attribute analysis of GPR and seismic reflection data in direct detection studies. Over the past 10 -15 years, direct detection has been used successfully in the energy industry to identify oil and gas reserves from exploration scale seismic reflection data, but is a new approach to the analysis of GPR and shallow seismic reflection data. Direct detection studies use reflected wave attributes such as amplitude, frequency content, and phase to estimate material properties.

I first present a detailed discussion of GPR amplitude vs. offset (AVO) analysis for direct detection of free phase non-aqueous phase liquid contaminants (NAPLs). The analysis is not straightforward and requires careful consideration of electromagnetic dynamic properties. Second, I present a shallow seismic case study where a predictable AVO response was detected. Finally, I present a new wavelet decomposition and time-frequency representation, and illustrate applications in GPR attenuation analysis for NAPL detection and lithology characterization.

ACKNOWLEDGMENTS

I would first like to thank my wife, Donnell, for being supportive when I needed it, particularly over the past few months when I have spent most of my waking hours huddled over the computer keyboard. I don't think this counts as quality family time. I thank my son Stian for being such a happy guy, and giving me plenty of reasons to smile in these stressful times. When are you going to learn to write code son? I also owe a great deal of gratitude to my parents who have given me the independence and drive to find a way to get things done.

It is difficult to single out a member of my advisory committee that was most helpful. My official advisors Dr. Dale Sawyer and Dr. Manik Talwani, and unofficial coadvisor Dr. John Anderson, each helped a great deal with various aspects of my research. I owe a special thanks to Dr. Dale Sawyer, for allowing me the freedom to pursue such a wide variety of projects, and for always finding funding when it was needed. It would be difficult to find a better situation. The always helpful and sometimes painful suggestions for text preparation have been most appreciated. I thank Dr. Manik Talwani for providing encouragement to pursue unexplored research topics and access to substantial resources that made the research possible. I thank Dr. John Anderson for providing a number of opportunities both to collect geophysical data, and to explore the world of sedimentology. The knowledge of sedimentary processes I gained working with Dr. Anderson and his research group has given me invaluable insight in my research as an environmental geophysicist.

I would like to thank the other members of my advisory committee, Dr. Colin Zelt

and Dr. Philip Bedient. Dr. Zelt's helpful suggestions, willingness to spend time in the field, and time spent helping me learn the inversion code are most appreciated. Dr. Bedient's willingness to listen to my various ideas for aquifer characterization and insight into hydrologic and contaminant processes have been very valuable. I hope that we may continue to examine the role of geophysical methods in groundwater studies.

I must thank Dr. Yafei Wu at the Houston Advanced Research Center for all of his valuable suggestions and with whom I developed the wavelet decomposition and attenuation analysis algorithms.

I thank Dr. John Oldow, now at the University of Idaho, for his valuable insight, and putting up with my stubborn arguments. Dr. Oldow managed the Guemes Island research project, and was my advisor at Rice prior to departing for the old country and IU.

I thank Dr. Alan Levander and Dr. Tim Henstock for giving me a deeper understanding of seismic data processing. I also owe thanks to Dr. Levander for allowing me free access to the seismograph and geophone array. The informal discussions and formal seminars with Dr. Levander's research group contributed a great deal to my research.

I thank Jamie Loughridge, M.S., for bouncing ideas around with me, and for all the hours spent building the pit, and subsequent hours spent dragging antennas across the pit. Hey you didn't order that here!

I thank Toni Rodriguez for the hours of helpful sedimentology discussions and the opportunity to join him for a few cruises on the Lone Star. When are we going to write that book?

A great deal of thanks goes to the usual suspects for help with the field work, and without whom this research would not have been possible, Jamie (the moose) Loughridge, Peeter (the master) Akerberg, Jim (the hammer) Lemeaux (I can't be expected to spell that), Diana (the Bison) Dana, Stig (no thank you) Helstholm (whose bizarre but effective Norwegian style of swinging a sledge hammer mystified us all), Toni (powder burn) Rodriguez, Dr. Phil (the chef) Bart (now how do you make et tufe again?), Dr. Colin Zelt, Dr. Dale Sawyer, Dr. John Anderson, and the students in the Exploration Geophysics class.

I thank Dr. Mark Everett and Veit Matt at Texas A&M University for getting me access to the hydrogeologic test site, and for help with the field work. I thank Dr. Thomas Pratt and the USGS for the use of the geophone array for the Guemes study and for his help in data acquisition.

Funding for this research has come from a variety of sources: the EPA STAR graduate fellow program which funded my stipend and tuition for two years and part of the Texas A&M study, the Department of Geology and Geophysics at Rice University which provided funding for field expenses in the Guemes Island study, NSF Grant EAR - 9316711 which was used to purchase the seismograph, geophone array, and energy sources, GRI contract # 5094 - 260 - 2963 and the Houston Advanced Research Center which funded all of the GPR research, and the attenuation consortium at HARC.

TABLE OF CONTENTS

ABSTRACT	ii
ACKNOWLEDGMENTS	iv
TABLE OF CONTENTS	vii
LIST OF FIGURES	xiii
LIST OF TABLES	xxx
CHAPTER 1. INTRODUCTION	1
THE STATE OF ENVIRONMENTAL GEOPHYSICS	1
WAVE-PROPAGATION BASED GEOPHYSICAL METHODS	6
DISSERTATION RESEARCH SUMMARY	11
Imaging	13
Attribute analysis	15
CHAPTER 2. IMAGING SHALLOW AQUIFERS IN DEPTH USING	
PRE-STACK DEPTH MIGRATION	
.....	17
INTRODUCTION	17

PROBLEMS WITH RECORDING AND PROCESSING REFLECTIONS

ORIGINATING BELOW THE WATER TABLE	20
Attenuation of source energy	22
Coherent noise	24
Geometric loss of resolution	28
Departure from NMO	33
Error prediction for NMO processing	40
Summary	46

PROCESSING STRATEGIES

Pre-stack depth migration	48
Method 1 : The two layer model	48
Method 2: NMO analysis and the progressive stack.	49
Method 3: Traveltime inversion	49
Additional considerations.	50

CASE STUDIES

Synthetic example	51
Model design.	51
Error prediction for NMO processing.	53
Synthetic data generation.	58
NMO processing.	61
PSDM processing.	65
Velocity model comparison.	74

Summary	78
FIELD EXAMPLES	79
Fluvial environment	82
Refraction survey.	82
Processing the dense survey.	85
Problems with the near-zero offset survey.	88
Summary.	98
Coastal plain environment	98
NMO processing.	100
PSDM processing.	102
Velocity model comparison.	107
Summary.	108
Coastal environment	108
CONCLUSIONS	117

CHAPTER 3. CASE STUDY: IMAGING A SHALLOW AQUIFER IN TEMPERATE

GLACIAL SEDIMENTS USING SEISMIC	
REFLECTION PROFILING WITH DMO PROCESSING	119
INTRODUCTION	119
Field Site Conditions	121
DATA ACQUISITION	123
DATA PROCESSING	124

Numerical modeling as an aid in data interpretation	124
Data preparation	128
Velocity analysis	129
Dip moveout processing.....	132
INTERPRETATION OF REFLECTION PROFILE AND	
COMPARISON WITH LITHOLOGIC CONTROL	137
Surficial sediment package	137
The Whidbey confining unit	140
The Double Bluff aquifer	140
CONCLUSIONS	141
CHAPTER 4. NAPL DETECTION WITH GPR USING AVO ANALYSIS	
INTRODUCTION	143
THEORY	146
Zero conductivity case	146
Frequency dependent parameterization	155
Practical considerations	161
MODELING	171
Travel time computation	172
Wavelet modeling	173
PHYSICAL MODEL AND COMPARISON TO SYNTHETIC MODEL ...	179
Image processing	180

Synthetic data generation	185
AVO processing	186
LNAPL detection.	194
LNAPL and DNAPL detection in an aquifer model	202
CONCLUSIONS	214
CHAPTER 5. CASE STUDY: SEISMIC AVO ANALYSIS OF LOW VELOCITY, SHALLOW SANDS (<50 m)	218
INTRODUCTION	218
DATA ACQUISITION	220
DATA PROCESSING AND INTERPRETATION	224
AVO ANALYSIS	226
CONCLUSIONS	235
CHAPTER 6. TIME-FREQUENCY ATTRIBUTE ANALYSIS	236
INTRODUCTION	236
THE WAVELET TRANSFORM AND A NEW TIME-FREQUENCY REPRESENTATION	238
MODELING THE ATTENUATION AND DISPERSION EFFECTS IN 2-D	247
Travel time computation	249
Wavelet modeling	249

CALCULATING THE ATTENUATION ATTRIBUTE	250
Practical considerations	251
Estimating the attenuation attribute in synthetic and field data	252
Application to hydrocarbon exploration	252
Application to GPR: DNAPL detection	259
GPR application: Lithology identification	266
SUMMARY	268
REFERENCES	271
APPENDIX A: DERIVATION OF THE WIGNER DISTRIBUTION	
FOR A RICKER WAVELET	281
APPENDIX B: DERIVATION OF EQUATIONS FOR	
ATTENUATION ATTRIBUTE CALCULATIONS	284

LIST OF FIGURES

Figure 1.1: Sign indicating concern with saltwater intrusion into the sole source aquifer system on Guemes Island in the Puget Sound.	2
Figure 1.2: Field location and geophysical methods used in work relevant to this study. Red indicates sites discussed specifically in this dissertation.	7
Figure 2.1: P and S velocities for a quartz sand as a function of water saturation. The curves are calculated with Gassman's equations assuming a depth of 10 m.	21
Figure 2.2: Ray diagrams indicating; A) severe ray bending across the piezometric surface, and B) parameters used in modeling. All energy reflected from the base of the second layer must pass through the pre-critical aperture. Indicated velocities are in km/s.	23
Figure 2.3: Visco-elastic synthetic seismogram based on a velocity model derived from travel time inversion of picks from Figure 2.4 (see Figure 2.31). W, PSP, and Im are the water table reflection, a PSP converted mode, and an interbed multiple respectively. No reflection from the aquitard is evident.	25
Figure 2.4: Shot record illustrating features commonly observed in shallow seismic studies. H_w and R are the water table refraction and deeper reflections respectively. The yellow region indicates the noise cone in this case.	26
Figure 2.5: Reflection and transmission coefficients for primary and converted modes for a P-wave incident on the piezometric surface. Velocities are taken from Figure 2.1. Significant P-S conversion occurs for $\theta > 14^\circ$	27
Figure 2.6: A) Velocity contrast vs. ratio of lateral to vertical component of wave motion	

for the transmitted wave at $\theta_1 = 14^\circ$. B) Head wave convergence ($x = 30$ m) as a function of velocity contrast for a reflection 10 m below the piezometric surface (Figure 2.2), where $dt = t_{|R} - t_{|Hw}$. t_h is the head wave travel time, t_r is the correct reflection travel time and t_{rms} is the NMO approximation. 30

Figure 2.7: Acoustic seismogram for a model with four reflectors ($R_5 - R_{20}$) spaced at 5 m intervals below the water table (W). W is at a depth of 10 m. Head wave convergence decreases resolving power at far offsets. 32

Figure 2.8: Heterogeneity factor, g , as a function of velocity contrast and depth ratio. 35

Figure 2.9: Reflection traveltimes curves A) using the full offset range to calculate v_{stk} , and B) using only the far offset range. Using only far offsets increases the velocity and t_0 overestimates. The two term approximation to the traveltimes curve is reasonable at near offsets, but provides a poor estimate at far offsets. 38

Figure 2.10: Error estimates as functions of z_1 and z_2 for a two layer model with $v_1 = 400$ m/s and $v_2 = 1600$ m/s. A) σ_{z2} , B) σ_d with full $v_{stk}(t)$, and C) σ_d with partial $v_{stk}(t)$ 43

Figure 2.11: σ_{z2} as a function of offset with $v_1 = 400$ m/s, $v_2 = 1600$ m/s, vs. A) z_2 , and B) z_1 44

Figure 2.12: σ_{z2} as a function of v_{nc} (minimum offset) vs A) z_2 , and B) z_1 . $v_1 = 400$ m/s, $v_2 = 1600$ m/s, and $x_{max} = 80$ m. 46

Figure 2.13: σ_{z2} as a function of v_1 vs. A) z_2 , and B) z_1 , with $v_2 = 1600$ m/s 46

Figure 2.14: Velocity model used to generate synthetic data. Velocities are in m/s. ... 52

- Figure 2.15:** Ray paths for the horizontally layered portion of the velocity model in Figure 2.14. Velocites are in km/s. 55
- Figure 2.16:** Travel times A), velocity bias B), σ_{hxx} C), and σ_{dxx} D), for NMO processing and Dix inversion for the velocity model in Figure 2.14. The full offset range was used to calculate the errors. 56
- Figure 2.17:** Travel times A), velocity bias B), σ_{hxx} C), and σ_{dxx} D), for NMO processing and Dix inversion for the velocity model in Figure 2.14. In this case, only the far offset portion of the travelttime curves were used to calculate the errors. 57
- Figure 2.18:** Synthetic shot gathers for the velocity model in Figure 2.14. A) raw data, and B) after top-muting and inside muting the potential noise cone region. Data were generated with a 4th order, acoustic finite-difference code. 60
- Figure 2.19:** Stacks of data generated from the velocity model in Figure 2.14. The data were processed with a standard NMO processing flow including F-K migration. The stacks were depth converted A) with a partial $v_{stk}(t)$, and B) with the full $v_{stk}(t)$ 63
- Figure 2.20:** Synthetic CDP's for the aquifer model. CDP 50 is over the horizontally layered portion of the model. CDP 145 is over the steeply dipping portion of the bedrock interface. 66
- Figure 2.21:** A) Water table reflection CIP before and after migration with a constant velocity of 400 m/s. B) CIPs after migration with the full velocity field. The tails of W are not migrated to the correct location. Top mute pick is shown in red. 67

- Figure 2.22:** PSDM CIP's A) with the correct velocity field, and B) with the velocity field determined from PSDM velocity analysis. Top mute picks are shown in red. . . 70
- Figure 2.23:** PSDM stacks for the aquifer model A) with the correct velocity model, and B) with the velocity model determined from PSDM velocity analysis. 71
- Figure 2.24:** Velocity functions for the aquifer model. 75
- Figure 2.25:** Heterogeneity factor for the velocity model in Figure 2.14. 76
- Figure 2.26:** Bias as a function of velocity contrast for a two layer model. 77
- Figure 2.27:** Location of three field studies discussed in this paper. The areas represent differing sedimentary and hydrologic environments. 80
- Figure 2.28:** CMP fold for the 120 receiver RAST acquisition procedure. The diagram is taken from the Rice survey. 81
- Figure 2.29:** Layout of the Texas A&M hydrogeologic test site near Bryan, Texas. . . 83
- Figure 2.30:** Cross-section from the Texas A&M site. Modified from (Sananikone, 1997) 84
- Figure 2.31:** A) Inverted velocity model and rays paths, and B) traveltimes curves and picks from one of seven shot gathers used for traveltimes inversion at the Texas A&M site. The data are shown in Figure 2.4. Velocities are in km/s. 86
- Figure 2.32:** Shot gathers and a stacked time section from the dense survey at the Texas A&M site. Various modes of surface noise are labeled in the shots gathers. No primary reflections are visible below W. The event labeled as CS cannot be interpreted with confidence, although the arrival time is correct. There may some evidence of a reflector at this depth at source point 113.5. The horizontal position

on the stack indicates survey x position in meters (compare to Figure 2.35) . . . 87

Figure 2.33: Representative shot gathers from the coarse survey at the Texas A&M site

A) with a low cut of 50 Hz, and B) with a low cut of 60 Hz. The lower band better preserves energy from W, while filtering at the higher band helps resolve the aquitard reflector, SH which is roughly 10 m below the water table. The entire portion of W that is visible is post-critical, but phase rotation is not obvious. . . 93

Figure 2.34: CIP 171 after migration of the low velocity field (A) with a partial velocity

function and the high velocity field (B) with the full velocity function (note difference in depth scale). W and SH are flattened across the range of offsets that they are visible. The red line indicates top mute position. 94

Figure 2.35: PSDM image after merging the low and high velocity fields (A) and depth

converted stack using velocities from Dix inversion (B). In the PSDM image, W and SH are consistent with known depths to the water table and shale aquitard. The stretch of SH corresponds to the velocity increase in the saturated zone. Depth to SH in B), is significantly overpredicted. 96

Figure 2.36: Comparisons of velocity models derived through PSDM velocity analysis

and Dix inversion. Dix inversion significantly overpredicts velocities below the water table. 97

Figure 2.37: Location of the Rice profile, and position relative to campus buildings. Air

wave reflections from the buildings are a major source of coherent noise at later times (Figure 2.38). 99

Figure 2.38: The data quality at the Rice site is excellent and the water table reflection is

clearly identified as well as primary reflections deeper than 500 ms. Air wave reflections from buildings interfere with deeper primary reflections. 101

Figure 2.39: Rice profile after NMO, stacking, and depth conversion (A) and a PSDM image (B). Red lines indicate reference reflectors. Significant differences are evident to about 250 m. PSDM significantly reduced random noise and effectively attenuated coherent air wave reflections deep in the section. 103

Figure 2.40: Shallow portion of the Rice profile after NMO, stacking and depth conversion (A), and a PSDM image (B). Reference reflectors are shown in red. All reflectors below W are overestimated by about 10 m in the NMO section. W only migrates coherently from about $x = 140 - 200$ m. W is not shown in the NMO section. 104

Figure 2.41: CIP 161 after PSDM of the full section. All reflections in the CIP are flattened. The strong reflection at 450 m is evident in this CIP. The strong events from 450 - 550 m are out-of-plane air-wave reflections. 105

Figure 2.42: Velocity models determined from Dix inversion and PSDM velocity analysis. Dix inversion velocities are a poor representation of the velocity field above 120 m. 106

Figure 2.43: Location of Bolivar Peninsula survey area. 109

Figure 2.44: Cross-section of the Trinity River incised valley. The top-of-fluvial sand correlates with a high amplitude reflection, and AVO analysis indicates the presence of gas. [Adapted from Siringan and Anderson (1993)]. 110

Figure 2.45: Representative shot gather from the Bolivar Peninsula survey. Base-of-

barrier sands (BB), top-of-fluvial sand (TS), and base-of-incision (BI) are clearly evident. 112

Figure 2.46: PSDM image (A) and NMO stack with depth conversion (B) of a portion of the Bolivar Peninsula profile. In this case, depth prediction error from Dix velocities is relatively small (green and brown lines indicate interpreted depths from the PSDM image). The dipping reflectors (red) truncated by the incision (brown) are more clearly imaged with PSDM. 113

Figure 2.47: Velocity functions derived for the Bolivar profile. In this case, the Dix velocities are a reasonable representation of the average interval velocity. ... 115

Figure 3.1: The field area was located on Guemes Island, in the Puget Sound, north of Seattle, Washington. We conducted the seismic experiment along a rural road that was located parallel to, and approximately 80 m from, a 50 m high sea cliff. Outcrop observations and water well boring descriptions provided detailed lithologic control for the experiment. 120

Figure 3.2: Common-receiver gathers (CRG), modeled data, and velocity models showing the effect of a thin, high velocity layer near the surface. The data are modeled using a fourth-order finite difference code, and a 120 Hz, zero-phase Ricker wavelet as the source pulse. A) Data generated using Model 1, with a 15 m thick high velocity zone, is similar to CRG 40. The reflection from the base of the high velocity zone (shown with a black dashed line) has non-hyperbolic moveout at an offset of about 33 m. For a reflector at a depth of 35 m (shown with a white dashed line), departure from NMO becomes apparent at an offset of about 75 m.

Non-hyperbolic moveout is the result of energy being channeled along the high velocity zone. B) As the high velocity layer in the model thins to 7m, the high frequency components are trapped in the high velocity layer as guided waves, and the reflection from the base can no longer be differentiated. The reflection from the interface at 35 m shows no significant departure from NMO to the maximum offset of 100 m, because the low frequency components are not efficiently channeled in the high velocity layer. This modeled data is similar to CRG 106.

..... 125

Figure 3.3: CRG 22, A) with only bandpass filtering and AGC, and B) after F-K filtering via tau-p trace interpolation. No interpolated traces are included for this example. Although F-K filtering effectively attenuated all coherent noise inside the mute cone, little or no reflected energy could be extracted. Inside muting was employed to avoid stacking filter noise. This resulted in denoising of the window in which reflections could be observed. 130

Figure 3.4: Stacking velocity models, A) before iterative DMO velocity analysis, and B) the final model after two iterations. The most obvious effect is smoothing of the velocity field. This is expected by analogy with a synthetic DMO example (Figure 3.5). 131

Figure 3.5: Synthetic stacked data, A) F-K migrated with a velocities determined before DMO corrections, and B) F-K migration with velocities determined from DMO corrected data. The flat reflectors lie at depths of 30 m and 50 m, and the dipping reflectors have dips of 45° and 25° for the segment on the left and right

respectively. Indicated velocities are the true model interval velocities. Velocity errors resulting from dipping reflectors, conflicting dips, and diffraction tails severely degrade the migration result (A). DMO processing accounts for these effects resulting in a more accurate velocity field that is appropriate for migration(B). The data were generated with a fourth-order, acoustic finite difference code, using a 150 Hz, zero-phase Ricker wavelet as the source pulse, and 30-fold CMP's with a spacing of 1 m. 134

Figure 3.6: A) the stack (without DMO), with a velocity model V2 (Figure 3.4b).

Coherent, flat lying reflectors can be followed continuously across large portions of the section. B) The DMO corrected stack; steeply dipping noise has been effectively attenuated, and reflector coherence has been improved, particularly deeper in the section. C) Kirchhoff depth migration of 6b with depth interval velocities derived from V1 (Figure 3.4a). The stack has been severely degraded. D) Kirchhoff depth migration with depth interval velocities derived from V2 (Figure 3.4b). 135

Figure 3.7: A) Interpreted time section (not migrated), B) interpreted depth-migrated section , C) stratigraphic sketch of sea cliff exposure adjacent to the line, and D) photo mosaic of the northern portion of the line. Compare A) and B) to the corresponding uninterpreted sections in Figures 3.6B and 3.6D respectively. The major features are the four erosional surfaces (E-1 - E-4), the Whidbey Formation (WF), the top of the water saturated zone (WS), and the Double Bluff Formation (DB). The colored stratigraphic column in B) is taken from a water well boring

description located adjacent to the profile. The seismic section shows relatively good correlation with the exposure. There is no lithologic control below 52 m.

.....	138
Figure 4.1: Antenna and electric field orientations for parallel and transverse polarization configurations. For purposes of this figure, k and E are the unit vectors for the wavenumber and electric field respectively.	147
Figure 4.2: PP reflection coefficients and reflection phase for; case 1: $K_1 = 12$, $K_2 = 6$, and case 2: $K_1 = 6$, $K_2 = 12$	150
Figure 4.3: TP reflection coefficients and reflection phase for; case 1: $K_1 = 12$, $K_2 = 6$ and case 2: $K_1 = 12$, $K_2 = 6$	151
Figure 4.4: θ_B vs. K_2/K_1 for a range of K that might be observed in GPR studies. Note that for $K_2 < K_1$, θ_B is always less than 45° , which is reasonable for reflection studies.	153
Figure 4.5: Model of an aquifer contaminated with LNAPL and DNAPL. The Cole-Cole parameters are given in Table 4.1.	158
Figure 4.6: Reflection coefficients for potential reflecting boundaries in the aquifer model shown in Figure 4.5.	160
Figure 4.7: Rays paths for a typical negative velocity gradient. Note that the rays curve toward the vertical with increasing depth. Velocities are given in in/ μ s. Scaling to these units is necessary to use the ray tracing code which was designed for seismic data modeling (Loughridge, 1998).	163
Figure 4.8: Angle of incidence vs. increasing relative permittivity (decreasing velocity) at	

various take-off angles assuming a linear gradient in K . K_0 is the permittivity at the surface. Typically K increases with depth due to increasing moisture content.

.....	164
Figure 4.9: Definition of parameters for a two-layer model.	165
Figure 4.10: Gabor wavelets with phase shift of 0, $\pi/4$, and $\pi/2$, and the envelope function. Note that the amplitude and shape of the envelope function is phase independent.	168
Figure 4.11: Gabor wavelets with the same arrival time and modulus, but with phase varying smoothly from 0 to $-\pi$. Maximum amplitude of the real wavelet is shown with a dotted line. Maximum amplitude of the envelope function yields the desired result (solid line).	169
Figure 4.12: Antenna orientations and the associated radiation pattern for a single antenna. Patterns are calculated assuming an infinitesimal dipole at the earth-air interface with $K_{\text{EARTH}} = 4$	176
Figure 4.13: Geometric approximation for the radiation coefficients of a dipole, and the modified coefficients used in this paper.	177
Figure 4.14: Comparison of AVO response for field data, and predicted using the ray theory (geometric approximation) and modified radiation coefficients.	178
Figure 4.15: Schematic of the LNAPL AVO experiment. The containers are 46 cm x 30 cm x 41 cm and buried at a depth of 0.53 m.	181
Figure 4.16: Pre-stack depth migrated common-image-point gather (CIP) for the gasoline saturated sand. The reflections from the top and base of the can (.525 and .838 m	

respectively) are flattened and in the correct depth position indicating that the velocity model is approximately correct.	183
Figure 4.17: Pre-stack depth migrated image of the containers filled with gasoline (red) and water (blue) saturated sand. Colored regions indicate actual positions and dimensions of the containers.	184
Figure 4.18: Synthetic and field TP response for the LNAPL physical model. The reflections from the water and gasoline saturated sands are centered at about 9 ns.	188
Figure 4.19: TP AVO response for synthetic and field data for the LNAPL physical model. Data are shown in Figure 4.18.	189
Figure 4.20: Synthetic and field PP data for the LNAPL model. The gasoline and water reflections are centered at about 9ns.	190
Figure 4.21: PP AVO response for synthetic and field data for the LNAPL physical model. The data are shown in Figure 4.20.	191
Figure 4.22: Variation in θ vs. offset for the LNAPL physical model assuming straight rays and a linear gradient.	193
Figure 4.23: Synthetic and field TP AVA curves for the physical model. Data are shown in Figure 4.18.	195
Figure 4.24: Synthetic and field PP AVA curves for the physical model. Data are shown in Figure 4.20.	196
Figure 4.25: NMO corrected TP field data and AVA comparison. The dashed line is the water sand reflection	197

Figure 4.26: NMO corrected PP field gathers and AVA comparison. The dashed line is the water sand reflection amplitudes.	198
Figure 4.27: AVA attribute image and pre-stack time migrated wiggle trace overlay. Red indicates a large AVA gradient associated with the top-of-LNAPL reflection. Compare with the depth image in Figure 4.17.	201
Figure 4.28: Contaminated aquifer model and CMP locations for four cases. Each location has a different velocity profile and reflector configuration.	204
Figure 4.29: Ray paths for case 3 in Figure 4.28. Velocities are given in in/ μ s. Scaling to these units is necessary to use the ray tracing code which is designed primarily for crustal seismology problems.	205
Figure 4.30: θ vs. offset for case 3 (Figure 4.28) reflectors. θ increases much more slowly for the DNAPL reflector due to the large negative velocity contrast from the LNAPL to water saturated zones.	206
Figure 4.31: Variation in the angle of incidence vs offset at the base of the aquifer with and without a thin LNAPL layer.	207
Figure 4.32: TP CMP's for the four cases in Figure 4.28.	209
Figure 4.33: PP CMP's for the four cases indicated in Figure 4.28.	210
Figure 4.34: TP and PP AVO response for the upper reflectors indicated in Figure's 4.32 and 4.33.	211
Figure 4.35: TP and PP AVO response for the lower reflectors indicated in Figure's 4.32 and 4.33.	212
Figure 5.1: P and S velocities for a quartz sand as a function of water saturation. The	

curves are calculated with Gassman's equations assuming a depth of 10 m. . .	219
Figure 5.2: Location of field site.	221
Figure 5.3: Cross section of the Trinity River incised valley. The sediments represent a typical valley fill sequence. (modified from Siringan and Anderson, 1993) . . .	222
Figure 5.4: Three shots taken from the Bolivar Peninsula line. The top-of-sand reflector has a zero offset arrival time of around 40 -50 ms. Variation along this reflector is obvious in the shot gathers.	223
Figure 5.5: Interpreted seismic profile indicting primary unit boundaries. Compare to Figure 5.3. (The data showing the lateral boundary of the incised valley are not included in this study)	225
Figure 5.6: Shot point locations used for travel time inversion are shown with red asterisks.	227
Figure 5.7: Velocity field derived from travel time inversion.	228
Figure 5.8: Expected and measured AVO response for velocity structure at CMP 1150 for case 1) partial gas saturation, and case 2) no gas present. The measured AVO gradient approaches the curve for partial gas saturation.	231
Figure 5.9: ITG display showing the increase in absolute amplitude associated with the top and base of the fluvial sand unit.	232
Figure 5.10: Absolute value of normalized amplitudes for the top of sand reflection with increasing angle of incidence, for CMP supergathers 1127, 1137, 1147, and 1157. The increase in amplitude is visibly evident in the representative gather between 40 ms and 55 ms. Angles of incidence were calculated by ray tracing through the	

velocity model. 234

Figure 6.1: In the upper figure, a seismic trace is plotted along with the first 25 atoms of the decomposition. The reconstructed trace (green) is plotted with the residual (blue) in the lower figure. The energy of the residual, E_r , is less than $0.001 E_0$. The reconstructed trace is a linear summation of 96 wavelets which were extracted in three iterations. 241

Figure 6.2: Different t-f representations of a 20 Hz Ricker wavelet. The WD of the analytic wavelet is similar to our t-f distribution. The WD of the real wavelet has a large DC component. Note that these are the absolute values of the distributions, and that the WD has negative terms for both the real and analytic cases. 243

Figure 6.3: Cross sections through the t-f distributions at $t=t_0$. In this comparison, we are interested in the shapes of the distributions, not the amplitude scaling. Horizontal labels are frequencies in Hz. The WD of the analytic trace has essentially the same shape as our distribution. The WD of the real trace has a large DC component, but is similar at high frequencies where the ω^4 term dominates. 245

Figure 6.4: A multi-component signal, and t-f representations via 1) our distribution, TF; 2) the WD of the analytic trace; and 3) the WFT. The WD has severe cross-term interference which has amplitudes near that of the desired signal. The WFT has no cross-term problems, but provides relatively poor time resolution. 246

Figure 6.5: Seismic profile over a known hydrocarbon deposit. The well location is shown with a dashed line. The strong reflection at the high in the discontinuity is associated with hydrocarbon accumulation. 254

- Figure 6.6:** Seismic profile taken from the windowed area in Figure 6.5. The hydrocarbon accumulation is between traces 30 and 100 and from 2.5 - 2.9s. The spectral trend is essentially the same at both trace 10 and trace 76, which is not what we suspect. This is not too surprising given the heavy processing applied prior to attenuation analysis, and spectral estimates may be indicative of processing artifacts. This example illustrates the need for pre-stack analysis, with minimal data manipulation. 255
- Figure 6.7:** Attenuation model used to generate multi-offset synthetic seismograms. The black box corresponds to a zone of high attenuation with $Q=10$ 256
- Figure 6.8:** A zero-offset section generated using the attenuation model in Figure 6.7. Band-limited noise was added to the data. The zone of high attenuation is delineated. The banding is related to random noise and becomes more prominent deeper in the section where the signal to noise ratio approaches 1. 257
- Figure 6.9:** CMP gathers of the data generated using the model in Figure 6.7, and CMP gathers of the attenuation attribute. The attribute stack is a significant improvement over Figure 6.8. 258
- Figure 6.10:** Attenuation model for an aquifer contaminated with DNAPL, and 6-fold stack of synthetic data. 261
- Figure 6.11:** Stacked data after adding band-limited noise and the $1/HA$ attribute. The zones of residual DNAPL are clearly delineated as anomalous regions, but the response across the free DNAPL at the base of the aquifer is essentially random. 264

- Figure 6.12:** Comparison of $1/HA$ (high attenuation attribute) and LA (low attenuation attribute). A zone of low attenuation associated with the free DNAPL is consistently and definitively resolved with LA. 265
- Figure 6.13:** Zero offset GPR profile from the test pit at HARC. Note reflections from the QS/CS boundary (yellow), CS/CL boundary (green), and a diffraction from a buried PVC pipe (red). 267
- Figure 6.14:** HA attribute with wiggle traces overlain for the GPR profile shown in Figure 6.14. The interference from the pipe diffraction, tuning as the wedge pinches out, and random noise effect the consistency of HA. Overall, the wedge of CS appears darker than the overlying material indication high relative attenuation. This is consistent with our expectations. 268

LIST OF TABLES

Table 3.1. Characteristics of major hydrogeologic units at the site. (Kahle and Olsen, 1995)	122
Table 4.1. Cole-Cole parameters used for hypothetical aquifer model	159
Table 4.2. Factors affecting GPR amplitudes (source: Castagna, 1993)	166
Table 5.1. Parameters used for calculating R_{pp} vs. angle of incidence.	229
Table 6.1. Parameters for velocity model.	253
Table 6.2. Aquifer model parameters for GPR simulation	260

CHAPTER 1. INTRODUCTION

THE STATE OF ENVIRONMENTAL GEOPHYSICS

I begin with a general discussion of the role of geophysics in environmental studies, and contrast this with geophysics in oil exploration, which is analogous in many respects. This discussion serves to establish a basis for the importance and relevance of my doctoral research. My experience has primarily been in ground-penetrating-radar (GPR) and shallow seismic reflection, and while the following discussion is probably most relevant to these disciplines, much of it is applicable to environmental geophysics in general. I begin with an observation from Bedient et. al.'s (1994) textbook on groundwater contamination

“Because of the difficulty in locating NAPLs [(non-aqueous phase liquid contaminants)] in the subsurface, borehole and surface geophysics are becoming more popular for site characterization Currently, the application of geophysics at hazardous-waste sites is limited by the paucity of results from research sites and by the small number of personnel that are trained to use geophysics for ground water remediation problems”

This statement encompasses three important points:

- 1) Site characterization in groundwater remediation remains a significant problem (Figure 1.1).
- 2) Groundwater specialists recognize that geophysical methods hold significant potential in site characterization.
- 3) Shallow geophysical methods remain at a relatively early stage of development, and as such, the full potential has not been recognized nor have geophysical



Figure 1.1: Sign indicating concern with saltwater intrusion into the sole source aquifer system on Guemes Island in the Puget Sound.

methods been fully accepted by the environmental remediation industry as a standard tool in site characterization.

The third point is perhaps the most surprising and ironic aspect of environmental geophysics, particularly when compared to the oil industry where geophysical methods, primarily seismic reflection, have become standard instruments in oil exploration and reservoir monitoring. Certainly the scales are different. In groundwater studies we may be interested in features as small as a few centimeters at depths less than 5 m whereas oil exploration is concerned with features on the order of tens or hundreds of meters at depths greater than 1 km. However, the basic problem faced in both regimes is the same: identifying subsurface features in a cost effective and accurate manner. Given that the basic problem is the same, it is clear that potential benefits derived from geophysical methods are also analogous. Characterization costs are reduced by minimizing the number of boreholes, and many subsurface details can be extracted with geophysical methods through effectively continuous sampling of the subsurface as opposed to point sampling with borehole methods. Additionally, surface geophysics are relatively non-invasive which is an important aspect in many environmental studies.

Given the many favorable aspects of applying geophysical methods in the shallow regime, it may be surprising that geophysics is not as common and accepted in the environmental world as it is in the oil industry. There are several reasons for this. First consider that the shallow regime presents specific challenges that are not often encountered in oil exploration (this will be discussed in greater detail below), and although

the physics governing various processes are identical, certain aspects may have more significance in one regime relative to the other. For this reason, standard methodologies employed in the oil industry require a greater effort than simply scaling down the technology, and without proper analysis and application these methods can and do fail. Thus, a certain amount of methodology must be developed specifically for environmental geophysics and this must take place independently of developments in the oil industry. Given this limitation in technology transfer, consider development of geophysical methods in oil exploration. For several decades, vast sums of money have been invested in research and development of geophysical methods, and therefore exploration geophysics is currently a relatively sophisticated and well developed science. The oil industry is a market driven business with high cash flow, and therefore companies are willing to invest large sums of money in potentially innovative methodologies that will give them market advantage, even if there is some risk to that investment. This is in sharp contrast to the environmental industry, where significant sums of money and demand for geophysical research have only come about in the past 15 - 20 years. Funding for environmental research is driven primarily by government spending related to environmental policy, or spending in the private sector to comply with government regulation. Since the environmental industry is not market driven, available funds are necessarily limited. With limited research funds, fewer scientists are attracted to environmental geophysics. However, a more recent trend has seen geophysicists from established research disciplines, such as deep crustal seismology, delving into environmental research. Again, the primary driving force seems to be economics, where although funding is limited for environmental

research, the competition for funds in pure research disciplines is even greater.

Up to this point, I have identified the two primary reasons for the relatively immature state of environmental geophysics: 1) it is a young science, and 2) limited funding is available for research. I now turn to the general status of geophysics in the environmental industry. In the past four years, I have had the opportunity to meet and discuss various aspects of geophysical research with a variety of environmental professionals from both academia and the remediation industry. The attitude toward the value of geophysical methods has been at best guarded optimism, and more often I have been met with more than a healthy amount of skepticism. I suspect that the somewhat negative attitude arises for two reasons; 1) unfamiliarity with geophysical methods, and 2) previous negative experience with geophysical vendors or consultants that either purposely or mistakenly misrepresented the limitations and/or capabilities of a specific technique. I personally have seen blatant misrepresentation of geophysical capabilities by hardware vendors at professional meetings. It is important to recognize that all geophysical methods work best for certain site conditions (i.e. one method may work well at a given site while another method performs poorly), and that no geophysical tool works well under all conditions.

Based on the above discussion, I make three important observations:

- 1) Geophysics is an important and relevant aspect of environmental studies. It is my feeling that geophysical methods in general can and should be a standard tool in site characterization.
- 2) For full acceptance in the environmental community, it is of utmost importance

that geophysicists present results in a realistic manner, carefully pointing out the limitations and capabilities without bias. This is particularly relevant when the audience is not familiar with geophysical methods.

3) Limited funds and the fact that no geophysical method works well under all conditions make it important that the environmental geophysicist is familiar with a variety of geophysical tools, and in that sense is a generalist.

I have attempted to carry out my research with a philosophy consistent with these three points. I have had the opportunity to carry out field work at a number of sites with a variety of geophysical tools (Figure 1.2). While all of the work was applicable to my own research, much was carried out in support of the research of others. My research has not been funded under any single project, and I have had the good fortune to have, and tried to take full advantage of, the numerous and varied research opportunities that have arisen during the past four years.

WAVE-PROPAGATION BASED GEOPHYSICAL METHODS

I refer to two general types of waves: 1) elastic waves, and 2) electromagnetic waves. Elastic waves include a number of modes that are either compressional (the direction of motion is parallel to the direction of wave propagation) or transverse (the direction of motion is perpendicular to the direction of wave propagation), or some combination of these two types of motion. In reflection seismology, compressional waves are the type most commonly measured and analyzed, although shear wave reflection

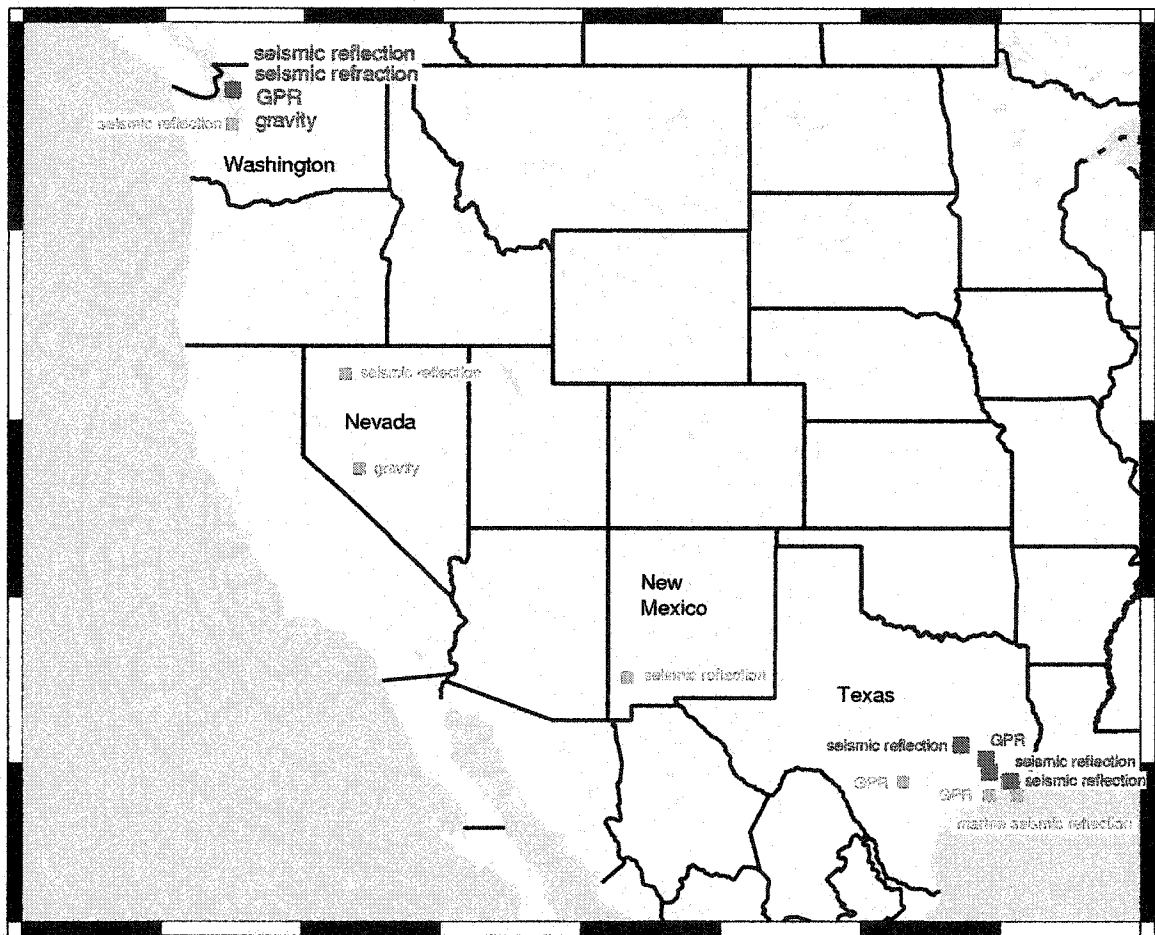


Figure 1.2: Field location and geophysical methods used in work relevant to this study. Red indicates sites discussed specifically in this dissertation.

surveys are common. Often, shear waves must be considered in compressional wave analysis since a purely compressional wave generates reflected and transmitted shear waves when it is incident on a boundary separating materials with differing acoustic impedance, which is the product of seismic velocity and material density (Aki and Richards, 1980).

All electromagnetic waves are transverse, and consist of coupled electric and magnetic fields that are orthogonal. Maxwell's equations, which describe electromagnetic fields, can be decoupled so that the electric and magnetic fields can be considered independently (Griffiths, 1989). In ground penetrating radar (GPR), we consider the propagating electric field exclusively. An oscillating electric field is generated through an antenna that then propagates through the earth and is reflected at boundaries separating materials with differing electric contrast which is a complex relationship of electric permittivity, magnetic permeability, and conductivity (I do not use the term electric impedance since this is associated with AC transmission in conductors). For most earth materials in which the GPR signal will propagate efficiently the magnetic permeability is roughly constant and the conductivity is low, so we are primarily concerned with differences in permittivity. Electric field propagation methods contrast with electromagnetic induction methods where an oscillating electromagnetic current is induced in the earth and the resulting electric or magnetic field is measured at the surface. Induction methods are well suited to high conductivity earth materials and operate in the frequency band below 1 MHz whereas propagation methods are suited to low conductivity soils and operate in the frequency band between 10 MHz and 1 GHz.

Seismic waves and electromagnetic waves are analogous in many respects (Szaraneic, 1976; Szaraneic, 1979; Ursin, 1983). Both classes of waves are reflected and transmitted at material boundaries and the kinematic behavior is completely analogous. This being the case, many of the acquisition procedures and sophisticated processing tools developed for reflection seismology can be applied directly to GPR data by simply scaling the units so that the magnitudes of electromagnetic velocities, frequencies, and depths are similar to those encountered in seismology (Bradford et al., 1995; Loughridge, 1998). The concepts and principles involved in image processing are essentially the same for the two methods, with differences in the emphasis on certain aspects of the processing flow such as coherent noise removal and velocity gradients. The subsurface representation resulting from the two methods is similar to a cross section of the earth's stratigraphy with reflections from various boundaries appearing as amplitude highs along the profile. Imaging is used to determine the location of material boundaries, but does not indicate the type of material.

The analogy between electromagnetic and seismic waves breaks down when the dynamics of wave propagation are considered. Obviously the mechanism of wave propagation is different and this effects the amplitude, frequency content, and phase of the reflected wavelet. Study of variations in these properties forms the basis of attribute analysis which is used to predict and constrain the types of subsurface material through which the wave is propagating or from which it is reflected. Attribute analysis has been successfully applied to seismic data for direct detection of hydrocarbons. Since the principles governing attribute variations differ in GPR studies, we may only borrow the

concepts of attribute analysis from seismology. Implementation and analysis require careful consideration of the physics governing electromagnetic wave propagation.

For both seismic and GPR studies, high frequencies correlate with high resolution and shallow penetration, whereas low frequencies correlate with lower resolution and deeper penetration. In shallow seismic reflection (on land), dominant signal frequencies are typically between 100 and 200 Hz with the practical upper limit (given current technology) of around 500 Hz (Steeple, 1998). Compressional wave velocities in dry, unconsolidated sediments vary from as low as 100 m/s (Bachrach et al., 1998; Bachrach and Nur, 1998) to as high as 2000 m/s for lodgement tills. Velocities in water saturated sediments are on the order of 1500 - 2500 m/s. Typical velocities for the vadose and saturated zone are around 400 m/s and 1700 m/s respectively. Given the range of expected frequencies, and based on a $\lambda/2$ criteria, we can expect to resolve features on the order of 0.4 - 2 m in the vadose zone and 2 - 10 m in the saturated zone. Compressional wave reflections are rarely observed at depths less than 3 m. High resolution data (> 100 MHz) can be extracted at depths up to 100 m or more. A depth range of 3 m - 200 m can reasonably be considered to fall into the realm of shallow seismic, or high resolution studies. These are just rough guidelines and actual results are strongly site dependent. Resolution and depth of penetration can be much higher or lower depending on the source and energy absorption characteristics of the earth materials. The best results are generally obtained in moist or damp, but not wet, clays.

In GPR studies the velocities and frequencies are much higher, but the ratio of velocity to frequency is similar to seismic studies, and therefore wavelengths and resolving

power are on a similar scale. GPR operates in the frequency band from 10 MHz - 1 GHz, with a frequency of 100 - 225 MHz typical for groundwater studies. Velocities in dry and water saturated sands are on the order of 0.15 m/ns and 0.05 m/ns respectively. Thus we can expect to resolve features on the order of 10 - 20 cm in the water saturated zone and 30 - 60 cm in the vadose zone. Depth of penetration varies from ~ 0 m under the worst conditions to as much as 50 m under ideal conditions¹. Under good conditions we can typically expect 10 - 20 m of penetration depending on the frequency of antenna used. Reflections can essentially be detected just below the surface and there is not a significant problem with the minimum depth of penetration. The best results in GPR studies are obtained in dry sandy environments (low conductivity), but excellent results have been obtained below the water saturated zone in many areas (Loughridge, 1998).

DISSERTATION RESEARCH SUMMARY

In the course of the introductory discussion, I referred to processing methodologies and analysis concepts developed in the oil industry for oil exploration scale seismic reflection data. Since a great deal of sophistication already exists in oil exploration, it is advantageous to environmental geophysics to utilize direct technology transfer when possible. I refer specifically to two classes of reflected wave-field data analysis: 1) imaging, and 2) attribute analysis. In imaging, the concepts of data processing

¹GPR signals will actually propagate several kilometers in ice, and GPR has been used to image the base of the Antarctic and Greenland ice sheets.

are exactly analogous for oil exploration, shallow seismic reflection or GPR, but significant differences exist in the velocity gradients and coherent noise fields for the three methods. These differences require consideration and imaging must be approached with the appropriate tools and analysis to produce accurate images. In attribute analysis, as long as we consider differences in the velocity fields, the processes and methods used in oil exploration can be applied directly to shallow seismic data. In GPR attribute analysis significant differences exist in the dynamics of wave propagation, and although some tools developed for seismic attribute analysis may be appropriate, interpretation of the results requires careful consideration of the physical principles governing electromagnetic wave propagation.

Given the significant number of similarities in the two classes of wave propagation it is natural to combine, or at least conduct research in both areas simultaneously. This is particularly true in environmental research given the need for a generalist approach. The two methods tend to work best under very different conditions, and expertise in both areas provides a complimentary set of tools that can be used to approach many site characterization problems. My research has been focused on investigating and developing non-traditional approaches to shallow aquifer characterization with shallow seismic reflection and GPR. I have investigated methods of determining aquifer geometry (imaging), and for direct detection of non-aqueous phase liquid (NAPL) contaminants (attribute analysis). Much of this research has involved technology transfer (evaluation and implementation) from the oil industry, and a significant portion has been devoted to new methods of data analysis for both seismic and GPR data. The dissertation research

consists of five stand alone research projects that involve seismic reflection and GPR data processing and analysis. There are two important aspects that link each of the projects

- 1) Each project involves processing and analysis of wave propagation geophysical methods
- 2) Each of the projects involves a new approach to data analysis either through alternative processing strategies that are not widely applied in environmental studies or development of new processing methods and/or algorithms.

Imaging

Accurately determining the velocity field is the most important step in producing good quality, accurate images from seismic reflection data. Compressional wave velocities can change by a factor of four or more as the wave travels from dry or moist sediments in the vadose zone to fully saturated sediments in the saturated zone. This degree of velocity heterogeneity is rare in conventional seismic reflection studies and severely violates many of the assumptions inherent in normal-moveout (NMO) data processing. Conventional methods of velocity analysis fail and velocities can be severely over estimated. In shallow seismic reflection, this problem is compounded by very low signal to noise in the near offset regime, and we are forced to use relatively large offset-to-depth ratios which increases the divergence from standard assumptions, and NMO processing can lead to very large errors in depth and layer thickness estimates. Nevertheless, most shallow seismic reflection data are processed using standard NMO methodologies with little or no consideration of the errors involved. Pre-stack depth

migration (PSDM) is one of the most powerful imaging tools developed in the oil industry and is an appropriate method for dealing with the large vertical velocity gradient in shallow seismic studies. In Chapter 2, I present a detailed discussion of the errors that can result from conventional NMO processing, discuss special considerations in the application of PSDM to shallow reflection data, and present a synthetic and three field case studies illustrating PSDM imaging of shallow aquifer systems. In GPR imaging, an extreme decrease in velocity occurs across the piezometric surface. As for a positive velocity contrast, conventional velocity analysis tends to over predict the velocity, although the effect is more severe in the case of a negative velocity contrast. As such, many of the arguments presented in Chapter 2 are also relevant for GPR data processing, and I do not present a specific discussion of imaging GPR data (although one example of PSDM of GPR data is presented in Chapter 4).

In Chapter 3, I present a seismic reflection case study from a glacial sedimentary environment. The data were acquired as part of a study to determine the feasibility of imaging a shallow aquifer system on a small island in the Puget Sound (Figures 1.1 and 1.2). In this case, I apply Dip Moveout (DMO) processing which is rarely applied in environmental studies, but can improve velocity analysis and image quality where there are dipping layers or scattering events. An additional complicating factor in this case was the presence of a laterally variable, thin layer of high velocity lodgement till within the first few meters of the surface. The target zone was entirely below the high velocity layer. Thin high velocity layers reduce the amount of energy that is reflected from below and complicated image processing.

Attribute analysis

I begin this discussion with another quote from Bedient et. al. (1994)

“Because of the difficulty in locating NAPLs in subsurface ... surface geophysics [is] becoming more popular for site characterizations. Ground-penetrating radar ... [is] better suited for detecting subtle changes in subsurface conditions, such as a moving free-phase NAPL mass, than in assessing static conditions.”

This statement is entirely true for conventional GPR studies where only imaging is used to determine geometric relationships of subsurface features. Based only on the reflection image, no body can be confidently identified as a contaminant unless the body changes shape through time. Direct detection is a new approach to the analysis of GPR data that has been used successfully in the energy industry to identify oil and gas reserves from seismic reflection data. Direct detection refers to a general method of data analysis through which material properties are determined remotely by quantification of reflected wave attributes (attribute analysis). Attribute analysis is the study of reflected wave characteristics such as amplitude, frequency content, and phase. Direct detection can be used to predict the presence and location of NAPL contaminants in the subsurface, even under static conditions.

In Chapter 4, I present a detailed discussion of GPR amplitude vs. offset analysis for direct detection of free phase NAPLs. Although I borrow interpretive tools from seismology, the analysis is not straightforward and requires careful consideration of electromagnetic dynamic properties.

In Chapter 5, I present a shallow seismic case study where a predictable amplitude vs. offset (AVO) response was detected. This example illustrates the potential to use

AVO analysis in shallow seismic. I know of no example in the literature in which a predictable AVO response was successfully measured. Additional research is needed to determine potential for contaminant detection.

In Chapter 6, I present a new wavelet decomposition and time-frequency representation, and illustrate applications in attenuation analysis for hydrocarbon exploration and NAPL detection using GPR. While AVO analysis holds potential for direct detection of free phase NAPLs, attenuation analysis holds more promise in the detection of residual contaminant.

CHAPTER 2. IMAGING SHALLOW AQUIFERS IN DEPTH USING PRE-STACK DEPTH MIGRATION

INTRODUCTION

As interpreted shallow reflection data become more prevalent as input for quantitative groundwater and engineering studies, it is necessary to evaluate our ability to accurately predict depth and layer thickness based on conventional processing methodologies. Typically, multi-offset reflection data are processed by applying a normal moveout (NMO) correction based on a stacking velocity (v_{stk}) profile that moves all energy to its zero-offset equivalent arrival time (t_0). Traces are then summed in common midpoint (CMP) gathers to produce a stacked section. The inherent NMO assumption is $v_{stk} \approx v_{rms}$, where v_{rms} is the root-mean-square velocity. When this approximation is valid, we can extract a depth profile based on the Dix equation (Dix, 1955). While the NMO assumption is often valid above the saturated zone, it breaks down across the piezometric surface due to the large velocity contrast that typically exists across this boundary. It is common for the compressional wave velocity to increase by a factor of four or more where shallow, unconsolidated sediments change from a dry or partially saturated regime to a full saturation. Although this severe velocity gradient has received much attention in the literature (Bachrach et al., 1998; Bachrach and Nur, 1998; Miller and Xia, 1998; Steeples and Miller, 1990), there has been no quantitative discussion of the errors resulting from the NMO approximation under these conditions, even though NMO and

stacking are the methods most commonly used to process the data. The objective of this study is to present a detailed and quantitative discussion of the errors resulting from the NMO approximation, and to present alternative processing schemes that will result in more accurate subsurface prediction. Although the discussion is focused on the transition from a partially saturated to fully saturated regime, the arguments are applicable to any large vertical velocity gradient such as the transition from unconsolidated sediments to bedrock or a sediment - salt interface.

NMO processing can provide an acceptable image in time, however there are significant problems with data distortion when trying to image features both above and below the piezometric surface. Miller & Xu (1998) discuss this problem, but do not address the depth prediction errors inherent in the method. The optimum window (Hunter et al., 1984) to observe reflections above the saturated zone typically occurs at much smaller offsets than that to observe reflections below the water table. Since the optimum window technique is commonly used in shallow reflection applications (Steeple, 1998), it is important to consider the relationship of the stacking velocity function to the offset range, and how this dependence effects depth and layer thickness estimates. If we are interested only in targets below the piezometric surface, we may acquire relatively long offset data to avoid near offset problems with surface related noise. In this case, we have little or no velocity control for the shallowest part of the section and stacking velocities are measured only from reflections originating beneath the water table. Often such a stacking velocity function will appear well behaved (no large gradients and gradual increase with depth) and there will be no obvious indication of the large velocity gradient.

Naively assuming that a well behaved stacking velocity profile indicates the validity of the NMO assumption can lead to severe errors in depth prediction and incorrect data interpretations. We must consider the low velocity portion of the velocity field to accurately predict the subsurface.

For a typical velocity profile across the piezometric surface, v_{stk} is significantly larger than v_{rms} for reflections within about the first 30 m below the saturated zone. This leads to significant depth prediction errors if the Dix equation is assumed valid. The problem is exaggerated in the shallow environment because extremely low signal-to-noise ratios in the near-offset regime, often require us to record reflections at large offset-to-depth ratios (Baker et al., 1998; Hunter et al., 1984; Miller and Xia, 1998). Stacking velocity increases with increasing offset range, leading to greater divergence from the NMO assumption.

When conventional velocity analysis fails, we must resort to pre-stack depth migration (PSDM) or other inverse methods. We typically think of PSDM as only necessary for laterally heterogeneous velocity fields, however, it is also necessary when the vertical velocity gradient is very large. While there are less computationally intensive methods of obtaining accurate velocity - depth profiles, PSDM will provide the most accurate and detailed images. In this paper, I first present a detailed discussion of problems associated with recording and processing reflections originating below the piezometric surface with the focus on errors resulting from the NMO assumption. I then discuss improving accuracy through alternative processing schemes with a focus on pre-stack depth migration. I complete the discussion with a synthetic example and three case

studies from differing sedimentary, and hydrologic environments that illustrate some problems and benefits of pre-stack migration.

PROBLEMS WITH RECORDING AND PROCESSING REFLECTIONS ORIGINATING BELOW THE WATER TABLE

According to Gassman's equations (Bachrach et al., 1998; Bachrach and Nur, 1998; Castagna et al., 1993; Gassman, 1951), compressional wave velocity remains relatively constant to around 99% saturation then increases abruptly to the velocity at full saturation (Figure 2.1)². While in the non-ideal field setting the change in velocity may be a somewhat more gradual function of saturation³, we expect the velocity change across the piezometric surface to be a sharp boundary relative to the seismic wavelength. This expectation is supported by field observations. Bachrach and Nur (1998) present an example of sand, with very high volumetric water concentrations (near full saturation), that has a velocity very close to the velocity of the dry sand and much lower ($\sim 1/13$) than the velocity of the saturated sand. Their example also illustrates that in a dynamic system, the piezometric surface does not necessarily correspond to the zone of saturation. In this discussion, I will only refer to the piezometric surface of a static system. The sharp velocity contrast leads to several significant problems which can be broken into four

²The velocity actually is a minimum between 90 and 100% saturation then increases slightly as the saturation goes to 0%, however for purposes of this discussion, this small change is insignificant compared to the large increase at full saturation.

³This is related to non-uniform distribution of gas in the pore space as opposed to the uniform distribution assumed by Gassman (1951).

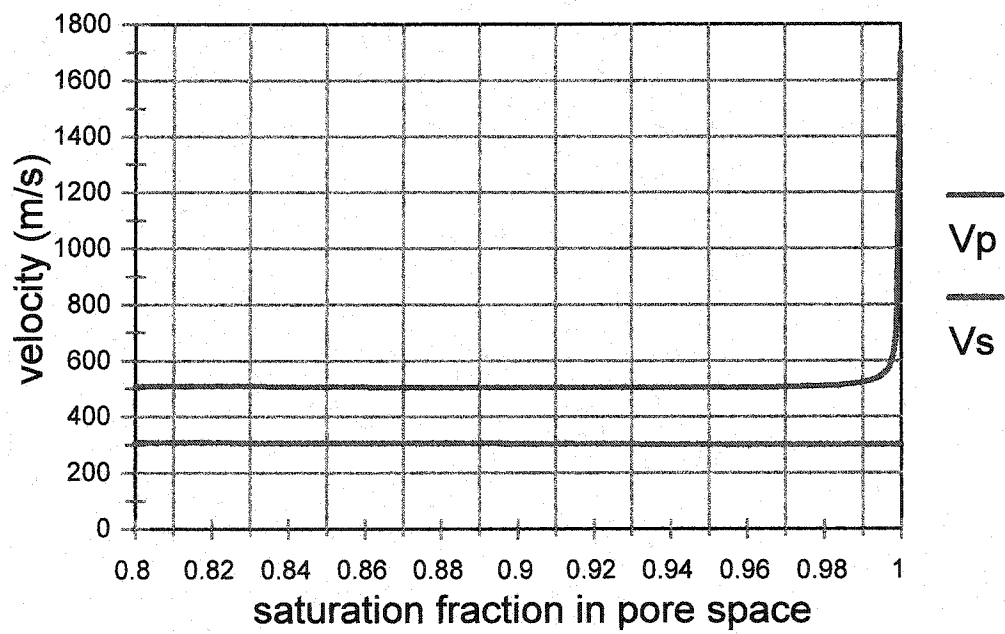


Figure 2.1: P and S velocities for a quartz sand as a function of water saturation. The curves are calculated with Gassman's equations assuming a depth of 10 m.

primary categories:

- 1) Geometric attenuation of source energy and transmission losses
- 2) Additional sources of coherent noise
- 3) Geometric loss of resolution
- 4) Departure from normal moveout (NMO)

The first three categories represent general problems that must be considered in any processing scheme, whereas the fourth poses problems specific to conventional NMO processing. In this section, I briefly discuss the first three categories, focusing on their adverse effect in conventional processing schemes. The remainder of the discussion will be devoted to errors that can result from conventional NMO processing.

Attenuation of source energy

Considering the two dimensional, acoustic case, and assuming a typical saturated velocity (v_{sat}) to dry velocity (v_{dry}) ratio of $v_{\text{sat}}/v_{\text{dry}} = 4$, the critical angle is 14.5° . Further assuming spherical spreading, and that there are no intrinsic or transmission losses above the water table, only 16.1% ($29.0^\circ/180^\circ$) of the original source energy is incident on the piezometric surface within the pre-critical aperture (Figure 2.2). This small fraction of energy is further attenuated by transmission losses across the piezometric surface.

Assuming a density increase of 25% across the boundary, the normal incidence reflection coefficient is $R_w = 0.667$ so the ratio of transmitted energy for the up and down going paths to the original incident energy is $(1 - R^2 = 0.555)^2 = 0.308$. Most of the energy is reflected back into the vadose zone or trapped beneath the piezometric surface. Typically,

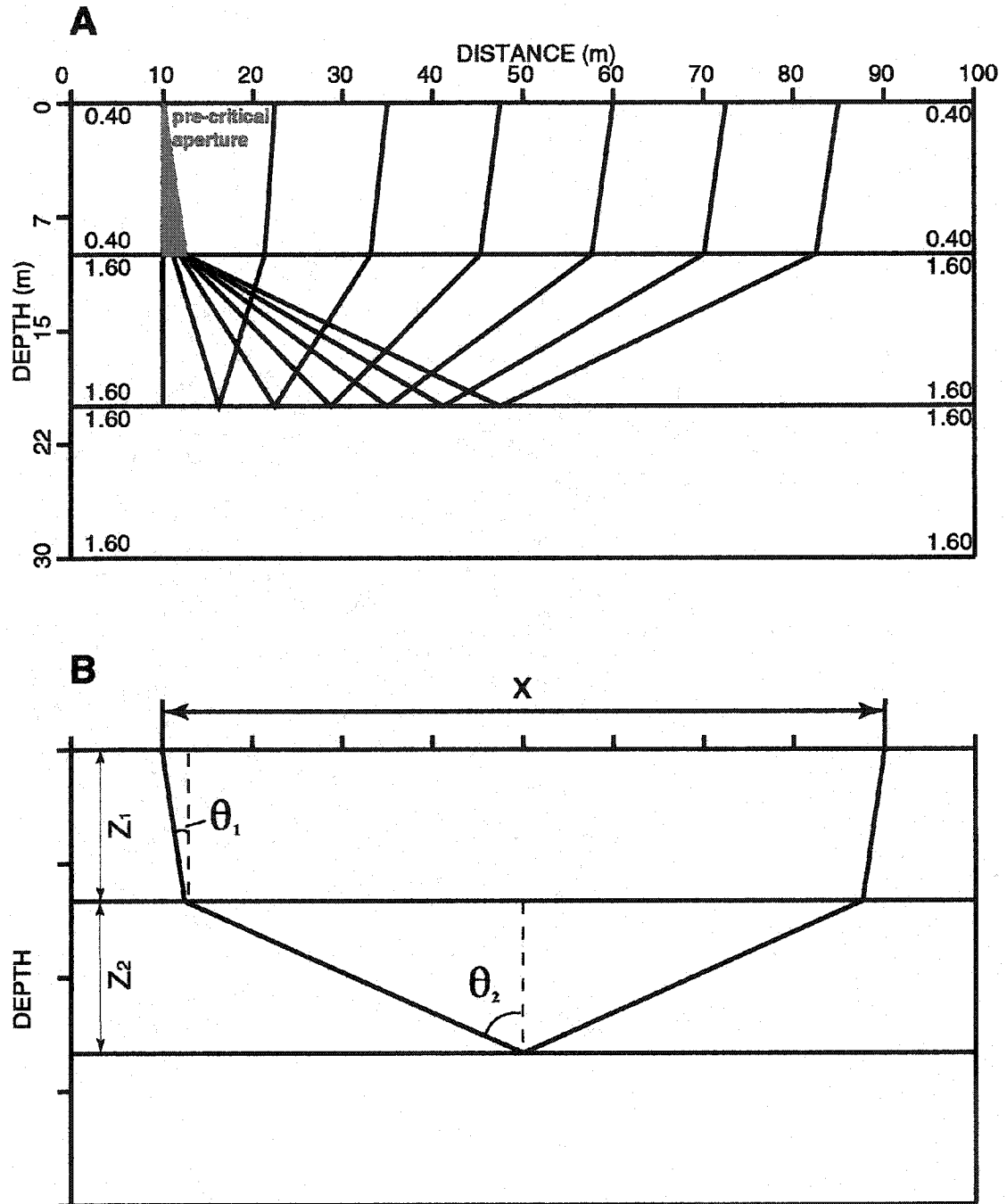


Figure 2.2: Ray diagrams indicating; A) severe ray bending across the piezometric surface, and B) parameters used in modeling. All energy reflected from the base of the second layer must pass through the pre-critical aperture. Indicated velocities are in km/s.

$R < 0.15$ for impedance boundaries within the saturated zone, so relative to R_w , a much smaller fraction of energy is reflected. All of the factors mentioned above combine to significantly reduce the energy that returns to the surface for reflections below the piezometric surface.

Coherent noise

The air wave and ground roll are strong sources of coherent noise that are almost always problematic in shallow reflection surveys. Depending on the depth to the piezometric surface, heterogeneity of the vadose zone, and the velocity contrast across the water table, additional sources of high-amplitude, low-velocity, coherent noise can be generated which interfere with deeper, primary reflections. This includes guided waves trapped between the surface and saturated zone (Robertsson et al., 1996), interbed multiples where significant impedance contrasts exist within the vadose zone, and converted modes generated at the piezometric surface (Figure's 2.3, 2.4, and 2.5). Each of these noise signals travel at velocities lower than the highest P-wave velocity (v_{ph}) above the saturated zone, so that for $v_{sat}/v_{dry} \gg 1$, interference with deeper reflections occurs in the near offset regime. Interbed multiples, generated above the saturated zone, pose an exceptional problem since they can have stacking velocities consistent with an increase in velocity with depth, leading to misinterpretation. The travel time curve and arrival time of these events, at near zero-offset, may not be substantially different from primary reflections (although they are easily identified with sufficient offset), and velocity filtering is not effective at removing this energy at near offset.

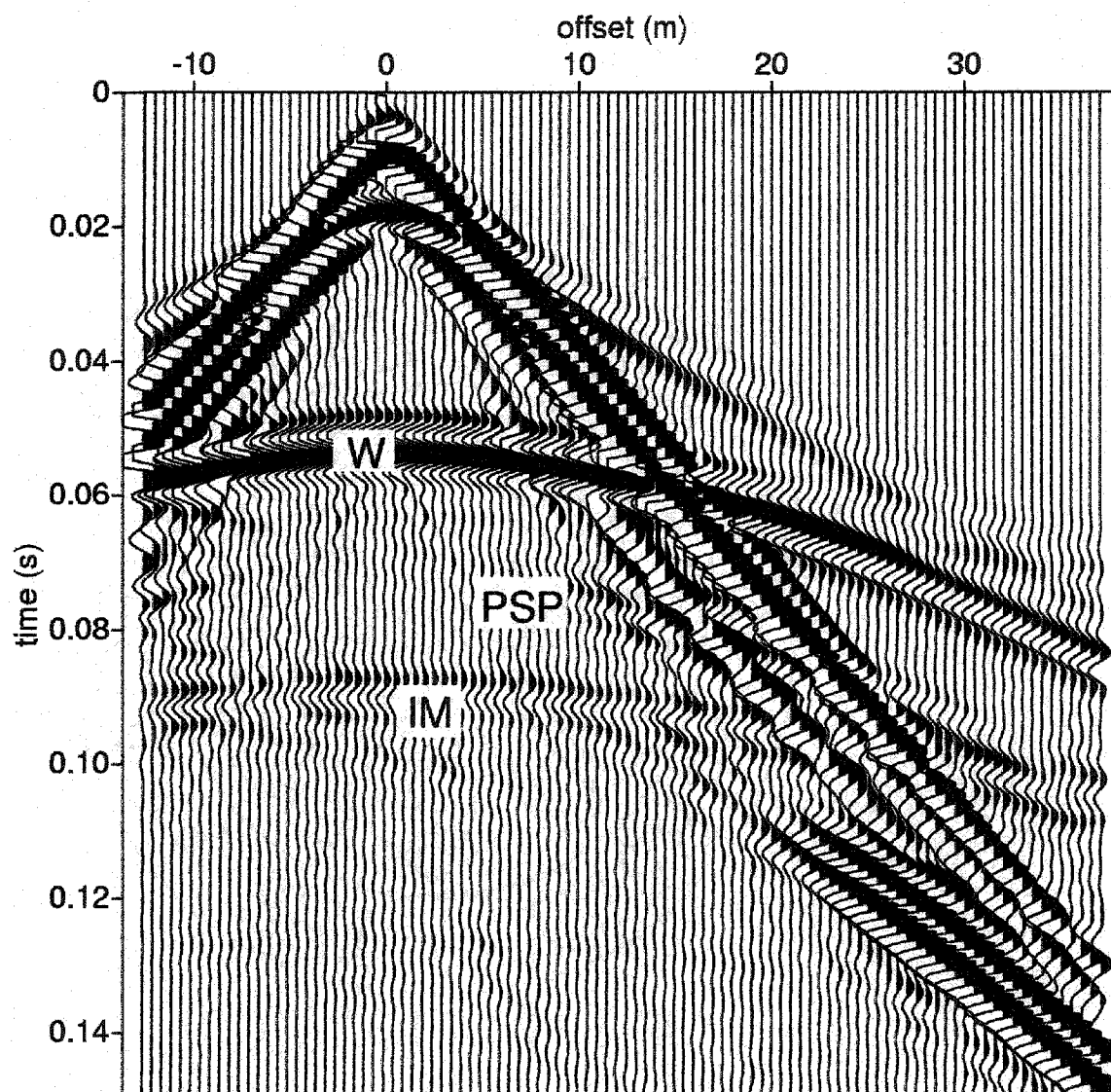


Figure 2.3: Visco-elastic synthetic seismogram based on a velocity model derived from travel time inversion of picks from Figure 2.4 (see Figure 2.31). W, PSP, and Im are the water table reflection, a PSP converted mode, and an interbed multiple respectively. No reflection from the aquitard is evident.

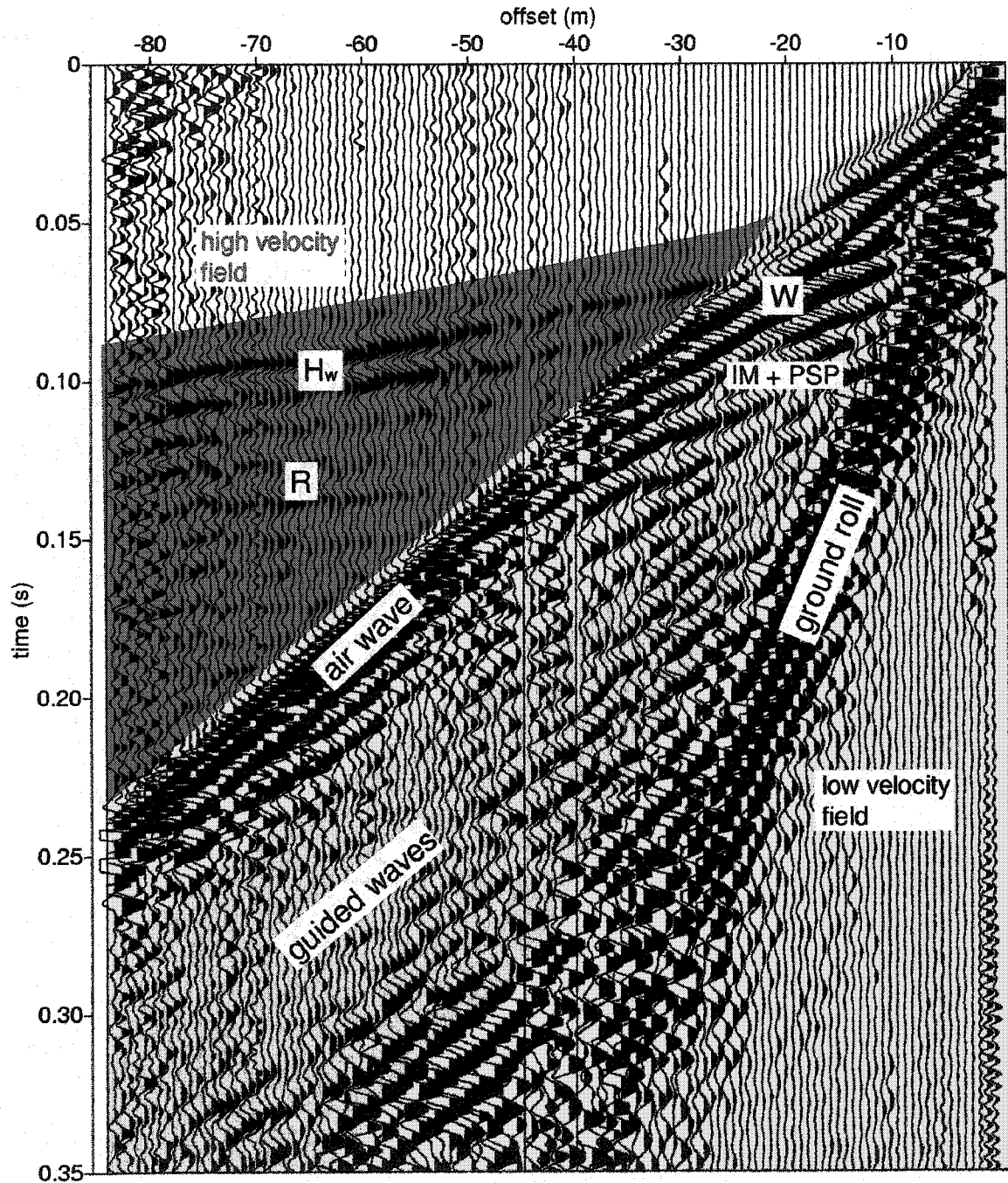


Figure 2.4: Shot record illustrating features commonly observed in shallow seismic studies. H_w and R are the water table refraction and deeper reflections respectively. The yellow region indicates the noise cone in this case.

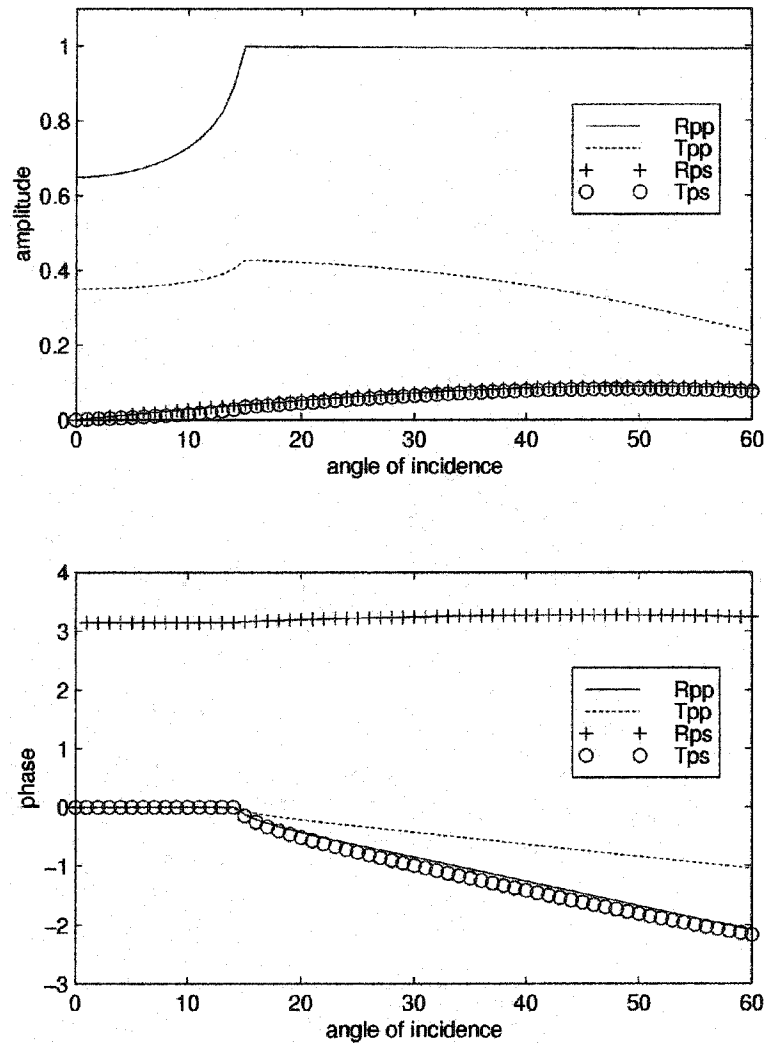


Figure 2.5: Reflection and transmission coefficients for primary and converted modes for a P-wave incident on the piezometric surface. Velocities are taken from Figure 2.1. Significant P-S conversion occurs for $\theta > 14^\circ$.

I define a region called the noise cone, (Figure 2.4) within which primary reflected energy is entirely masked by slow, high-amplitude coherent noise. This differs from the noise cone discussed by Baker et. al. (1998) only in that my definition refers to total masking of reflections rather than Baker et. al.'s slightly less restrictive definition of very low signal-to-noise ratios. The noise cone is contained within the linear t-x boundary defined by linear moveout at v_{nc} . The noise cone velocity (v_{nc}) depends on site conditions and may be defined by the direct wave, a guided wave mode, a ground roll mode, or the direct air wave. Below W, additional noise is generated, and reflected energy is relatively weak. Therefore, the noise cone is typically different above and below the piezometric surface with $v_{nc|<W} \leq v_{nc|>W}$, where W is the water table reflection (Figure 2.4). In many cases, coherent noise within this region has amplitudes that are one or more orders of magnitude greater than primary reflections, may be in the same frequency band (depending on the type of noise), and is often aliased. It is often difficult or impossible to remove this noise effectively, and we can extract primary reflected energy only at offsets greater than those defined by v_{nc} , particularly when the target reflectors are only a few meters (<30 m) below the piezometric surface.

Geometric loss of resolution

Vertical resolution is controlled by the value of the vertical wavenumber. As the vertical component of the wavenumber decreases, resolution potential decreases. As offsets increase, the lateral component of motion increases and the vertical wavenumber decreases resulting in decreased vertical resolution. Therefore, the theoretical resolution

limit of $\lambda/4$ is only valid at zero offset. As a wave travels across a large positive velocity contrast, the lateral component of motion becomes large at relatively small offsets due to severe ray bending (Figure 2.6A).

The second factor that contributes to loss of resolution at further offsets, arises due to traveltime convergence with the water table refraction. For a two layer case, traveltimes for the head wave traveling along the top of the second layer and the reflection from the base of the second layer are given by

$$t_h = \frac{2z_1}{v_1 \cos[\sin^{-1}(v_1/v_2)]} + \frac{x - 2z_1 \tan[\sin^{-1}(v_1/v_2)]}{v_2} \quad 2.1$$

$$t_r = \frac{2z_1}{v_1 \cos[\sin^{-1}(v_1/v_2 \sin \theta_2)]} + \frac{x - 2z_1 \tan[\sin^{-1}(v_1/v_2 \sin \theta_2)]}{v_2 \sin \theta_2} \quad 2.2$$

With nomenclature defined in Figure 2.2. For t_r ,

$$\frac{x}{2} = z_1 \tan \theta_1 + z_2 \tan \theta_2 \quad 2.3$$

$$\tan \theta_2 = \frac{x/2 - z_1 \tan \theta_1}{z_2} \quad 2.4$$

Clearly, as $\theta_1 \rightarrow \theta_c$, $x \rightarrow \infty$, or as $z_2 \rightarrow 0$, $\theta_2 \rightarrow \pi/2$ and in either case $t_r \rightarrow t_h$. More importantly, we also find that t_r approaches t_h as v_1/v_2 decreases. This is in sharp contrast to the divergence of t_r and t_h that is predicted with the NMO approximation (Figure 2.6B).

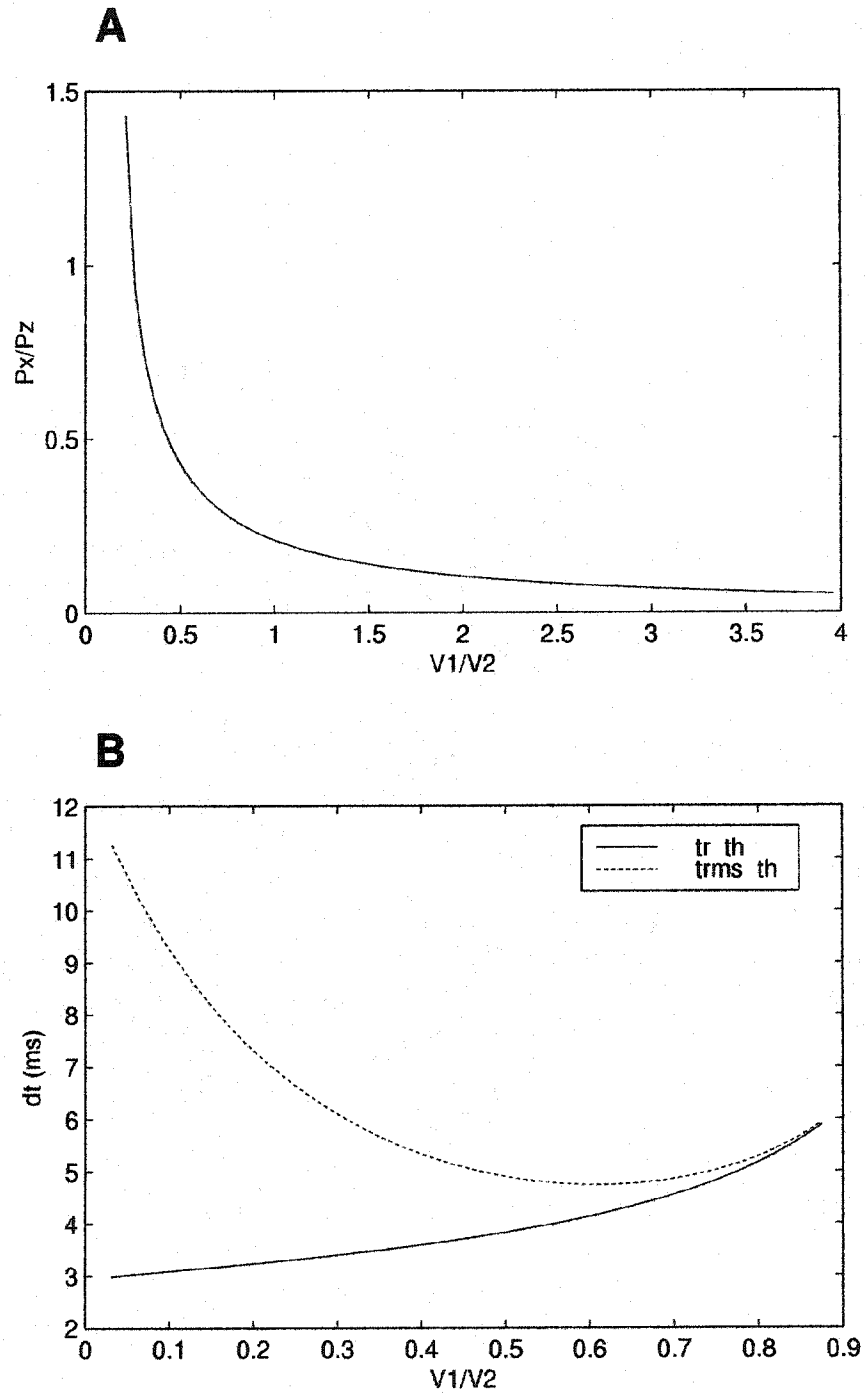


Figure 2.6: A) Velocity contrast vs. ratio of lateral to vertical component of wave motion for the transmitted wave at $\theta_1 = 14^\circ$. B) Head wave convergence ($x = 30$ m) as a function of velocity contrast for a reflection 10 m below the piezometric surface (Figure 2.2), where $dt = t_{lR} - t_{lHW}$, th is the head wave travel time, tr is the correct reflection travel time and $trms$ is the NMO approximation.

In the context of the present discussion, the presence of a large velocity contrast across the piezometric surface means that energy reflected from within the saturated zone will interfere with the water table refraction at relatively small offsets. Not only do we lose resolution, but since we may be limited to a small region between the noise cone and head wave, we may observe only a small part of the reflection or not at all.

To illustrate the effect of head wave convergence, first consider a piezometric surface at a depth of 10 m, vadose zone velocity of 400 m/s, and saturated velocity of 1600 m/s. I construct a model with four reflecting interfaces (R_5 , R_{10} , R_{15} , R_{20}), at 5 m intervals below the water table. I then generate a synthetic shot gather using a 4th order, finite-difference acoustic modeling code (Figure 2.7). The center frequency of the source wavelet is 500 Hz which is near the upper limit that is currently observed in field studies (Steeple, 1998). This gives a wavelength of 3.2m in the saturated zone corresponding to a theoretical resolution of 0.8 m. From this criteria we would expect to easily resolve the four reflectors below the water table. At zero offset, all reflecting interfaces are clearly resolved. With increasing offset, the reflections begin to converge with the water table refraction. R_5 begins to interfere significantly with the head wave at an offset of around 10 m and the two wavelets cannot be distinguished at an offset of 25 m. The useable portion of R_5 lies entirely within the 400 m/s direct arrival cone. If we were unable to effectively remove coherent noise within this region, we could not resolve R_5 . We can distinguish R_{10} to an offset of about 40 m, R_{15} to 50 m, and R_{20} to the maximum offset of 60 m.

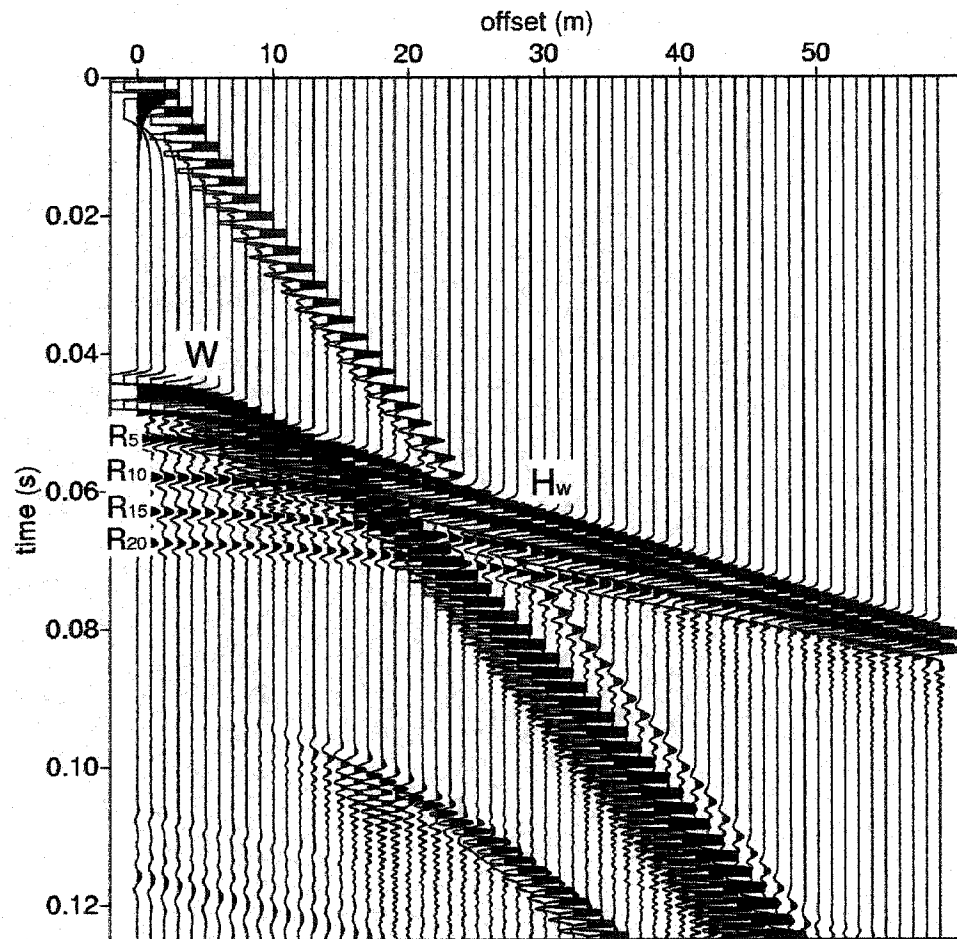


Figure 2.7: Acoustic seismogram for a model with four reflectors (R_5 - R_{20}) spaced at 5 m intervals below the water table (W). W is at a depth of 10 m. Head wave convergence decreases resolving power at far offsets.

Departure from NMO

Considering the ground to be composed of uniform horizontal layers, the traveltime t_r for a reflection from the N^{th} layer, and offset x , are related by the parametric equations (Al-Chalabi, 1974)

$$t_r = 2 \sum_{k=1}^N (h_k/v_k)(1-p^2v_k^2)^{1/2} \quad 2.5$$

$$x = 2p \sum_{k=1}^N (h_k/v_k)(1-p^2v_k^2)^{1/2} \quad 2.6$$

where v_k and h_k are the velocity and thickness of the k^{th} layer, and p is the ray parameter.

These equations cannot be solved in closed form. To obtain a direct t - x relationship,

Taner & Koehler (1969) derived the traveltime curve in terms of an infinite series with the following form

$$t_r^2 = C_1 + C_2x^2 + C_3x^4 + \dots + C_jx^{2j-2} + \dots \quad 2.7$$

In standard NMO processing, it is assumed that the two term truncation of this series is a reasonable approximation to the reflection traveltime and is given by

$$t_r^2 = t_0^2 + \frac{1}{v_{rms}^2}x^2 \quad 2.8$$

where t_0 is the zero offset traveltime and v_{rms} is the root-mean-square velocity at the base

of layer N. In practice, the stacking velocity, v_{stk} , and t_0 are found by fitting the $t^2 - x^2$ reflection travelttime curve, measured from the data, with Equation 2.8. Then $1/v_{stk}^2$ is the slope of the curve and the intercept is t_0^2 . In conventional processing it is assumed that $v_{stk} \approx v_{rms}$. Interval velocity, v_N , is then typically estimated using Dix inversion given by (Dix, 1955)

$$v_N^2 \approx \frac{v_{stk0|N}^2 - v_{stk0|N-1}^2}{t_{0|N} - t_{0|N-1}} \quad 2.9$$

Al Chalabi (1973) defines the heterogeneity factor g

$$g = v_{rms}^2 / v_a^2 - 1 \quad 2.10$$

where v_a is the time average velocity $\left(v_n = \frac{1}{t_n} \sum_{i=1}^n v_i t_i \right)$. The heterogeneity factor is a positive parameter that gives a measure of the velocity heterogeneity in the earth. It is zero for a homogeneous earth and increases as the degree of heterogeneity increases. For the two layer case, I can write g in terms of the ratios $a = z_1/z_2$, and $b = v_1/v_2$

$$g = \frac{a(b + 1/b - 2)}{(a + 1)^2} \quad 2.11$$

Examining Equation 2.11, we find that for $b=1$, $g=0$, which is of course the homogeneous case. The medium is also homogeneous when $a \rightarrow 0$, or $a \rightarrow \infty$, and for either of these cases $g=0$ as expected. As b becomes very large, or very small, the degree of heterogeneity increases, and according to Equation 2.11 as $b \rightarrow 0$, or $b \rightarrow \infty$, $g \rightarrow \infty$ as

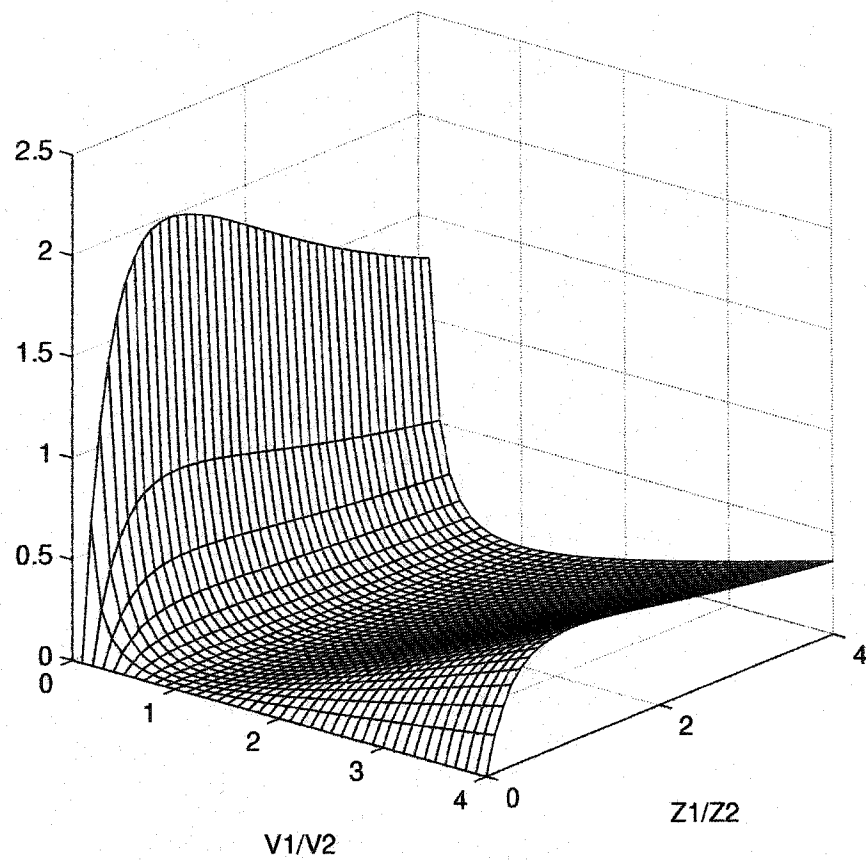


Figure 2.8: Heterogeneity factor, g , as a function of velocity contrast and depth ratio.

expected. Plotting g for a range of a and b of interest in shallow reflection (Figure 2.8), we find a maxima in g for $a = 1$ ($z_1 = z_2$) (this can easily be shown by setting $\delta g / \delta a = 0$), and a local minima at $b = 1$ ($v_1 = v_2$) which is obvious from the above discussion (or shown by setting $\delta g / \delta b = 0$). When $a < 1$, g decreases rapidly with decreasing a . When $b < 1$, g increases rapidly with decreasing b . For the current discussion, we are interested in the special case of $b \ll 1$.

Al Chalabi (1973) defines the bias as the error in the approximation $v_{stk} \approx v_{rms}$

$$B = v_{stk} - v_{rms} \quad 2.12$$

He shows that $B \geq 0$ and increases as the minimum or maximum offset increases. Al Chalabi also shows that B increases as g increases, so that over a highly heterogeneous earth, B can be quite large, even at relatively small offsets. Again, considering the two layer case, $B=0$ for the first layer but can be quite large for the second layer when $b \ll 1$. For $B > 0$, $v_{stk} > v_{rms}$, and it is obvious from Equation 2.9 that v_2 will be overestimated.

For the purposes of hydrologic or engineering studies, we want to examine how errors in the velocity estimation effect depth and layer thickness estimates. There are two sources of error that result from the assumption that $v_{stk} = v_{rms}$. The first is overestimating the interval velocity as discussed above, and the second is in overestimating t_0 . As I will show below, these two sources of error combine constructively to increase depth and layer thickness errors. First, I assume that a least squares fit to the traveltime curve is a good approximation to the velocity analysis procedure actually used when estimating v_{stk} from field data. Next, consider the example of $v_1 = 400$ m/s, $v_2 = 1600$ m/s, and $z_1 = z_2 = 10$ m,

and the target reflection from the base of the second layer. We find that at near zero offset, the two term approximation to Equation 2.7 provides a good estimate of the actual traveltime, but as offsets increase, the curves diverge significantly (Figure 2.9A).

Additionally, we see that least squares fitting of the true traveltime curve over predicts t_0 . Recall that in many cases, reflection data cannot be extracted inside the noise cone. For the reflector from the base of the second layer, we are limited to using offsets greater than 30 m. Calculating v_{stk} from larger offset range increases the bias, B , and increases the amount that t_0 is over predicted (Figure 2.9B). This leads to significantly larger depth and layer thickness errors.

Layer thickness estimate and corresponding error for the 2nd layer are given by

$$z_2 = \frac{1}{2}[v_2(t_{02} - t_{01})] \quad 2.13$$

$$\delta z_2 = \frac{1}{2}[\delta v_2(t_{02} - t_{01}) + v_2(\delta t_{02})] \quad 2.14$$

and the depth estimate and corresponding error are given by

$$d_2 = z_1 + z_2 \quad 2.15$$

$$\delta d_2 = \delta z_2 \quad 2.16$$

(assuming $\delta t_{01} = 0$, and $\delta z_1 = 0$). We see that in the two layer case, the contributions from δv_2 and δt_{02} add constructively since both are positive.

The error is compounded if we compute the depth, d_2 , based only on a reflection

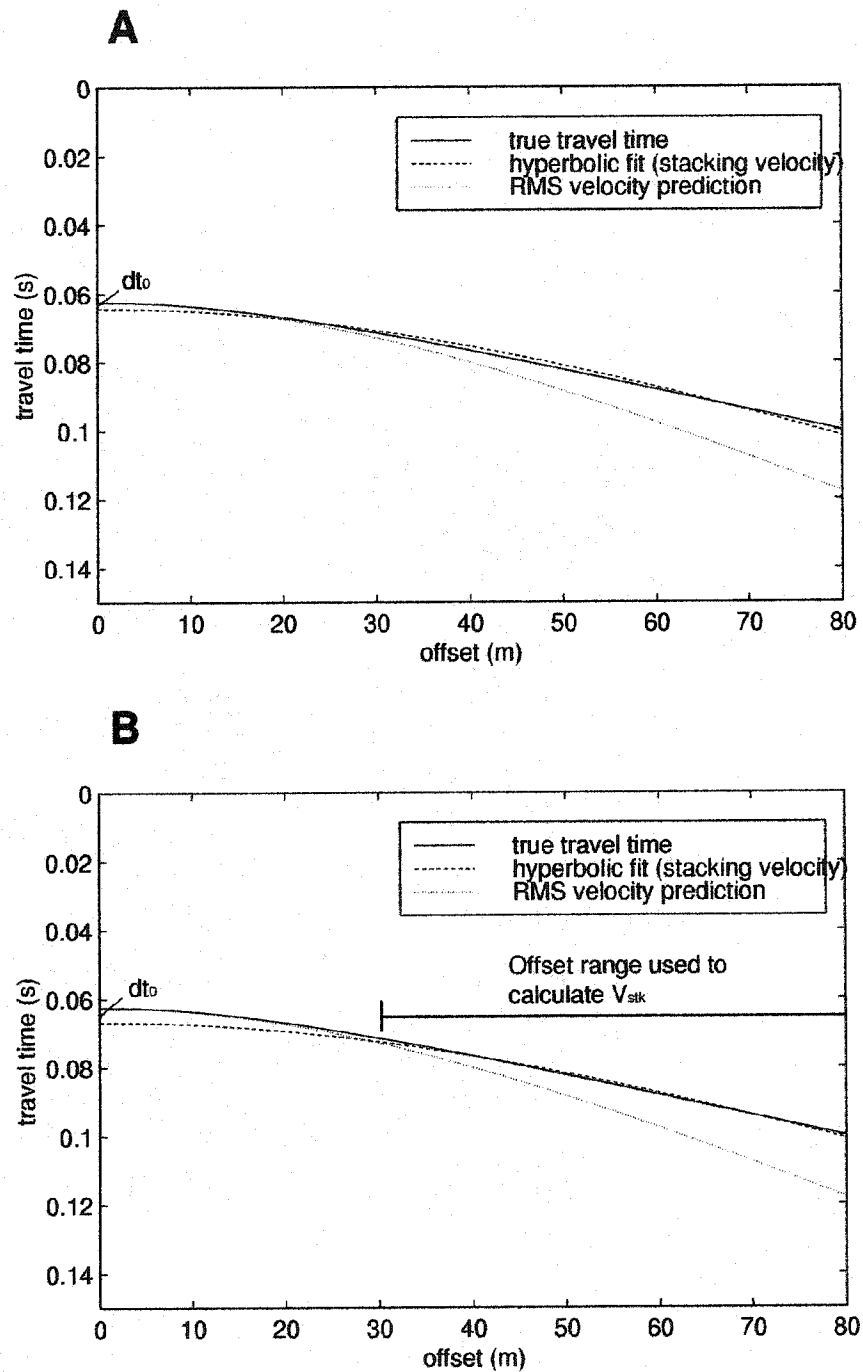


Figure 2.9: Reflection traveltime curves A) using the full offset range to calculate v_{stk} , and B) using only the far offset range. Using only far offsets increases the velocity and t_0 overestimates. The two term approximation to the traveltime curve is reasonable at near offsets, but provides a poor estimate at far offsets.

from the base of layer 2. This is the case if we use the optimum window technique (Hunter et al., 1984) and the base of layer 2 is the target. Typically, for the first reflection in the profile we assume $v_{stk} \approx v_a$. The depth to the first reflection under consideration is calculated by

$$d' \approx \frac{1}{2} v_{stk} t_0 \quad 2.17$$

When the material above the reflector has a high heterogeneity factor, this is a very poor approximation, and in fact $v_{stk(2)} \sim v_2$. The error in depth estimate becomes

$$\delta d_2' = \frac{1}{2} [\delta v_{avg}(t_{02}) + v_{stk2}(\delta t_{02})] \quad 2.18$$

where $\delta v_{avg} = v_{stk} - v_{avg}$.

we see that not using v_{stk1} in the computation introduces an additional error term in the depth estimate given by

$$d' - d = \delta d' - \delta d \quad 2.19$$

At infinite offset, $v_{stk2} = v_2$, so we can calculate the left side of Equation 2.19 from Equations 2.13, 2.15, and 2.17 giving $d' - d = (v_2 - v_1)t_{01}$ as the maximum additional error. The minimum error will occur when $v_{stk} = v_{rms}$. In this case $\delta v_{avg} = v_{rms} - v_{avg}$, and $\delta v_2 = 0$, and we compute the minimum additional error from the right side of Equation 2.19 using Equations 2.14, 2.16, and 2.18 giving $\delta d' - \delta d = \frac{1}{2} (v_{rms} - v_{avg})t_{02}$. For a homogeneous medium, $\delta d' - \delta d = 0$, but for a highly heterogeneous medium the error can be quite large,

even if we perfectly estimate v_{rms} . In reality we will always overestimate v_{rms} , and $\frac{1}{2}(v_{rms} - v_{avg})t_{02} < \delta d' - \delta d < \frac{1}{2}(v_2 - v_1)t_{01}$. As the above analysis indicates, it is very important to consider the low velocity layer in depth conversion, even if we are not interested in reflections at or above the water table. We should always acquire sufficient near offset data to obtain at least a rough estimate of the thickness and average velocity of the vadose zone.

Error prediction for NMO processing

I would like to quantify the errors discussed up to this point in a practical context. This requires consideration of all parameters that systematically effect velocity estimates, and ultimately how these parameters effect the accuracy of depth and layer thickness estimates. Important factors to consider are:

- 1) The thickness of the vadose zone and depth to targets below the piezometric surface
- 2) The range of offsets available to define v_{stk}
- 3) The relative contrast of vadose and saturated zone velocities

In the following discussion, I consider a two layer model with the top layer consisting of a relatively low velocity material (representing the vadose zone) and the second layer consisting of a high velocity material (representing the saturated zone). I will calculate and discuss how each of the factors mentioned above affects the estimate of the thickness of the second layer. I adopt the following nomenclature:

z_1 : thickness of the low velocity layer

z_2 : thickness of the high velocity layer

d : depth to the base of the second layer

v_1 : velocity of the low velocity layer

v_2 : velocity of the high velocity layer

x : offset

W : reflection from the base of the low velocity layer (water table reflection)

Bu : target reflector within the high velocity zone

σ_{z2} : fractional error in thickness estimate ($\delta z_2/z_2$)

σ_d : fractional error in depth estimate ($\delta d/d$)

To compute traveltimes for the two layer case, I use the following procedure. The traveltime for a reflection from the lower boundary of the two layer model is given by

$$t_x = 2 \left(\frac{z_1}{v_1 \cos \theta_1} + \frac{z_2}{v_2 \cos \theta_2} \right) \quad 2.20$$

where θ_1 and θ_2 are the angle of incidence at the lower boundary of the first and second layer respectively. Using Snell's law we find the offset, x , as a function of θ_1 ,

$$\frac{x}{2} = z_1 \tan \theta_1 + z_2 \tan \left[\sin^{-1} \left(\frac{v_2}{v_1} \sin \theta_1 \right) \right] \quad 2.21$$

I solve for θ_1 numerically using the Newton-Raphson method, with the constraint that

$|\sin\theta_1| < v_1/v_2$. θ_2 is then given by Snell's law. I find that it usually requires less than five iterations to find θ_1 to a tolerance of less than 1%, even under the most extreme conditions (large velocity contrast, large offset, small z_2).

The stacking velocity for Bu is found by fitting Equation 2.8 to the traveltime curve using a least squares routine. The stacking velocity for W is v_1 . The interval velocity, v_2 , is estimated with the two-layer Dix equation (Equation 2.9), and z_2 and d are estimated with Equations 2.13 and 2.15. In considering how the error varies with each of the parameters listed above, the fractional error, σ , is displayed as a function of two variables in a variable color display. I display the plots in terms of $\log(\sigma)$ to provide sufficient dynamic range in the color display for the reader to discriminate some of the finer details.

I first consider the effect of varying the thickness of z_1 and z_2 . I calculate v_{stk} using offsets from 0 - 80 m, and vary z_1 from 2 m - 40 m and z_2 from 4 m - 40 m. The velocities v_1 and v_2 are held fixed at 400 m/s and 1600 m/s respectively. In general, σ_{z_2} and σ_d increase with decreasing z_2 (Figure 2.10). For all values of z_1 , σ_{z_2} increases rapidly when $z_2 < 20$ m, and becomes very large when $z_2 < 5$ m. The dependence of σ_{z_2} on z_1 is relatively weak, but does show a local maximum along the z_1 axis that varies in location with increasing z_2 . When the full stacking velocity field is used to estimate v_2 , σ_d is less than 20% for most values of z_1 and z_2 , but becomes very large when z_1 and z_2 are less than about 15 m. When d is estimated based only on v_{stk} for Bu (Equation 2.17), σ_d is larger than 30% over a large range of z_1 and z_2 (the reasons for this were discussed in the previous section). This example illustrates that failing to incorporate the low velocity

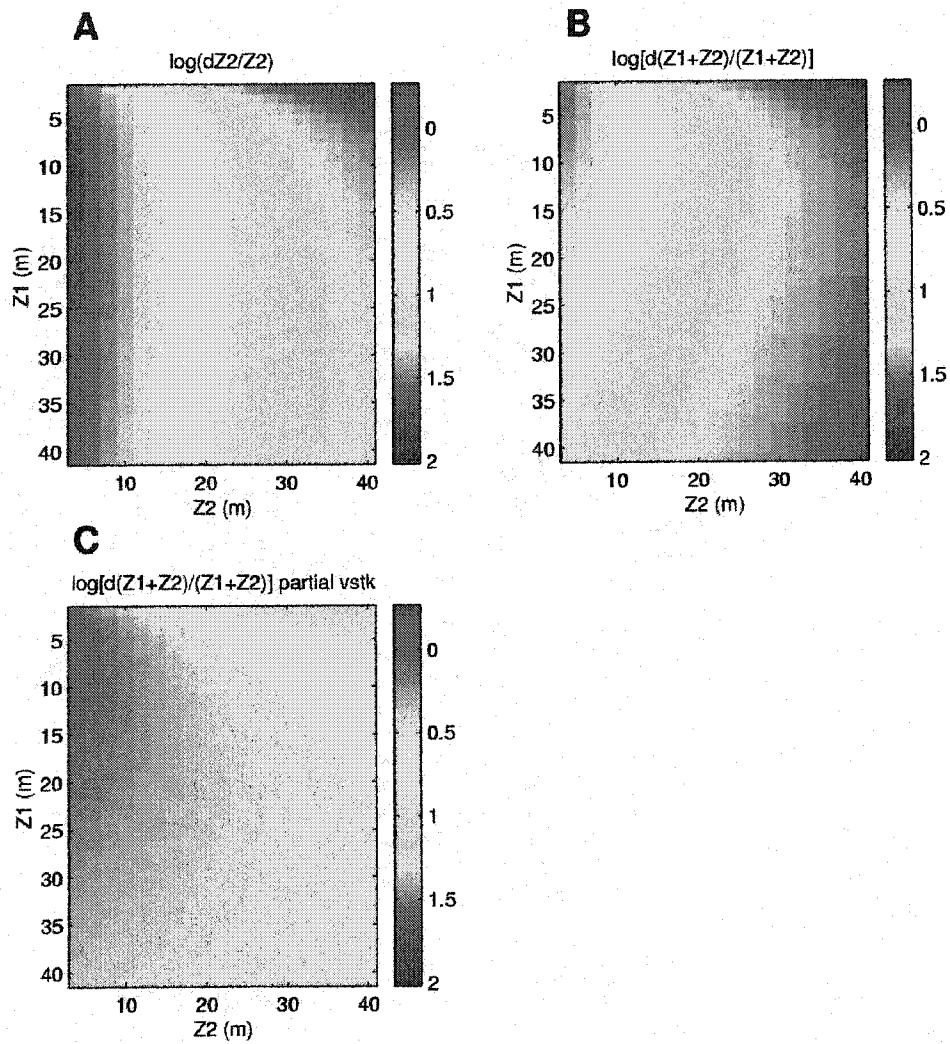


Figure 2.10: Error estimates as functions of z_1 and z_2 for a two layer model with $v_1 = 400$ m/s and $v_2 = 1600$ m/s. A) σ_{Z_2} , B) σ_d with full $v_{stk}(t)$, and C) σ_d with partial $v_{stk}(t)$.

zone in depth conversion can lead to very large errors in depth estimate. The problem can be minimized by estimating v_{rms} using the progressive stack method discussed in the Processing Strategies section.

I next consider the effect of varying the offset range used to define v_{stk} . There are two factors that contribute to the available offset range; 1) maximum offset, which is controlled by spread length, and 2) minimum available offset which is controlled by the shot to near-receiver gap or by the prevalence of near-offset coherent noise. As mentioned in the previous section, $B(v_{stk}-v_{rms})$ increases as the minimum or maximum offset increases. I first compute σ_{z2} as a function of x_{max} and z_2 , and x_{max} and z_1 . I calculate v_{stk} using offsets from 0 m - x_{max} , and vary z_2 from 4 m to 40 m holding z_1 fixed at 10 m, and then vary z_1 from 2 m to 40 m holding z_2 fixed at 10 m. The velocities v_1 and v_2 are held fixed at 400 m/s and 1600 m/s respectively. In general, the error is less than 10% when $x_{max}/(z_1+z_2) < 1$ (Figure 2.12), but as previously discussed, it is often not

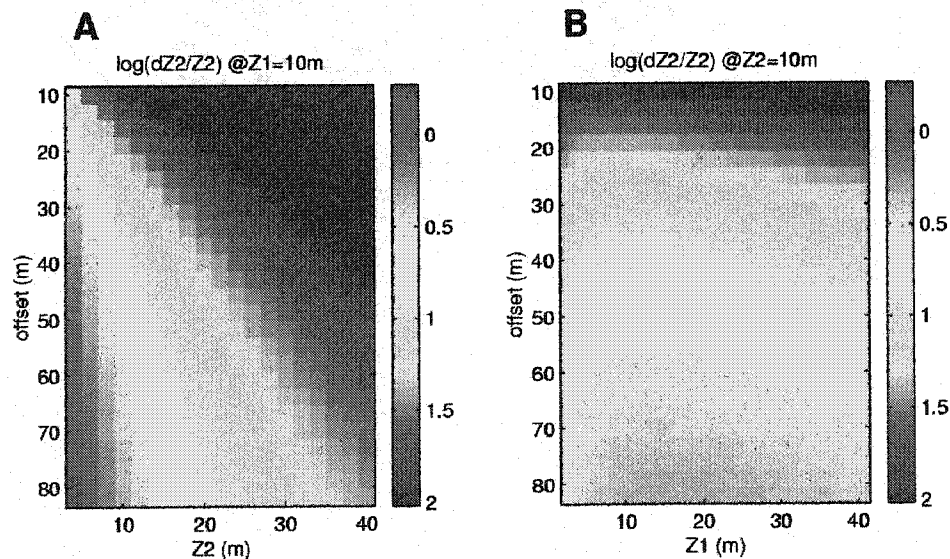


Figure 2.11: σ_{z2} as a function of offset with $v_1 = 400$ m/s, $v_2 = 1600$ m/s, vs. A) z_2 , and B) z_1 .

possible to extract reflected energy at offsets this small. In general, σ_{z2} is a relatively simple function of x_{\max} and z_2 , increasing as x_{\max} and z_2 increase, but is a somewhat more complicated function of z_1 with a maximum along the z_1 axis at $z_1 = z_2$ [recall that $z_1 = z_2$ also corresponds to a maximum in the heterogeneity factor (Figure 2.8)].

I now compute σ_{z2} as a function of minimum offset, z_1 and z_2 . I hold the maximum offset fixed at 80 m, and vary z_1 from 2 m to 20 m and z_2 from 4 m to 40 m. Again v_1 , and v_2 are held constant at 400 m/s and 1600 m/s respectively. I vary the minimum offset in terms of the noise cone velocity (v_{nc}). Depending on local site conditions, this could represent ground roll, guided waves, or the direct P-wave. I vary v_{nc} from 10 m/s to 400 m/s. The minimum offset (x_{\min}) increases with increasing v_{nc} and B increases as x_{\min} increases. In general, σ_{z2} is not strongly dependent on v_{nc} , but increases with increasing v_{nc} as expected (Figure 2.12). For $z_2 < 30$ m, σ_{z2} is greater than 10 % for most values of v_{nc} . For the full range of z_1 used in the calculation, σ_{z2} is greater than 25%.

The final parameter I consider is the variation of v_1 . I use offsets from 0 m - 80 m to define v_{stk} , vary the thickness of z_1 from 2 m to 20 m, and z_2 from 4 m to 40 m. The velocity in the saturated zone is held constant at 1600 m/s. Typically, we find that there is less relative variation in the saturated velocity than in the vadose velocity, and the parameter of interest is the ratio v_1/v_2 . By varying only v_1 , we can view the trend in σ_{z2} over wide range of v_1/v_2 , so varying v_2 would not contribute significantly to our understanding. In general, σ_{z2} decreases with increasing v_1 , which is what we expect since as $v_1 \rightarrow v_2$ the heterogeneity factor, $g \rightarrow 0$, and $B \rightarrow 0$ (Figure 2.13).

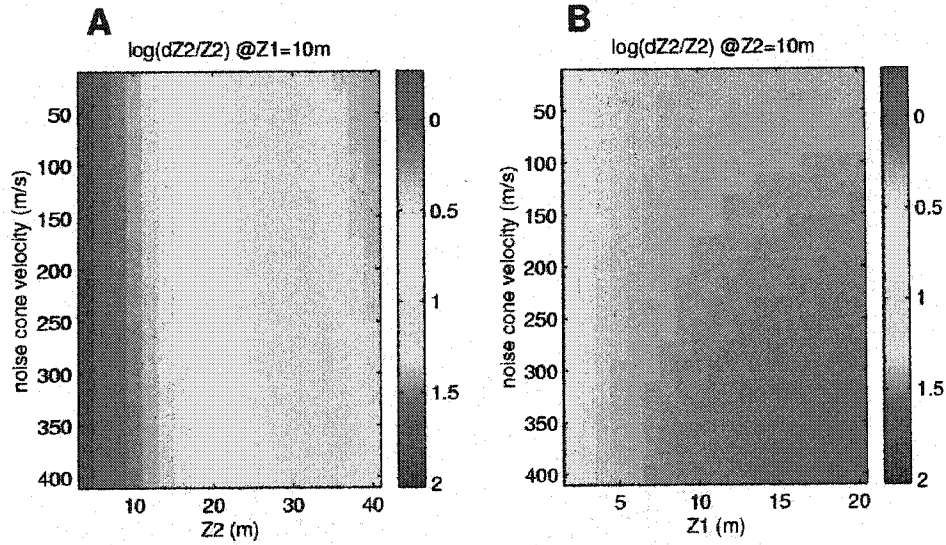


Figure 2.12: σ_{z_2} as a function of v_{nc} (minimum offset) vs A) z_2 , and B) z_1 . $v_1 = 400$ m/s, $v_2 = 1600$ m/s, and $x_{max} = 80$ m.

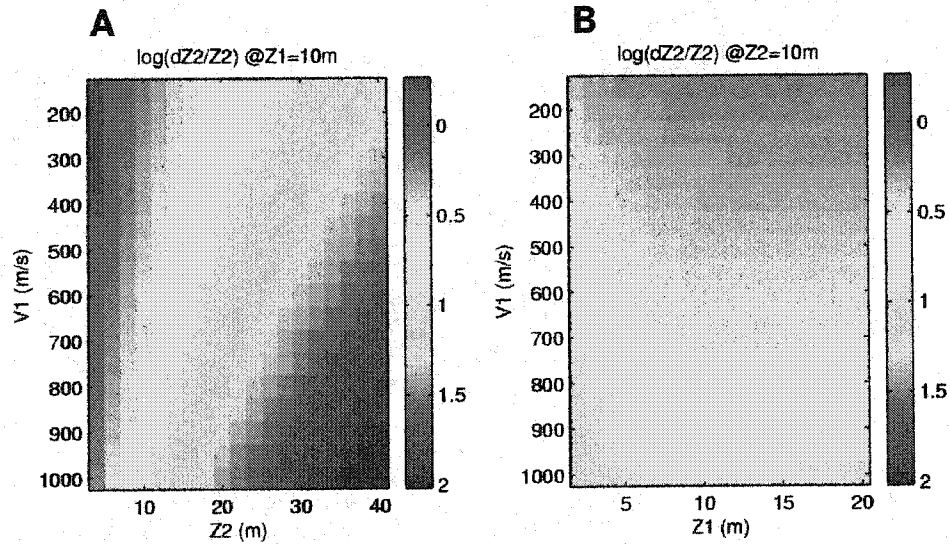


Figure 2.13: σ_{z_2} as a function of v_1 vs. A) z_2 , and B) z_1 , with $v_2 = 1600$ m/s

Summary

In general we find that σ_{z_2} , and σ_d are relatively simple functions of z_2 , and decrease as z_2 increases. The error is a more complicated function of z_1 with a minimum at $z_1 = 0$, a local maximum that depends on the offset range, ratio v_1/v_2 , and z_2 , then a

gradual decrease with increasing z_1 . The error increases as maximum, and minimum offset increase, and decreases as the ratio v_1/v_2 approaches 1. The error can be very large (> 100%) for a relatively thin saturated layer (<10 m), but even under a broad range of reasonably scenarios the errors will be greater than 50% with typical noise cone velocities of 150 m/s - 400 m/s. This level of uncertainty is unacceptable in quantitative studies. Since the error is predictable within the limits of our ability to determine velocities, we should devise processing strategies to minimize the uncertainty thereby improving our prediction of the subsurface.

PROCESSING STRATEGIES

I have shown that conventional velocity analysis fails to predict interval velocity, with an acceptable level of accuracy, for a saturated layer less than about 30 m thick. To improve depth and layer thickness estimates it is necessary to pursue alternative processing strategies, or at a minimum, estimate the bias in our prediction.

Al-Chalabi (1974) presents three methods of improving interval velocity estimates

- 1) Model simulation
- 2) Progressive stack method
- 3) Three term stack

The model-simulation, and progressive stack methods provide graphical estimates of B with minimal computation requirements. The three term stack is not an appropriate option in this case due to rapid divergence of the three term approximation to Equation 2.7,

which is related to the severe velocity gradient.

The progressive stack method appears to be the simplest, and most valuable method, but requires good reflection quality over a large range of offsets. To apply this method we calculate stacking velocities over several discrete offset intervals. We then construct a plot of x_{avg} vs. v_{stk}^2 (where x_{avg} is the average offset of the interval over which v_{stk} is calculated) and extrapolate to find v_{stk} at zero offset ($v_{\text{stk}}|_{x=0} = v_{\text{rms}}$). With the correct value of v_{rms} we can accurately compute the interval velocity using Dix inversion.

Pre-stack depth migration

Ultimately we would like to employ a processing scheme that does not depend on the approximations of conventional processing. Ray-based inversion methods can provide an accurate description of the gross velocity structure, but lack detail since only a few key interfaces are used in the analysis. Pre-stack depth migration (PSDM) is the most accurate and detailed imaging method, and the remainder of the paper will focus on this method as a means of improving depth and thickness estimates.

The accuracy of the migration depends on an accurate and detailed velocity model which must be obtained using an inverse method which could include ray-based inverse methods and/or PSDM velocity analysis. Typically, iterative PSDM velocity analysis is used with a starting model that may be estimated using a variety of methods. I suggest three methods of obtaining a starting model that progress from relatively simple to relatively complex and computationally intensive.

Method 1 : The two layer model . The simplest starting model is a two-layer, 1-D model.

The upper layer is constant velocity estimated from the moveout of the water table reflection and/or the direct arrival. The second layer has a linear velocity gradient with the velocity at the top of the layer estimated from the moveout of the water table refraction. I then calculate the stacking and interval velocities (using Dix inversion) of a reflector that is much deeper (> 30 m) than the piezometric surface. Assuming the Dix interval velocity is approximately equal to the average interval velocity, I adjust the velocity gradient in the starting model so that average velocity in the second layer matches the Dix interval velocity. This method generally works well when the velocity function is 1-D, and the heterogeneity above and below the piezometric surface is minimal. In the case studies section, I present a synthetic and field example (coastal plain example) where this method was used.

Method 2: NMO analysis and the progressive stack. This method will be more useful when there is significant heterogeneity beneath the piezometric surface and if the velocity field varies horizontally. In this approach, one uses the progressive stack method to estimate the rms velocity function at key CMP's. This method will provide a reasonably accurate and detailed velocity model, as long as lateral velocity variation is greater than a spread length, with minimal computation requirements.

Method 3: Traveltime inversion. In this case, I refer specifically to ray-based traveltime inversion methods. This will provide the most accurate starting model and will work with relatively complex velocity fields that vary vertically and horizontally. I use Zelt and Smith's (1992) inversion code which relies on an arbitrary combination of traveltime picks of turning waves, refractions, and reflections. The velocity model output using inverse

methods should be very close to the final migration velocity model, but may require fine tuning. I present two field examples (fluvial and coastal environments) where inversion is used to estimate the starting model.

Additional considerations. Migration velocity analysis involves an iterative approach in which the velocity model is updated in a top-down manner on each iteration. The velocity model is correct (to the extent that it mimics the wavefield kinematics) when reflectors in Common-Image-Point (CIP) gathers (the PSDM analog to Common-Mid-Point (CMP) gathers) are flattened. Pre-stack depth migration velocity analysis is discussed by several authors (Kamal, 1989; Lafond and Levander, 1993; Liu, 1997).

With PSDM, as with NMO processing (Steeple and Miller, 1998), refractions can migrate and stack coherently, appearing as reflections in the final stack leading to misinterpretation. Additionally, migrating high amplitude noise within the noise cone will severely degrade the signal-to-noise ratio in the final processed image. Prior to PSDM, the data should follow the same noise suppression scheme as is followed for NMO processing. This includes muting the first break and refraction (although under certain conditions acceptable results may be obtained if this step is bypassed (Pasasa et al., 1998)), and attenuating the noise cone with any of the commonly used approaches including f - k filtering and muting the noise cone (Baker et al., 1998).

In this paper, all data are migrated using a Kirchhoff PSDM algorithm. The data are migrated in the common-offset domain and resorted to CIP gathers for velocity analysis and stacking. I find that for the severe velocity gradient under consideration, the best results are obtained using a finite difference solution to the eikonal equation to calculate

the Green's function. Ray tracing methods require interpolation. In the case of a severe vertical velocity gradient, the ray path changes significantly for very small changes in the take off angle. Since the problem is non-linear, interpolation results in significant errors and the migration result is poor.

CASE STUDIES

Synthetic example

Model design. I begin with a two-dimensional synthetic example which includes features we have observed in field data, and are typical of targets of interest to environmental or engineering seismology. The model is constructed with typical velocities for the various materials and includes a sandy vadose zone and unconfined aquifer, a sandy confined aquifer with biogenic gas inclusion, and bedrock interface (Figure 2.14). Very low velocities are predicted by Gassman's equations with a very small percentage of gas displacing water in the pore space (Figure 2.1). I have observed very low velocities associated with confined aquifers at two field sites (see coastal and coastal plain field examples) and attribute this to inclusion of biogenic gas in the pore space (Bradford et al., 1997). Degassing of groundwater from confined aquifers is commonly necessary in water treatment, so an anomalously low velocity may be common in shallow, confined aquifers, and is a realistic and relevant feature to include in this synthetic example.

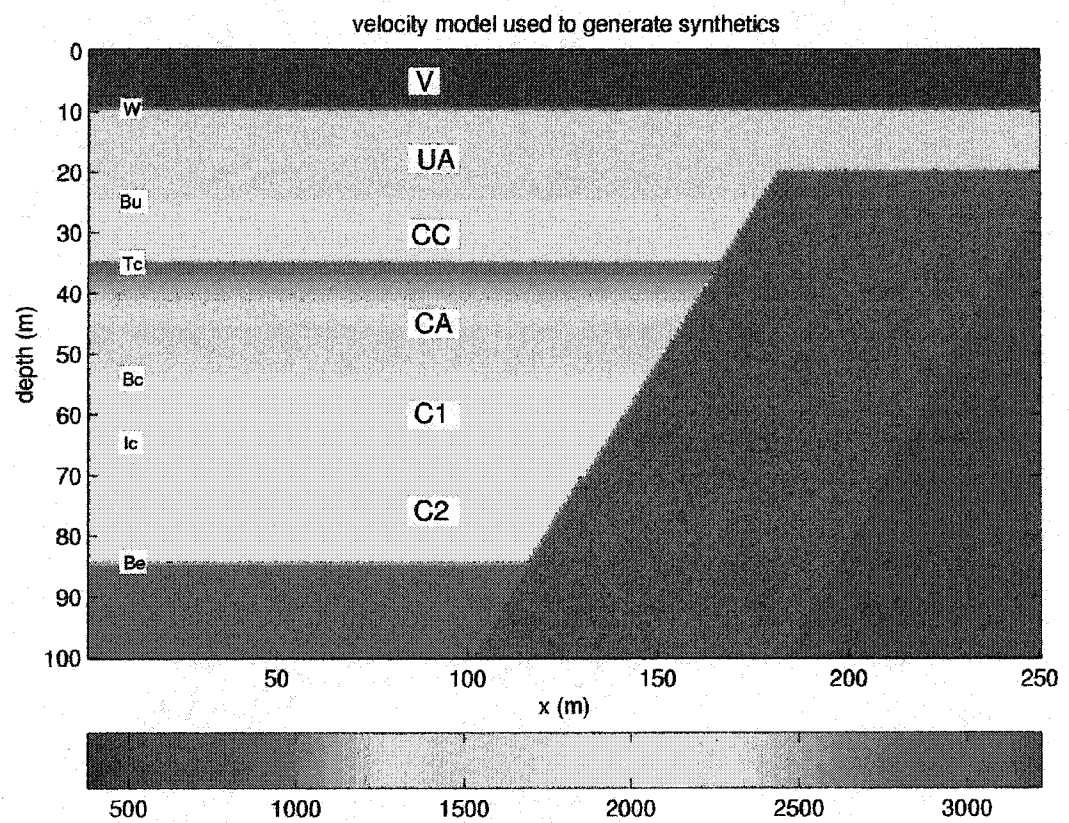


Figure 2.14: Velocity model used to generate synthetic data. Velocities are in m/s.

I adopt the following nomenclature to refer to the various reflecting interfaces and layers in the model.

Reflections

W: water table (10 m)

Bu: base of unconfined aquifer (25 m)

Tc: top of confined aquifer (35 m)

Bc: base of confined aquifer (55 m)

Ic: intra clay (65 m)

Be: bedrock (85 m - 20 m)

d_{xx} : depth to layer xx

σ_{dxx} : fractional depth error for reflector xx

Layers

V: sandy vadose zone (0 m - 10 m)

UA: sandy unconfined aquifer (10 m - 25 m)

CC: clay confining unit (25 m - 35 m)

CA: sandy confined aquifer (35 m - 55 m)

C1: clay layer 1 (55 m - 65 m)

C2: clay layer 2 (65 m - 85 m)

h_{xx} : thickness of layer xx

σ_{xx} : fractional layer thickness error for layer xx

Error prediction for NMO processing. The NMO assumption implies approximately

straight ray paths. Travel paths through the horizontally layered section of the model deviate significantly from the straight ray approximation (Figure 2.15). This is expected since the model includes two zones of high heterogeneity represented by the large velocity contrast from V to CA, and the sharp velocity inversion across UA. Using the offset range from 0 m - 65 m to define stacking velocities, $B (v_{stk} - v_{rms})$ is zero for W, then increases to 14% for Bu (Figure 2.16). B decreases gradually with depth from 14% at Bu to 1% at Be.

The large value of B for Bu leads to $\sigma_{CA} = 18\%$. The thickness of the remaining layers is underestimated, with the maximum of $\sigma_{CC} = -7\%$. The magnitude of the error decreases gradually below this layer. To understand why layer thickness is underestimated, even though there is a positive velocity bias, I consider the equation, $h_n = v_n(t_{0n} - t_{0n-1})$. The error is given by

$$\delta h_n = \delta v_n(t_{0n} - t_{0n-1}) + v_n(\delta t_{0n} - \delta t_{0n-1}) \quad 2.22$$

So the second term on the right side of Equation 2.22 will be negative if $\delta t_{0n} < \delta t_{0n-1}$, which holds if B decreases with depth which is typically the case (this is not always true since B also depends on g and x_{min}). The error, δh , will be negative if the magnitude of the second term is greater than that of the first term.

The depth error is a maximum at Bu ($\sigma_{dBu} = 11\%$), then decreases with increasing depth, with a trend similar to that for B (Figure 2.16). For multiple layers

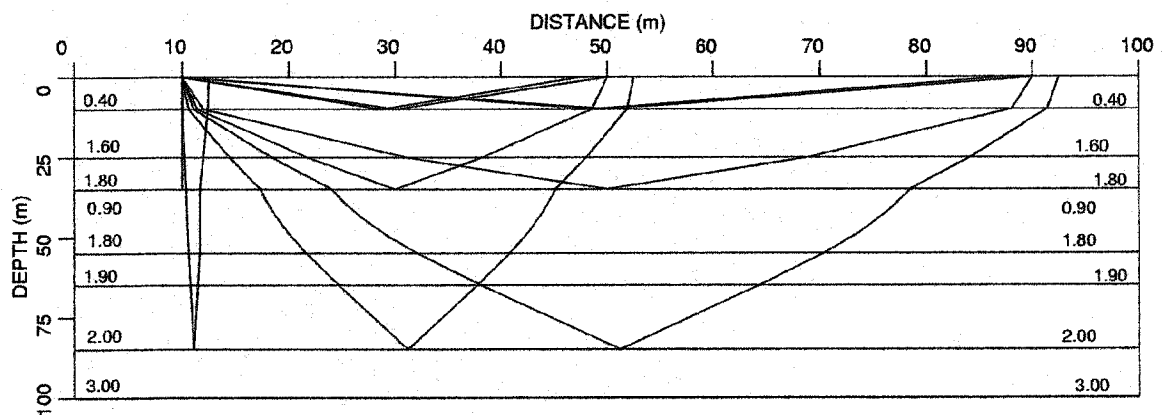


Figure 2.15: Ray paths for the horizontally layered portion of the velocity model in Figure 2.14. Velocites are in km/s.

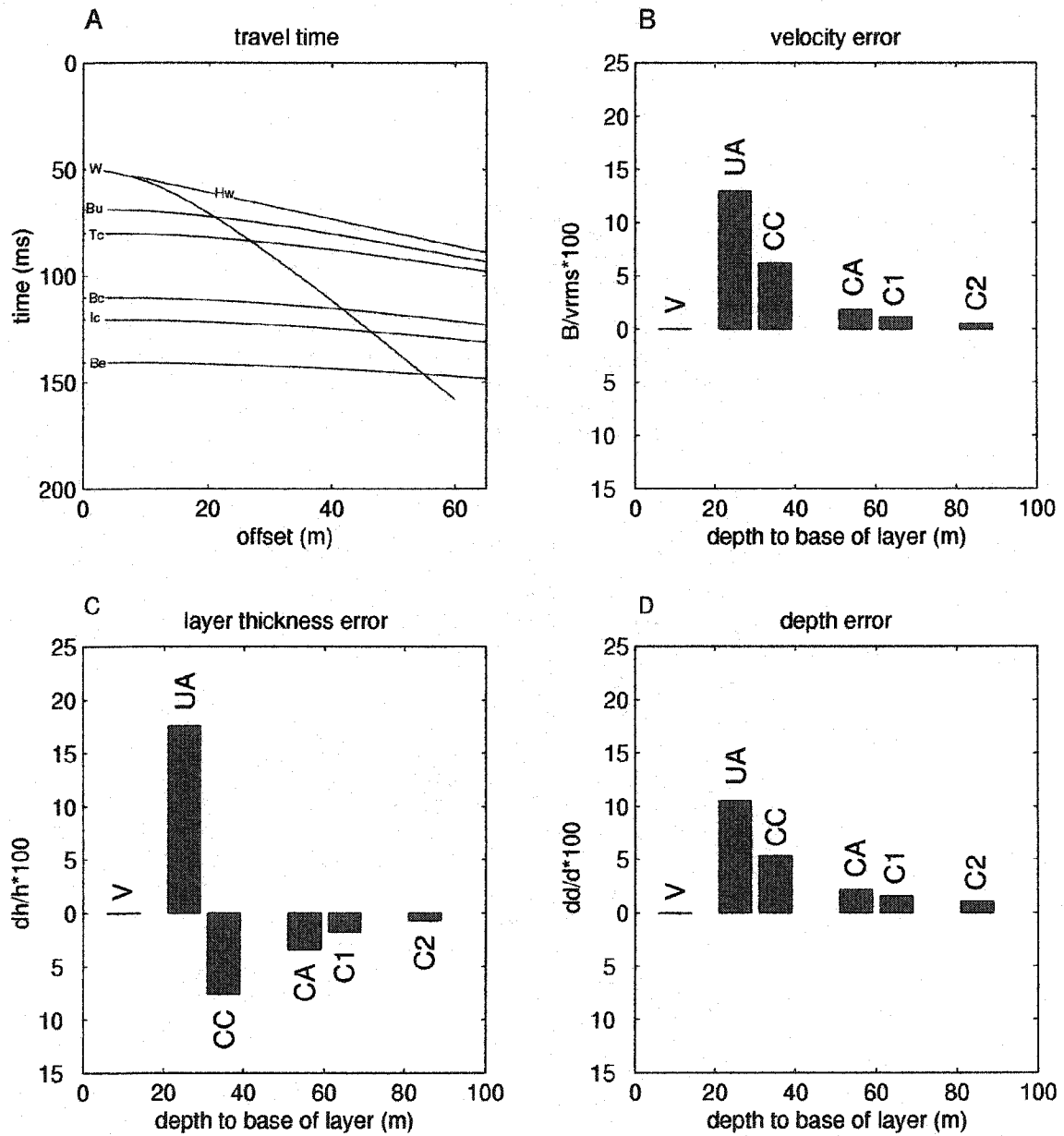


Figure 2.16: Travel times A), velocity bias B), σ_{hxx} C), and σ_{dxx} D), for NMO processing and Dix inversion for the velocity model in Figure 2.14. The full offset range was used to calculate the errors.

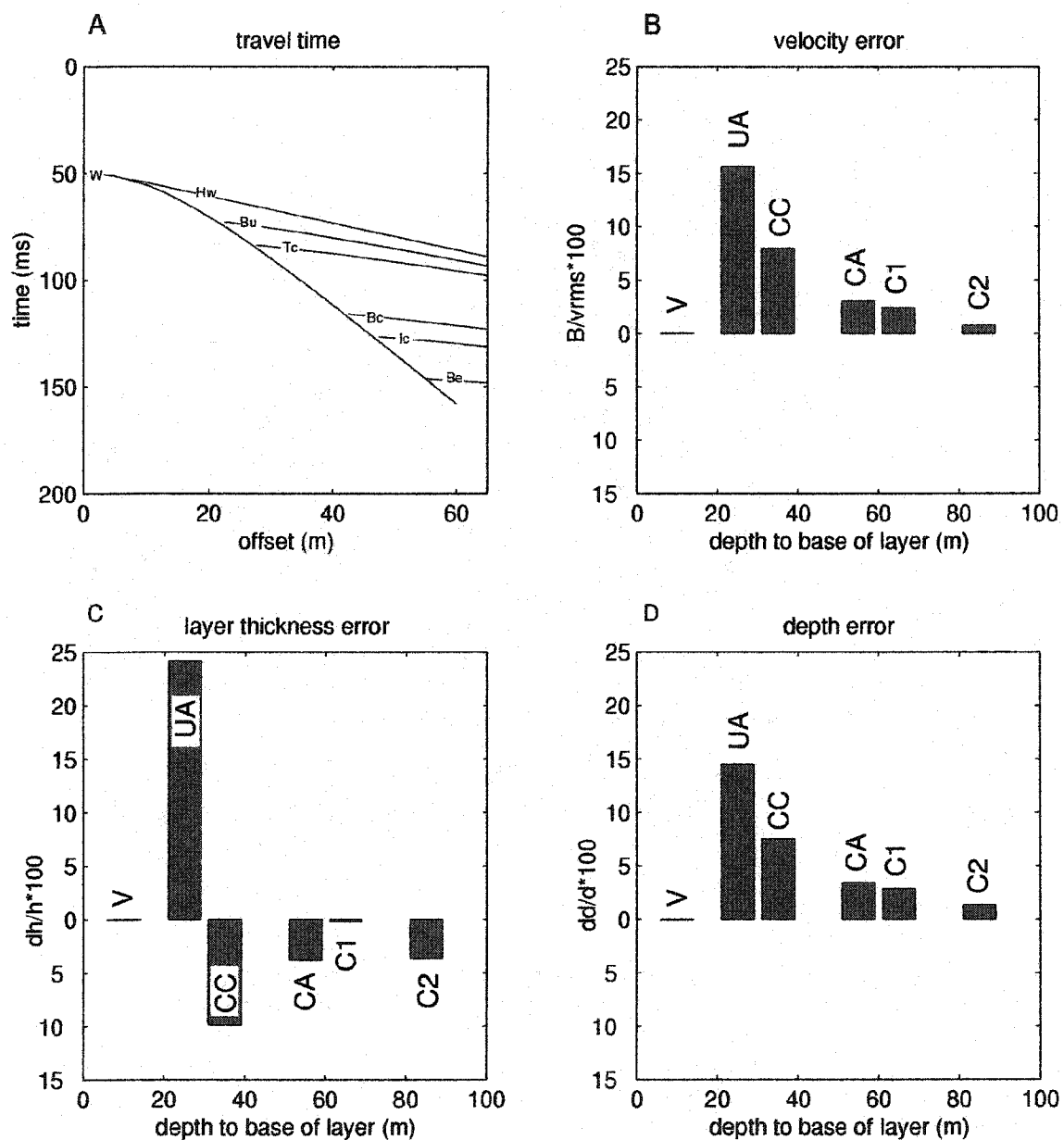


Figure 2.17: Travel times A), velocity bias B), σ_{hxx} C), and σ_{dxx} D), for NMO processing and Dix inversion for the velocity model in Figure 2.14. In this case, only the far offset portion of the traveltimes curves were used to calculate the errors.

$$\delta d_n = \sum_i^n \delta h_i \quad 2.23$$

so the equivalence of δh and δd doesn't necessarily hold below the second layer. In this case, δh_{UA} is so large that it masks a negative δh for each of the other layers, and $\delta d > 0$ for all reflectors.

I now consider the worst case scenario, where v_{nc} is defined by W , and the effective minimum offset increases with depth (Figure 2.17A). The error trends for B and d are similar to those when the full offset range is used to define v_{stk} , but the values are larger (Figures 2.17B and 2.17D). The most notable difference is in σ_{xx} (Figure 2.17C). The maximum error of close to 25% is at UA , and is negative for all deeper layers as in the previous case. However, this time the trend is not smooth. There is a local minima at $C1$ which is not present when the full offset range is used, and $\sigma_{dc2} \approx \sigma_{dca}$. The difference in the two cases is attributed to increasing x_{min} with depth. This changes the variation of δt_0 with depth and δh varies according to Equation 2.22.

Synthetic data generation. Synthetic data were generated using a 4th order, acoustic finite difference code (Kelly and Marfurt, 1990). Two hundred shots were generated in standard roll-along acquisition geometry, with a source and receiver spacing of 2 m, 60 receivers, and a 15-45 split spread. The minimum absolute value of offset is 0 m and the maximum is 88 m. The source pulse is a zero-phase Ricker wavelet with a center frequency of 110 Hz. This is at the lower end of desirable frequencies for most shallow reflection studies, but is valuable in this example to test geometric and processing

resolution limits, and is in the same range as the field examples that follow. For purposes of this discussion, shot points correspond to x position along the line. A spherical spreading correction, based on the correct velocity model, has been applied to all data presented.

The synthetic shot gathers illustrate many of the features commonly observed in field data (Figure 2.18). The energy recorded in the seismogram is naturally divided into two distinct groups (Figure 2.4)

1) *low velocity field*: energy traveling at or below the lowest compressional wave velocity above the piezometric surface

2) *high velocity field*: energy that has some portion of its travel path within the saturated zone, has high velocity moveout, and traveltimes that become tangential to the water table refraction at far offsets.

Although this natural division of energy can present significant problems for conventional processing streams, we can devise a processing strategy that takes advantage of this division to produce the best possible image of the low and high velocity field in a single survey (see discussion of one and two pass processing strategies below).

Acoustic modeling lacks much of the coherent noise found on field records, or in elastic modeling (ground roll, converted modes etc.). Linear coherent noise can easily be added after generating the synthetics, but was not in this case for simplicity. The direct wave ($v = 400$ m/s), the first water table multiple (WM1, $t_0 = 100$ ms), and the head wave traveling along the piezometric surface (H_w , $v = 1600$ m/s) interfere with reflections and are considered coherent noise in reflection processing. In this case, there is also a

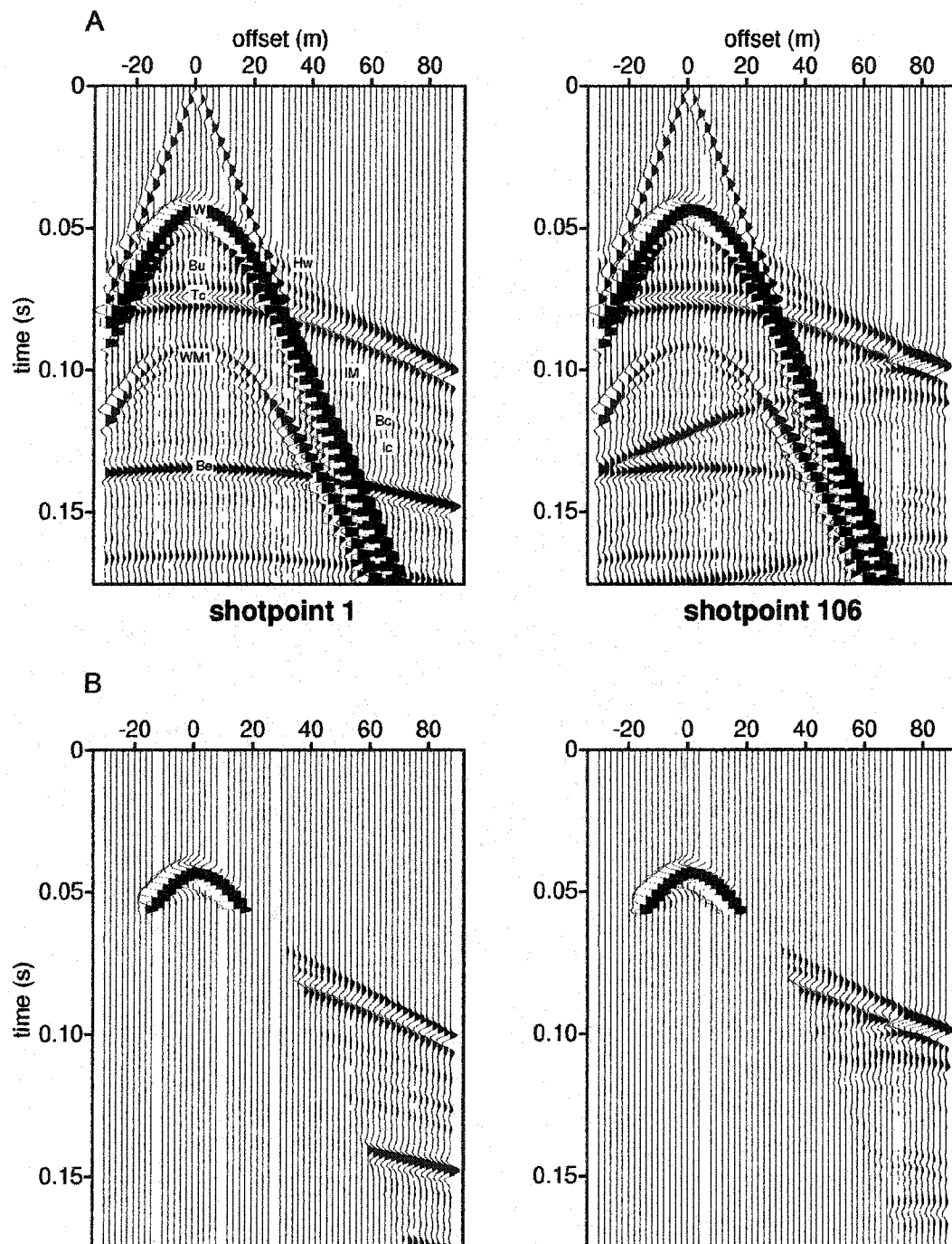


Figure 2.18: Synthetic shot gathers for the velocity model in Figure 2.14. A) raw data, and B) after top-muting and inside muting the potential noise cone region. Data were generated with a 4th order, acoustic finite-difference code.

significant interbed multiple (IM) present, which presents the most difficulty in processing and interpretation, and will be discussed in greater detail later.

UA, CC, and C1 have thickness $h_{UA} \approx \lambda$, $h_{CC} \approx 3/5 \lambda$, and $h_{C1} \approx 3/5 \lambda$, and have a relatively low impedance contrast at either the upper or lower boundary and therefore present the most difficult resolution problem. Bu is the first reflection below the piezometric surface so we also expect resolution problems as the reflection converges with H_w with increasing offset. Bu is clearly resolved at zero offset but becomes obscured outside the direct arrival as it begins to interfere with H_w and Tc. It can be differentiated to an offset of about 48 m. Tc has negative polarity due to the velocity inversion at CA, and is easily resolved to the maximum offset of 78 m, but the earliest arriving part of the wavelet begins to interfere with H_w at far offsets. Interference with Bu has little effect on the appearance of Tc, because Tc is of much higher amplitude. Bc and Ic are relatively weak reflections, but are resolved to the maximum offset of 78 m. The two reflectors are approximately parallel and do not converge within the spread length. Be is a high amplitude reflection and is well resolved across the entire profile. The asymmetry at shotpoint 106 is indicative of the steep dip in Be at this location.

NMO processing. In processing the data, I will consider only the case where no reflection information can be extracted inside the W traveltime boundary (Figure 2.18B). This essentially represents the worst case scenario, but is fairly typical. This leads to the largest velocity and corresponding depth errors, and presents the most difficult processing challenge in terms of resolution. I assume the water table reflection (low velocity field) will be properly imaged, using a standard NMO correction and depth conversion, but that

it will be imaged separately from the deeper part of the section (high velocity field) to avoid loss of fold and data distortion associated with NMO stretch and stretch muting (Miller and Xia, 1998). With that explanation, I will not consider W in the discussion of NMO processing and errors, but include it later as part of the PSDM discussion. The data are prepared for NMO processing by muting all traces inside the W travel time curve (Figure 2.18B). I apply the following processing flow :

1) Dip-Moveout velocity analysis

(Bradford et al., 1998; Deregowski, 1986; Hale, 1991)

4) NMO, DMO and stacking (with partial $v_{stk}(t)$, excluding $v_{stk(W)}$)

5) F-K migration

6) depth conversion via smoothed gradient DIX inversion: a) with partial $v_{stk}(t)$, excluding $v_{stk(W)}$, and b) with full $v_{stk}(t)$

Qualitatively, NMO processing produces a good image of the model, but there are significant problems with the accuracy (Figure 2.19). When the partial $v_{stk}(t)$ is used for depth conversion (as would be the case for the optimum window technique) (Figure 2.19A), B_u and T_c are too deep by about 10 m which is on the order of one wavelength. B_c , I_c , and B_e have estimated depths of 78 m ($\delta d_{B_c} = 23$ m), 86 m ($\delta d_{I_c} = 21$ m), and 107 m ($\delta d_{B_e} = 22$ m). The depth error for these three reflectors is about 1.5λ , but is not associated with the resolving power of the data and would be the same regardless of the frequency content (although stacking velocity estimates would be more precise with higher frequency data, which would minimize the random uncertainty).

When the full $v_{stk}(t)$ is used for depth conversion (Figure 2.19B), accuracy is

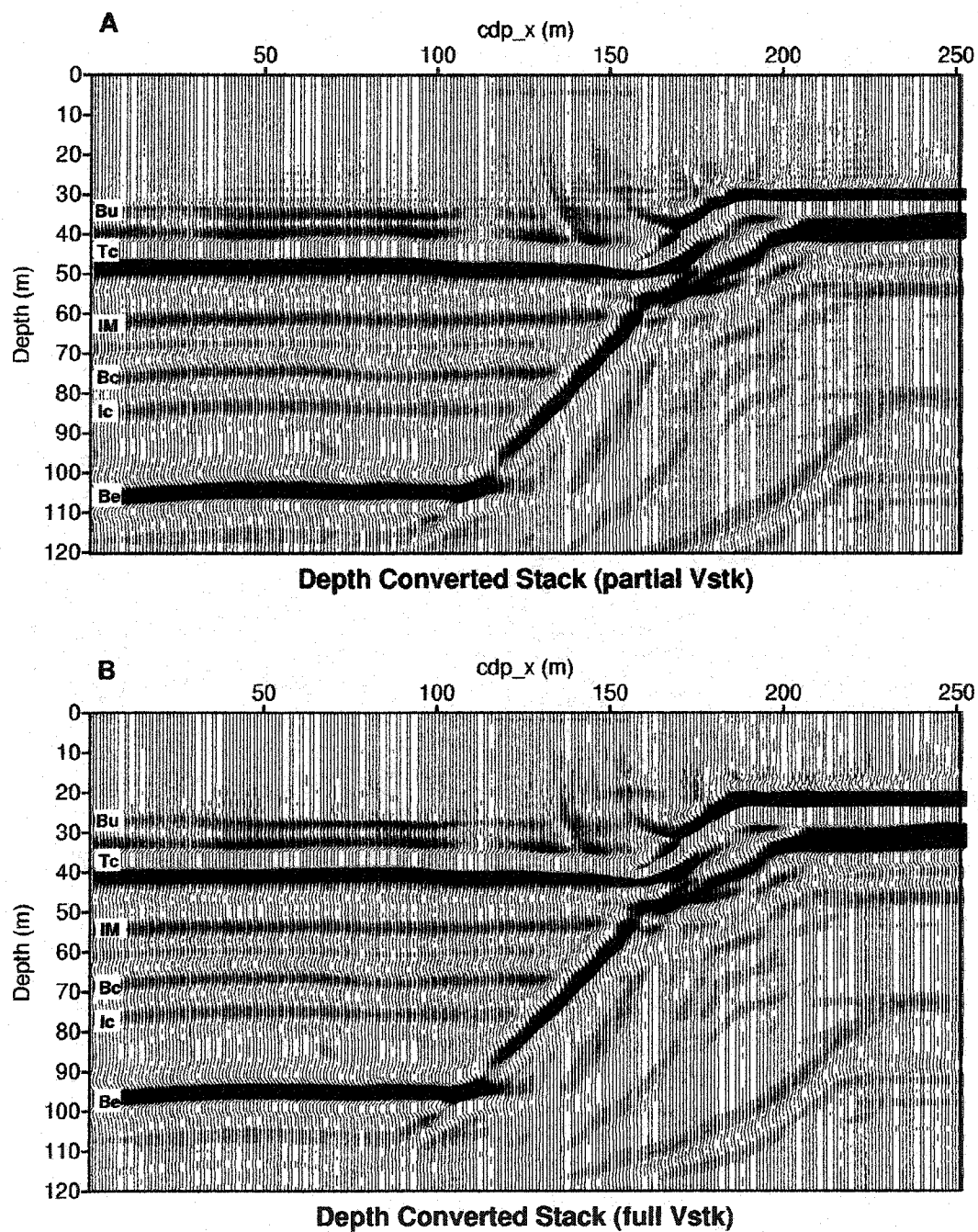


Figure 2.19: Stacks of data generated from the velocity model in Figure 2.14. The data were processed with a standard NMO processing flow including F-K migration. The stacks were depth converted A) with a partial $v_{stk}(t)$, and B) with the full $v_{stk}(t)$.

improved but the error is still significant. For Bu and Tc, $\delta d = 3$ m which is about 0.2λ , however, $\delta d_{Bc} = 14$ m. This is larger than the predicted error, which is primarily attributed to not explicitly picking v_{stk} at this weak reflection. Therefore, the low velocity zone is not correctly accounted for, even within the limitations of $v_{stk}(t)$. The error propagates to the deeper reflectors with Ic and Be being overestimated by about 12 m ($.67 \lambda$).

It is interesting to note that the thickness error in each case is relatively small. The error for UA is 66% when the partial $v_{stk}(t)$ is used for depth conversion. This is clearly unacceptable, particularly when it is improved significantly with relative ease. When the full stacking velocity function is used for depth conversion, $\sigma_{UA} = 20\%$. This is in close agreement with the predicted value of 24% from the traveltimes curves (Figure 2.17). For CC, the thickness is about 10 m, giving $\sigma_{CC} \approx 0$. The predicted error for this layer is less than 10% (Figure 2.17) which would be less than 1 m and not likely resolved at these frequencies. For CA, $\sigma_{UA} = 70\%$ which can be attributed to not explicitly picking v_{stk} at this weak reflection (Bc), as discussed above. The thickness errors of the deeper layers are negligible as predicted (Figure 2.17).

The most troubling problem in the stacked image is that the strongest event between Tc and Be is the interbed multiple (Im) that stacks in with an apparent depth of about 62 m. In field data it would be difficult, or impossible to differentiate this event from a primary reflection. The multiple originates between W and Tc so it travels at an average velocity that is greater than that for Tc. It has a moveout that is consistent with a smooth increase in stacking velocity, and if interpreted as a primary reflection, the velocity function would appear to be well behaved below the water table (gradual increase in

velocity with depth) and we would miss the large velocity inversion across CA. This is even more likely given the low amplitude of Bc. Correctly identifying Tc and Im as in phase relative to each other, but opposite phase relative to W would lead one to the correct interpretation, but this is not always trivial in field data. We must take great care in interpreting events below high impedance layers that have the potential to generate high amplitude interbed multiples (a relatively common condition in shallow reflection).

PSDM processing. First I examine the migration response when the data are migrated with the correct velocity model. Surprisingly, even when migrated with the correct velocity model, not all primary reflected energy is migrated to the correct location. In this case, I refer specifically to the wide aperture tails of W (Figure 2.20). The critical angle at the water table interface occurs at an offset of only 5 m, so in our case, with a 2 m receiver spacing, almost all observed energy is post-critical. There is a phase rotation associated with the post critical reflection, but the shape of the travel time curve is still hyperbolic with velocity defined by v_1 . If adjacent wavelets with variable phase rotation are stacked constructively, the apparent stacking velocity will be incorrect, but velocity analysis and stacking, without phase deconvolution, result in minimal error so the phase rotation can safely be ignored in most cases. Migrating the data at a constant velocity of 400 m/s flattens W across all offsets that energy is observed (Figure 2.21A). However, if the full velocity field is used for migration the strongly aliased tails of the reflector are not migrated to the correct location, and remain as coherent noise at depths greater than W (Figure 2.21B). I can stack the data, but the high amplitude tails of W do not fully cancel in stacking and the remaining energy obscures deeper low amplitude reflectors.

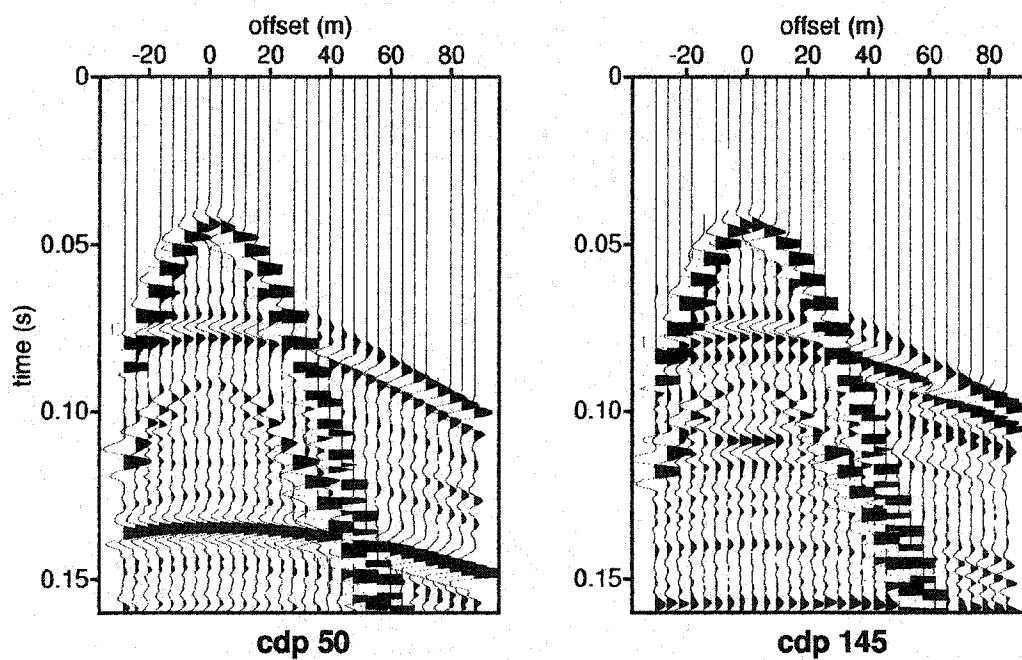


Figure 2.20: Synthetic CDP's for the aquifer model. CDP 50 is over the horizontally layered portion of the model. CDP 145 is over the steeply dipping portion of the bedrock interface.

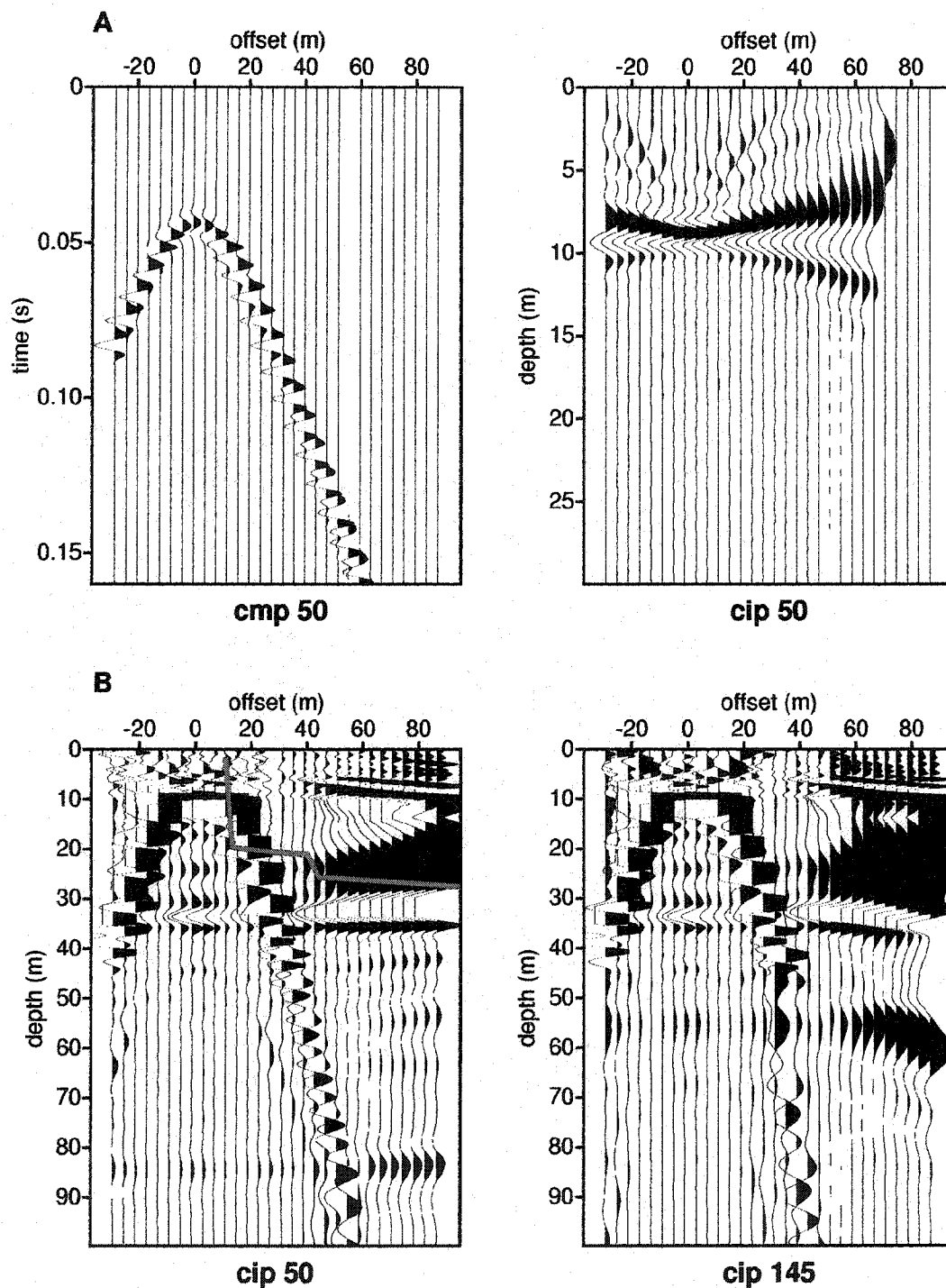


Figure 2.21: A) Water table reflection CIP before and after migration with a constant velocity of 400 m/s. B) CIPs after migration with the full velocity field. The tails of W are not migrated to the correct location. Top mute pick is shown in red.

I find that muting the wide aperture tails of W prior to stacking yields a better signal-to-noise ratio in the final image. The drawback to this approach is that the fold for W can be very low, particularly if the survey is relatively coarse, and the smallest offset traces cannot be used because of ground-roll or other coherent noise. However, if the data quality is good, this will produce acceptable results. If not, we have two alternatives. We have the option of shooting two surveys, one with very fine receiver spacing to image W and above, and another coarser survey to image the deeper portion of the profile. Since field work is time consuming and labor intensive, we would prefer to image all target reflectors with a single survey. The second alternative is a two pass processing strategy, in which we migrate the low and high velocity fields separately which will allow us to image the full section with a single survey. A similar two pass approach based on the natural separation of high and low velocity fields was recommended by Miller (1998) for NMO processing.

In the two-pass approach, the low velocity data are migrated with a modified velocity field, in which the velocity is held constant across and well below W . This is essentially constant velocity migration (although we should account for velocity variations above W) which avoids the problem of migrating the wide aperture tails when the full velocity field is used. The high velocity, far-offset data are then migrated separately with the full velocity field. The two images can be combined after migration. If minimal heterogeneity exists in the low velocity part of the section, we can minimize computation time by using a conventional NMO processing stream for the shallow section, and PSDM only for the deeper part of the section. In this synthetic example I use the one-pass

approach, migrating both low and high velocity data simultaneously with the full velocity field after muting the far offset tails of W . In the field data discussion, I present examples of both the one and two pass processing approach.

As the angle of incidence increases, the vertical wavenumber decreases, and there is a corresponding loss of resolution. The depth migrated wavelet appears “stretched” at far offsets due to the decrease in vertical wavenumber (Figure’s 2.21 and 2.22). For homogeneous media, this stretch can be shown to be equivalent to NMO stretch (Henstock and Levander, in preparation). To produce an acceptable image, we must pick a top mute where the wavelet stretch is too large. This is analogous to NMO stretch muting. In this synthetic case, I chose the top mute where B_u and T_c converge (Figure’s 2.21 and 2.22). This ensures that the two reflectors will be resolved in the final stack.

I produce a benchmark PSDM image using the correct velocity model. The data are processed assuming no reflected information can be extracted inside the W traveltimes curve. Only, the near offset portion of W , and the far offset portion of the high velocity reflections are retained for migration (Figure 2.22A). The resulting profile essentially the best image that can be extracted given current processing methodologies (Figure 2.23A). It is an excellent image of the model aquifer system, but there are two significant problems.

First, B_c is slightly overmigrated and does not stack effectively. This occurs because of the large velocity gradient above B_c resulting in significant velocity changes in less than one wavelength. Since B_c has finite bandwidth, its energy is stretched across the velocity gradient with differential error depending on the offset. The resulting migration is

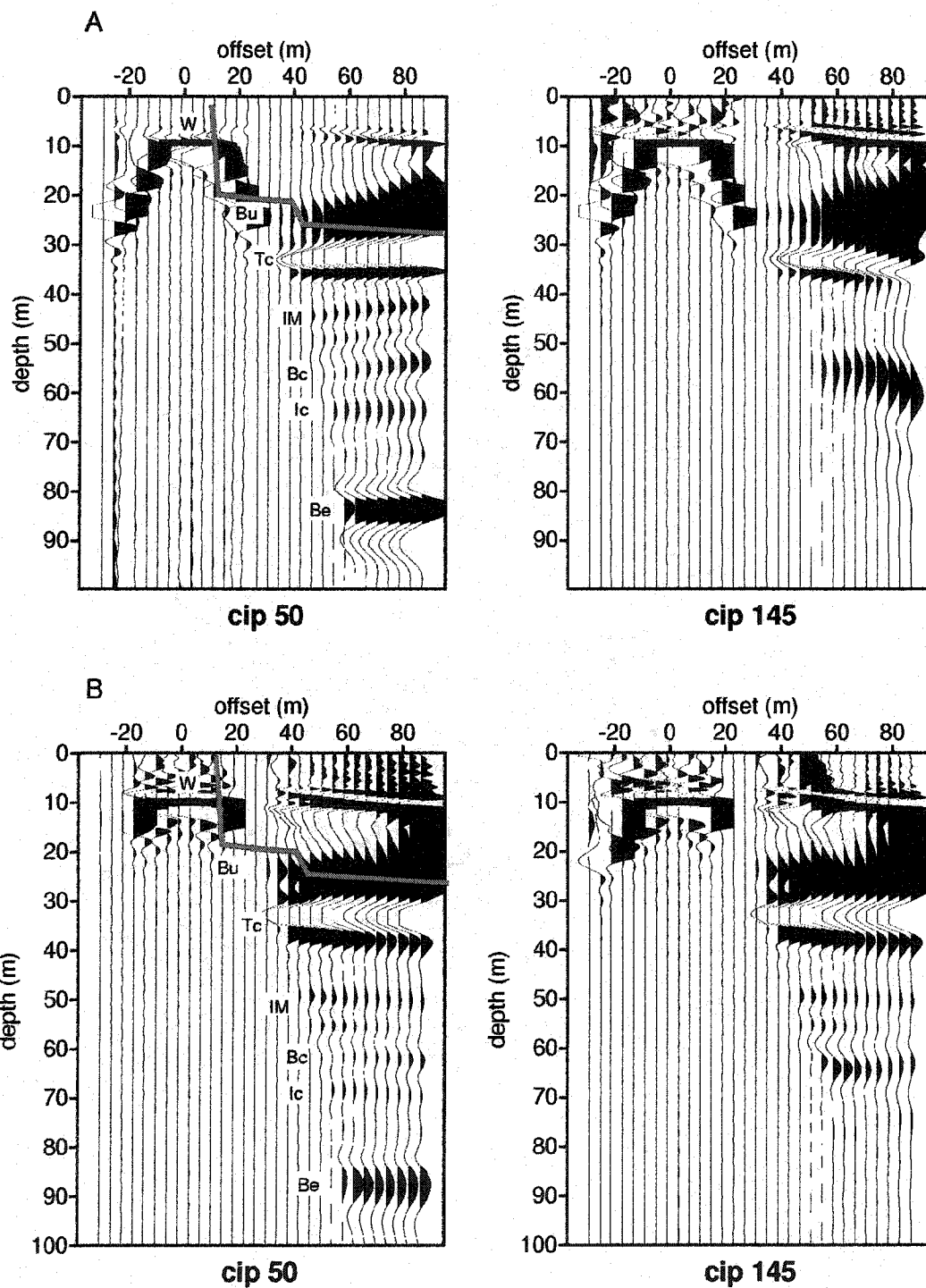
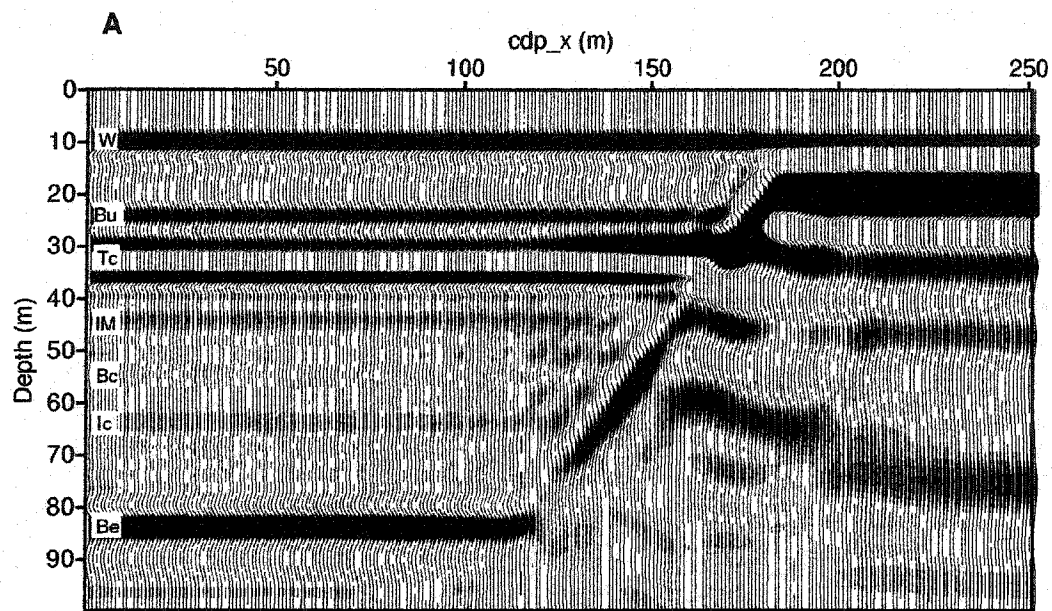
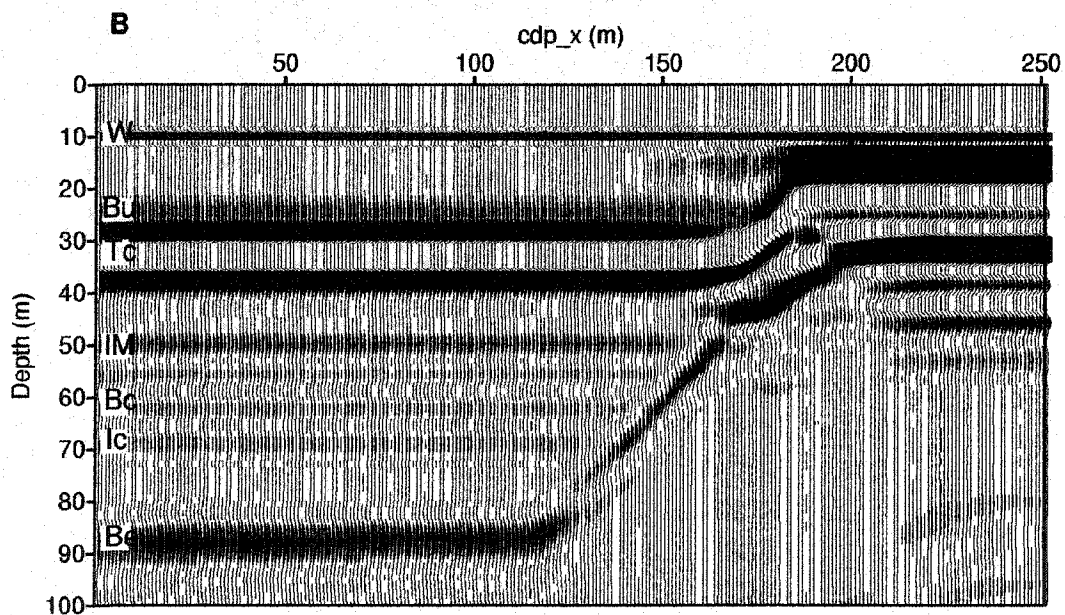


Figure 2.22: PSDM CIP's A) with the correct velocity field, and B) with the velocity field determined from PSDM velocity analysis. Top mute picks are shown in red.



PSDM w/ correct velocity model



PSDM w/ inverted velocities

Figure 2.23: PSDM stacks for the aquifer model A) with the correct velocity model, and B) with the velocity model determined from PSDM velocity analysis.

incorrect. When the full reflection aperture is used in the migration, the resulting stack is approximately correct and the problem is insignificant. This problem is also somewhat artificial, since in field setting, there would likely be sharp velocity boundaries differentiating the zones with partial gas saturation rather than diffuse zones with significant velocity gradients (Figure 2.1). Field data support this observation (see coastal plane and coastal case studies).

The second problem is the interbed multiple which stacks coherently, and again is the highest amplitude event between Tc and Be. A somewhat less troubling problem (since there are no reflections in this region) is significant high-amplitude migration noise present in the thick portion of the bedrock on the right side of the section. This is attributed to migration operator smearing across the large lateral velocity contrast, noise reflected from the model boundaries, and an interbed multiple generated between W and Be, where Be is shallow. There is a small amount of numerical error in the migration that places Tc and Be at slightly shallower depths than the model boundaries ($\delta d_{Tc} \approx \delta d_{Be} \approx -2$ m \rightarrow 5.7%, 2.5%), which is about $1/8\lambda$ and $1/9\lambda$ respectively, which is certainly negligible at this frequency, and would be acceptable for many applications.

I now estimate the velocity model using Method 1 to obtain a starting model followed by PSDM velocity analysis. Again, the harshly muted data are used in the analysis (Figure 2.22B). For PSDM velocity analysis, I use W, Tc, and Be as primary reflecting boundaries, and assume a linear velocity gradient between each boundary. I use only a 1-D velocity model for migration. This is acceptable since there are no reflectors below Be so nothing is lost by migrating this section with the incorrect velocity field.

The resulting image is a decent representation of the original model (Figure 2.23B). Although the accuracy is significantly improved over the NMO processed sections, there are some important problems that must be considered. I first consider the estimated depth of W, Tc, and Be which are the primary reflecting boundaries used for velocity analysis. The estimated depth of W is 10 m, so there is virtually no error for the first reflector. The estimated depths of Tc, and Be are 32 m ($\delta d_{Tc} = -3 \text{ m} \rightarrow 8.6\%$), and 88 m ($\delta d_{Be} = 3 \text{ m} \rightarrow 3.5\%$) respectively. These are small errors and are on the same order as errors resulting from migration with the correct velocity model.

The problem arises when we consider depth estimates of Bu, Bc, and Ic. By using only the primary reflecting boundaries and assuming linear gradients in the intermediate zones, the resulting interval velocities represent a kind of average or effective velocity. Only the reflections used in the analysis are migrated correctly. If the local heterogeneity factor (g) is low, this error is small, however, if g is large the error for intermediate reflectors can be significant because the effective velocity at that particular depth is incorrect. In the case of Bu and Tc, the depths are approximately correct, but the average, or effective velocity at Bu is too high, and the apparent wavelength is larger. The velocity below Tc is overestimated and the velocity boundary is placed slightly higher than in the correct velocity model. This results in increased stretch of Tc. Thus, Bu and Tc are no longer well resolved (Figure 2.22B). Assuming a linear gradient between Tc and Be requires that the velocity across the low velocity zone be overestimated to produce the correct effective velocity. Both Bc and Ic stack coherently but have low amplitudes relative to the NMO sections. This is because they are not properly migrated, and

therefore do not stack in as effectively. The effective velocity is too low at both Bc and Ic and the result is a depth overestimate of 8 m and 5 m respectively. Again, the interbed multiple is the strongest event between Tc and Be.

Overestimating the velocity between W and Bu results in incorrect placement of the shallow part of Be on the right side of the profile. The estimated depth is 15 m which is an error of -25 %. This could be improved using a 2-D velocity model with the shallow part of Be as a primary reflector on the right side of the profile.

The most significant problem in velocity analysis is the small segment of the reflectors available for analysis. The small segment of the reflector that is used may appear relatively flat in the migrated CIP if the velocity error is not too large. Using the full reflection aperture, particularly the near-zero offsets, significantly improves our ability to determine if the reflection has truly been migrated correctly and the accuracy of the velocity model is improved significantly. Unfortunately, this is often not possible with field data.

Velocity model comparison. It is interesting to compare the interval velocity models obtained through Dix inversion and PSDM velocity analysis (Figure 2.24). It is clear that the PSDM model represents some kind of average interval velocity model. This also could be said of the Dix model below Tc where the two models are very similar. Above Tc Dix inversion of stacking velocities significantly over predicts interval velocities and oscillates. This is due to the breakdown of the NMO assumption across W as discussed in the previous section. Neither model correctly predicts the degree of heterogeneity across the velocity inversion (CA), although both models indicate a small velocity inversion. This

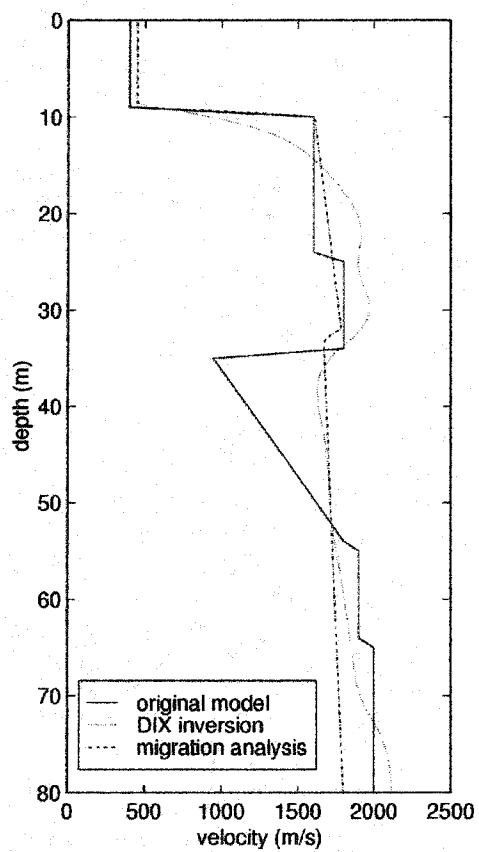


Figure 2.24: Velocity functions for the aquifer model.

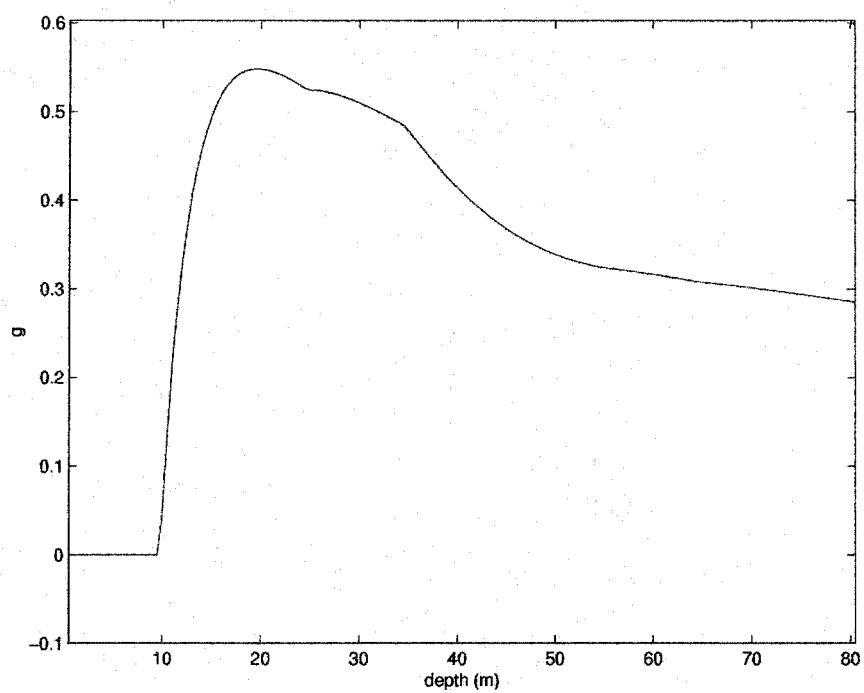


Figure 2.25: Heterogeneity factor for the velocity model in Figure 2.14.

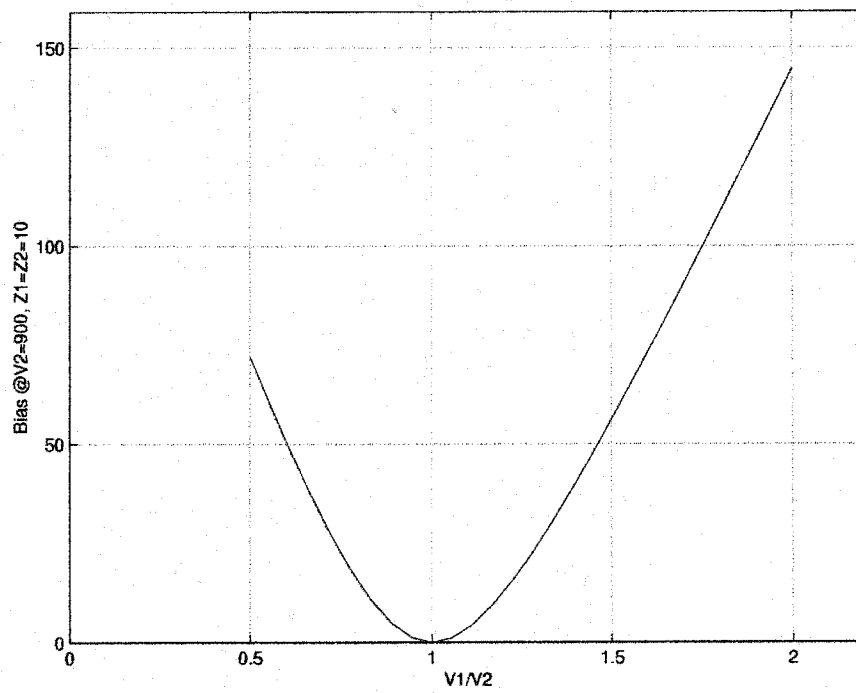


Figure 2.26: Bias as a function of velocity contrast for a two layer model.

is related to the heterogeneity factor between W and Bc, and since the weak reflector Bc was not used in velocity analysis. Plotting the heterogeneity factor (g), we see that large gradients in g correspond to areas of greatest concern (Figure 2.25). Large gradients in g correspond to large local velocity changes, and in these areas, it is necessary to complete more detailed velocity analysis if possible. This is especially critical in the case of a large velocity inversion, since $B(v_{stk} - v_{rms})$ is more sensitive to velocity inversions than velocity increases (Figure 2.26). If Bc were used in the analysis, migration velocity analysis would very closely predict the velocity inversion, and the estimate from Dix inversion would be a much better, although not perfect. It would be somewhat artificial to carry out this analysis for this synthetic example, since I am trying to simulate a realistic processing scenario and Bc is very weak. The main point here is to illustrate problems that can arise when layers are not bounded by strong impedance contrasts.

Summary. This synthetic example serves to illustrate errors inherent in standard NMO processing. I have shown that, even for a 1-D velocity medium, significant improvements in accuracy can be made using PSDM velocity analysis and imaging. Lack of near-zero offset information and large velocity changes over intervals less than one wavelength have an adverse effect on the migration result. When there is strong heterogeneity, the estimated velocity field, while potentially resulting in the correct migration of reflections used in velocity analysis, may result in poor migration results for low amplitude intermediate reflections. It is therefore of utmost importance to try and identify zones of heterogeneity and include bounding reflectors in the velocity analysis. This may be done by examining the migration response of weak intermediate reflectors in the CIP gathers.

FIELD EXAMPLES

I now discuss three field examples from differing sedimentary and hydrologic environments (Figure 2.27)

- 1) Fluvial environment, Bryan, Texas ($d_w = 10$ m)
- 2) Coastal plain environment, Houston, Texas ($d_w = 6$ m)
- 3) Coastal environment, Bolivar Peninsula, Texas ($d_w = 3$ m)

Each of the datasets were acquired using a 60 channel seismograph, and a 120 station cable spread with single, 28 Hz geophones. Two modes of acquisition were used: 1) roll-along/static shoot-through (RAST) combination, and 2) standard roll-along technique. In the RAST method, the 120 station cable spread is held static for the experiment. For the first 60 shots, the data are acquired with a standard roll-along procedure in either off-end or split-spread mode. The recording stations are incremented until the live spread corresponds to receiver stations 61 - 120. For the final 60 shots, stations 61 - 120 are live and held static as we shoot through the spread. This acquisition procedure divides the profile into a 30-fold, roll-along section, and a 60-fold, RAST section (Figure 2.28). This is a convenient procedure for small scale experiments since we can smoothly vary several acquisition parameters along the line (gap, minimum and maximum offset, and spread geometry: i.e. symmetric or asymmetric split-spread, off-end). In all of the examples that follow, the data are pre-stack depth migrated using a 2-D Kirchhoff algorithm.

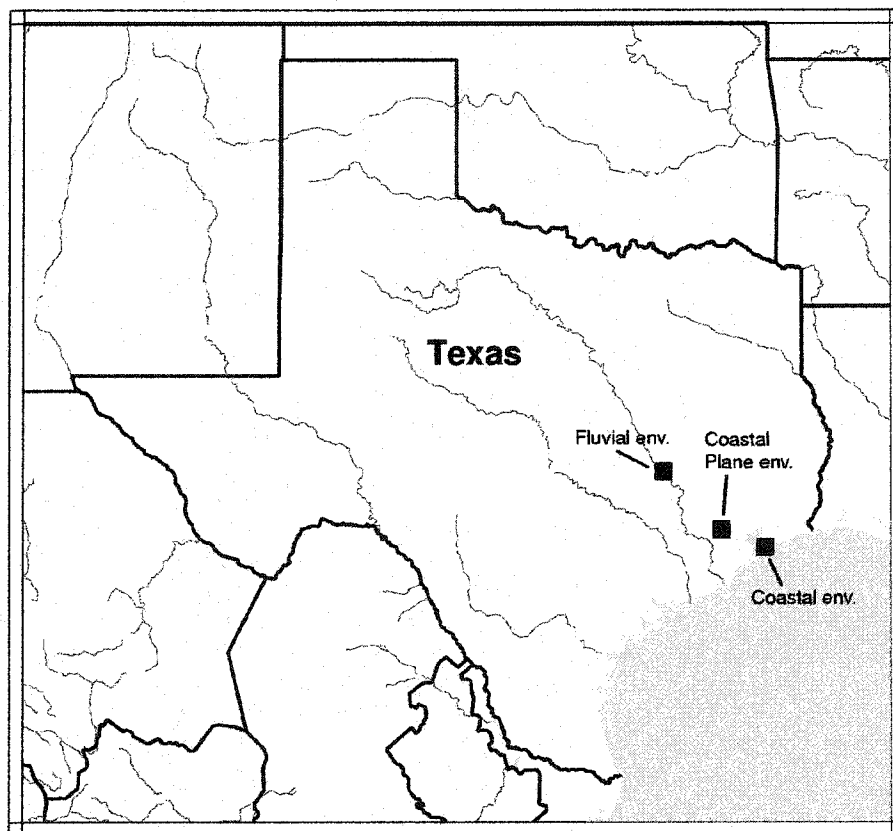


Figure 2.27: Location of three field studies discussed in this paper. The areas represent differing sedimentary and hydrologic environments.

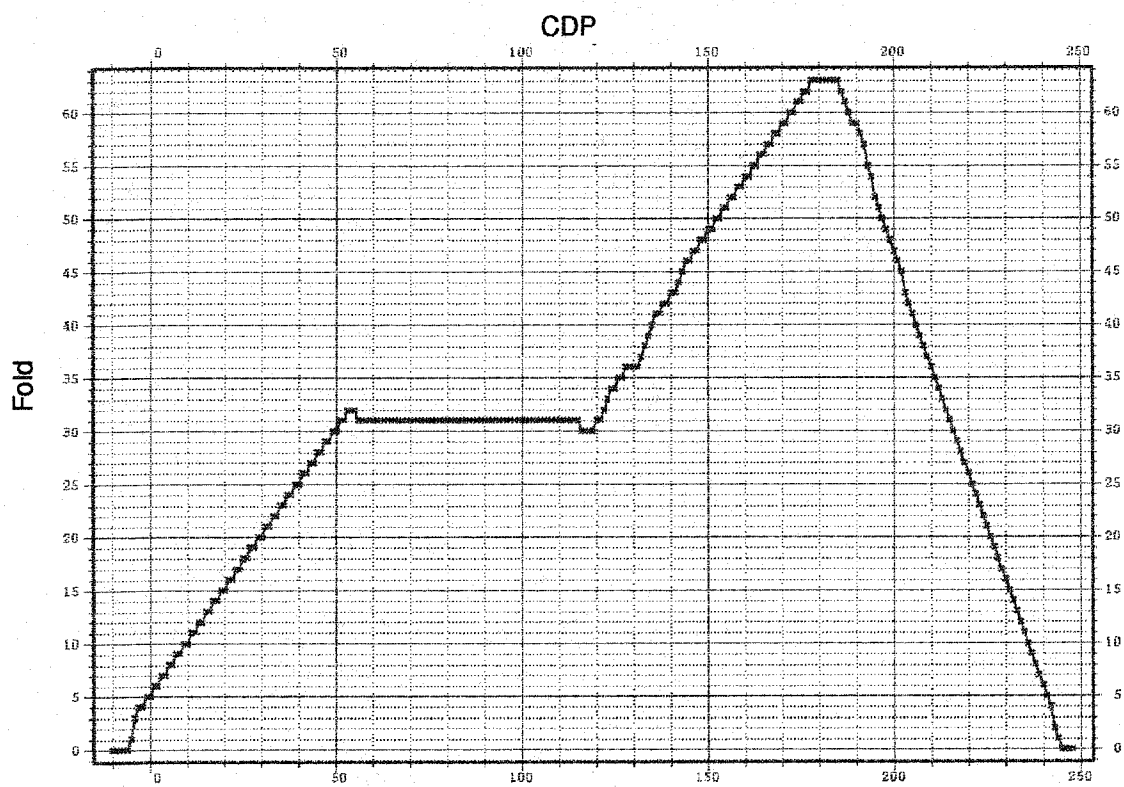


Figure 2.28: CMP fold for the 120 receiver RAST acquisition procedure. The diagram is taken from the Rice survey.

Fluvial environment

Three surveys were acquired at an agricultural test site near Bryan, TX (Sananikone and Everett, 1997) in cooperation with the Department of Geology and Geophysics at Texas A&M University (Figure's 2.27 and 2.29). The field site provides an ideal setting for a controlled experiment with well characterized stratigraphy (Sananikone and Everett, 1997), $d_w = 10$ m, and a shallow aquiclude (≈ 20 m) with a large acoustic impedance contrast with the overlying unconfined aquifer. The shallow (< 20 m), Holocene sediments are fluvial in nature (point bar sequence) having been deposited in the Brazos River Valley. These sediments contact Tertiary shale of the Yegua Formation at a depth of about 20 m. The primary features of the shallow sediments are illustrated in Figure 2.30.

The experiment objective is a comparison of multiple acquisition and imaging methodologies to image the shallow hydrologic system including the vadose zone, unconfined aquifer and contact with the shale aquiclude. The three surveys consist of:

- 1) a dense (0.7 m receiver spacing), 120 channel refraction survey
- 2) a coarse (2 m source and receiver spacing), broad offset range, RAST survey
- 3) a dense (0.5m source and receiver spacing) near offset, RAST survey

These datasets are a good example of total masking of primary reflections inside the W travelttime curve.

Refraction survey. Originally, the refraction experiment was designed to image water table drawdown during a pump test. The 120 channel spread was held static, and seven

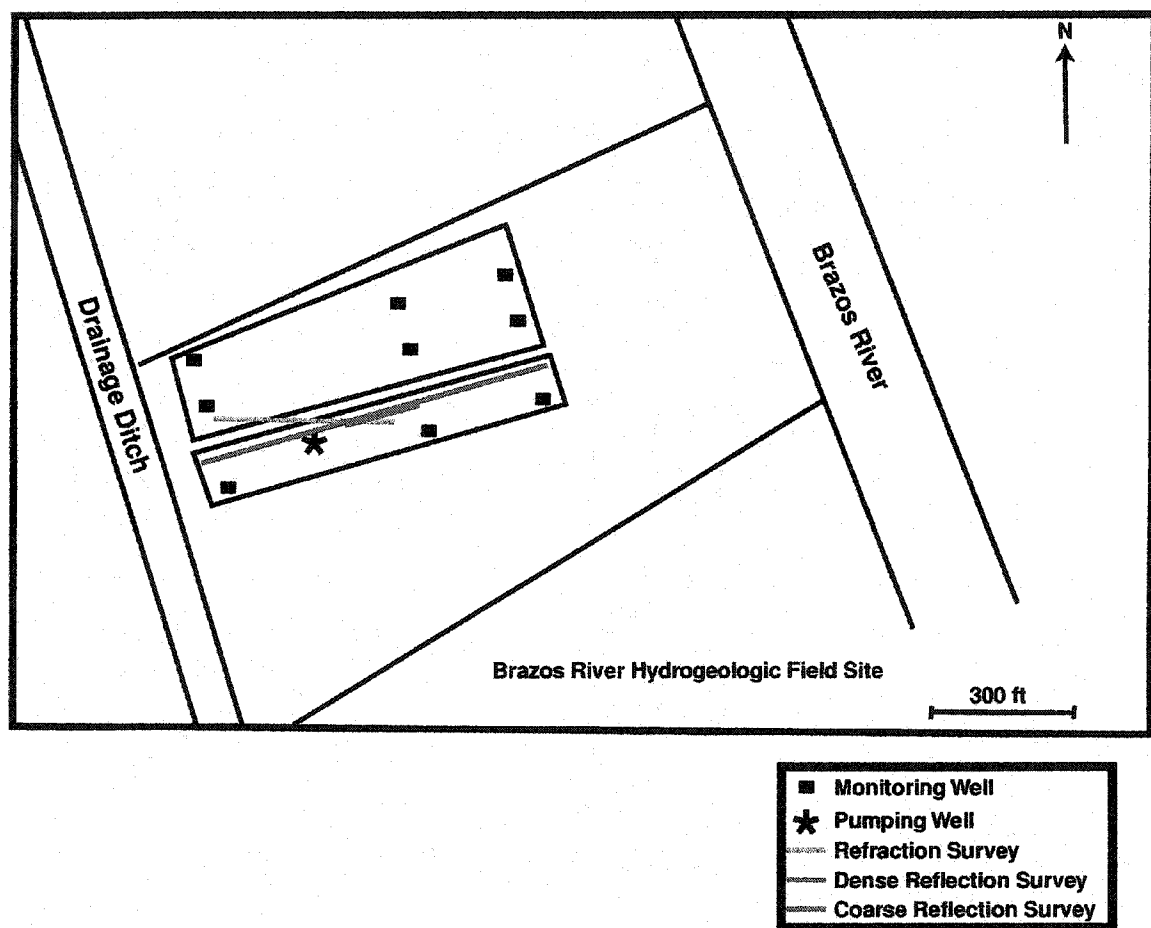


Figure 2.29: Layout of the Texas A&M hydrogeologic test site near Bryan, Texas.

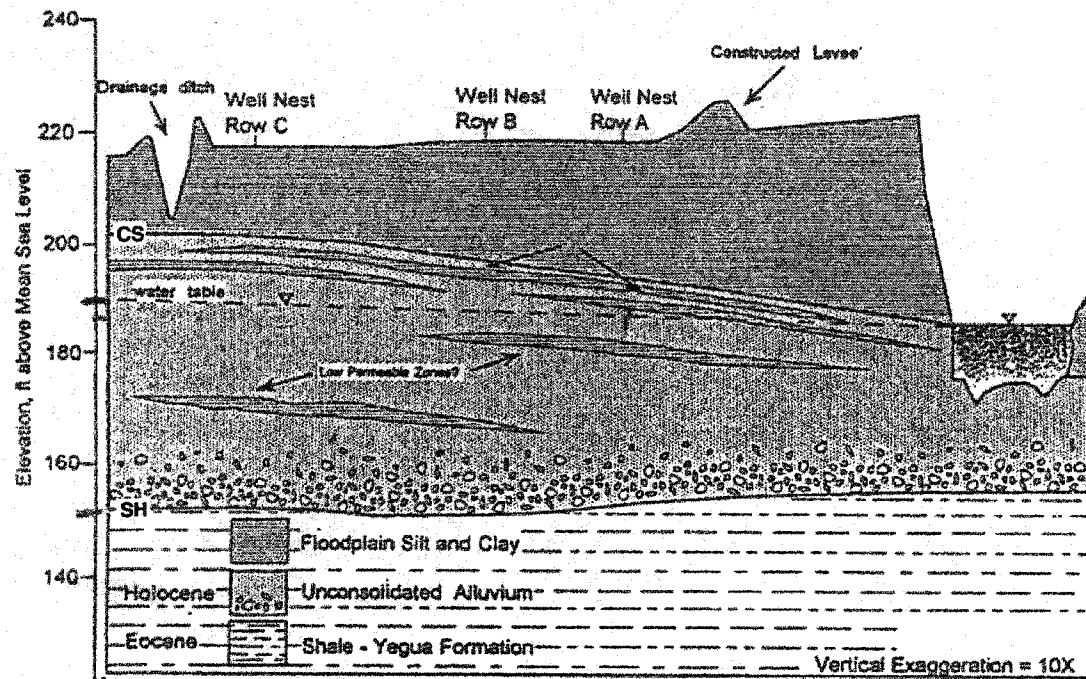


Figure 2.30: Cross-section from the Texas A&M site. Modified from (Sananikone, 1997)

shotpoints were placed at equally spaced locations along the line. At each shotpoint, two shot gathers were recorded separately, first with recording stations 1 - 60 live, then with stations 61 - 120 live resulting in 120 channel common-shotpoint gathers. The shot - near receiver gap was about 0.5 m. The source was a 16 lb sledge hammer and plate with 12 hammer blows stacked and recorded per shot (Figure 2.4). Although I was not able to detect water table drawdown [the frequency content of the data was too low (120 Hz, $v \approx 500$ m/s, $\lambda = 4$ m) relative to the drawdown (< 1 m)], the experiment was successful in the sense that an accurate velocity model was constructed for the aquifer system (Figure 2.31). The model was derived from traveltime inversion of first break and reflection picks using the method of Zelt and Smith (1992).

Processing the dense survey. We acquired the dense near-offset RAST survey (60 m long) to determine how well the low velocity portion of the section ($d < 10$ m) can be imaged using dense data relative to the coarser survey. Note that the maximum offset of 30 m roughly follows the data acquisition convention (Evans, 1997) of $x_{\max} = d_{\max}$ where x_{\max} is the maximum offset and d_{\max} is the maximum depth of interest. A second objective was testing various methods to remove low velocity coherent noise to reveal primary reflected events below W. The source was a 20 lb post-driver impacting on a steel pole with metal plate welded to its base. Twelve impacts per source station were recorded and stacked. The data were acquired with a 20 -40 split-spread configuration with a source / near-receiver gap of roughly ~ 0 m. We hoped that this source would provide significantly higher useable frequencies than the hammer and plate, but unfortunately provided roughly the same range and a center frequency of about 120 Hz could be

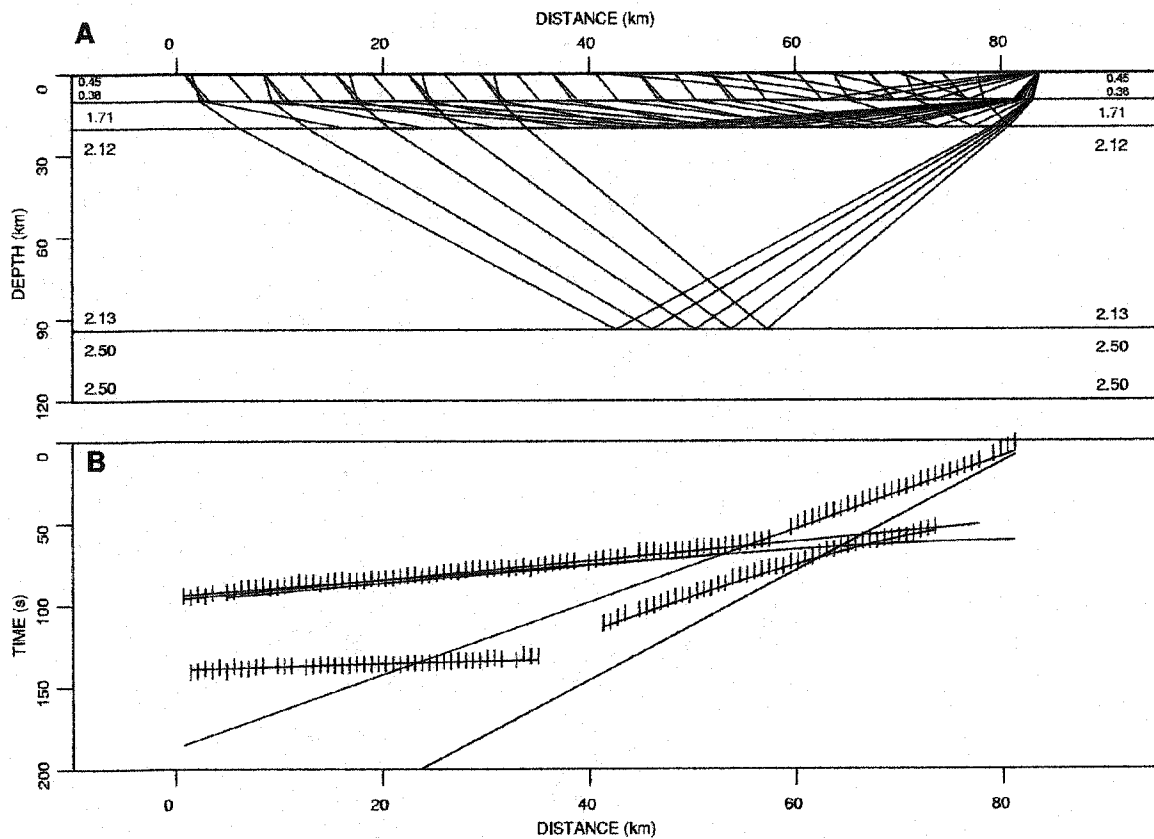


Figure 2.31: A) Inverted velocity model and rays paths, and B) traveltime curves and picks from one of seven shot gathers used for traveltine inversion at the Texas A&M site. The data are shown in Figure 2.4. Velocities are in km/s.

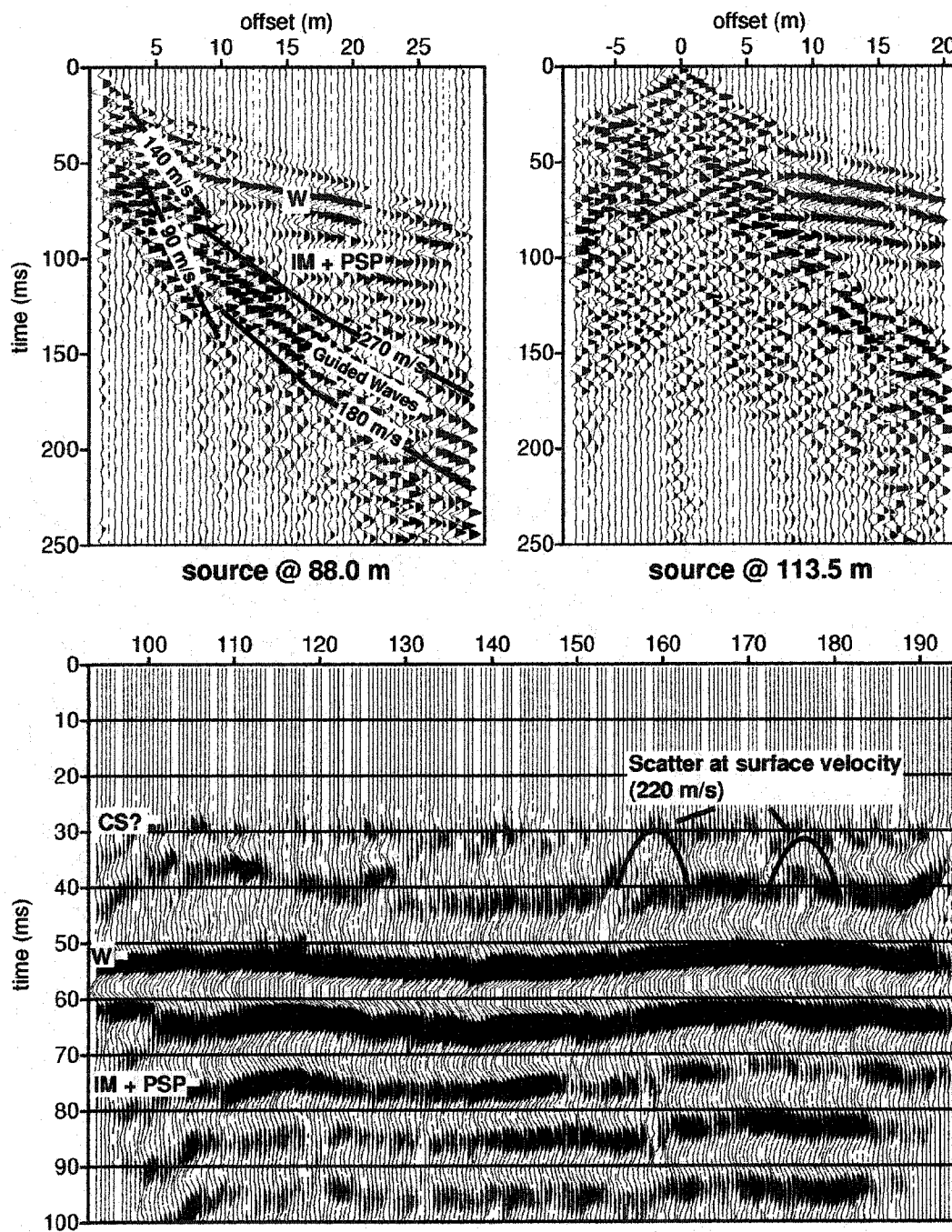


Figure 2.32: Shot gathers and a stacked time section from the dense survey at the Texas A&M site. Various modes of surface noise are labeled in the shots gathers. No primary reflections are visible below W. The event labeled as CS cannot be interpreted with confidence, although the arrival time is correct. There may some evidence of a reflector at this depth at source point 113.5. The horizontal position on the stack indicates survey x position in meters (compare to Figure 2.35)

retained in the filtered records.

Problems with the near-zero offset survey. The dense survey produced some interesting, if discouraging, results. The prominent reflection event in the filtered shot records is the water table reflection with $t_0 \approx 50$ ms (Figure 2.32A). There are several other events of interest however. We can see several modes of linear coherent noise, with moveout velocities of 220 m/s, 144 m/s, and 90 m/s. With a nominal frequency of 120 Hz, and receiver spacing of 0.5 m, energy moving at a velocity below 120 m/s will be spatially aliased. The lowest phase velocity I measured in the ground roll was 90 m/s, but this was effectively removed with bandpass filtering. Most of the remaining surface noise had a phase velocity of greater than 140 m/s (Figure 2.32A), and maximum frequency of about 180 Hz so aliasing is not a significant problem. The air wave was effectively removed using a local slant stack filter.

Above W, I cannot identify reflected energy inside the 140 m/s cone, and below W no reflected energy is evident inside the 270 m/s cone. Several methods were used to remove the coherent noise including f - k filtering, τ - p filtering (both local and global), and datuming followed by wave-field extrapolation. These methods were effective at removing the noise, but no coherent reflected energy remained inside the noise cone, including the high amplitude water table reflection. Amplitude analysis of the data indicates that, even in the filtered records, the ground roll amplitude is about 10 times greater than the amplitude of W. I expect W to have about 10 times greater amplitude than a reflection from the shale aquitard (SH) so the noise has amplitudes about 100 times greater than SH. This amount of amplitude variation falls well within the dynamic range

of the 24-bit recording system. Any filtering process distorts the data and produces artifacts with amplitudes directly related to the amplitude of the original noise (high amplitude noise results in relatively high amplitude artifacts). I conclude that reflected energy inside the ground roll cone is distorted beyond recognition by the filtering process which removed the high amplitude coherent noise. Therefore, at these frequencies, we cannot extract near offset reflection information.

The problem of imaging reflectors below W is exaggerated by coherent noise generated at the high impedance boundary. The large velocity and density contrast result in a reflection coefficient of around 0.7. Therefore, most of the energy is reflected. We expect strong surface multiples, and there is a potential for strong interbed multiples between W and the shallow clay-sand (CS) interface. I also expect strong S-wave conversion at the piezometric surface due to the large velocity contrast and small critical angle.

To aid in interpretation of the various arrivals, I generate a synthetic shot gather based on the velocity model derived through traveltimes inversion in the refraction survey (Figure 2.3). I use an 8th order, finite difference, visco-elastic code. Based on the elastic model, I interpret both an interbed multiple, generated between W and CS, and a PSP mode (Figures 2.4 and 2.32A). The PSP mode is converted to a reflected S-wave at the piezometric surface then converted back to a P-wave by transmission across CS. These events are of much higher amplitude and have an arrival time similar to that expected for SH at small offsets. We cannot realistically expect to extract the SH reflection at offsets less than 30 m. Failure to properly identify these events could clearly lead to

misinterpretation. Note that the *minimum* offset we can expect to see the SH reflector is greater than the convention $x_{\max} = d_{\max}$ for reflection surveys revealing yet another example of the divergence of shallow reflection from conventional exploration methodologies .

After concluding that no primary, near-zero offset reflected energy can be extracted for the SH reflector, I look for converted modes that might be reflected from this interface which could be used to image the unconfined aquifer. The most likely candidate is a PSSP arrival (converted to an S wave at W, reflected as an S wave at SH, then converted to an up going P wave at W). I first look to the elastic model. A significant PSSP event is observed in the finite-difference snapshots, however, the interbed multiple previously identified, has nearly an identical arrival time and moveout velocity, and much higher amplitude, than expected for the PSSP mode. I conclude that in this case, converted energy cannot be extracted to image SH.

Above W, we would like to extract primary reflected energy to image CS. Careful examination of the shot gathers and synthetic data indicates that very little of this energy is clearly resolved. The near-zero part of the reflection is obscure by ground roll, and outside the 140 m/s ground roll cone, the reflected energy converges very quickly with the first arrival, which in this case, is higher amplitude than the reflection (Figure 2.32A). I conclude that, at these frequencies, the sand-clay interface cannot be effectively imaged.

Thus, the only primary reflection we can interpret with confidence in the dense near offset survey is W. Inside muting the ground-roll, top muting the first arrival and stacking at 410 m/s produces a good quality image of W across the profile (Figure 2.32B).

Depth conversion using the stacking velocity (410 m/s) and t_0 yields a depth of about 10 m which is very close to the known depth of the water table, and I conclude that NMO processing is appropriate for imaging the low velocity field in this case. In the stack, an event at the appropriate time for CS is coherent across the profile. Two scattering events with moveout at the surface velocity of about 250 m/s are evident just above this event which may be interpreted as indirect evidence that the coherent event corresponds to CS although this is not a strong argument. No useful energy, reflected below the piezometric surface could be extracted in this near-offset survey.

Processing the coarse survey. We acquired the coarse RAST survey (240 m long) to determine how well the slow, shallow, vadose zone and fast, deeper, saturated zone could be imaged using a single reflection survey. The roll-along portion of the profile was acquired with a 20 - 40 split-spread configuration. The source was a 16 lb sledge hammer and steel plate with 12 hammer blows at each source location. The source / near-receiver gap was roughly ~ 0 m. As shown in the previous section, the dense near offset survey was not adequate to image SH, so it would be valuable to image all targets of interest with a single broad offset range survey. In the coarse survey we can identify W at near-offsets, and the SH reflector outside the W traveltime curve (Figure 2.33). W is clearly evident with a 50-100-200-350 bandpass filter, although it is obscured within the 140 m/s cone we can identify the tails of the reflection to a minimum offset of about 6 m (Figure 2.33A). All of the observed reflected energy is post-critical ($d_c = 4$ m) although the phase rotation with increasing offset is not obvious. The SH reflection is best observed after muting inside W and filtering with a 60-120-240-350 bandpass (Figure

2.33B). The SH reflection is clearly differentiable from H_w in an offset range from 36 m - 64 m. Beyond this offset, the travel time curves converge, and the wavelets from the two events interfere. Fortunately, in this case, the reflection amplitude is significantly larger than the refraction amplitude. The majority of the far offset energy can be confidently identified as reflected energy, and can safely be used in imaging.

In processing these data, I use the two pass approach, where the low and high velocity fields are imaged separately, then combined to produce the final depth profile. To process the low velocity field, I apply an inside mute below the water table reflection, and a top mute above the direct arrival at about 420 m/s. I then pre-stack, depth migrate the low-velocity data with the velocity model derived through traveltimes inversion, modified to assume constant, low velocity across and well below the piezometric surface. W is flattened effectively across the profile with a 1-D velocity function (Figure 2.34A).

I prepare the data for processing the high velocity field by muting inside the 420 m/s direct arrival cone (Figure 2.33B), and top mute H_w . I use the full velocity field from inversion as a starting model. To get good migration results (Figure 2.34B), I reduce the velocity in the saturated sand from 1710 m/s to 1600 m/s (about 6 %). When migrated with the full velocity field, a significant amount of migration noise is generated at the sharp boundary between the low and high velocity fields. This can be reduced by smoothing the velocity field but this comes at the cost of reducing accuracy. My approach is to simply mute above d_w , which in the case of processing only the high velocity field, is known to contain only noise.

Combining the low and high velocity field stacks results in a good quality image of

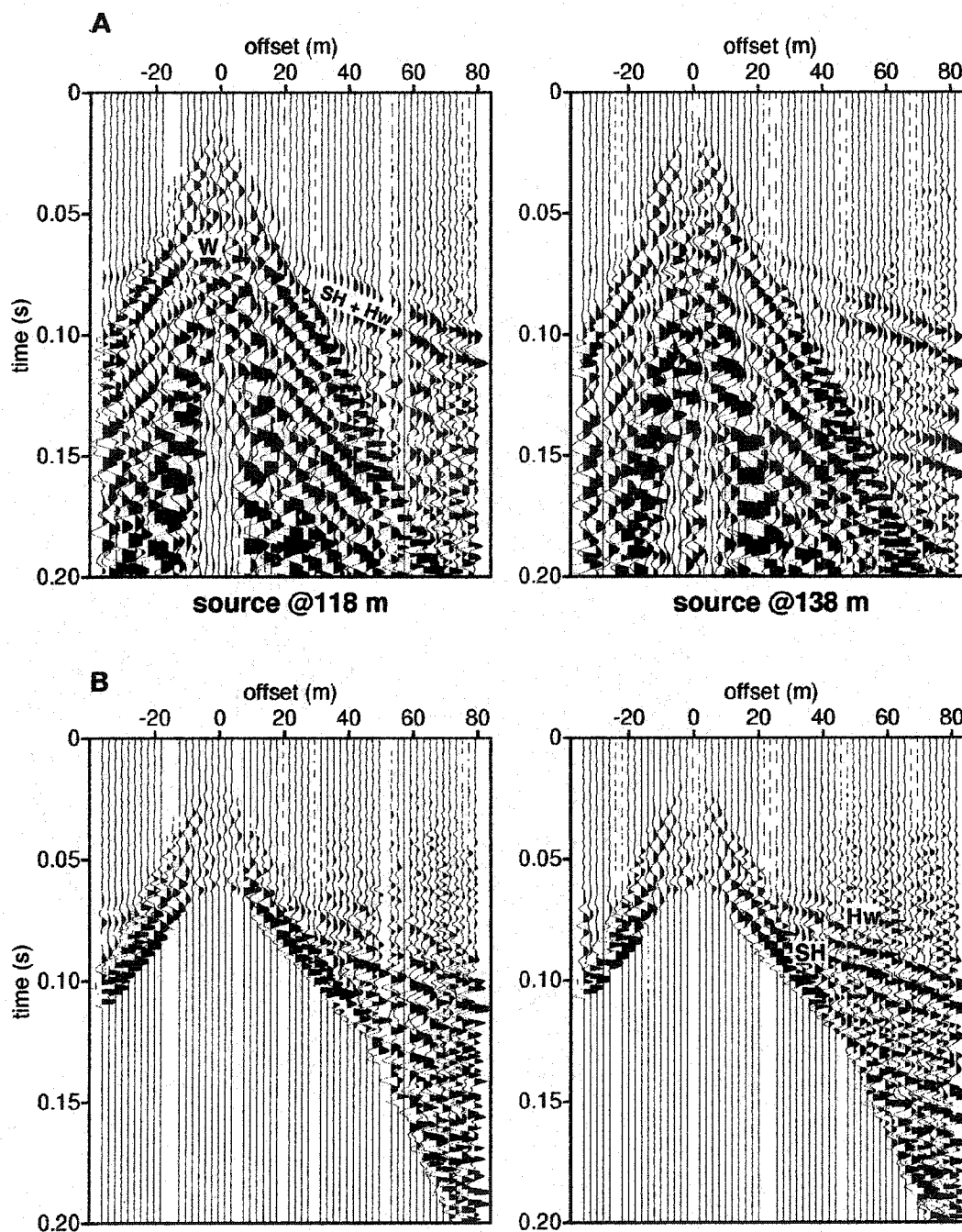


Figure 2.33: Representative shot gathers from the coarse survey at the Texas A&M site A) with a low cut of 50 Hz, and B) with a low cut of 60 Hz. The lower band better preserves energy from W, while filtering at the higher band helps resolve the aquitard reflector, SH which is roughly 10 m below the water table. The entire portion of W that is visible is post-critical, but phase rotation is not obvious.

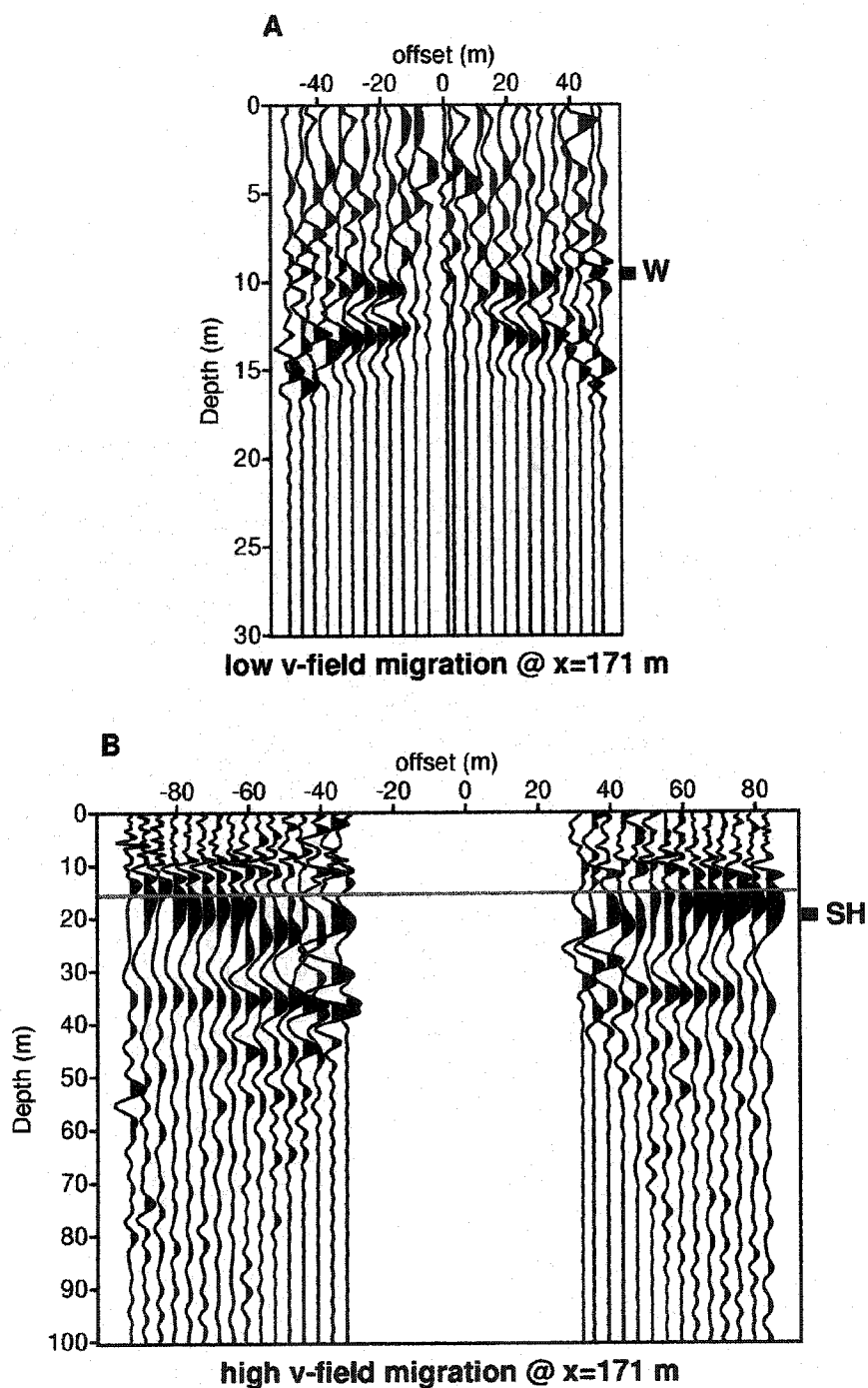


Figure 2.34: CIP 171 after migration of the low velocity field (A) with a partial velocity function and the high velocity field (B) with the full velocity function (note difference in depth scale). W and SH are flattened across the range of offsets that they are visible. The red line indicates top mute position.

W and SH (Figure 2.35A). W is clearly imaged at a depth of 10 m, and SH at a depth of about 18 m - 20 m which is consistent with stratigraphic descriptions. There is a significant amount of migration noise present above W. I did not top mute the low v-field CIP's prior to stacking in the hope that the CS reflection would stack coherently. While there may be some hint of a shallower reflection at 6 m, it is masked by migration noise.

The image has an odd appearance with a very large difference in the length of the wavelet reflected from the water table compared to that from the aquitard. This difference represents the physical increase of wavelength with increasing velocity, and is not a processing artifact. The width of the W wavelet is about 4 m, whereas the width of the SH wavelet is about 18 m. This gives a wavelet length ratio of 4.5. The wavelet length is roughly proportional to the wavelength at the peak frequency. Since the wavelength is directly proportional to the velocity, the predicted wavelength ratio is

$\lambda_{\text{fast}} / \lambda_{\text{slow}} = v_{\text{fast}} / v_{\text{slow}} = 383 / 1600 = 4.18$. Thus the observed ratio is very close to the predicted ratio. The slightly larger value for the wavelet length ratio can be attributed to differential stretch of SH vs W with increasing offset.

For comparison, SH was processed independently using NMO and stacking followed by Dix inversion and depth conversion (Figure 2.35B). The top of SH appears at depths that range from about 25 m - 32 m, which gives a maximum error of $\delta d_{\text{SH}} = 14$ m ($\sigma_{\text{SH}} \approx 80\%$). This is a significant error, and would be unacceptable for many applications. Comparison of the interval velocity obtained via DIX inversion with that obtained through migration velocity analysis shows that DIX inversion significantly over predicts interval velocity (Figure 2.36).

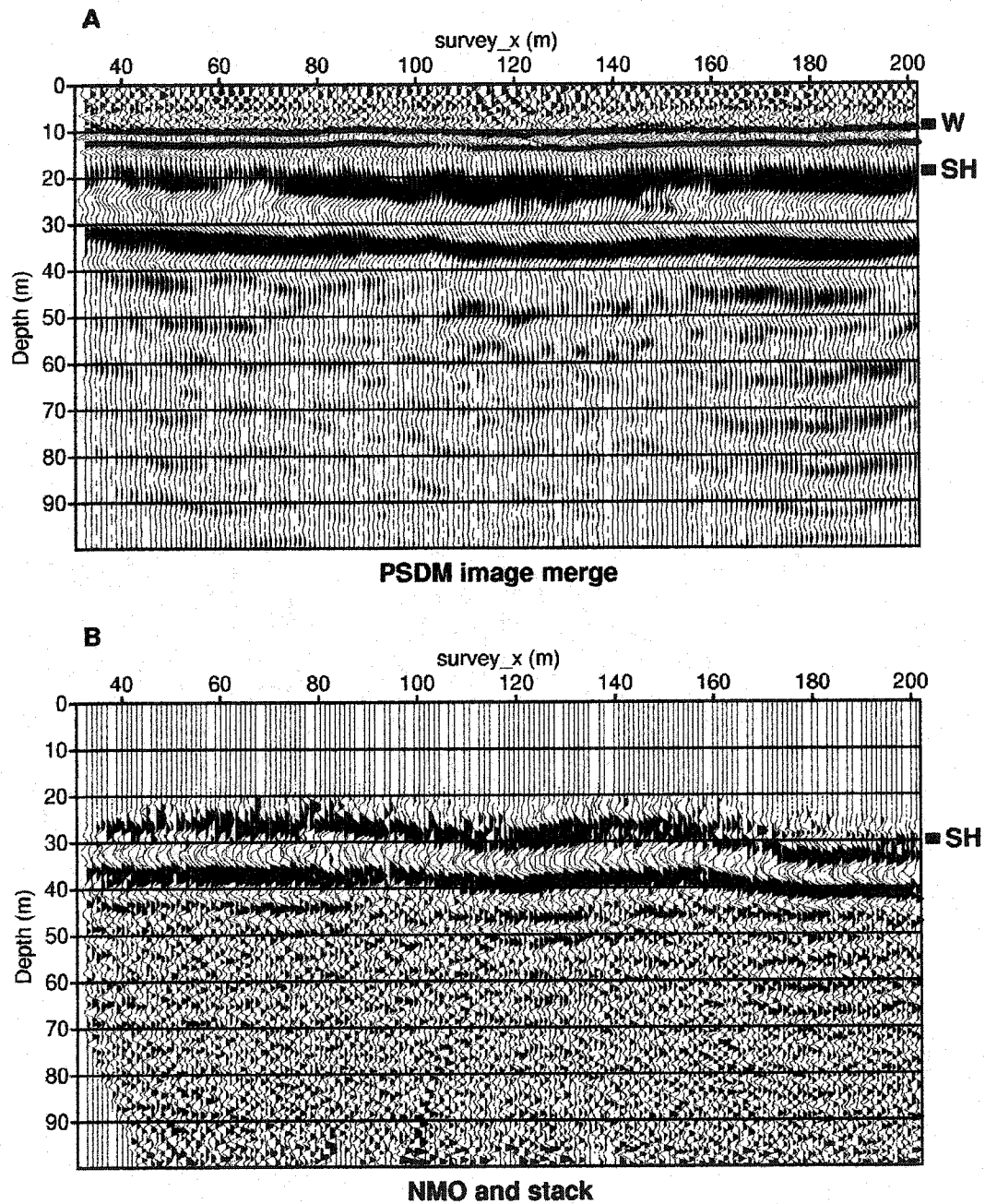


Figure 2.35: PSDM image after merging the low and high velocity fields (A) and depth converted stack using velocities from Dix inversion (B). In the PSDM image, W and SH are consistent with known depths to the water table and shale aquitard. The stretch of SH corresponds to the velocity increase in the saturated zone. Depth to SH in B), is significantly overpredicted.

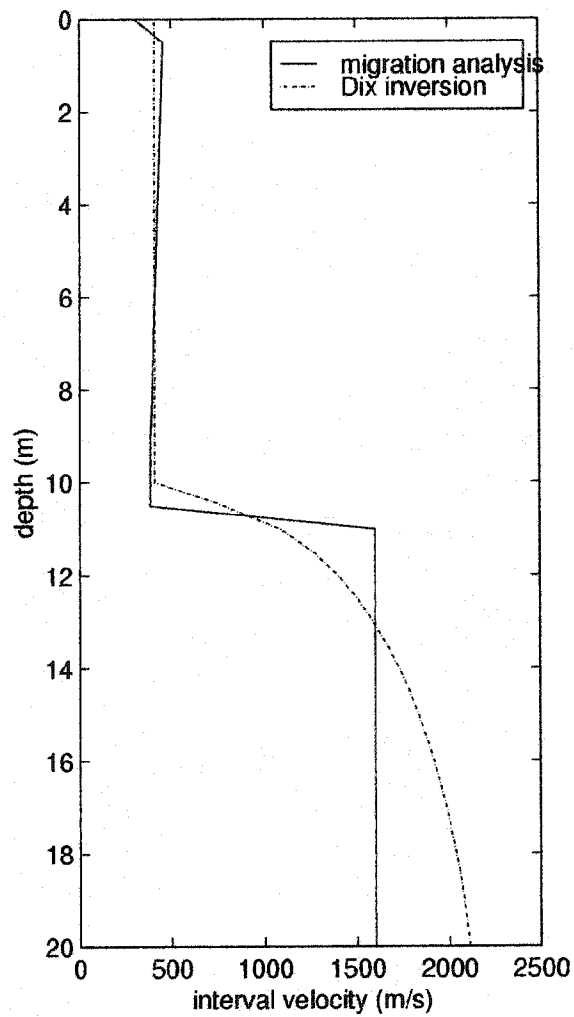


Figure 2.36: Comparisons of velocity models derived through PSDM velocity analysis and Dix inversion. Dix inversion significantly overpredicts velocities below the water table.

Summary. Clearly pre-stack depth migration improved accuracy. Both W, and Bu could be adequately imaged in qualitative terms, using NMO processing, but the resulting error is unacceptable in many applications. No benefit was obtained by acquiring a dense, near offset survey in which CS was not imaged well, no information was extracted from below the piezometric surface, and the image of W was not significantly better than in the coarse survey. A dense survey is more labor intensive to provide the same total line length, and will not necessarily improve the image of the shallowest targets. As always, this is site and survey dependent. With higher frequency content in the data, we would likely get better ground-roll suppression through filtering, thereby increasing the potential to image the shallower reflectors that must be observed in the near zero-offset regime. In any case, it is important to consider the potential for achieving the survey objectives with a coarse broad offset range survey which decreases acquisition time, and increases imaging potential below the water table.

Coastal plain environment

As a field exercise for the Exploration Geophysics class at Rice University we acquired a 240 m RAST (Figure 2.28) survey across a soccer/rugby field (note that many people drive golf balls and walk their dogs on this same field) on the Rice Campus (Figure's 2.27 and 2.37). The roll-along portion of the profile was acquired in off-end mode with a source / near - receiver gap of 10 m. The source was a 16 lb sledge hammer and plate with 12 hammer blows recorded at each source station. The shoot-through portion of the profile was acquired with a gap of ~0 m. The surface sediment consists of

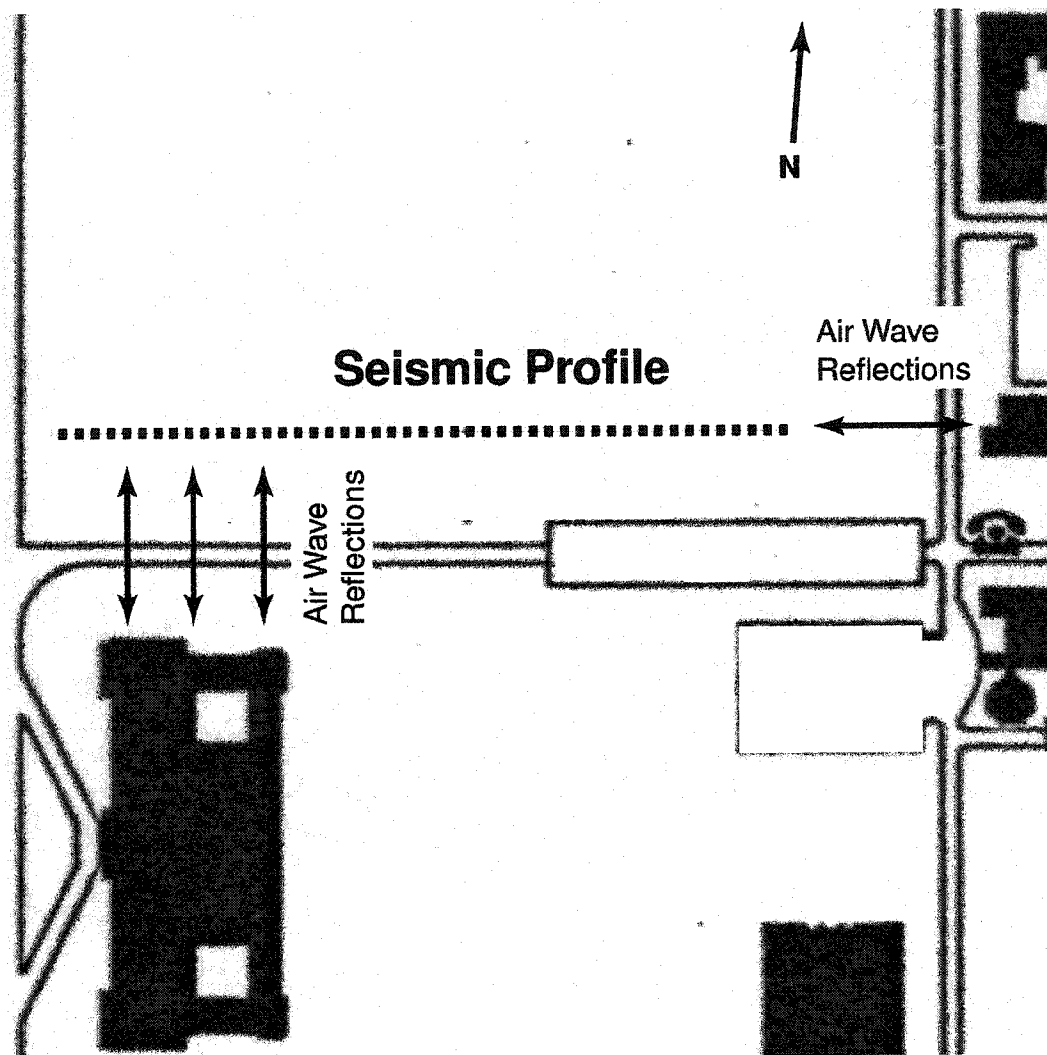


Figure 2.37: Location of the Rice profile, and position relative to campus buildings. Air wave reflections from the buildings are a major source of coherent noise at later times (Figure 2.38).

the dense clay of the Pleistocene age, Beaumont Formation, providing excellent source and receiver coupling. The stratigraphy consists of interbedded sands, gravels, and clays of variable thickness to a depth of least 454 m.

The data are of exceptional quality, and reflections can be observed to around 500 ms (Figure 2.38). A temporally and spatially varying bandpass filter was applied to the shot gathers to minimize low frequency ground roll. This varied from 70-140-280-460, at near offsets and small times to 30-60-120-240 at the maximum time displayed of 600 ms. All data displayed have been corrected for spherical divergence and gained to the first power of t . A high amplitude air-wave, and ground-roll at a maximum phase velocity of about 140 m/s are the primary source of coherent noise (Figure 2.38). Deep reflections are clearly observed inside the air-wave cone, but could not be extracted at offsets less than about 14 m. The scatter between 500 and 550 ms is an air-wave reflection from the corner of Alice Pratt-Brown Hall located adjacent to the line (Figures 2.37 and 2.38). Linear coherent noise below 400 ms on the east end of the profile is an off-end air wave reflection from the Anderson Biological Laboratories (Figure 2.37 and 2.38). The water table reflection (W) is clearly evident in the near offset portion (west) of the profile and reflected energy can be identified to a minimum offset of about 2 m on the best shot gathers (Figure 2.38). The quality of W is variable, and is totally obscured by ground-roll on some records. W is not present in the far offset (east) records.

NMO processing. Assuming W can be accurately imaged using NMO and stacking, and that the best image will be obtained by processing all data deeper than W with a partial stacking velocity field (excluding $v_{stk(W)}$) in a separate processing pass, I do not consider W

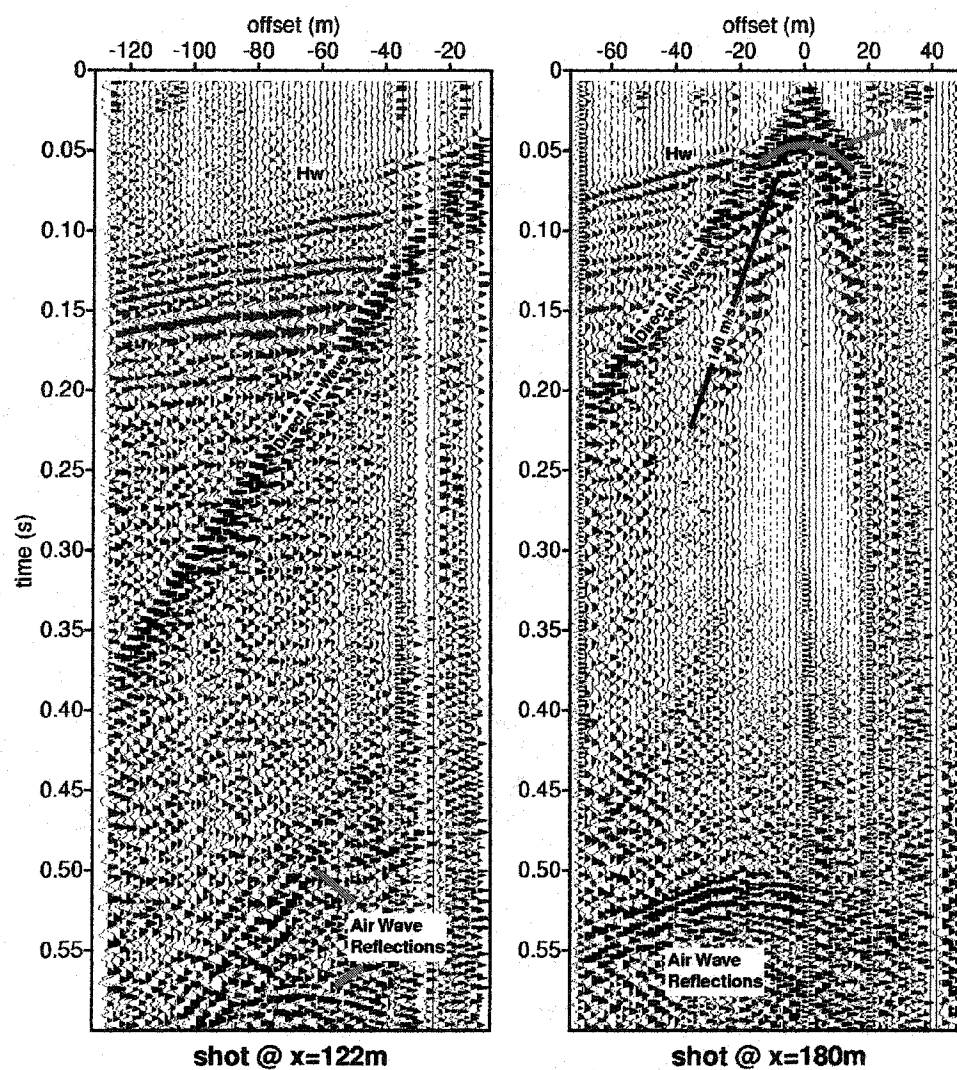


Figure 2.38: The data quality at the Rice site is excellent and the water table reflection is clearly identified as well as primary reflections deeper than 500 ms. Air wave reflections from buildings interfere with deeper primary reflections.

in this discussion. Data were filtered, gained (spherical spreading correction and t^1), semblance velocity analysis, correlation autostatics, NMO corrected and stacked (Figures 2.39 and 2.40). The full stacking velocity field was used in depth conversion. The stacked section is of good quality to a depth of about 400 m (Figure 2.39A). Reflections can be clearly identified to about 600 m, in the center of the section. The data quality decreases as fold drops off near the ends of the profile. Air wave reflections contaminate the east side of the profile at depths from 400 m - 650 m, and the west side at depths from 450 m - 550 m.

PSDM processing. I prepare the data by muting the far offset tails of the water table reflection, and inside muting the ground roll. The air blast is removed with a surgical mute. The starting velocity model was obtained by method 1, as discussed in the processing strategies section. Four iterations of PSDM velocity analysis produced good migration results (Figure's 2.39, 2.40, and 2.41), with a relatively simple 1-D velocity model (Figure 2.42). I found that applying statics corrections prior to migration significantly improve velocity analysis convergence and the migration result.

Stacking the migrated CIP's produces a high quality depth image with several qualitative improvements from the NMO processed sections (Figures 2.39 and 2.40). The air wave reflections have been efficiently suppressed and are not evident either on the left or right side of the section. Through PSDM processing, the full section has been imaged in a single pass, from the water table reflection to the deepest reflection I can pick with confidence, at around 550 m.

The quality of W varies significantly along the line (it is not present on the east side

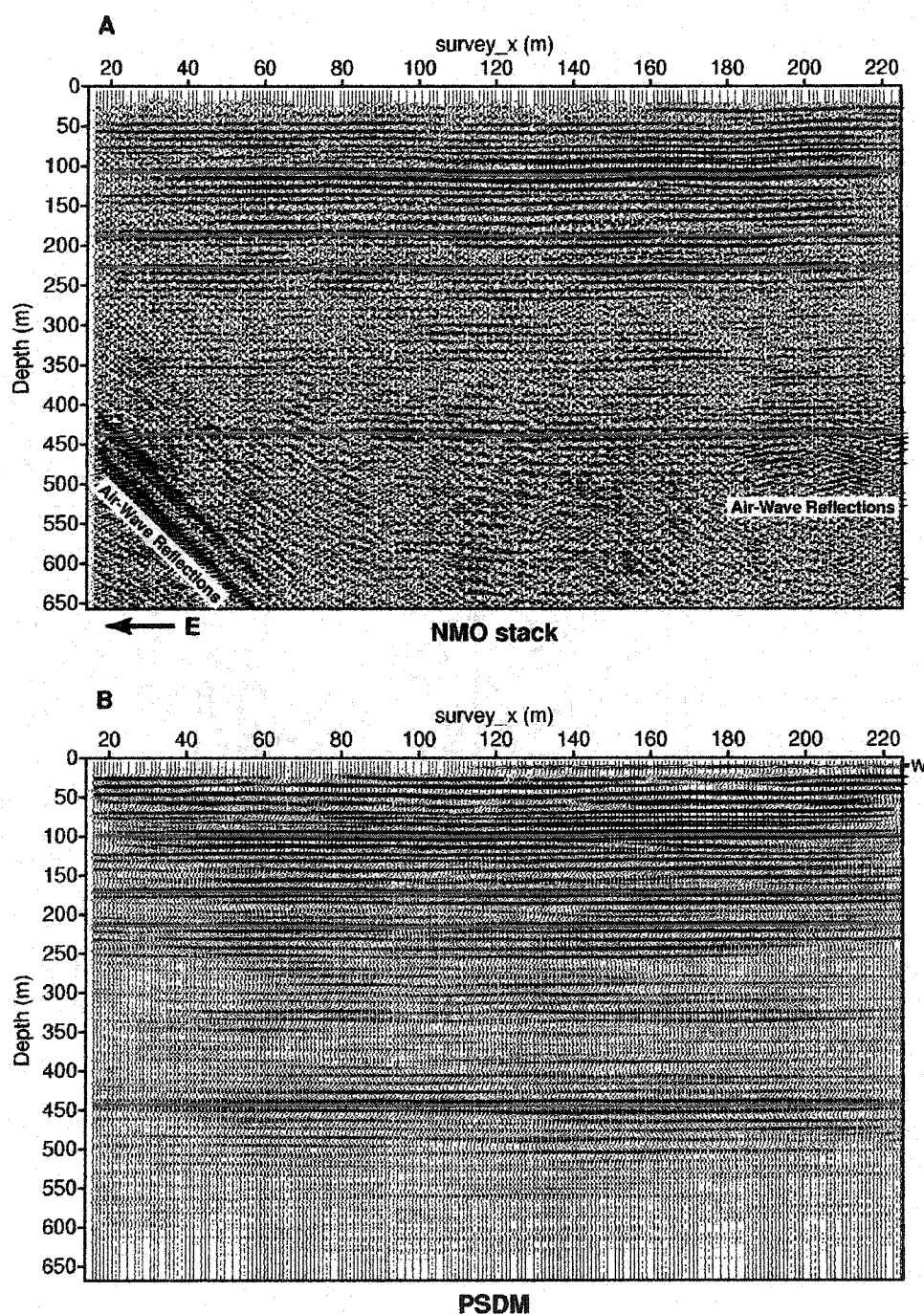


Figure 2.39: Rice profile after NMO, stacking, and depth conversion (A) and a PSDM image (B). Red lines indicate reference reflectors. Significant differences are evident to about 250 m. PSDM significantly reduced random noise and effectively attenuated coherent air wave reflections deep in the section.

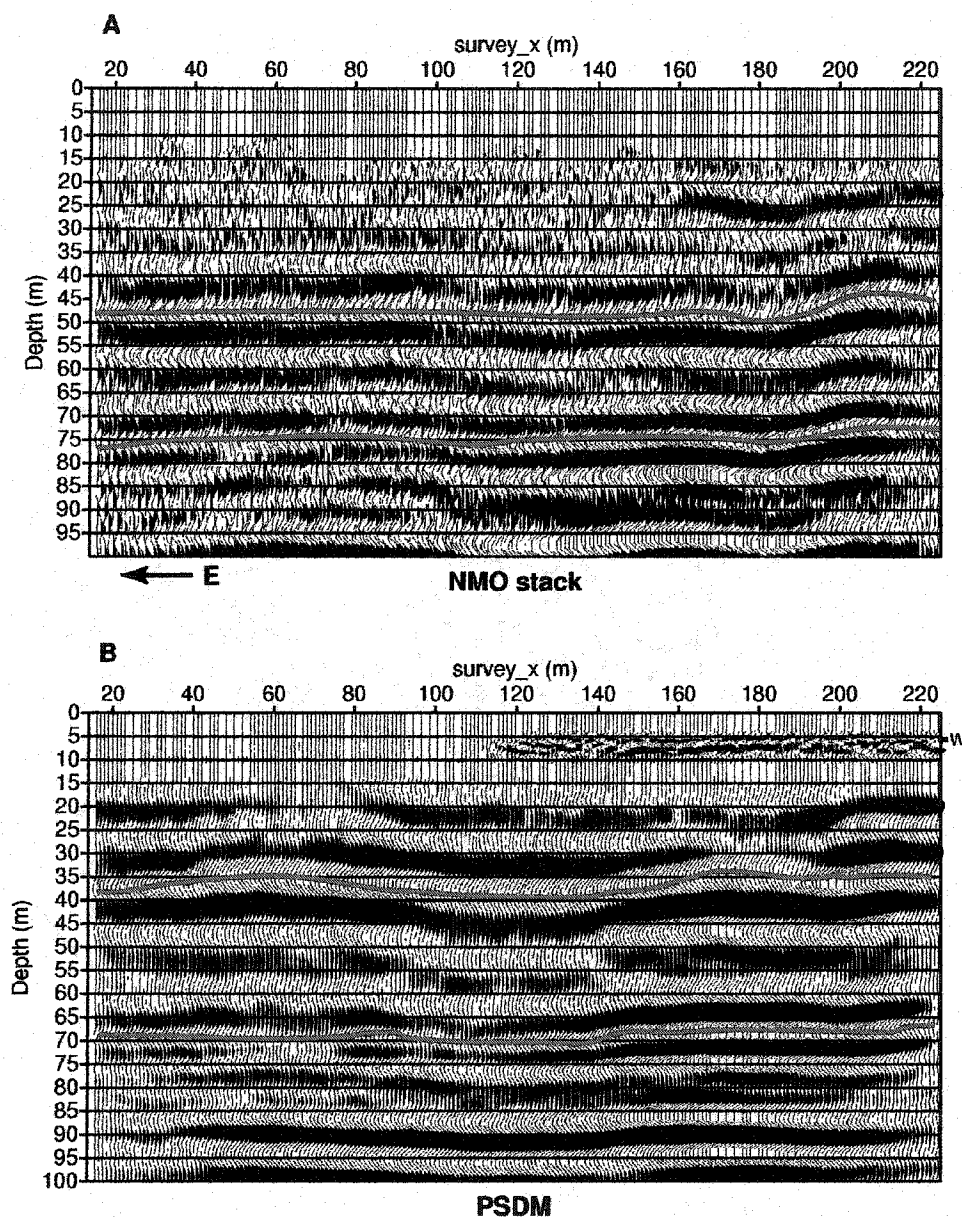


Figure 2.40: Shallow portion of the Rice profile after NMO, stacking and depth conversion (A), and a PSDM image (B). Reference reflectors are shown in red. All reflectors below W are overestimated by about 10 m in the NMO section. W only migrates coherently from about $x = 140 - 200$ m. W is not shown in the NMO section.

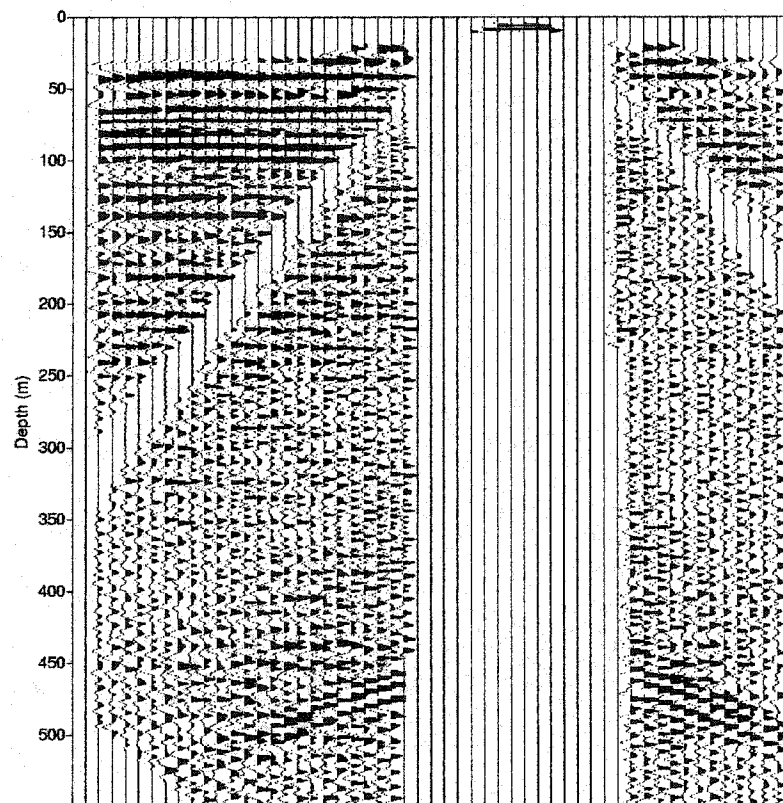


Figure 2.41: CIP 161 after PSDM of the full section. All reflections in the CIP are flattened. The strong reflection at 450 m is evident in this CIP. The strong events from 450 - 550 m are out-of-plane air-wave reflections.

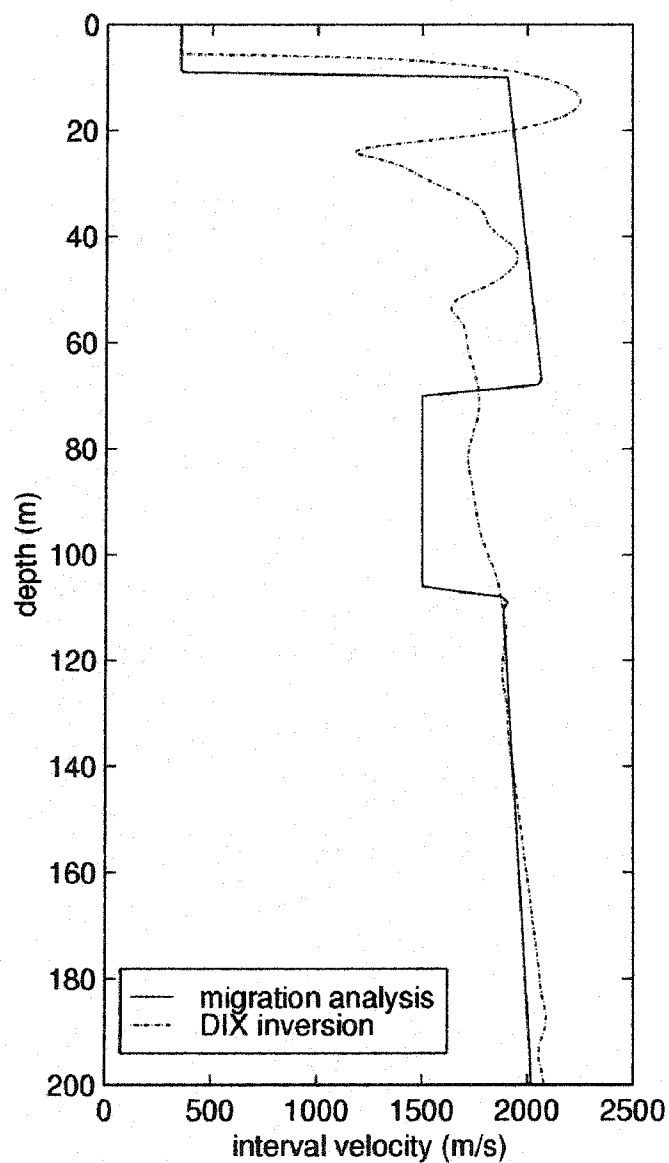


Figure 2.42: Velocity models determined from Dix inversion and PSDM velocity analysis. Dix inversion velocities are a poor representation of the velocity field above 120 m.

of the profile), but is clear at a depth of around 6 m, from about 145 m - 190 m (Figure 2.40B). The quality of this reflector is best where the fold is highest along the line. However, the change in data quality cannot be attributed to decreased fold since the effective fold (# traces per CMP that actually have energy from W) remains essentially constant from 120 m to 230 m. The decrease in reflector quality is due to data quality variations, and is not related to the change in fold.

For a quantitative comparison, I consider the shallowest 100 m of the NMO and PSDM profiles (Figure 2.40), I find that all of the reflectors in the PSDM section are roughly 10 m shallower than the corresponding events in the NMO processed section. Although there is no borehole “ground-truth”, the previous examples have illustrated that PSDM velocity analysis and imaging significantly improves accuracy, and in this case I assume the PSDM image is relatively accurate. The depth estimate error resulting from NMO processing and Dix inversion is about 50% for the shallowest reflector, then is proportional to $1/d$ and is around 11% for the deepest reflector at a depth of about 90 m.

Velocity model comparison. The most interesting feature of the velocity model is the sharp velocity inversion from about 65 m - 105 m (Figure 2.42). The velocity in this region is just slightly greater than water velocity, and I speculate that this is related to the inclusion of gas in the pore space, which, as mentioned previously, may be a fairly common occurrence in shallow confined aquifers. AVO analysis along this reflector has the potential to provide additional insight as to the nature of the low-velocity zone ((Bradford et al., 1997), but this analysis has not yet been performed with this dataset, although it is a good candidate given the quality of the data.

The DIX inversion model has dramatic oscillations between 5 m and 40 m (Figure 2.42) There is some indication of a velocity inversion between 65 m and 100 m, but it is not well defined, and the magnitude of the velocity change is significantly less than estimated with PSDM velocity analysis. This is not surprising since the stacking velocity is relatively insensitive to velocity inversions (Figure 2.26). In this case, there are significant reflections at both the top and bottom of the low velocity zone which increase the potential for accurate detection of the low velocity zone using PSDM velocity analysis. Below about 105 m, DIX inversion and migration velocity analysis give virtually identical results.

Summary. In this case PSDM imaging provides a significantly improved profile relative to the NMO processed section. This is in terms of both accuracy, and qualitative features such as effective noise suppression and imaging the entire section from 5 m to 550 m in a single processing pass. Computation requirements could be minimized by PSDM processing only the shallower portion of the section, and using standard NMO processing to image the deeper (>100 m) portion of the profile. This would come at the cost of reduced noise suppression, but should provide sufficient accuracy.

Coastal environment

We acquired a 30-fold, 1 km profile on Bolivar Peninsula near Galveston, Texas (Figure's 2.27 and 2.43). The experiment objective was to determine how well we could image the strata of an incised valley fill sequence to a depth of about 50 m (Figure 2.44). The data were acquired with 2 m source and receiver spacing, a source / near-receiver gap

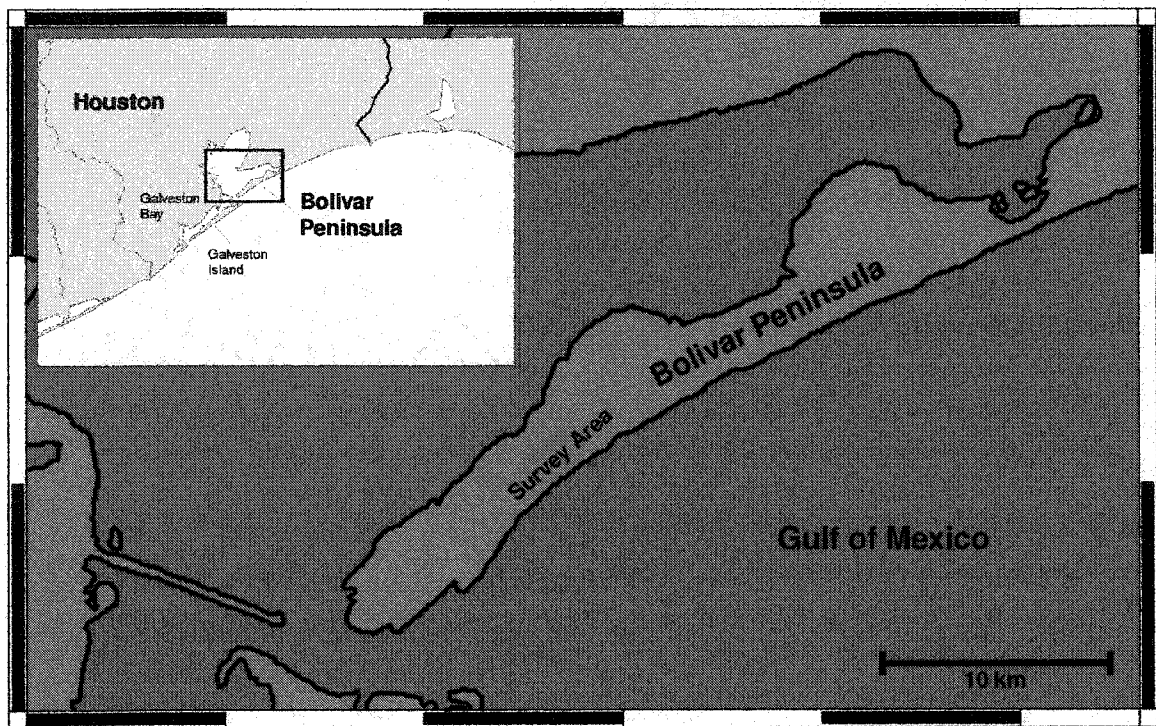


Figure 2.43: Location of Bolivar Peninsula survey area.

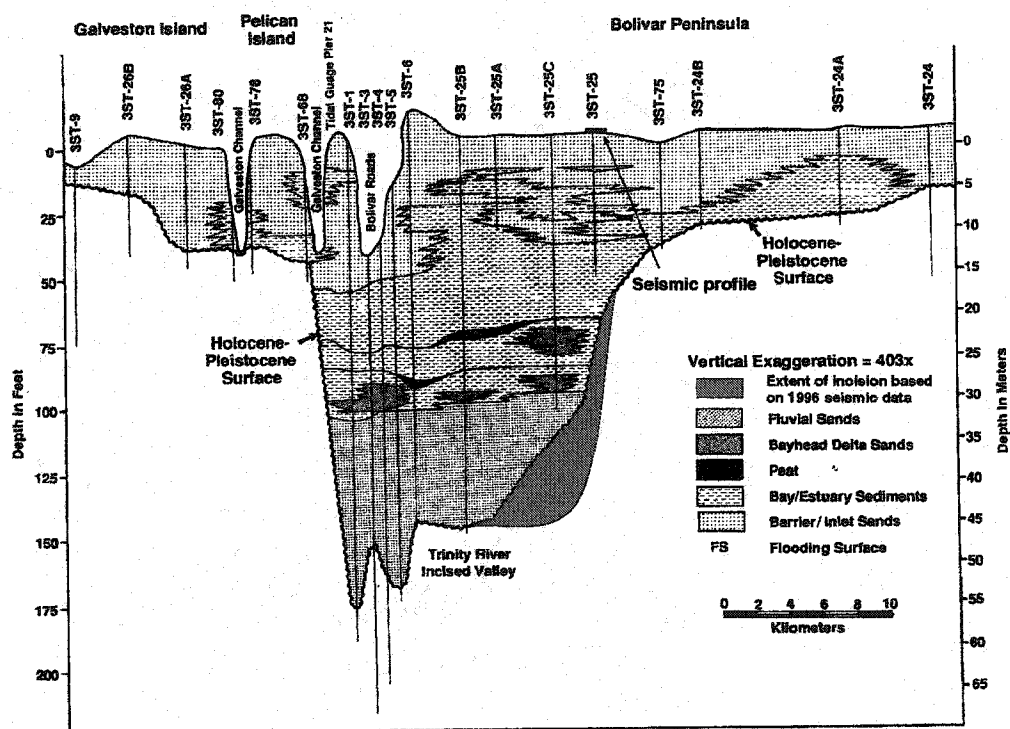


Figure 2.44: Cross-section of the Trinity River incised valley. The top-of-fluvial sand correlates with a high amplitude reflection, and AVO analysis indicates the presence of gas. [Adapted from Siringan and Anderson (1993)].

of ~ 0 m, and 30 - 30 split spread geometry. The source was a 16 lb sledge hammer and steel plate with four hammer blows stacked at each source point (Figure 2.45). A maximum peak frequency of about 120 Hz could be extracted in the filtered shot gathers. Sedimentary strata (Figure 2.44) consist of medium to fine grained barrier island sands to a depth of 5 m, fine grained bay sediments from 5 m - 25 m, and fluvial sand from 25 m to around 50 m which is the maximum depth of the Trinity River incision at this location. The incision cuts into older Pleistocene clays. The piezometric surface is relatively shallow, at depth of only 3 m.

A velocity model was constructed using traveltime inversion based on picks of both first arrivals and reflections (Bradford et al., 1997; Zelt and Smith, 1992). A low velocity zone is present in the fluvial sand unit which fills the lower 25 m of the incision. Previous AVO work suggests that the anomalously low velocity in the sand unit is likely due to the presence of biogenic gas (Bradford et al., 1997).

A 170 m portion of the 1 km line is discussed in this analysis (Figure 2.46). The data were migrated using a 1-D velocity function derived from local smoothing of the inversion velocity model (Figure 2.47). This yields acceptable results without additional PSDM velocity analysis (Figure 2.46A). A fully processed NMO stacked, depth converted section is included for comparison (Figure 2.46B). DMO was applied to the NMO section. Correlation autostatics were applied to both the PSDM and NMO sections.

The piezometric surface is very shallow (~ 3 m) and W is not imaged in either the PSDM or NMO section. The most important difference in the shallow part of the section

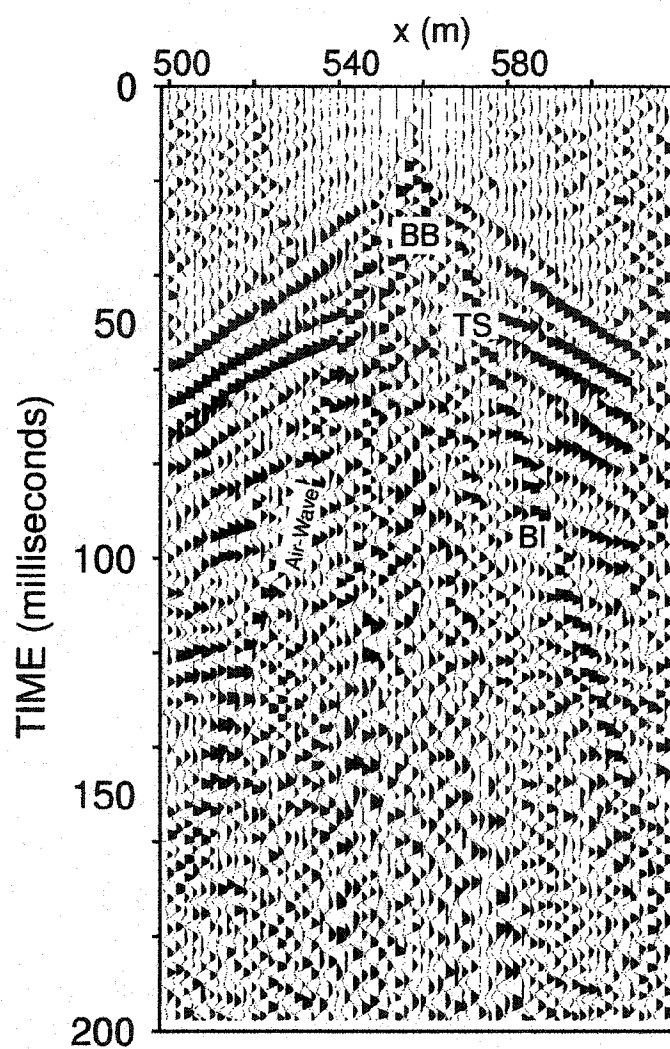


Figure 2.45: Representative shot gather from the Bolivar Peninsula survey. Base-of-barrier sands (BB), top-of-fluvial sand (TS), and base-of-incision (BI) are clearly evident.

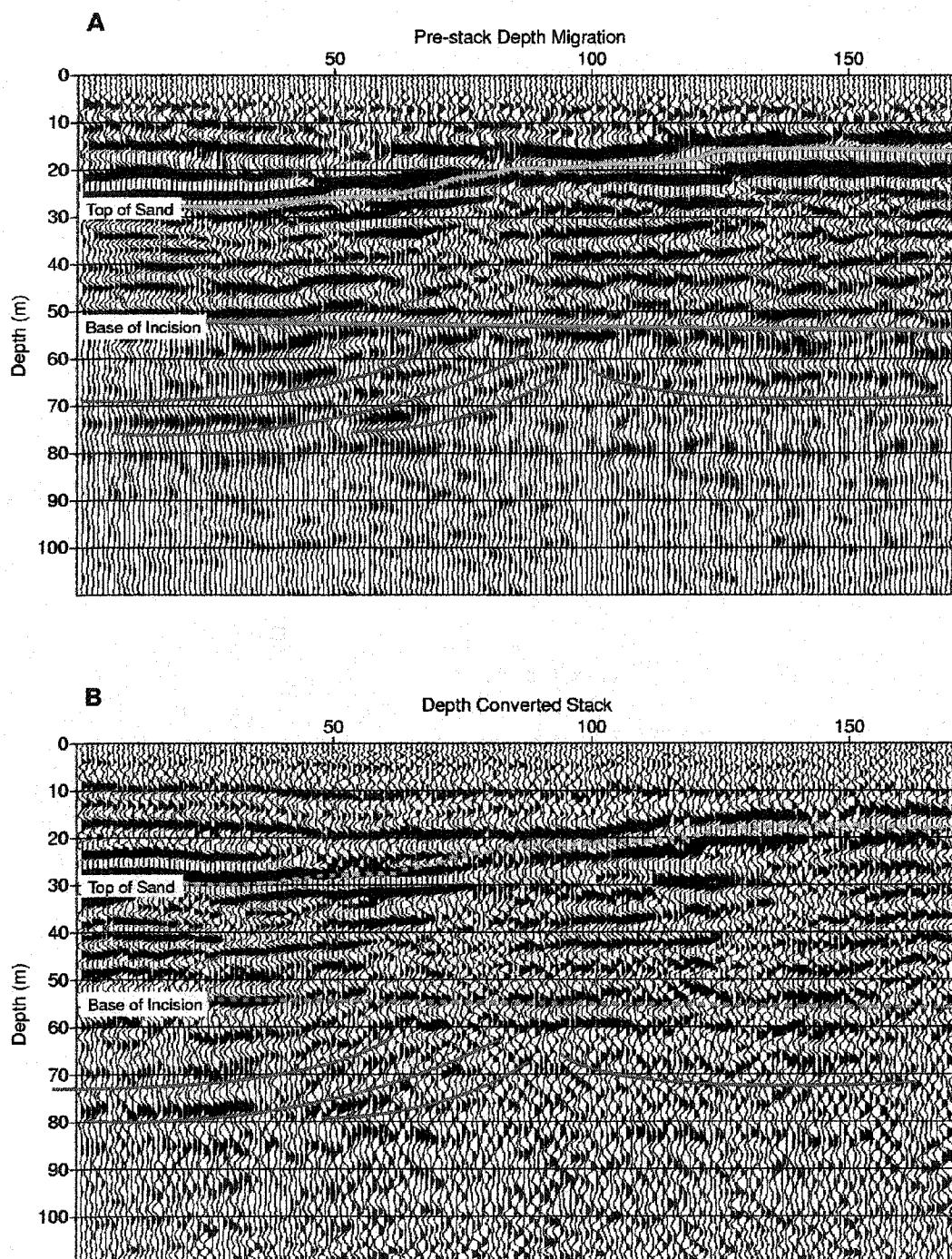


Figure 2.46: PSDM image (A) and NMO stack with depth conversion (B) of a portion of the Bolivar Peninsula profile. In this case, depth prediction error from Dix velocities is relatively small (green and brown lines indicate interpreted depths from the PSDM image). The dipping reflectors (red) truncated by the incision (brown) are more clearly imaged with PSDM.

is that the base-of-barrier reflection at a depth of about 6 m - 8 m, is imaged reasonably well in the NMO section, but is poorly imaged in the migrated section. This is attributed primarily to migration noise in the shallower part of the section. This boundary appears at a depth of about 6 m in the migrated section, compared to 8 m in the NMO section, this is an error of about 33% but is a minimal difference compared to the 13 m wavelength at the center frequency of 120 Hz. Each of the other reflectors in the section down to the bright top-of-fluvial sand reflector at about 25 m, are also placed about 2 m - 3 m deeper in the NMO section. This represents a minimum error of about 12% for the top-of-sand reflector. The more significant difference in precision becomes evident with examination of the base-of-incision reflection at about 50 m. This reflection is about 5 m deeper in the NMO section. This is only about a 10 % error in depth prediction but is roughly a 100% increase in δd relative to the shallower reflections. Traveltime inversion indicates that the average velocity across the velocity inversion is about 1170 m/s, while DIX inversion predicts an average velocity of 1300 m/s (Figure 2.47), so depth conversion with the Dix interval velocities adds an additional 3 - 4 m to δd . However, this error is still relatively small compared to the wavelength, the depth to the reflector, and the relative error observed for reflectors near the piezometric surface in the previous examples.

Comparing the travel time inversion and Dix inversion velocity models, there is a striking difference relative to the two previous field examples. In this case, Dix inversion actually under predicts the velocity contrast across the piezometric surface, and actually appears to represent a sort of running average interval velocity for the full thickness of the section. The velocity contrast across the piezometric surface is under predicted because I

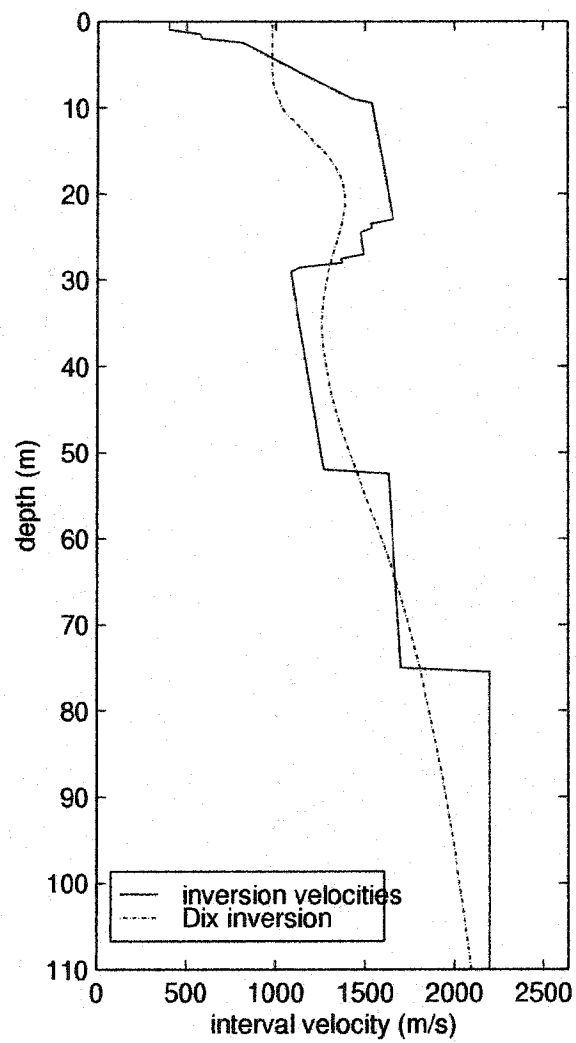


Figure 2.47: Velocity functions derived for the Bolivar profile. In this case, the Dix velocities are a reasonable representation of the average interval velocity.

did not include the low velocity vadose zone in the Dix inversion (i.e. partial $v_{stk}(t)$). This results in a reasonable velocity function only because the vadose zone is very thin. Recall that σ_{xx} and σ_{dxx} decrease rapidly when the thickness of the low velocity zone is less than about 5 m (Figure 2.10).

The more interesting difference in this example is more qualitative in nature. The strata at this site are more complex than either the fluvial or coastal plane examples. In this case, we have dipping and truncated reflectors, providing a good example of the additional detail that may be derived by completing the migration, as opposed to simply performing travel time inversion to derive a gross depth and velocity structure. In particular, there is a set of dipping reflectors between $x = 40$ m and 100 m that have been truncated by the fluvial incision at a depth of about 50 m (Figure 2.46A). The dipping strata appear to be part of an older depositional feature that included multiple levels of erosion. The truncated reflectors are imaged very clearly in the PSDM section. Although they are evident in the NMO section, they certainly are not clear, and the relationship indicating multiple levels of erosion cannot be discerned. The improved image can partially be attributed to noise suppression of the migration operator. More importantly, PSDM properly handles reflector point dispersal associated with dipping reflectors and conflicting dips in heterogeneous media without the constant velocity assumption inherent in DMO processing. Through pre-stack migration, we have not only improved the accuracy of the final image, but have brought out additional stratigraphic detail.

CONCLUSIONS

As seismic reflection data become more prevalent as input for quantitative environmental and engineering studies, there is growing need to assess and improve the accuracy of reflection processing methodologies. I have shown that conventional NMO processing techniques with depth estimates via Dix inversion can result in very large errors in depth and layer thickness estimates for subsurface conditions common in shallow reflection studies. PSDM is the most accurate and detailed imaging tool available. Through synthetic and field examples, I have shown that significant improvements in the accuracy of shallow reflection profiles can be made using PSDM processing.

Currently, PSDM imaging is not commonly used in shallow-seismic reflection studies. This is largely due to economics. Environmental seismology is constrained by financial limitations to a much greater extent than the oil industry, but as computing costs continue to decrease while computing power increases, it will become feasible to include pre-stack depth migration as a standard tool available to the environmental seismologist. It is interesting to note that PSDM is typically reserved for areas with large lateral velocity variations. However, I have shown that in some cases it is also necessary in the case of 1-D velocity fields, where there are very large velocity contrasts. Although there are less computationally intensive methods for solving the problem, they will be less accurate and provide less detailed images than PSDM.

The degree of velocity contrast discussed here is rarely observed in conventional exploration seismology, and therefore, has received little attention. However, in shallow

seismology this is a common scenario, and must be considered in detail, if we are to predict the subsurface with the accuracy necessary for detailed groundwater modeling. Additionally, careful consideration of accuracy and noise problems discussed in this paper may lead to more realistic expectations and informed decisions about the capabilities of the seismic method in groundwater studies.

CHAPTER 3. CASE STUDY: IMAGING A SHALLOW AQUIFER IN TEMPERATE GLACIAL SEDIMENTS USING SEISMIC REFLECTION PROFILING WITH DMO PROCESSING

INTRODUCTION

The Puget Sound region, of the Pacific Northwest, is underlain by Quaternary glacial marine strata that host the primary subsurface water sources. With a rapidly increasing population density, particularly in coastal areas, the quantity and quality of water becomes a rate limiting parameter in land management. Proper water resource management is dependent on the development of accurate predictive groundwater flow models. The accuracy of the models, however, is largely dependent upon the ability to adequately determine the geometry of hydrologic systems. Seismic reflection profiling can potentially provide an accurate spatial representation of hydrogeologic units. Success depends largely on surficial conditions and complexity of the subsurface strata. During the summer of 1995, we conducted a seismic experiment on Guemes Island, a small island in the San Juan Archipelago (Figure 3.1), to test the feasibility of using seismic reflection profiling to image hydrogeologic systems hosted by temperate glacial sediments.

Extreme facies variability is observed in the temperate glacial sedimentary successions present on Guemes Island, and is typical of the Puget Sound region (Domack, 1982). This results from the myriad of glacial and periglacial environments that co-exist in

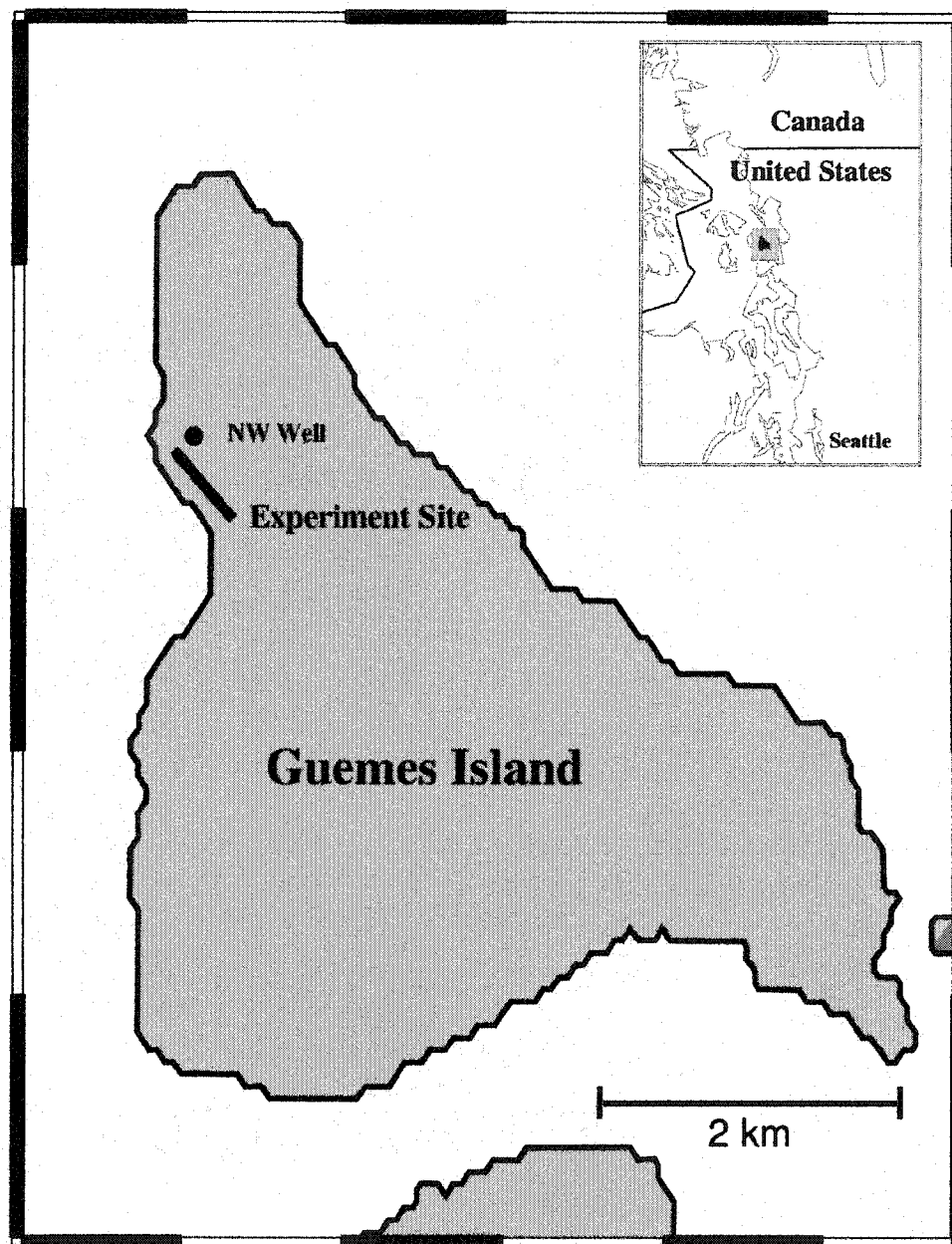


Figure 3.1: The field area was located on Guemes Island, in the Puget Sound, north of Seattle, Washington. We conducted the seismic experiment along a rural road that was located parallel to, and approximately 80 m from, a 50 m high sea cliff. Outcrop observations and water well boring descriptions provided detailed lithologic control for the experiment.

temperate shallow marine settings (Edwards, 1986). Truncated strata and steeply dipping surfaces associated with small scale erosional features (on the order of tens of meters or less) are common. The acoustic properties of the strata are highly variable, ranging from lodgement tills (high density, high velocity) to dry, unconsolidated sands and gravels (variable density, low velocity) (Haeni, 1986). These factors combine to make this an extremely challenging environment for seismic reflection profiling. Other authors have met with some success in glacial sedimentary environments (Keiswetter et al., 1994; Lanz et al., 1996; Siahkoohi and West, 1996), but with the possible exception of Lanz et.al., these studies were carried out in terrains lacking the complexity associated with grounding-zone proximal glacial marine settings, such as that found on Guemes Island.

Field Site Conditions

Guemes Island is an ideal test site due to the availability of an extensive hydrologic system database compiled in a previous water resources study by the U.S. Geological Survey (Kahle and Olsen, 1995). This includes an abundance of lithologic information in the form of water well boring descriptions and outcrop observations. We chose our experiment site to optimize use of these data. Our seismic line is located along a rural road that is parallel to, and approximately 80 m from, a 45 m high sea cliff. We compiled a detailed stratigraphic sketch of the cliff face, and assembled a photo mosaic, to provide the primary source of stratigraphic and lithologic control for the shallowest 45 m of the profile. Kahle and Olsen's (1995) study provides gross lithologic descriptions for this area, and a boring description from a water well located ~50 m from the northwest end of

the line is available; providing lithologic control to a depth of 52 m.

The primary targets for the experiment were the Whidbey confining unit, at a depth of approximately 35 m, and the Double Bluff aquifer at a depth of about 45 m (Table 3.1). The Double Bluff Formation is bounded at its base by bedrock, but the depth to this contact is not known. We designed our survey to image to a depth of 100 m which is Kahle & Olsen's (1995) estimate of depth-to-bedrock.

Table 3.1. Characteristics of major hydrogeologic units at the site. (Kahle and Olsen, 1995)

Hydrogeologic Unit	Lithologic and Stratigraphic Characteristics	Thickness along profile
Surficial sediments	Complex discontinuous stratigraphy with multiple levels of erosion. Consists of sand, gravel, and clay (glacial till, glacial fluvial, and glacial marine sediments)	35 m - 46 m
Whidbey confining unit	Relatively simple stratigraphy with local erosional surfaces. Consists of clay silt and fine grained sand.	~ 10 m
Double Bluff aquifer	Complex stratigraphy. Consists of sand and gravel	250 m ?

We expect the strongest impedance contrasts, and thus the strongest reflecting boundaries, at: 1) the contact of the surficial sediment package with the Whidbey Formation, 2) the contact between dry sediments and the water saturated zone, expected to lie at or just above sea level (based on well boring descriptions), and 3) the top-of-Double Bluff contact.

We expect the surficial sediment package will complicate seismic reflection imaging. The bulk of the unit is comprised of sands and gravels showing cut-and-fill

stratigraphy at scales ranging from a few meters to several hundred meters. Dipping surfaces (up to 45°) and truncated strata associated with erosional stratigraphic features complicate velocity analysis. An additional problem is the potential for the presence of lodgment till above the primary target zone. Lodgement tills typically have velocities (Haeni, 1986; Siahkoohi and West, 1996) that are higher, by a factor of two or more (~ 2000 m/s), than velocities for dry, unconsolidated sands and gravels (Lankston, 1990). Reflection surveys intended to image below thin, high velocity layers are often unsuccessful (Evans et al., 1996) because much of the reflected energy is trapped below the high velocity layer, travels along its base as a head wave, or is channeled within the layer as guided waves (Evans et al., 1996). Our primary objective for the experiment is to determine if commonly used acquisition procedures, and available processing routines can be used to produce a useful stacked seismic section under these difficult conditions.

DATA ACQUISITION

We tested a shotgun (12 gauge, 350 gr. blanks) and a 20 lb weight drop, and found that both sources provided similar depth of penetration (80 m - 100 m) while the weight drop provided higher useable frequencies (up to 250 Hz), and a more consistent source signature. Based on these results, we chose the weight drop as the energy source.

A Bison, 24 bit, 60 channel seismograph was used for all data recording. Data were acquired using standard CMP roll-along techniques. We used a 10-50 split-spread geometry to maintain a large (100 m) maximum offset while increasing near offset

coverage. The receiver array consisted of 60 channels with five, 28 Hz geophones per group, planted close together (within a 0.3 m radius). Receiver group spacing was 2 m, and shot spacing was 1 m. This provided 30-fold CMP coverage, with a CMP spacing of 0.5 m. Four hammer blows were recorded separately at each shotpoint, then vertically stacked during processing.

DATA PROCESSING

Numerical modeling as an aid in data interpretation

In this experiment, we found it difficult to interpret the early arrivals (Figure 3.2). At common-receiver gather (CRG) 40, we can clearly identify a direct arrival with a linear moveout of 420 m/s, and a high amplitude first break refraction with a linear moveout of 1950 m/s and an intercept time of around 15 ms. This is consistent with a low velocity package overlying a high velocity layer at a depth of roughly 3 m. Assuming the “typical” case of increasing velocity with depth, we expect that a reflection at around 70 ms would have hyperbolic moveout velocity of no less than 1700 m/s. However, the reflection between 70 ms and 110 ms has a moveout of only 1150 m/s. Also note that the dominant frequency decreases very little with depth at CRG 40 remaining close to the low bandpass corner frequency of 120 Hz. As we move north along the line to CRG 106, we see that the high velocity first arrival has shallowed significantly. The early, linear arrivals are cyclic, and the amplitude drops off rapidly with increasing offsets. Additionally, the early

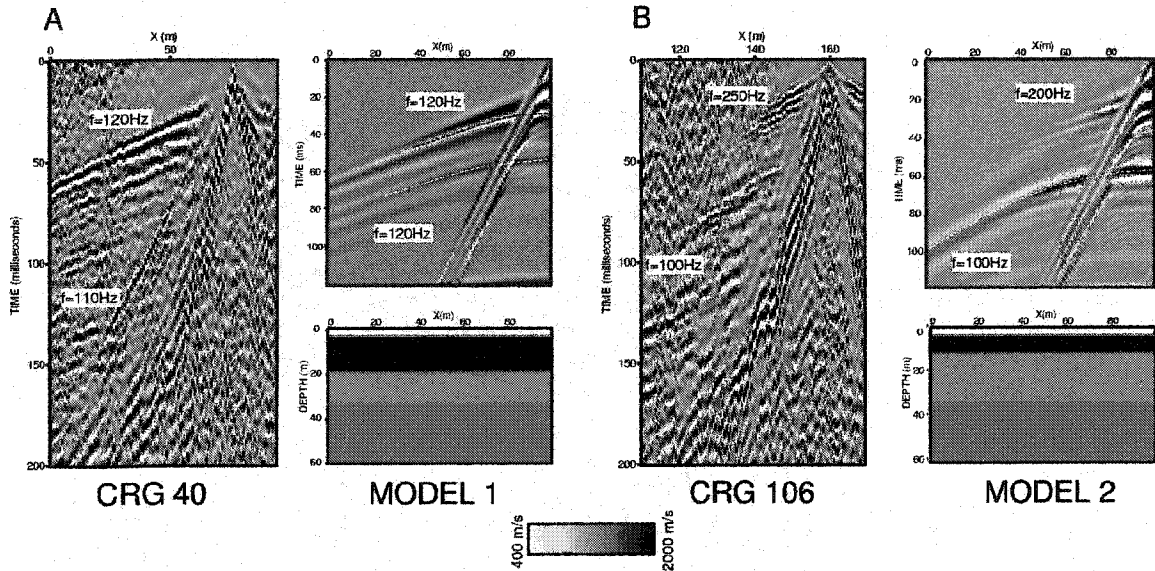


Figure 3.2: Common-receiver gathers (CRG), modeled data, and velocity models showing the effect of a thin, high velocity layer near the surface. The data are modeled using a fourth-order finite difference code, and a 120 Hz, zero-phase Ricker wavelet as the source pulse. A) Data generated using Model 1, with a 15 m thick high velocity zone, is similar to CRG 40. The reflection from the base of the high velocity zone (shown with a black dashed line) has non-hyperbolic moveout at an offset of about 33 m. For a reflector at a depth of 35 m (shown with a white dashed line), departure from NMO becomes apparent at an offset of about 75 m. Non-hyperbolic moveout is the result of energy being channeled along the high velocity zone. B) As the high velocity layer in the model thins to 7m, the high frequency components are trapped in the high velocity layer as guided waves, and the reflection from the base can no longer be differentiated. The reflection from the interface at 35 m shows no significant departure from NMO to the maximum offset of 100 m, because the low frequency components are not efficiently channeled in the high velocity layer. This modeled data is similar to CRG 106.

arrivals have a dominant frequency around 250 Hz, while the deeper reflected events have a dominant frequency of only 100 Hz. The reflection at 70 ms to 100 ms has a low moveout velocity (relative to CRG 40) of 1050 m/s. The geometry and spectral character of the early arrivals suggests that a thin, high velocity zone exists near the surface.

It is known that discontinuous deposits of lodgment till are present in the surficial sediments (Kahle and Olsen, 1995). The presence of a thin, laterally variable layer of high impedance lodgment till near the surface could explain the character of the early seismic events. To evaluate this as an explanation for our observations from the field data, we construct two, simple, 1-D velocity models with a high velocity zone starting at a depth of 4 m, and thickness of 15 m, and 7 m for model 1 and model 2 respectively. A reflecting interface is placed at a depth of 35 m in each model. We then generate a seismogram for each velocity model using a fourth-order acoustic finite difference code (Kelly and Marfurt, 1990).

We find that the reflection from the base of the 15 m thick high velocity zone can be identified (Figure 3.2), but hyperbolic fitting indicates departure from normal-moveout (NMO) at relatively near offsets (33 m), even though there is no critical angle as we go from high to low velocity. The traveltime curve is non-hyperbolic because; 1) severe raypath bending due the large velocity gradient violates the near-normal incidence assumption, and 2) the reflected energy at larger offsets is channeled along the high velocity layer. Non-hyperbolic moveout occurs for reflections that originate below the high velocity layer, but this occurs at greater offsets as the depth to the reflecting interface increases. For the reflecting interface at a depth of 35 m, departure from NMO (1335

m/s) occurs at an offset of 75 m. If we include the full offset range, and approximate the traveltime curve as a hyperbola, we find a stacking velocity of 1480 m/s, an error of 10%. This would translate to a depth estimate error of about 3 m, which is insignificant given a wavelength of around 10 m.

As the high velocity layer thins, it increasingly acts as a low pass filter. For model 2, the dominant frequency of the channeled waves is around 200 Hz, while the dominant frequency of the reflection at 35 m is only 100 Hz. The high frequency components are trapped in the high velocity layer as guided waves (Evans et al., 1996). As offsets increase, high frequency energy is channeled more efficiently and little energy returns to the surface, resulting in a sudden drop of recorded amplitudes. The reflection from the base of the high velocity zone becomes impossible to distinguish. Since the low frequency components are passed, the travel path for the deeper reflection is not significantly distorted, and the NMO assumption is valid for the full range of offsets.

Modeling indicates that our observations from the receiver gathers are consistent with a near surface layer of high velocity till, that thins and shallows toward the north, and that the high velocity zone causes deviations from hyperbolic moveout for reflections from the target zone. However, these deviations are minimal and we conclude that standard NMO processing techniques and stacking will provide a suitable means of imaging the primary target zone.

We have considered the potential for an out of plane reflection from the sea cliff. The earliest arrival would travel along the high velocity till layer as a head wave, be reflected at the cliff-air interface, and return as a head wave. This would appear as a

reflection in the gathers with a moveout velocity of roughly 1800 m/s at a time of about 90 ms. No arrival of this type is observed in the data. We also use a simple velocity model and a ray tracing method (Zelt and Smith, 1992) to estimate cliff-face reflection travel times for an overall increase in velocity with depth, which is valid below the till layer. We conclude that a cliff face reflection would arrive at a minimum of 160 ms which is later than any useable part of the data.

Data preparation

As with most shallow seismic reflection data, coherent, low-velocity noise, such as the direct wave, air wave and ground-roll, obscure near offset reflections. To minimize spatial aliasing problems, we used tau-p trace interpolation in the shot domain to double the trace density. The tau-p transform is less sensitive to aliasing problems than the Fourier transform, and the original traces can be retained to minimize artifacts. Besides improving the aliasing problem, trace interpolation in the pre-stack domain is effectively a robust, dip independent, coherency filter which improves velocity estimates, and attenuates random noise in the stacked data. Amplitude balancing prior to interpolation improves the results. In this case we apply AGC with a 50 ms time window.

F-K filtering of the interpolated shot gathers worked well to attenuate coherent noise with velocities from 150 m/s to 700 m/s, but little or no reflected energy could be extracted inside the 300 m/s cone. Based on this observation, we limit our fan filter to the 300 m/s to 700 m/s slice and apply an inside mute to avoid stacking filter noise. A band-pass filter (70-120-240-280) was applied after F-K filtering. The effect of this data

preparation is denoising of the window in which reflected energy can be observed (Figure 3.3).

Velocity analysis

As is often the case, detailed velocity analysis proved to be the most important and time consuming step in the processing flow. The initial velocity model, which we refer to as V1 (Figure 3.4a), was developed through detailed analysis of semblance plots, constant velocity stacks, and constant velocity gathers. The stacked section shows good lateral reflector coherence over segments on the order of 100 m at times of around 120 ms, while primary reflecting boundaries between 50 and 100 ms are coherent over 200 m or more. However, the migration result is poor because the velocity field contains erratic lateral variation that is not a likely manifestation of the geology. Such apparent variations can be caused by reflectors with conflicting dips, or scattering events. The stacked section (Figure 3.6) clearly shows conflicting dips, and there is potential for significant scattering associated with truncated strata. Of course, these effects are three-dimensional in nature, and we are trying to account for them as a two-dimensional problem. The hope, as with any 2-D method, is that 3-D effects are minimal. In any case, we need to adapt our processing strategy to account for these effects in the 2-D approximation. Standard dip dependent NMO velocity analysis methods alone are insufficient. Dip-moveout processing can be described as a partial pre-stack migration that attempts to move every trace to its zero-offset equivalent. If this process is successful, stacking velocities become independent of dip and conflicting dips are handled correctly.

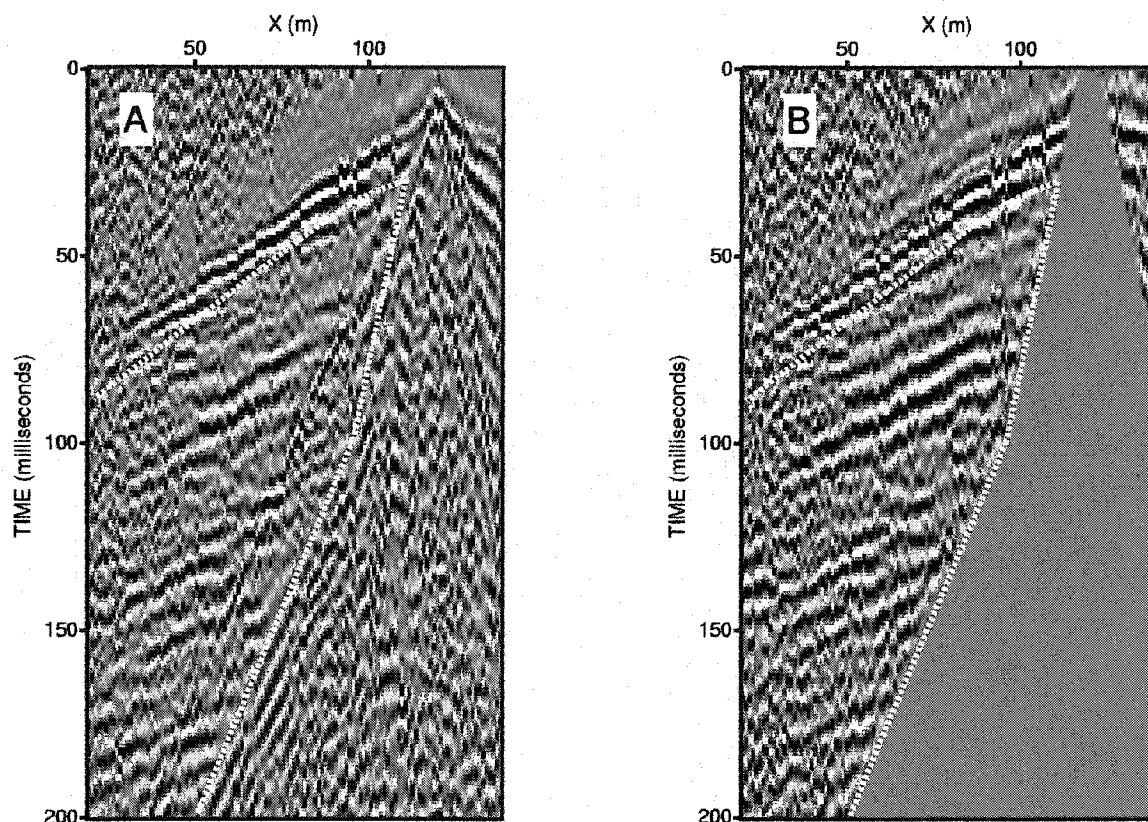


Figure 3.3: CRG 22, A) with only bandpass filtering and AGC, and B) after F-K filtering via tau-p trace interpolation. No interpolated traces are included for this example. Although F-K filtering effectively attenuated all coherent noise inside the mute cone, little or no reflected energy could be extracted. Inside muting was employed to avoid stacking filter noise. This resulted in denoising of the window in which reflections could be observed.

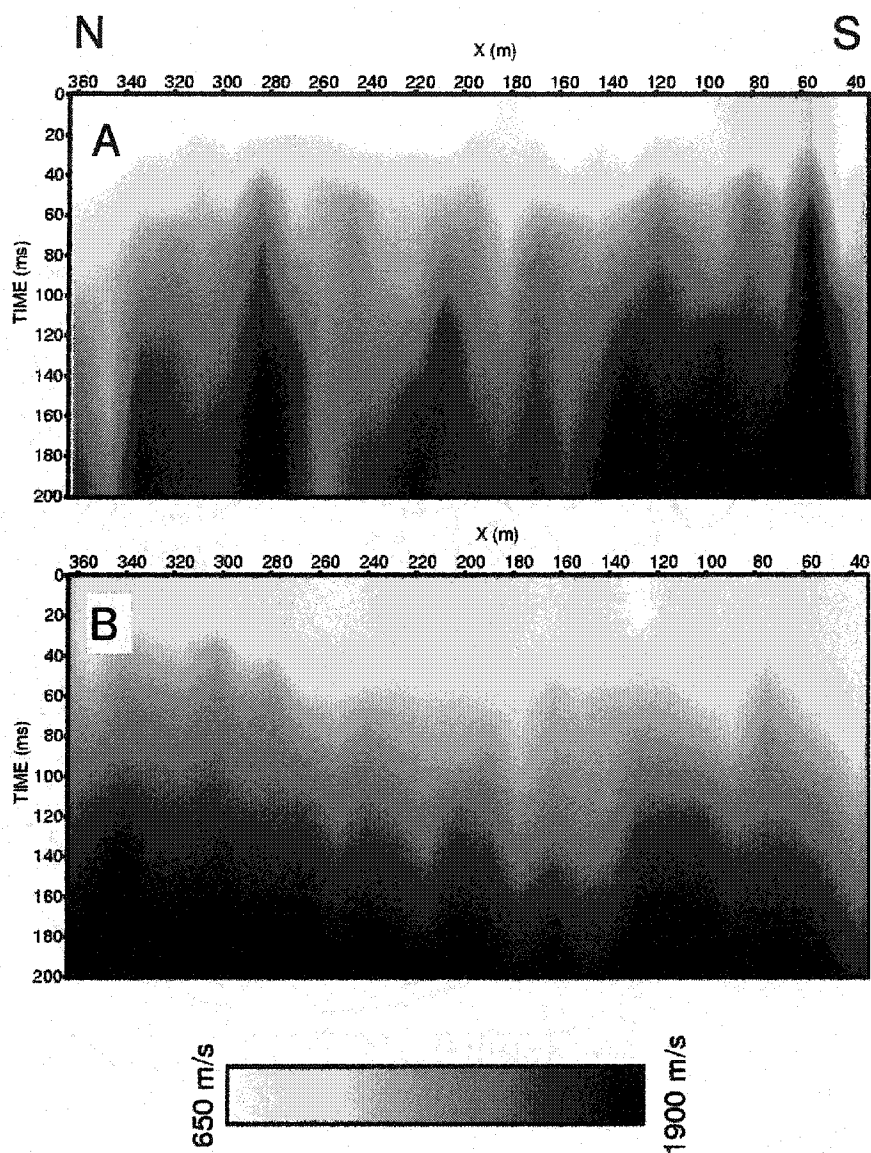


Figure 3.4: Stacking velocity models, A) before iterative DMO velocity analysis, and B) the final model after two iterations. The most obvious effect is smoothing of the velocity field. This is expected by analogy with a synthetic DMO example (Figure 3.5).

Dip moveout processing.- Of the ten benefits Deregowski (1986) claims for DMO processing, we are most interested in improved velocity estimates, and attenuation of steeply dipping, coherent noise. Dip-move out routines were developed specifically to deal with the problem of reflector point dispersal associated with dipping reflectors (Deregowski, 1986). Steep and/or conflicting dip events result in erroneous stacking velocities, which degrade the stack and yield poor migration results. More accurate and reliable velocities can be derived from DMO corrected data, and additionally, DMO followed by post-stack time migration becomes approximately equivalent to pre-stack time migration, but at significantly reduced computing cost (Jakubowicz, 1995). These benefits can be illustrated with a simple synthetic example.

Profile 5a (Figure 3.5) was F-K migrated using a velocity field derived from an analysis of the pre-DMO corrected data. Normal-move-out velocity analysis yielded RMS velocities that ranged from 1580 m/s to 2400 m/s; a substantial deviation from the true velocity field. Neither of the dipping events are properly migrated and the steep event on the left is severely distorted. All regions with conflicting dips are improperly migrated. This is in sharp contrast to profile 5b which was migrated using a velocity field derived from the DMO corrected data. Normal move out velocity analysis using the DMO corrected data yields velocities ranging from 1600 m/s - 1690 m/s; only a 2.5% deviation from the true velocity field. All areas of the DMO corrected profile are properly migrated.

Hale (1991) suggests that DMO is likely to help when the following condition holds:

$$\frac{4Fh^2\sin^2\theta}{v^2t_n} > 1 \quad 3.1$$

where h is the half offset, θ is the dip angle from horizontal, v is the velocity, t_n is the dip-independent NMO time, and F is the dominant frequency of the signal. In this case, we expect dips up to 45° , and assuming a nominal half-offset of 35 m (offsets are biased toward relatively high values due to the lack of near zero-offset reflected energy), a velocity of 1200 m/s, an NMO time of 50 ms, and a dominant frequency of 120 Hz, yields a value of 4 for the left side of equation 3.1. We conclude that DMO processing is likely to improve velocity estimates in the more complex regions of our profile.

Although DMO is not strongly velocity dependent, large velocity errors can significantly decrease its accuracy. It then becomes necessary to adopt an iterative velocity analysis approach to converge on the optimal velocity field for NMO and DMO corrections. This iterative procedure is outlined by Deregowski (1986), and we will refer to it as iterative DMO velocity analysis.

We tested three DMO routines, that are available with Promax™ data processing software (Ensemble DMO in the T-X domain, Common offset F-K DMO, and Dip Decomposition DMO), and had essentially the same results. Ensemble DMO in the T-X domain (applied to common-offset gathers) was used to produce the DMO corrected stacks shown in this paper. After two iterations of DMO velocity analysis, the velocity model changed by less than 5% at any given location, and we conclude that additional iterations would provide minimal benefit. We refer to the final velocity model as V2

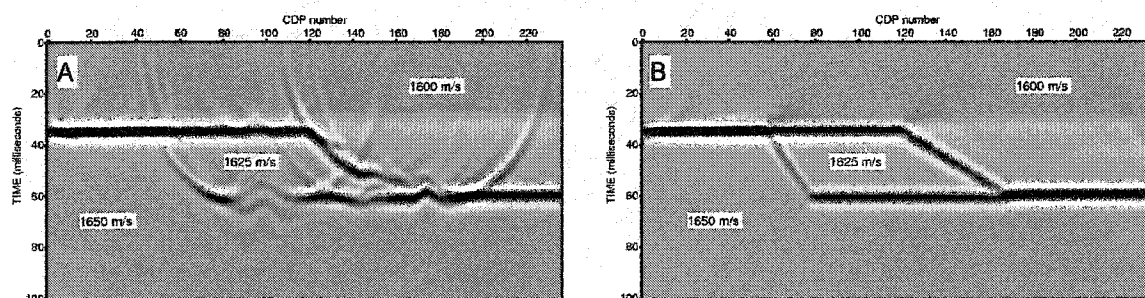


Figure 3.5: Synthetic stacked data, A) F-K migrated with a velocities determined before DMO corrections, and B) F-K migration with velocities determined from DMO corrected data. The flat reflectors lie at depths of 30 m and 50 m, and the dipping reflectors have dips of 45° and 25° for the segment on the left and right respectively. Indicated velocities are the true model interval velocities. Velocity errors resulting from dipping reflectors, conflicting dips, and diffraction tails severely degrade the migration result (A). DMO processing accounts for these effects resulting in a more accurate velocity field that is appropriate for migration(B). The data were generated with a fourth-order, acoustic finite difference code, using a 150 Hz, zero-phase Ricker wavelet as the source pulse, and 30-fold CMP's with a spacing of 1 m.

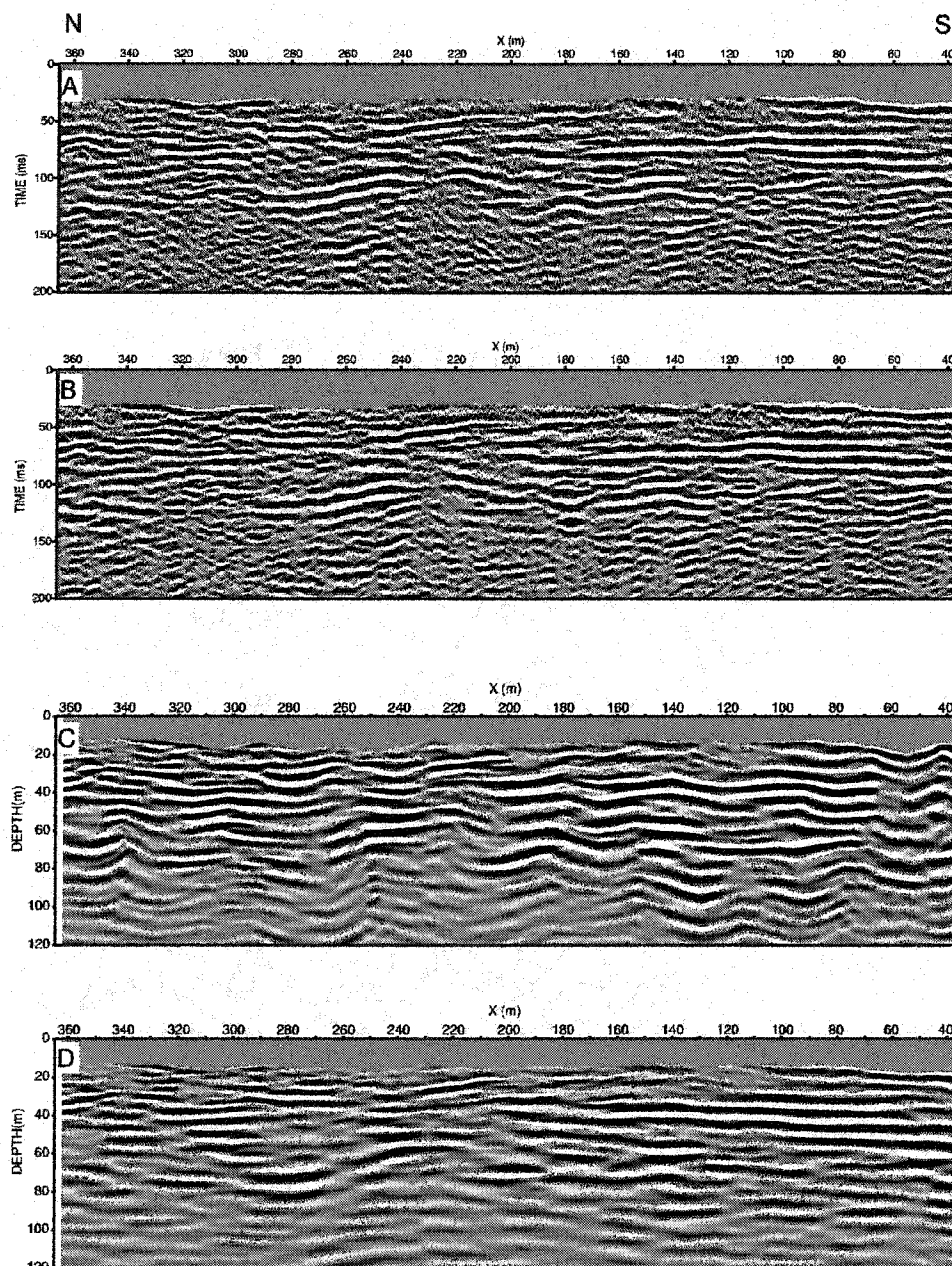


Figure 3.6: A) the stack (without DMO), with a velocity model V2 (Figure 3.4b). Coherent, flat lying reflectors can be followed continuously across large portions of the section. B) The DMO corrected stack; steeply dipping noise has been effectively attenuated, and reflector coherence has been improved, particularly deeper in the section. C) Kirchhoff depth migration of 6b with depth interval velocities derived from V1 (Figure 3.4a). The stack has been severely degraded. D) Kirchhoff depth migration with depth interval velocities derived from V2 (Figure 3.4b).

(Figure 3.4b).

The most significant result of DMO velocity analysis is smoothing of the velocity field (Figure 3.4). This is expected by analogy with our synthetic example. Although there is significant lateral velocity variation, we find that the gradient is smooth which indicates that DMO followed by post-stack depth migration is an appropriate processing strategy.

The unmigrated stack derived from V2 (Figure 3.6a) is not substantially different from the stack derived from V1 (not shown). The DMO corrected stack does show significant improvement (Figure 3.6b). The steeply dipping, coherent noise (an aliasing artifact from the tau-p trace interpolation) has been effectively eliminated. Reflector coherence has been improved, particularly deeper in the section. Some artifacts are introduced such as at $x=180$ m, $t=120$ ms, where smearing has resulted in artificial alignment of energy. It is important to interpret the data at various levels of processing so that artifacts can be identified and avoided. Overall, DMO has improved the stack, but some artifacts are introduced.

The advantage of DMO processing is most obvious in the migrated sections. For depth migration, the stacking velocity models were converted to depth interval velocities using a smoothed gradient inversion. Both migrated sections are derived from the DMO corrected stack. It is clear that migration from the V1 derived model (Figure 3.6c) has not improved the stack and has actually degraded it severely. Migration from the velocity model derived from V2 (Figure 3.6d) shows dramatic improvement over the stack migrated from V1. Velocity pull ups associated with thickening of the shallow till layer have been accounted for, and the migrated section should be incorporated in the

interpretation. The primary reflecting horizons are evident, and can be correlated with the pre-migration stacks. Overall we conclude that DMO followed by post-stack depth migration is a valuable contribution to the interpretation.

With an accurate velocity model, depth migration allows for improved interpretation through more accurate depth determination, focusing, and correct positioning of scattering and dipping reflectors. However, the smearing effect of the Kirchhoff migration operator can obscure some details, and produce artificial alignments. For this reason we choose to draw our interpretation from the pre-migration time section, and the depth-migrated section simultaneously (Figure 3.7)

INTERPRETATION OF REFLECTION PROFILE AND COMPARISON WITH LITHOLOGIC CONTROL

Surficial sediment package

Inability to differentiate reflected arrivals from channeled waves, multiples, and etc. associated with the shallow high velocity layer limits our interpretation to events deeper than 18 m (~30 ms) (Figure 3.7). The surficial sediment package is characterized by four major erosional surfaces which we identified in the outcrop, and have labeled E-1 through E-4 (Figure 3.7c). In the cliff exposure, E-1 appears as a flat surface that is truncated near the southern portion of the survey area by E-2. It extends continuously from E-2 to the northern extent of our seismic profile. In the seismic sections, we have interpreted E-1 as the reflector that lies at an average depth of about 20 m (50 ms) that

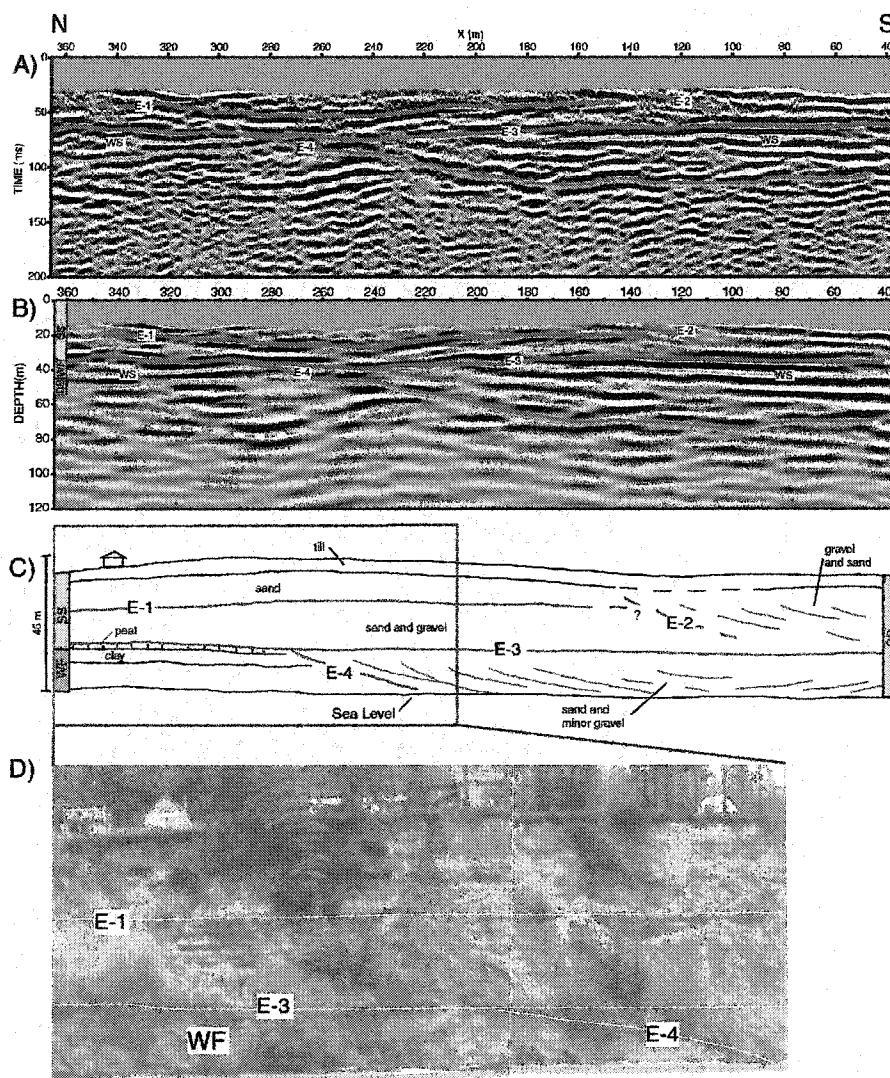


Figure 3.7: A) Interpreted time section (not migrated), B) interpreted depth-migrated section, C) stratigraphic sketch of sea cliff exposure adjacent to the line, and D) photo mosaic of the northern portion of the line. Compare A) and B) to the corresponding uninterpreted sections in Figures 3.6B and 3.6D respectively. The major features are the four erosional surfaces (E-1 - E-4), the Whidbey Formation (WF), the top of the water saturated zone (WS), and the Double Bluff Formation (DB). The colored stratigraphic column in B) is taken from a water well boring description located adjacent to the profile. The seismic section shows relatively good correlation with the exposure. There is no lithologic control below 52 m.

can be followed continuously from $x=140$ m to $x=340$ m. At around $x=135$ m, E-1 is truncated by E-2, which is a steeply dipping channel cut that penetrates to a depth of about 30 m (55 ms). The dip of this surface is about 45° in the exposure as opposed to 30° in our seismic profile. This indicates either dip or strike variation, the former being a 2-D effect and the latter being a 3-D effect projected on our 2-D seismic line. In the outcrop to the south of E-2, we see clinoforms dipping steeply toward the south. This is consistent with trends observed in the seismic data, although the clinoforms are not resolved with any detail.

In the exposure, E-3 is observed as a flat surface that extends across the entire survey area. In the seismic profile, we interpret the strong reflecting interface that is nearly continuous, at a depth of 30 m - 35 m, as E-3. The interpreted E-1 and E-3 reflectors indicate greater topographic variation than expected from our outcrop observations. This could merely be indicative of three-dimensional erosional character and the 80 m lateral displacement from our line to the outcrop. However, we must consider that vertical variations of these reflectors are on the order of 5 m to 10 m which is close to the wavelength of the signal ($\lambda \approx 8$ m). This amount of variability, relative to the wavelength, is within a reasonable margin of error.

Only a short segment of E-4 is exposed in the outcrop, where it is observed to incise the Whidbey Formation (WF), dipping toward the south and disappearing below the waterline. In the seismic profile, E-4 is one of the most prominent features at depths greater than 40 m (70 ms) and continues from about $x=270$ m to the southern extent of the profile. We interpret E-4 as extending well into the Double Bluff Formation (DB).

The Whidbey confining unit

Our interpretation of the boring description places the top of the Whidbey Formation (WF) at a depth of 35 m at the north end of our profile. In the outcrop, we find that WF is bounded by E-3 at the top, and E-4 to the south. We extend this interpretation to our seismic profile. WF is present only in the northern 100 m of the profile. From $x=300$ m to $x=365$ m, E-3 forms the upper boundary of a zone of high amplitude, nearly horizontal reflectors that extend to a depth of about 45 m. We interpret the base of this zone as the base of WF which is known to lie just below sea level in this location. This interpretation is consistent with the boring description at the north end of the line which places the top of DB at a depth of 45 m. The zone of high amplitude reflectivity is associated with closely juxtaposed high impedance boundaries formed by the erosional contact E-3, the interface between the water saturated zone (WS) and dry sediments, and the contact between the fine grained sediments of WF and the coarse grained sediments of DB, all of which lie within 10 m vertically. This is on the same order as the wavelength of the filtered signal, and it may not be possible to clearly differentiate of each of these contacts. We expect WS to provide the largest impedance contrast, and associate the highest amplitude arrival (roughly in the center of WF) as this surface.

The Double Bluff aquifer

The Double Bluff Formation (DB) is not exposed along our profile, although the boring description indicates that it lies just below sea level. Near the northern end of the profile the lower contact of WF defines the top of DB. Along the southern portion of the

profile, WF has been incised and the top of DB is defined by E-4. E-4 defines the northern extent of a major incision into DB. Depth to the base of this incision was not previously known. From our seismic interpretation, we estimate the maximum depth of erosion at around 75 m - 80 m in this location.

A flat, high amplitude reflector extends continuously from the southern extent of the profile to $x=200$ m. We interpret this as the top of the water saturated zone (WS). It is surprising that this surface is not continuous near the center of the profile, from $x=210$ m to $x=250$ m. However, this is proximal to E-4, and complexities associated with truncated, dipping, and the likely three dimensional character of high impedance boundaries could account for the lack of a clear image in this region.

Another deep (55 m - 80 m), high amplitude reflector is imaged within the Double Bluff from $x=240$ m to $x=365$ m. No wells have penetrated to these depths, so there is no lithologic control. We favor an interpretation of an older erosional contact. This is consistent with the complex erosional history of the Double Bluff Formation documented in other areas.

CONCLUSIONS

We acquired a seismic profile using a small weight drop source in a temperate glacial sedimentary setting, at a site chosen for the availability of lithologic control. Analysis of the raw shot and receiver gathers, and comparison to acoustic models, indicates that a laterally variable, thin, high velocity zone lies within a few meters of the

surface. Geologic data indicate that this is a bed of lodgement till. We verified that the NMO assumption was valid for energy reflected from our primary target zone starting at a depth of about 30 m. DMO processing improved our ability to derive velocity structure which resulted in a dramatic improvement of the migrated profile. We were able to produce a relatively detailed shallow seismic reflection profile in an environment that is not conducive to seismic reflection profiling. Erosional features, with lateral extent on the order of 10 m, and dips as great as 30° , were clearly imaged at depths of less than 30 m. We were able to develop a relatively detailed interpretation, that was consistent with available lithologic control. However, based only the seismic data, other interpretations are reasonable that would not correctly represent the geology. This illustrates the need for lithologic control in shallow seismic studies, as with any geophysical method. This work indicates that a useful seismic reflection profile can be produced in this complex environment using commonly available processing routines and acquisition methods. Processing and interpretation are not straightforward, and detailed analysis is required.

CHAPTER 4. NAPL DETECTION WITH GPR USING AVO

ANALYSIS

INTRODUCTION

Previous workers have shown that GPR can be used to image non-aqueous phase liquid (NAPL) contaminants in the subsurface (Annan et al., 1992; Campbell et al., 1995; Daniels et al., 1995; Loughridge, 1998; Powers and Olhoeft, 1995). The goal of these studies was simply to determine if an identifiable reflection, originating from the surfaces bounding the contaminant, could be recorded. However, imaging alone is not adequate to determine the type of material through which the signal is propagating or is reflected from, and additional control (boring descriptions, etc.) is essential to confidently identify contaminated zones from a radargram.

Attribute analysis is a large group of tools used to quantify variations in amplitude, frequency content, and phase of a reflected waveform, and to relate these quantities to the physical properties of the medium in which the signal is propagating. When carefully integrated with attribute analysis, GPR can yield a rich source of data that includes geometric relationships and detailed material property information which can potentially lead to direct detection of contaminants. This represents a relatively new, and valuable approach to the analysis of GPR data which fully exploits the wealth of information contained in a reflected wavelet. In oil exploration, attribute analysis of seismic data is used to associate shear and compressional wave properties with the presence of oil or

natural gas (Allen and Peddy, 1993; Bradford et al., 1997; Bradford and Wu, 1997; Castagna, 1993; Castagna et al., 1993; Li and Ulrych, 1996). I make the distinction with seismic data in that only the concepts of attribute analysis are applicable for GPR, and careful consideration of the equations and physical properties that govern E-M wave propagation is required to develop valuable applications and meaningful interpretations.

Most GPR data are acquired in bi-static mode (a constant receiver-transmitter offset) and typical processing schemes are relatively simplistic. This is valuable as a rapid reconnaissance tool, but fails to make use of the full potential of GPR. The advantages of using multi-offset acquisition and processing methodologies to improve GPR images are well documented (Fisher et al., 1992a; Fisher et al., 1992b; Loughridge, 1998). I extend the multi-offset approach to include multi-offset attribute analysis.

In this study, I focus on the application of amplitude variation with offset (AVO) analysis in GPR studies. AVO analysis is a multi-offset attribute analysis technique used to study changes in reflection amplitude with increasing angles of incidence (Castagna, 1993). The dielectric constant (K) and conductivity (σ) depend strongly on the material type (i.e. dry earth, water, or DNAPL have very different K and/or σ). For E-M wave propagation, the AVO response depends strongly on the contrast of dielectric constants and conductivities between the incident and reflecting medium (Lehmann, 1996; Zeng et al., in review). Typically, K and σ increase with depth due to increasing moisture content. Many light NAPL (LNAPL) and dense NAPL (DNAPL) contaminants have much lower K and σ than water (Daniels et al., 1995; Olhoeft, 1986; Powers and Olhoeft, 1995) so that the introduction of a contaminant at depth (i.e. a migrating LNAPL plume, or DNAPL

pool at the base of an unconfined aquifer) can lead to a dramatic drop in K and σ as the contaminant displaces water in the pore space.

Although little work has previously been published in this area, it is receiving greater attention as GPR processing and analysis becomes more sophisticated. Lehmann (1996) discusses complex reflection coefficients $[R(\theta, \omega)]$ and the effects of conductivity, Bergmann et. al. (1998) briefly discuss AVO response in the context of a broader synthetic case study. Baker (1998) presents a modeling study indicating potential for detecting LNAPLs based on the transverse AVO response. Most recently Zeng et. al. (in review) present a detailed modeling study considering the effects of varying the Cole-Cole parameters on the AVO response. With the exception of Bergmann et. al. and Baker, these studies are general in nature, and Zeng et. al., Bergmann et. al., and Baker focus only on the response for a transversely polarized electric field. The focus of this study is on the specific, but valuable application of differentiating NAPL's from water saturated zones in contaminated aquifers, and I consider both transverse and parallel polarized electric fields. In this paper I discuss

- 1) E-M wave propagation in the context of AVO studies including reflection coefficients for the general case of $R(\theta, \omega)$ and $k(\omega)$.
- 2) a ray-based, multi-offset modeling algorithm which accounts for frequency dependent material properties via Cole-Cole parameterization.
- 3) field data from a physical model designed test data correlation with the modeling algorithm, and to evaluate potential for differentiating contaminants
- 4) a synthetic example of contaminant identification from a hypothetical aquifer

contaminated with both LNAPL and DNAPL.

THEORY

I begin with a discussion of reflection coefficients for two antenna orientations defined as follows (Figure 4.1): 1) parallel polarization (end-fire, PP) - the transmitting and receiving antennas are parallel, in-line, and oriented parallel to the survey profile, 2) transverse polarization (broadside, TP) - the antennas are parallel, but oriented perpendicular to the survey profile. I choose these definitions since they correspond to the polarization of the electric field (E) relative to the plane-of-reflection for a downgoing wave incident on a horizontal reflector (Figure 4.1), and in this sense follows standard nomenclature. Transverse polarization is the mode most commonly employed in GPR surveys, for both bi-static and multi-offset modes, but the AVO response for transverse and parallel polarization are dramatically different, and parallel polarization holds the greatest potential for identifying contaminant saturated zones, as I will show. In any case, it is valuable to acquire redundant surveys with both antenna orientations, as this provides essentially, two different AVO attributes, leading to redundancy in the analysis which is valuable for any geophysical method.

Zero conductivity case

I first consider the case of a half-space separating two media with zero conductivity but differing permittivity or permeability. The boundary conditions and

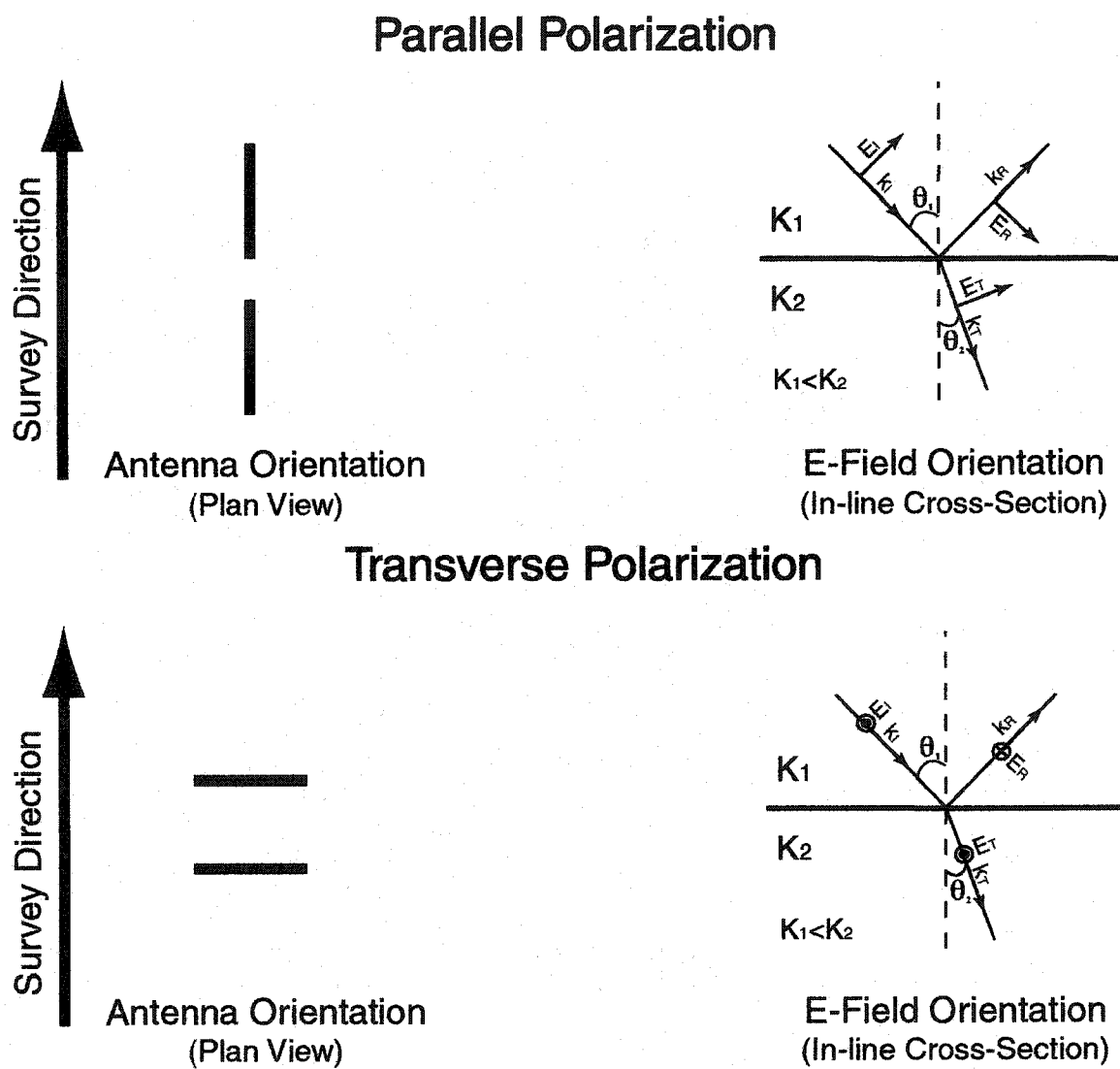


Figure 4.1: Antenna and electric field orientations for parallel and transverse polarization configurations. For purposes of this figure, k and E are the unit vectors for the wavenumber and electric field respectively.

reflection coefficients are derived by Griffiths (1989). At this point it is important to clarify that for the purposes of this discussion, I will refer to reflection coefficients as the amplitude reflection coefficient, following the convention used in the seismic industry, rather the e-m convention of reflection coefficient referring to reflected energy, since the AVO analysis will be done with reflected amplitudes rather than reflected energy. In terms of the wave number, the reflection and transmission coefficients for the two case are given by:

$$R_T = \frac{E_{RT}}{E_{IT}} = \frac{\mu_2 k_1 \cos \theta_1 - \mu_1 k_2 \cos \theta_2}{\mu_2 k_1 \cos \theta_1 + \mu_1 k_2 \cos \theta_2} \quad 4.1$$

$$T_T = \frac{E_{TT}}{E_{IT}} = \frac{2\mu_2 k_1 \cos \theta_1}{\mu_2 k_1 \cos \theta_1 + \mu_1 k_2 \cos \theta_2} \quad 4.2$$

and

$$R_P = \frac{E_{RP}}{E_{IP}} = \frac{\mu_2 k_1 \cos \theta_2 - \mu_1 k_2 \cos \theta_1}{\mu_2 k_1 \cos \theta_2 + \mu_1 k_2 \cos \theta_1} \quad 4.3$$

$$T_P = \frac{E_{TP}}{E_{IP}} = \frac{2\mu_2 k_1 \cos \theta_1}{\mu_1 k_2 \cos \theta_1 + \mu_2 k_1 \cos \theta_2} \quad 4.4$$

and

$$\sin\theta_2 = \frac{k_1}{k_2} \sin\theta_1 \quad 4.5$$

Where the R, I, and T subscripts indicate reflected, incident, and transmitted component respectively, μ is the magnetic permeability, k is the wavenumber, and θ_1 and θ_2 are the angle of incidence and transmission respectively (taken from the normal). It is useful to write the reflection coefficients in terms of the wavenumber when we generalize to the case of conductive, frequency dependent media. These equations also hold for the post-critical case, but θ_2 , and therefore R and T, becomes complex. We can typically assume that μ is equal to the permeability of free space so that $k=2\pi\omega K^{1/2}/c$, where ω is the frequency and c is the speed of light in a vacuum. ω and c cancel in Equations 4.1-4.4 so that we can simply replace k , with $K^{1/2}$ and we see that the reflection coefficients are frequency independent in the zero conductivity case (assuming frequency independent K).

I consider two cases, with the following parameters (for both cases the relative permeability is equal to 1):

case 1: $K_1=12$, $K_2=6$

case 2: $K_1=6$, $K_2=12$

As expected, at zero offset the amplitude of R_T and R_p are the same in both cases, with case 1 and case 2 having opposite signs (Figure's 4.2 and 4.3). In case 1, $v_2 > v_1$ and we reach the critical angle at $\theta_1 = 44^\circ$, where R_T and R_p have an absolute value of 1. In case

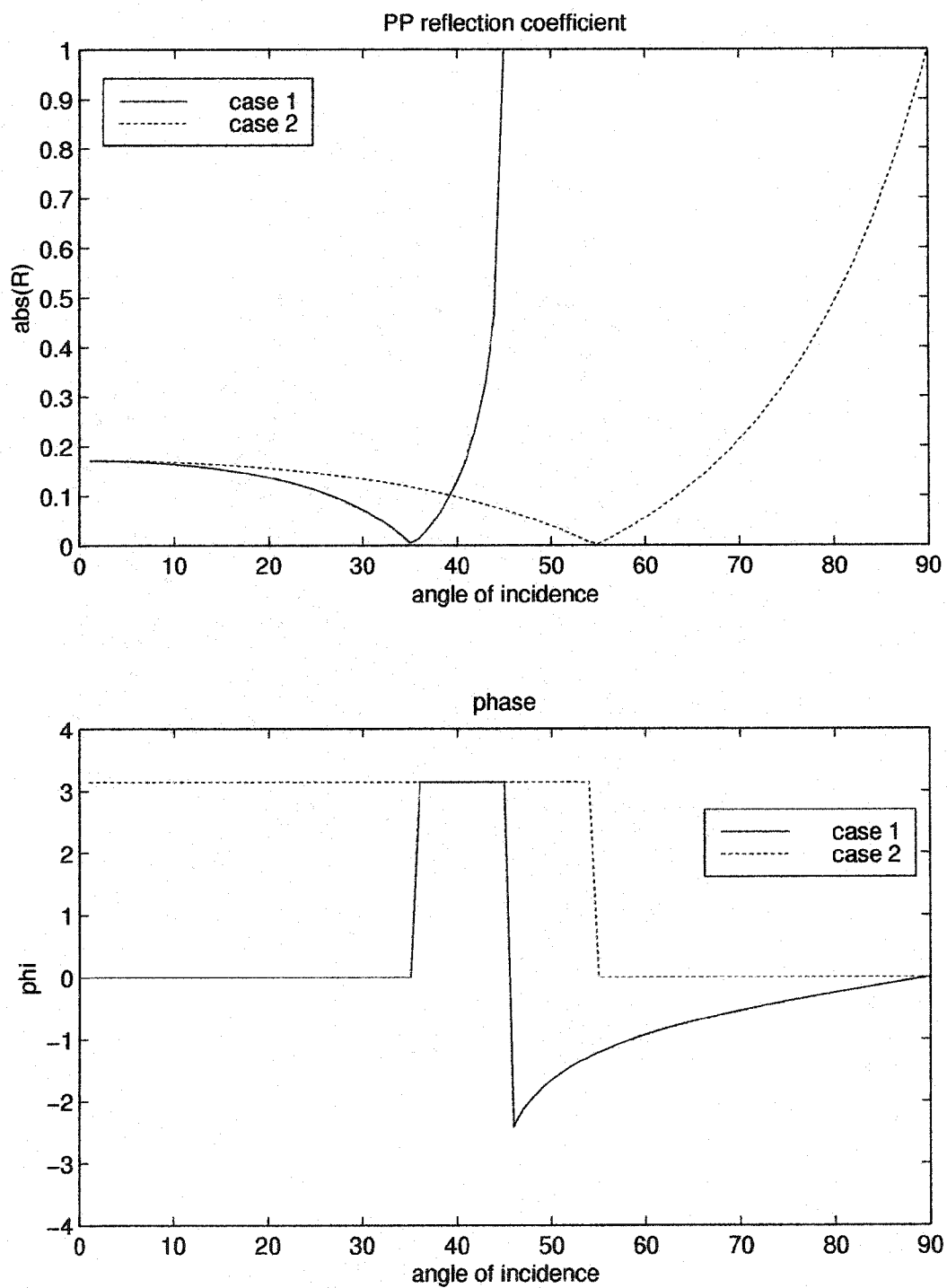


Figure 4.2: PP reflection coefficients and reflection phase for; case 1: $K_1 = 12$, $K_2 = 6$, and case 2: $K_1 = 6$, $K_2 = 12$.

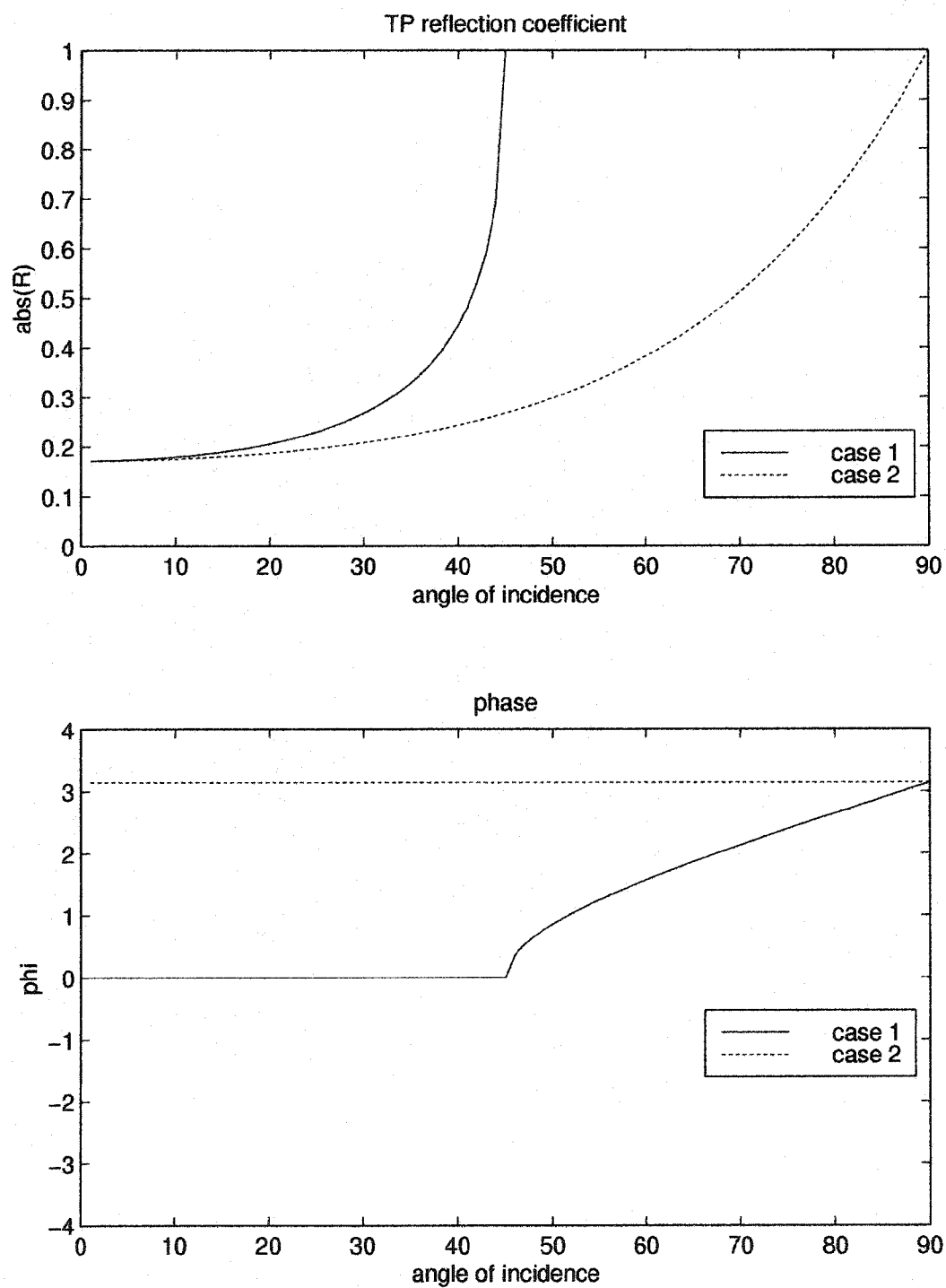


Figure 4.3: TP reflection coefficients and reflection phase for; case 1: $K_1 = 12$, $K_2 = 6$ and case 2: $K_1 = 12$, $K_2 = 6$.

2, $v_2 < v_1$ so there is no critical angle, and R_T and R_p approach 1 at $\theta_i = 90^\circ$. The most striking feature of the reflection coefficient curves, is the presence of Brewster's angle (θ_B) for R_p . At this angle, the reflected wave is balanced by the out-of-phase component of the incident wave and no energy is reflected. When $\theta_i > \theta_B$ the reflection coefficient reverses sign. Note that for case 1, $K_1 > K_2$, and θ_B occurs at a much smaller angle of incidence ($\theta_B = 34^\circ$) than for case 2 ($\theta_B = 55^\circ$).

For the zero conductivity case, θ_B is given by (Griffiths, 1989)

$$\tan \theta_B = \sqrt{\frac{K_2}{K_1}} \quad 4.6$$

Plotting θ_B vs. K_2/K_1 , we find that θ_B occurs at relatively small angles ($< 45^\circ$) and is strongly dependent on K_2/K_1 when $K_2/K_1 < 1$ (Figure 4.4). When $K_2/K_1 > 1$, θ_B occurs at relatively large angles and becomes weakly dependent on K_2/K_1 . If we consider a multi-chromatic signal, we see from Equation 4.6 that the amplitude of the wavelet only goes to zero for frequency independent K (for frequency dependent K , θ_B may be different for each frequency component). However, for a reasonably band limited wavelet, even when both materials have relatively large conductivities (0.1 S/m), there is a significant decrease in amplitude and a 180° phase rotation occurs, although the transition is diffuse rather than discreet.

Typically, K will decrease when NAPL's are present due to the displacement of water in the pore space by contaminant. For a signal reflected from the upper surface of a NAPL contaminated zone, $K_2/K_1 < 1$, and θ_B is small. If the wave is reflected from the top

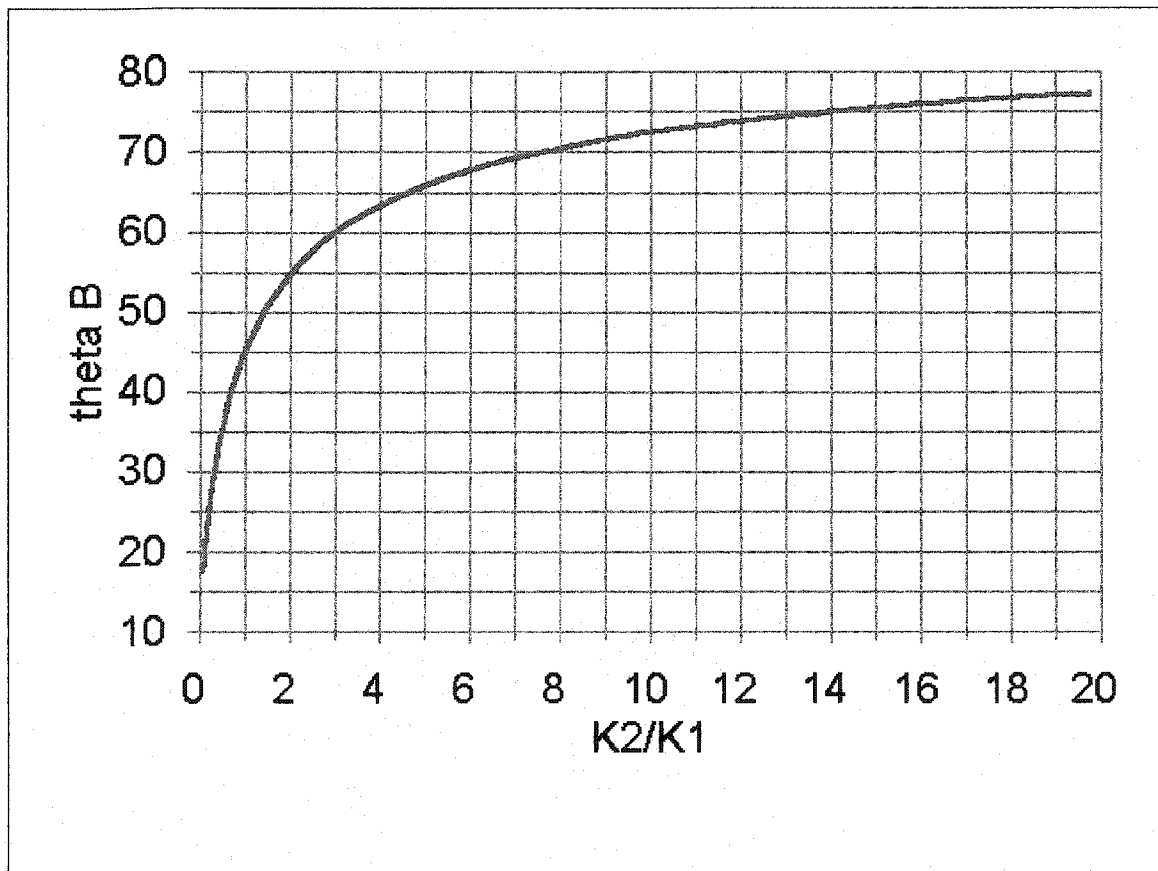


Figure 4.4: θ_B vs. K_2/K_1 for a range of K that might be observed in GPR studies. Note that for $K_2 < K_1$, θ_B is always less than 45° , which is reasonable for reflection studies.

of a water saturated zone, or a conductive clay at the base of an unconfined aquifer, we expect K to decrease across the boundary ($K_2/K_1 > 1$) and θ_B will be large.

Previous modeling studies (Bergmann et al., 1998; Zeng et al., in review) of the TP configuration suggest that AVO variations are subtle and detection of contaminants may be difficult in field data. However, returning to the first example, and considering angles less than 40° (reasonable angles in reflection studies and entirely in the pre-critical regime for this example), we find that in case 1 ($K_2 < K_1$), both R_p (Figure 4.2) and R_T (Figure 4.3) have a significantly larger amplitude vs. angle-of-incidence (AVA) gradient than in case 2 ($K_2 > K_1$). Additionally, θ_B is always pre-critical and less than 45° when $K_2 < K_1$ so that R_p undergoes a 180° phase rotation at a much smaller angle of incidence in case 1 than case 2. Based on these observations, I suggest that while AVO response may not be a robust attribute in the case of transverse polarization, variation in AVO response for parallel polarization can be dramatic. I will show that, for parallel polarization, the AVO gradient and θ_B are potentially valuable AVO attributes for detection of NAPL's in GPR contaminant studies. Considering the dramatic AVO effect, I expect these two attributes will be robust, even in noisy field records. In fact, the parallel polarized GPR AVO response is more substantial than is typically observed in seismic AVO studies for hydrocarbon exploration and I expect similar or better success rates in GPR studies.

The above discussion leads to an important conclusion: for AVO studies, parallel polarization potentially leads to the most valuable attribute information. However, the 180° phase change that occurs beyond θ_B presents a challenge in image processing, and makes stacking the full range of offsets impractical without phase deconvolution.

Additionally, data acquired with transverse polarization are typically of better quality in terms of signal-to-noise. It is therefore valuable to collect redundant multi-offset data sets with both transverse and parallel antenna configurations. The transverse data will be most valuable for imaging, and will provide redundant AVO properties.

It should be noted that in the ideal case, one could potentially look only at the reflection polarity to differentiate NAPL rich zones, since we are primarily trying to detect zones where the permittivity contrast has opposite polarity. However, when one considers phase rotations associated with frequency dependent properties, the phase of the reflection coefficient may not be obvious if the exact earth model is not known. Certainly in field data, reflection polarity is not always obvious, and in any case, it is valuable to have redundant indicators to produce more reliable interpretations. Most importantly, the AVO gradient and θ_B are robust parameters that can be used to determine detailed electric properties that cannot be determined from zero offset reflection polarity alone.

Frequency dependent parameterization

While the previous discussion was valuable to illustrate some basic AVO attributes, it is necessary to consider the frequency dependence of real earth materials to properly analyze field data. In considering the reflection and transmission coefficients, we can simply replace the real wavenumbers with their complex counterparts. The coefficients become complex and are therefore frequency dependent. Some further discussion of the complex wavenumber is useful at this point. In general, the monochromatic propagating e-field is given by

$$\tilde{E}(r,t) = \tilde{E}_0 e^{i(\tilde{k}r - \omega t)} \quad 4.7$$

where the complex wavenumber k , is given by

$$\tilde{k} = k_+ + ik_- \quad 4.8$$

$$k_{\pm} = \omega \left[\frac{\epsilon \mu}{2} \left(\sqrt{1 + \left(\frac{\sigma}{\epsilon \omega} \right)^2} \pm 1 \right) \right]^{\frac{1}{2}} \quad 4.9$$

We see from Equations 4.7 and 4.8 that the attenuation term is given by k_- , and the phase velocity can be found from k_+ .

In general ϵ , μ , and σ are also complex quantities. For many earth materials, the frequency dependence of the permittivity can be described using the Cole-Cole equation (Cole and Cole, 1941). The suitability of this parameterization for GPR studies is well documented and several workers have used Cole-Cole parameterization in numerical modeling (Powers and Olhoeft, 1995; Roberts and Daniels, 1992; Zeng et al., in review).

The Cole-Cole equation for permittivity has the following form

$$\epsilon_+ - i\epsilon_- = \epsilon_{\infty} + \frac{\epsilon_0 - \epsilon_{\infty}}{1 + (i\omega\tau_e)^2} \quad 4.10$$

Where ϵ_0 is the DC permittivity, ϵ_{∞} is the permittivity at optical frequencies, ω is the frequency, and τ is a relaxation time. The permeability μ , for many earth materials can be

described with similar parameterization (Olhoeft and Capron, 1994; Olhoeft and Strangway, 1974)

$$\mu_+ - i\mu_- = \mu_\infty + \frac{\mu_0 - \mu_\infty}{1 + (i\omega\tau_\mu)^2} \quad 4.11$$

The relative permittivity, K , and relative permeability, M , can also be computed using these equations since they differ only by a constant (i.e. $\epsilon = K\epsilon_0$ and $\mu = M\mu_0$). In the frequency range typical for GPR studies, the conductivity is approximately frequency independent, and can be taken as the DC conductivity. Note that the effective conductivity, which is proportional to the product of the frequency and complex permittivity can depend strongly on the frequency. Of particular interest to GPR studies is the case of high water content (Turner and Siggins, 1994).

I now consider a hypothetical aquifer contaminated with both LNAPL's and DNAPL's (Figure 4.5). The parameters for this model (Table 4.1) were published by Powers and Olhoeft (1995). I assume sharp boundaries at all interfaces, and compute the reflection coefficients for a monochromatic plane wave with $f = 100$ MHz. Additionally, I have parameterized the top layer as a dry sand, however, the moisture content of a pure sand unit would be gradational, with large gradients near the capillary zone, and the water saturated zone (Campbell et al., 1995). As a contaminant plume migrates along the top of the water saturated zone we expect it to displace moisture in the pore space, and to be bounded at the top by moist sand, and at the base by water saturated sand, with diffuse boundaries on both sides. How diffuse these boundaries are is not clear, and would likely

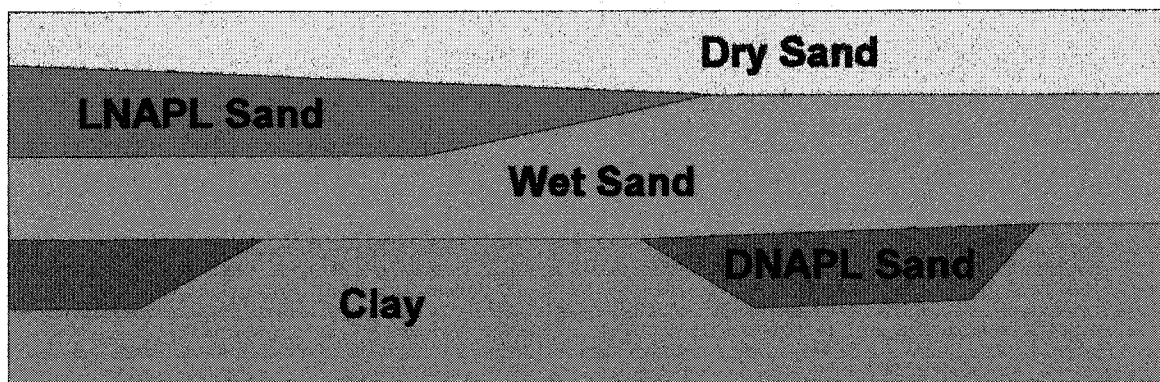


Figure 4.5: Model of an aquifer contaminated with LNAPL and DNAPL. The Cole-Cole parameters are given in Table 4.1.

depend on many factors including the thickness of the plume. Therefore, we must consider this model an approximation, and I have not tried to include all possible effects. This is acceptable, because I am trying to illustrate that the AVO attributes are sensitive to the changes induced by the presence of a contaminant. As long as the boundary is sufficiently discreet to reflect the GPR signal, an AVO response is detectible.

Table 4.1. Cole-Cole parameters used for hypothetical aquifer model

Layer	K_0	K_∞	τ_c (ns)	α_c	M_0	M_∞	τ (ns)	α_p	σ_0 (mS)
dry sand (ds)	5.7	3.4	8.0	0.7	1.14	1.02	15.0	1.0	0.45
LNAPL sand (Ls)	3.5	3.5	0	1.0	1.0	1.0	0	1.0	0.50
wet sand (ws)	29.0	25.6	22.2	0.88	1.17	1.0	15.0	1.0	6.06
DNAPL sand (Ds)	3.5	3.5	0	1.0	1.0	1.0	0	1.0	0.45
wet clay (c)	380.0	79.0	15.0	1.0	1.15	1.0	15.0	1.0	300.0
moist sand	8.9	5.6	11	0.75	1.15	1.01	15.0	1.0	2.0

The reflections from the upper surface of the contaminated zones have dramatically different PP AVO response than for any of the other possible reflecting interfaces (Figure 4.6). I will first consider the reflection from the top of the LNAPL plume (ds/Ls). In this case, θ_B is at 38° since K_{LNAPL} is very close to K_{ds} . Beyond this angle, R increases rapidly towards 1, as we approach θ_c . (Note that in the case of non-zero conductivity, there is no true critical angle, although R is very close to 1 at θ_c for the equivalent zero conductivity case). For the ds/ws, and Ls/ws reflections θ_B occurs at 66° and 71° respectively. As long as we record data at far enough offsets to observe θ_B for ds/Ls, we can easily differentiate the top-of-contaminant reflection from the top-of-water reflection based only on θ_B . The PP AVA gradient for ds/Ls is significantly larger than for

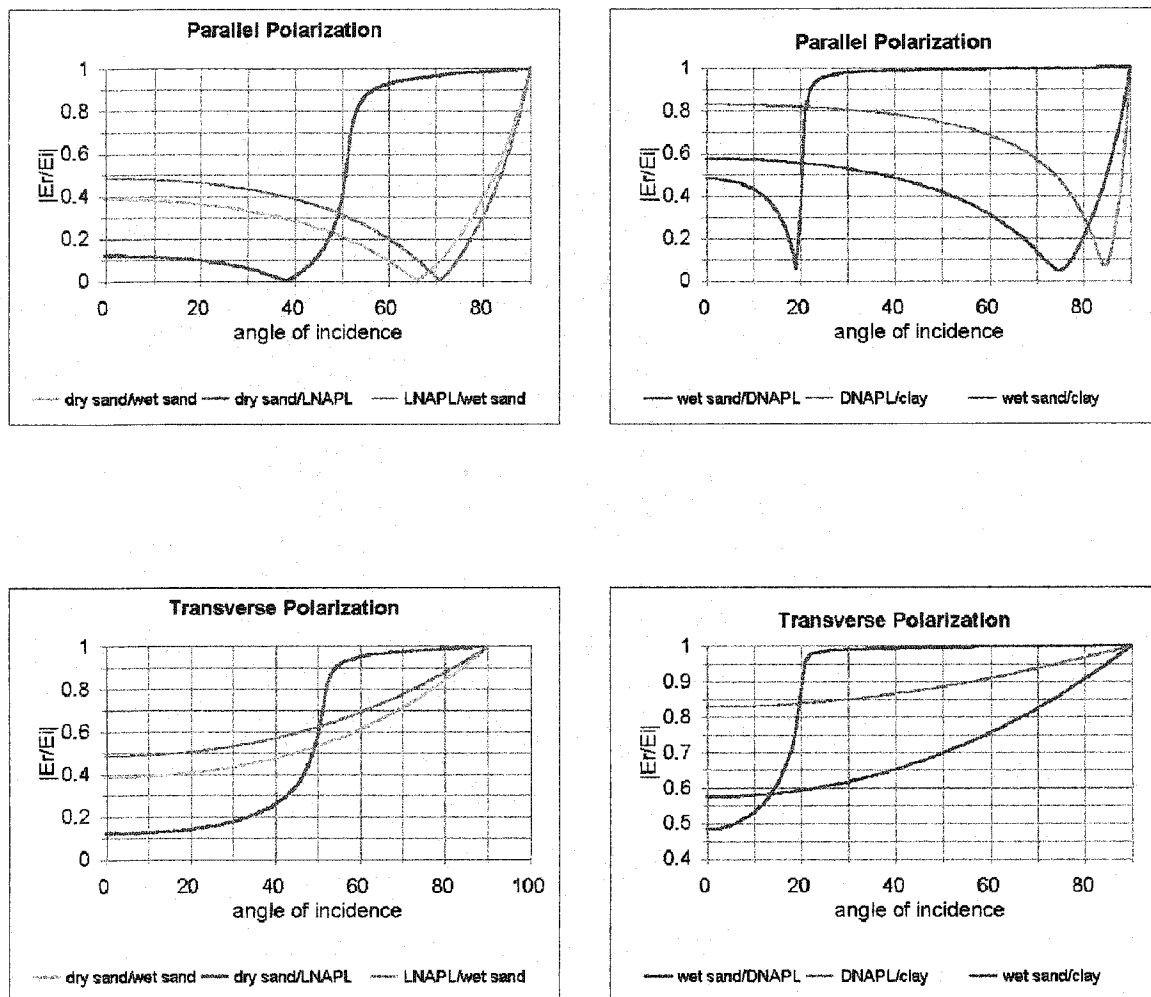


Figure 4.6: Reflection coefficients for potential reflecting boundaries in the aquifer model shown in Figure 4.5.

ds/ws or Ls/ws, and should also be a good contaminant indicator. Variation in the TP AVA gradient at angles less than 40° is subtle for the three cases, and may difficult to differentiate in field data. Beyond 40° , the TP reflection coefficient for ds/Ls increases rapidly to nearly 1 at the critical angle for the equivalent zero conductivity case (recall that there is no true critical angle for non-zero conductivity). I now consider a reflection from the top of the DNAPL pool (ws/Ds). In this case θ_B occurs at 19° , while θ_B for ws/c and Ds/c occur at 74° and 86° respectively. Therefore θ_B should be a good contaminant indicator. In both the case of PP and TP, we find that R for ws/c and Ds/c remains relatively flat out to very large angles, while for ws/Ds, R has a very large gradient out to about 21° . I expect in this case that both θ_B and the PP and TP AVA gradients will be good contaminant indicators.

Practical considerations

There are several factors which must be considered in any AVO analysis. The most obvious is the question of whether sufficient offset is achieved in the survey to observe the AVO effect of interest. This is complicated by the wave traveling through a heterogeneous medium. Typically, the velocity decreases with depth due to increasing moisture content, with a very large contrast at the piezometric surface. This causes the rays to bend toward the vertical (Figure 4.7), so that the vertical component of the wavenumber increases with depth. For horizontal layers, this means that θ decreases with depth (Figure 4.8), so that to achieve the necessary angles of incidence, relatively large offsets may be required. For a simple two layer model, the offset required to achieve a

specified angle of incidence at the base of the second layer is given by:

$$\frac{d}{2} = z_1 \tan \left[\sin^{-1} \left(\frac{v_1}{v_2} \sin \theta_2 \right) \right] + z_2 \tan \theta_2 \quad 4.12$$

where the parameters are defined in Figure 4.9. If we consider an aquifer with dry sand overlying water saturated sand at a depth of 3 m, and the base of the aquifer at a depth of 6 m ($v_1/v_2=2.7$) we find that a minimum offset of 13 m is required to reach $\theta_2 = 19^\circ$ (θ_B for ws/Ds in the previous example). This is significantly larger than the “rule-of-thumb” offset of $d=z_{\text{target}}$ (Evans, 1997), where z_{target} is the maximum depth of interest, which is usually considered necessary for good velocity control. This also leads to severe errors in depth estimates if we assume the NMO equation is valid and we must pursue alternative imaging methodologies. A detailed discussion of this problem is presented in chapter 2. In any case, it is clear that in AVO studies with targets below the water saturated zone, we should acquire data to offsets of at least twice the depth to the target, and in some cases, offsets as large as three times the depth to target may be necessary. If we assume a moist sand rather than dry in the surface layer ($v_1/v_2=1.8$), the minimum offset required to reach $\theta_2 = 19^\circ$ is 6.5 m, and we are close to the 1:1 offset vs z_{target} ratio. If we are interested in a reflection from the top of the water saturated zone ($z_{\text{target}} = 3$ m), we need an offset of 4.7 m to reach $\theta_1 = 38^\circ$ (θ_B for ds/Ls in the previous example), so that it is still necessary to acquire data to offsets significantly larger than z_{target} . This is independent of velocity in the upper layer assuming the straight ray path approximation is valid (of course

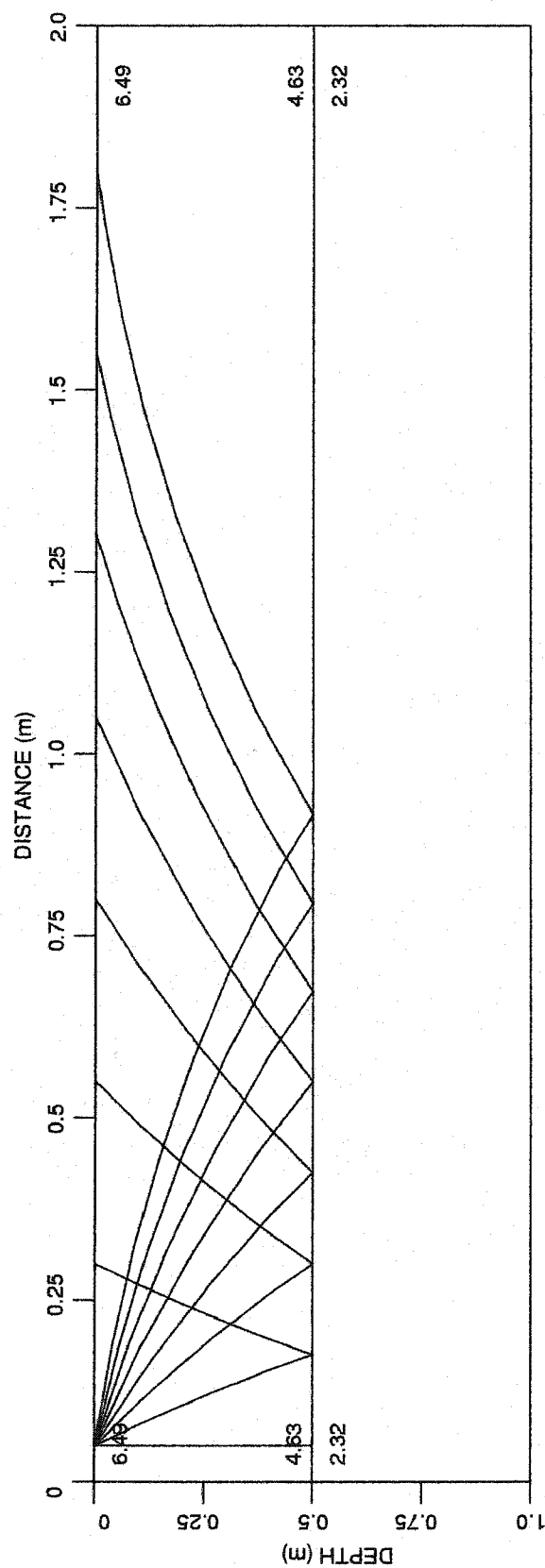


Figure 4.7: Rays paths for a typical negative velocity gradient. Note that the rays curve toward the vertical with increasing depth. Velocities are given in in/ μ s. Scaling to these units is necessary to use the ray tracing code which was designed for seismic data modeling (Loughridge, 1998).

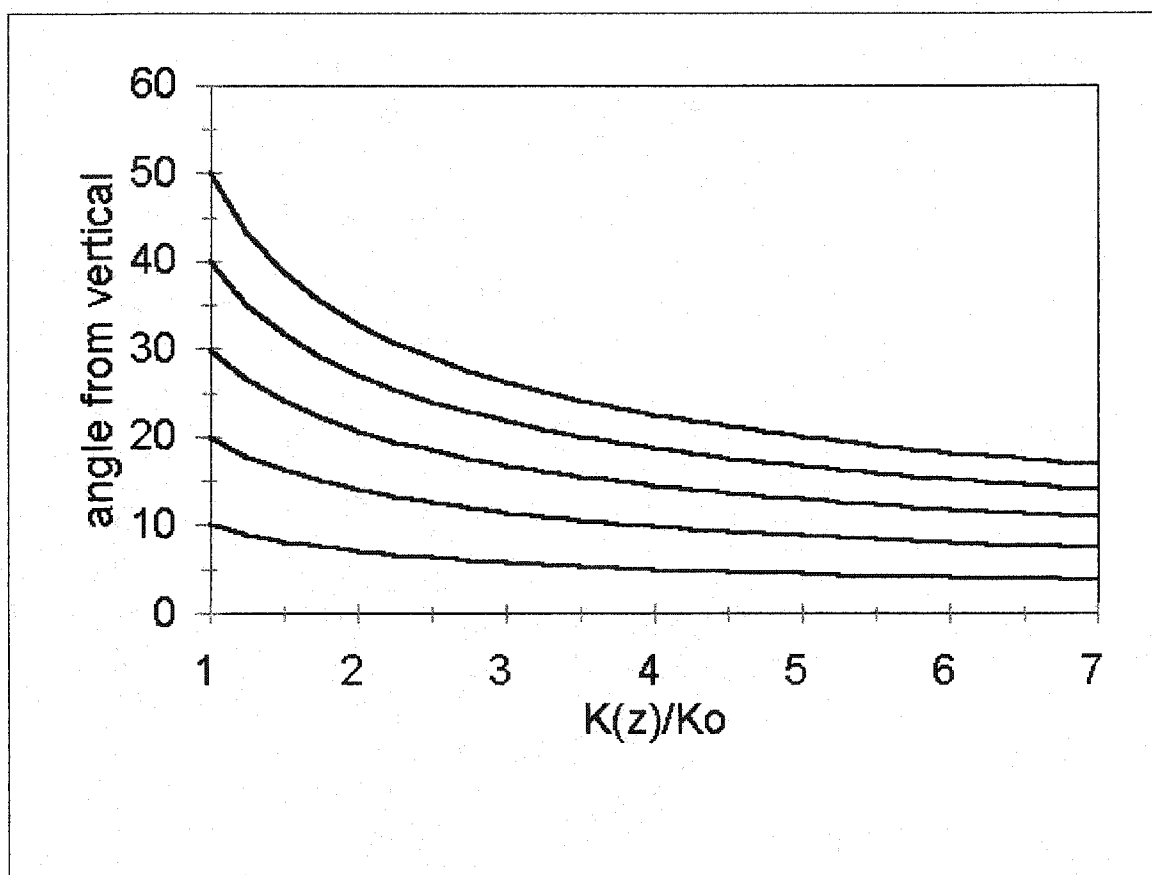


Figure 4.8: Angle of incidence vs. increasing relative permittivity (decreasing velocity) at various take-off angles assuming a linear gradient in K . K_0 is the permittivity at the surface. Typically K increases with depth due to increasing moisture content.

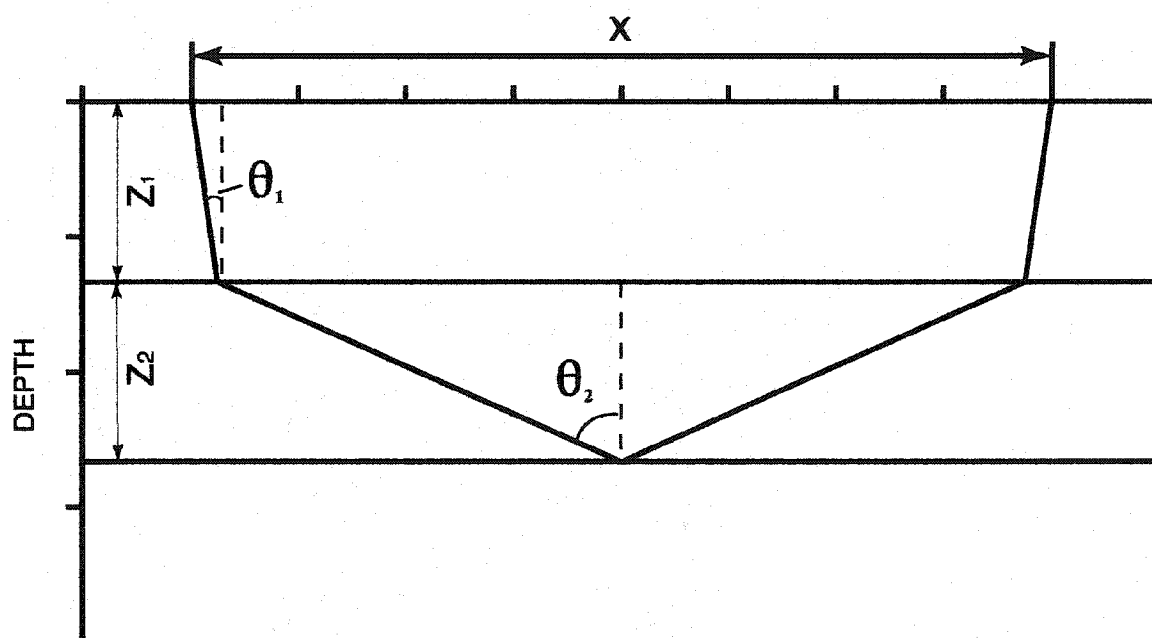


Figure 4.9: Definition of parameters for a two-layer model.

changing v_1 and leaving v_2 constant changes the value of θ_B).

The minimum angle of incidence we can observe is also a concern. As long as the source and receiving antennas are separate, we cannot acquire a true zero-offset record. We are limited not only by the physical dimensions of the antenna, but also by coherent noise generated by source/receiver antenna coupling and resonances. The minimum angle of incidence for any given reflection can be estimated by substituting λ for d in Equation 4.12. For most studies this will not be a limiting factor, but should be considered if the target zone is very shallow, and θ_B is very small.

In addition to the above considerations, which may be more relevant to GPR

Table 4.2. Factors affecting GPR amplitudes (source: Castagna, 1993)

-
- A. Desired information (signal)
 - 1. reflection coefficients versus angle of incidence
 - B. Potential information (considered noise for some methods; signal for others)
 - 1. composite reflections from multiple interfaces
 - 2. tuning caused by NMO convergence
 - C. Factors without offset dependence (noise)
 - 1. random noise
 - 2. instrumentation
 - 3. source/receiver coupling
 - D. Factors with offset dependence (noise)
 - 1. source/receiver directivity
 - 2. emergence angles
 - 3. coherent noise, multiples
 - 4. spherical spreading
 - 5. processing distortions, NMO errors and stretch
 - 6. inelastic attenuation and anisotropy
 - 7. transmission coefficients and scattering above target
 - 8. structural complexity
-

studies because of the large negative velocity gradient, Castagna (1993) discusses several factors affecting seismic amplitudes which must also be considered in GPR AVO studies. The list is reproduced here for the unfamiliar reader (Table 4.2). Of particular importance in GPR studies is source and receiver directivity. Since most GPR antennas are designed to behave like an oscillating dipole, the source and receiver radiation patterns have a strong angular dependence. This will be discussed in greater detail in the modeling section. Of less concern in GPR studies, although still important, are processing artifacts. Since velocity typically decreases with depth, surface noise (direct wave, air wave) typically travels at moveout velocities greater than that of deeper reflected events and there is little interference. Often, only bandpass filtering and spherical spreading corrections are required prior to performing AVO analysis, whereas seismic data typically require considerably more preparation. Additionally, source and receiver coupling is very consistent with GPR data, particularly with current technology since the same source and receiving antenna are used to acquire every trace. With future advent of multi-channel GPR systems, source and receiver consistency may become more of a problem. In general, when soil conditions are such that reflections can be obtained from the target zone, GPR data are relatively clean and well suited to AVO analysis.

A brief discussion of amplitude extraction for quantitative AVO analysis is appropriate. Consider three Gabor wavelets (a Gaussian modulated sine function) with the same modulus but phase rotations of 0 , $\pi/4$ and $\pi/2$ (Figure 4.10). The wavelets have exactly the same power spectrum, or in the time domain, the energy represented by each wavelet is the same, i.e. integration over time yields the same value. However, the

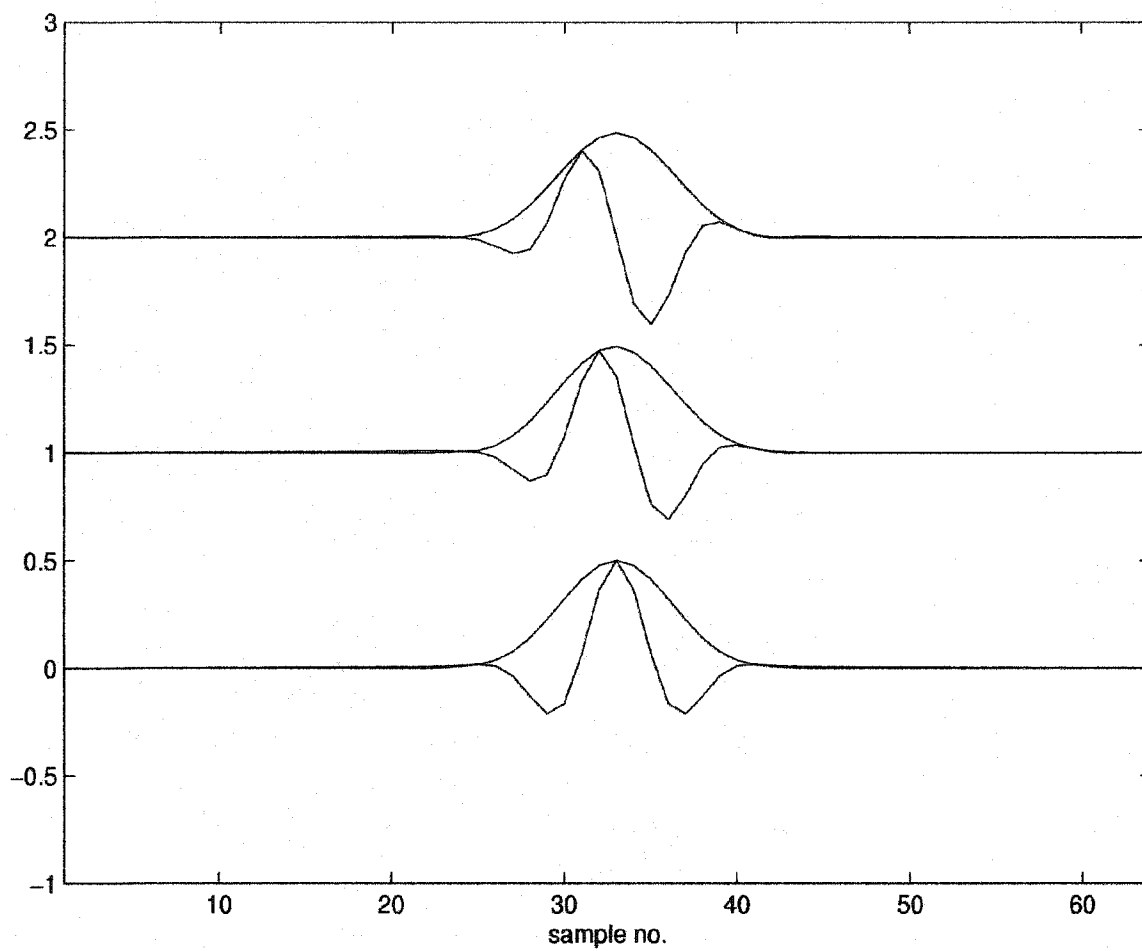


Figure 4.10: Gabor wavelets with phase shift of 0, $\pi/4$, and $\pi/2$, and the envelope function. Note that the amplitude and shape of the envelope function is phase independent.

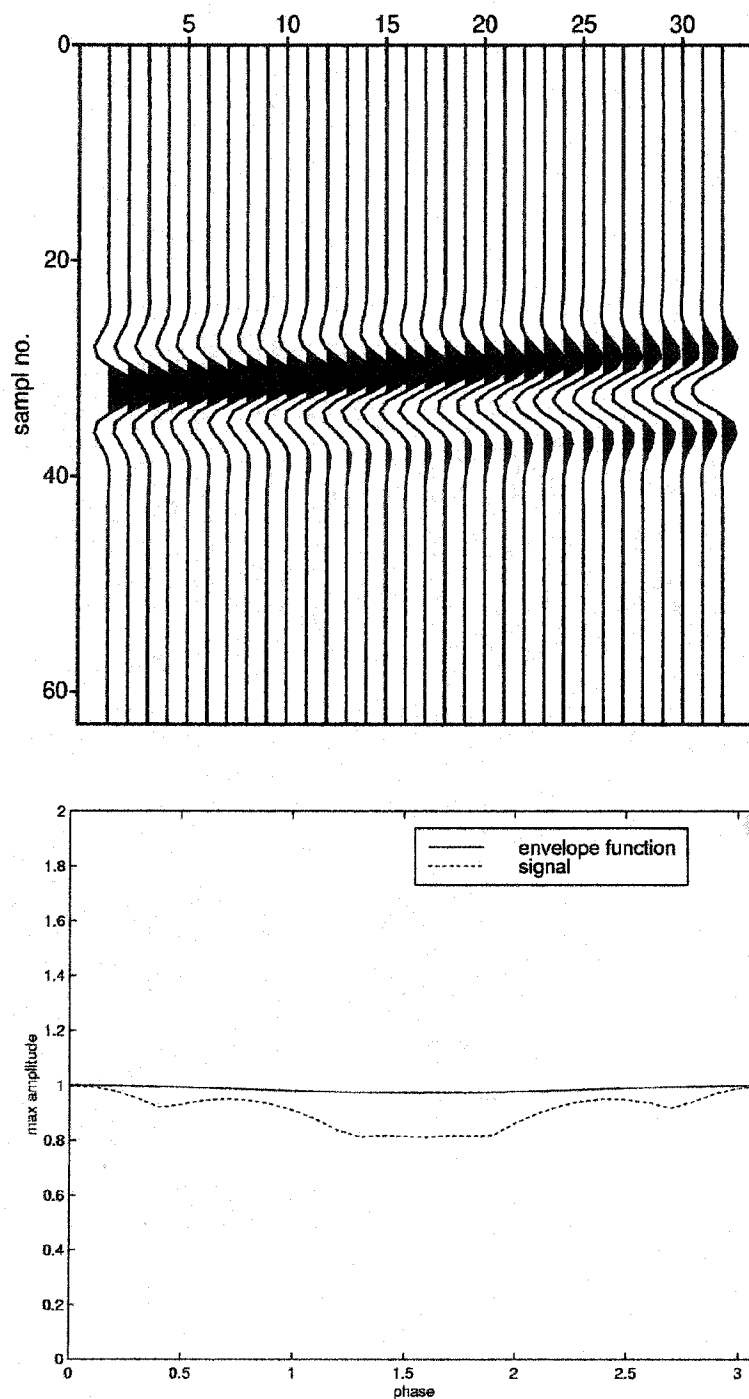


Figure 4.11: Gabor wavelets with the same arrival time and modulus, but with phase varying smoothly from 0 to $-\pi$. Maximum amplitude of the real wavelet is shown with a dotted line. Maximum amplitude of the envelope function yields the desired result (solid line).

maximum amplitude of the real wavelets are different (Figure 4.11). Consider a case where the reflection coefficient is equal to 1 for all angles of incidence but the wavelet phase depends on the angle of incidence (this in fact is the case for post-critical reflections). Excluding all other mechanisms (attenuation, spherical spreading etc), the ratio of wavelet amplitudes along the reflection should be equal to 1 (AVO gradient = 0). However, if one looks only at the real amplitudes along the reflector, the phase rotation causes an apparent AVO gradient that is not related to the reflection coefficient (Figure 4.11). Thus, we must account for phase effects in our AVO analysis. We must deconvolve the wavelets along any given reflector so that they all have the same phase (or shape). This can be done conveniently through complex trace analysis. The maximum amplitude of the envelope function (absolute value of the complex trace) is equivalent to the maximum amplitude of the zero phase wavelet, and therefore is a more appropriate representation of the wavelet for AVO analysis (Figure 4.10). Returning to our previous example, the AVO curve calculated from the envelope function yields the desired result (Figure 4.11). This also addresses the problem of NMO stretch. AVO attributes are typically extracted from NMO corrected data along constant time axes. NMO stretch changes the power spectrum, and if the amplitude analysis is based on wavelet energy this can lead to erroneous results. NMO stretch changes the shape of the envelope function, however the amplitude is not affected.

Based on the previous discussion, I use the envelope function of each trace for quantitative AVO analysis. Amplitudes are extracted from the envelope function by searching for the local maxima within a time gate bounding the reflection event. I then

normalize the amplitude of each wavelet to the maximum amplitude along the reflection event. Since the true zero-offset reflection coefficient is difficult to determine, this normalized comparison is a convenient and robust method of comparing relative amplitudes. With spherical spreading, attenuation, and source corrections, the relative amplitude curve is roughly proportional to the reflection coefficient curve and allows us to evaluate the AVO trend.

MODELING

Several workers have presented GPR modeling algorithms that are based in either ray theory (Cai and McMechan, 1995; Powers and Olhoeft, 1995), or wave equation formulations (Bergmann et al., 1998; Carcione, 1996; Casper and Kung, 1996; Roberts and Daniels, 1997; Wang and Tripp, 1996; Xu and McMechan, 1997; Zeng et al., 1995). However, with the exception of Roberts and Daniels (a full 3-D FDTD algorithm), none of these algorithms model the effect of both transverse and parallel antenna polarization configurations. I present a ray based modeling algorithm that simultaneously models both transverse and parallel antenna polarization configurations, is implemented for arbitrary 2-D multi-offset acquisition geometries, and uses Cole-Cole parameterization to model the frequency dependent material properties. The algorithm consists of two components; 1) travel time computation, and 2) waveform modeling.

Some discussion of the limitations of ray theory (the infinite frequency assumption) is appropriate. Failure to recognize these limitations leads to incorrect, or at best, fortuitous interpretations. There are examples in the literature where these limitations

were severely violated, yet the authors interpreted the model results with no discussion or consideration of the errors involved. There are frequency dependent attenuation, reflection, transmission and dispersion effects, related purely to geometry, that are not treated properly with ray theory. In general, ray theory is assumed valid when the scale of the features being studied, d , is much larger than the wavelength λ , ($\lambda \ll d$). The maximum ratio of λ/d for which ray theory is still valid continues to be the subject of some debate, and active research continues in the seismological community. Mukerji and Mavko (1993) present laboratory data indicating the transition from ray theory to effective medium theory ($\lambda \sim d$) occurs between $\lambda/d = 1$ and $\lambda/d = 10$ for compressional waves. I limit ray based models to the range of $\lambda/d < 1$, and in general, any ray based modeling carried out with $\lambda/d > 1$ should be treated cautiously. Additionally, ray theory does not account for diffractive effects, so that strictly only models with smooth lateral impedance variations are treated properly.

Travel time computation

For travel time computation, I use Zelt & Smiths ray tracing code (1992). I parameterize the model with constant velocity layers of arbitrary geometry, with the boundaries composed of straight line segments. The velocity within each layer is specified as the phase velocity at the peak frequency of the source wavelet. Two-point ray tracing is performed from the source to receiver and the length of each straight ray segment is stored in a table. The length of each segment is assumed frequency independent, which is only approximate for a dispersive media. To evaluate the error introduced by this

assumption, consider a simple two layer model with each layer 3 m thick. The upper layer is non-dispersive with $K=6$, and the lower layer is strongly dispersive with 25% dispersion over the bandwidth of the signal with $K_{f0}=29$ (most materials through which a signal will efficiently propagate have much lower dispersion across the GPR frequency band (Annan, 1996)). At zero offset, the frequency independent path length assumption is exact. The error increases as the offset increases. At an offset of 12 m (twice the depth to the target) the path length for the minimum and maximum phase velocities are 17.9 m ($t = 223$ ns) and 17.6 m ($t = 193$ ns) respectively; a difference in path length (Δr) of only 1.7%. The difference in travel time is 13.5%, and since $\Delta t \propto \Delta r$ only 12.6% of the travel time difference is due to differing travel paths. The majority of dispersion is due purely to velocity differences and in most cases we can safely assume frequency independent travel paths. The more important problem arises in AVO studies when we consider the angle of incidence for the reflection from the base of the second layer. The angle of incidence for the minimum and maximum phase velocities are 20° and 25° respectively. This amount of variation can be significant (consider the Ds/c curve in Figure 4.6). The large degree of dispersion (25%) represents conditions under which the GPR signal would not likely propagate efficiently and the angle of incidence error is much smaller and can be ignored in most cases.

Wavelet modeling

Several factors must be considered when modeling the amplitude, attenuation, and dispersion along a given travel path. These include source and receiver directivity, S_D and

R_D respectively, geometrical spreading, G , the reflection coefficient, R , transmission losses, T , attenuation, k , and dispersion, ω/k . Beginning with the known source wavelet spectrum, I calculate the amplitude and phase shift of each frequency component in the frequency domain. The wavelet for ray n , $w_n(t)$, is then the real part of the inverse Fourier transform, given by

$$w_n(t) = \text{Re} \left[\text{IFFT} \left(W_n(\omega) = \frac{S_{Dn} R_{Dn} \tilde{R}_n(\omega)}{G_n} \left(\prod \tilde{T}_i(\omega) e^{i\tilde{\phi}_i(\omega)} \right) A_0(\omega) \right) \right] \quad 4.13$$

Where $A_0(\omega)$ is the spectrum of the source wavelet, S_{Dn} and R_{Dn} are the source and receiver directivity factors, R_n is the reflection coefficient, G_n is the geometrical spreading term, and T_i is the transmission coefficient for each boundary the ray crosses. The phase, ϕ , includes a frequency dependent time shift component and the attenuation component given by:

$$\phi_i(\omega) = [k_{i+}(\omega) + ik_{i-}(\omega)] d_i \quad 4.14$$

Where $k_{i\pm}$ is the wave number along the i^{th} ray segment and d_i is the length of the i^{th} ray segment. The reflection and transmission coefficients are given by Equations 4.1-4.4, and the geometrical spreading term is discussed by Cai and McMechan (1995). Some care must be given to the application of the source and receiver directivity coefficients. Papas and Engheta (1982) derive the far field (geometric optics approximation) 3-D radiation pattern for a dipole antenna assuming the antenna is placed at the boundary of a half-space, with the lower half consisting of a low-loss dielectric

$$\vec{S} \propto \left[\left(\frac{-\sin^2\theta \cos\theta (1 - n^2 \sin^2\theta)^{1/2} - n \cos\theta}{n(1 - n^2 \sin^2\theta)^{1/2} + \cos\theta} - \frac{\cos^2\theta}{(1 - n^2 \sin^2\theta)^{1/2} + n \cos\theta} \right)^2 \cos^2\phi + \frac{\cos^2\theta \sin^2\phi}{[(1 - n^2 \sin^2\theta)^{1/2} + n \cos\theta]^2} \right] \hat{r} \quad 4.15$$

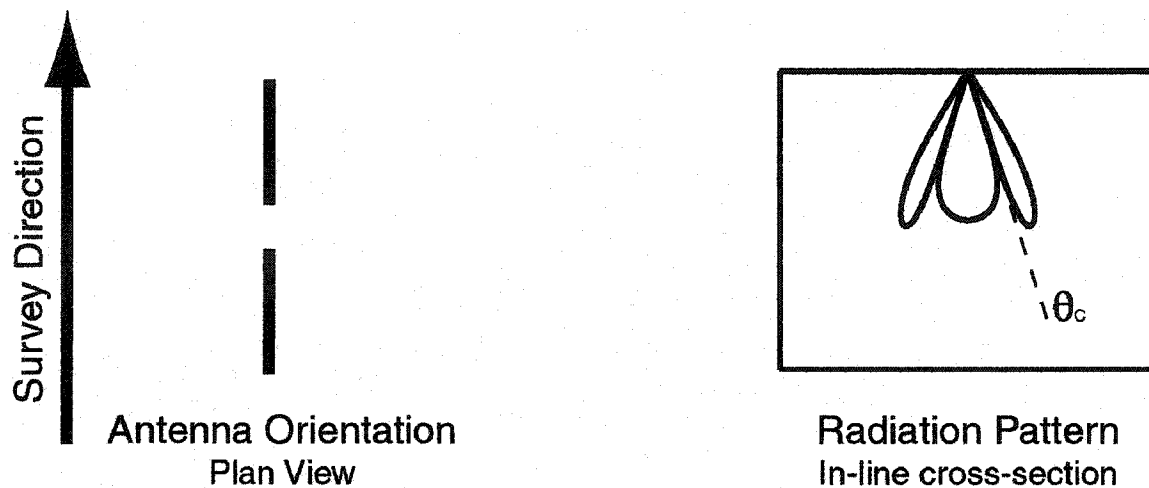
, for $\theta < \theta_c$ and

$$\vec{S} \propto \left[\frac{(n^2 - 1) \sin^4\theta \cos^2\theta \cos^2\phi - 2 \cos^2\theta \sin^2\theta \cos^4\theta}{n^2(n^2 \sin^2\theta - 1) + \cos^2\theta} + \frac{\cos^4\theta \cos^2\phi + \sin^2\phi \cos^2\theta}{(n^2 - 1)} \right] \hat{r} \quad 4.16$$

, for $\theta \geq \theta_c$, where S is the Poynting vector, θ is the take-off angle measured from the vertical (upward pointing is 0 and downward pointing is π), ϕ is the azimuthal take off angle, and θ_c is the critical angle at the free surface.

The source amplitude is proportional to the square root of the Poynting vector ($|\vec{E}| \propto |\vec{S}|^{1/2}$) so the source and receiver radiation coefficients are the normalized square root of S with $\phi=0$ for the case of parallel polarization, and $\phi = \pi/2$, for the case of transverse polarization. The coefficients have a lobate shape with a maximum and null at θ_c for the transverse and parallel polarizations respectively (Figure 4.12). These patterns have been discussed in considerable detail (Annan et al., 1975; Kong, 1972; Papas and Engheta, 1982; Smith, 1984; Tsang and Kong, 1973), and have been used to model the

Parallel Polarization



Transverse Polarization

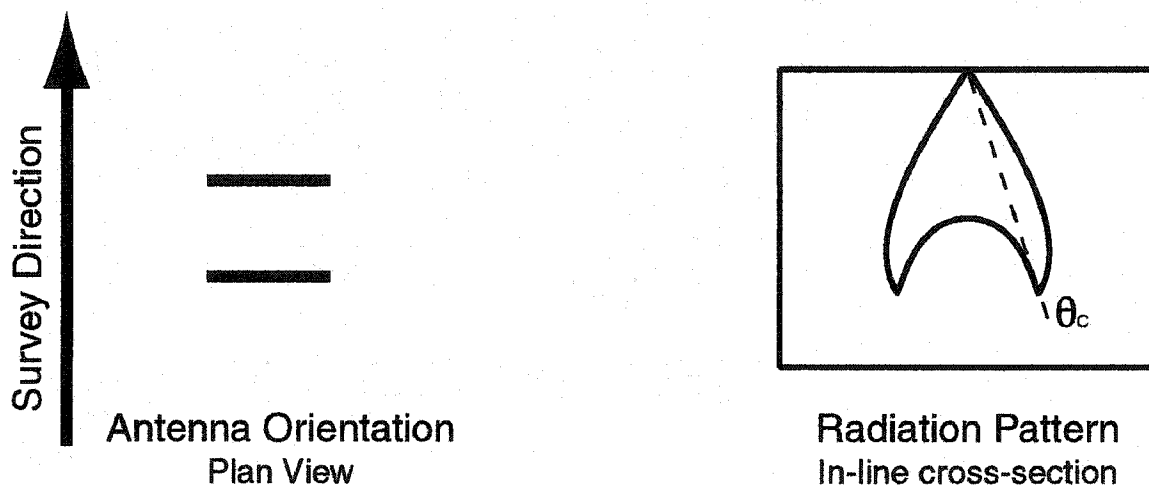


Figure 4.12: Antenna orientations and the associated radiation pattern for a single antenna. Patterns are calculated assuming an infinitesimal dipole at the earth-air interface with $K_{\text{EARTH}} = 4$.

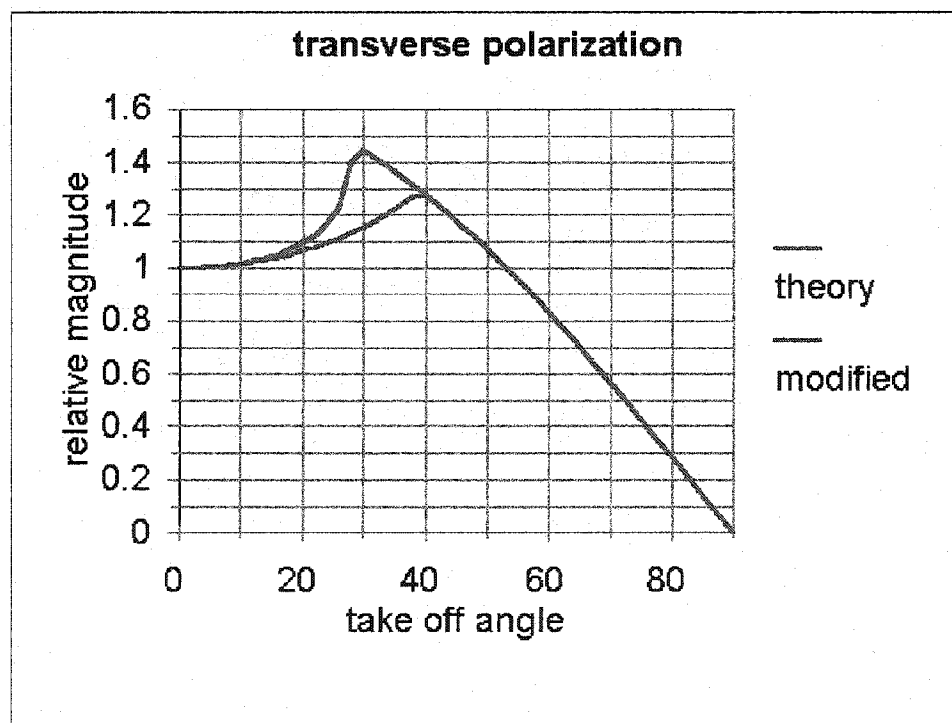
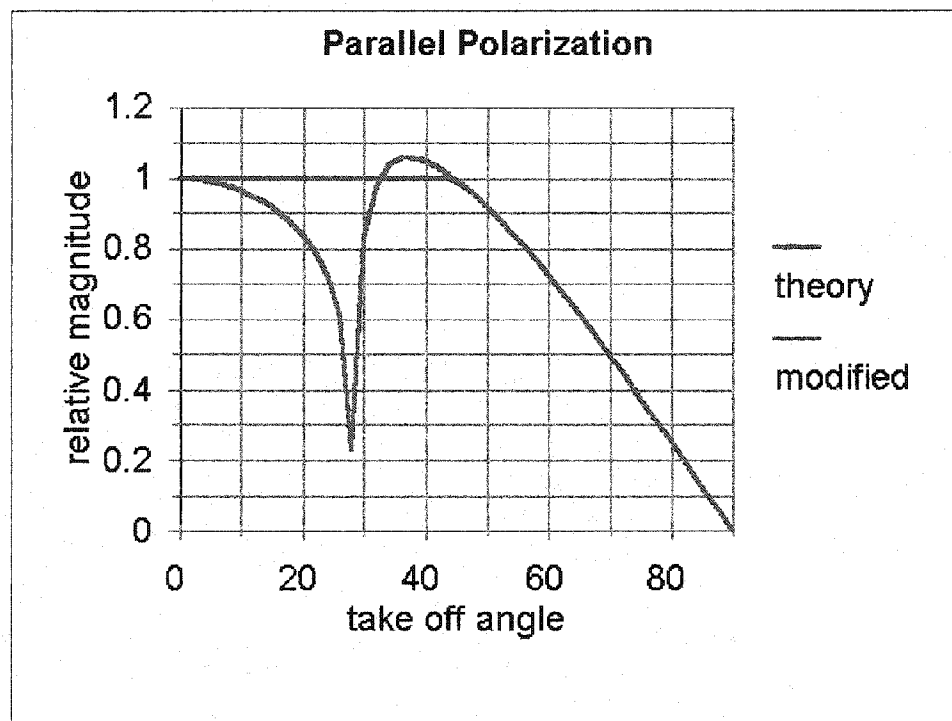


Figure 4.13: Geometric approximation for the radiation coefficients of a dipole, and the modified coefficients used in this paper.

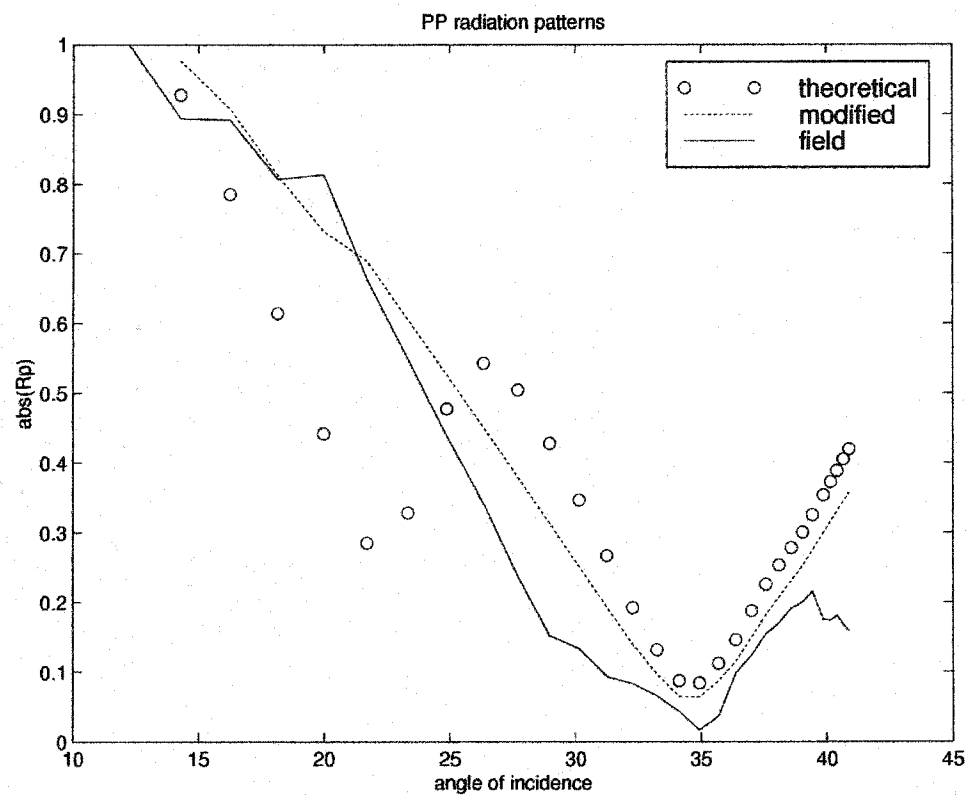


Figure 4.14: Comparison of AVO response for field data, and predicted using the ray theory (geometric approximation) and modified radiation coefficients.

transverse polarization case (Cai and McMechan, 1995). These are the radiation patterns for an infinitesimal dipole and are strictly only valid at infinite distance from the dipole. In many cases in GPR, particularly for buried object detection, or shallow contaminant studies, the reflecting target may be within 10λ or less. Annan et.al. (1975) present laboratory data indicating that when the reflecting target is within 6λ , a transverse radiation pattern of the form $1/\cos\theta$ may be more appropriate for near offsets. In the transverse case, I use $[S_{DT}, R_{DT}] = 1/\cos\theta$ for $\theta < \theta_{int(T)}$, where Equation 4.16 evaluated at $(\theta_{int(T)}, \phi = \pi/2)$ is equal to $1/\cos\theta_{int(T)}$. In the case of parallel polarization, I find that the assumption of uniform distribution is more appropriate in the near field. For parallel polarization, I use $[S_{DP}, R_{DP}] = 1$ for $\theta < \theta_{int(P)}$ where Equation 4.16 evaluated at $(\theta_{int(P)}, \phi = 0)$ is equal to 1. I use Equation 4.16 where $\theta \geq \theta_{int(T)}$, and $\theta \geq \theta_{int(P)}$ for the transverse and parallel radiation patterns respectively. These modified radiation patterns result in an AVO response that is a much better representation of field data than the true geometric optics approximation (Figure's 4.13 and 4.14).

PHYSICAL MODEL AND COMPARISON TO SYNTHETIC MODEL

Data acquisition

To test the modeling algorithm and determine if water saturated sand can be differentiated from sand saturated with a common LNAPL, based only on the AVO response, I constructed a physical model. We buried two plastic containers, one containing water saturated sand (WC), and the other containing sand saturated with

gasoline (GC) (Figure 4.15) in a sand-filled test pit (Loughridge, 1998). The containers (46 cm x 30 cm x 41 cm) were buried at a depth of 0.53 m, with the long axis oriented parallel to the survey direction (Figure 4.15). The pit sand is a coarse grained, washed quartz sand, and the same sand was used to fill the containers. The water table in the pit was maintained at a depth of 0.61 m, which is about 8 cm below the top of the containers.

Two, 2-D, CMP surveys, were acquired with a Sensor's and Software™ Pulse_Ekko 1000 system using 450 Mhz antennas. The data were acquired in expanding-spread CMP gathers, and the total length of each survey was 1.2 m. The first survey (S1) was acquired with parallel polarization antenna configuration, 2.5 cm CMP spacing, 5 cm offset increments, a minimum offset of 28 cm (antenna center-to-center distance) and 30 traces/CMP (30-fold) giving a maximum offset of 1.73 m. The second survey was acquired with transverse polarization antenna configuration, 5 cm CMP spacing, 5 cm offset increments, a minimum offset of 20 cm, and 32 traces/CMP (32-fold) giving a maximum offset of 1.78 m. Assuming straight ray paths, the maximum angle of incidence for the target reflectors is about 59° for both surveys. The minimum angles of incidence are 11° and 15° for the transverse and parallel configurations respectively.

Image processing

Imaging is an integral part of any attribute analysis study and yields velocities which are an important parameter in material evaluation. Although rarely employed due to computational requirements and perhaps lack of exposure in the environmental industry, pre-stack depth migration (PSDM) is a valuable tool in GPR studies due to the

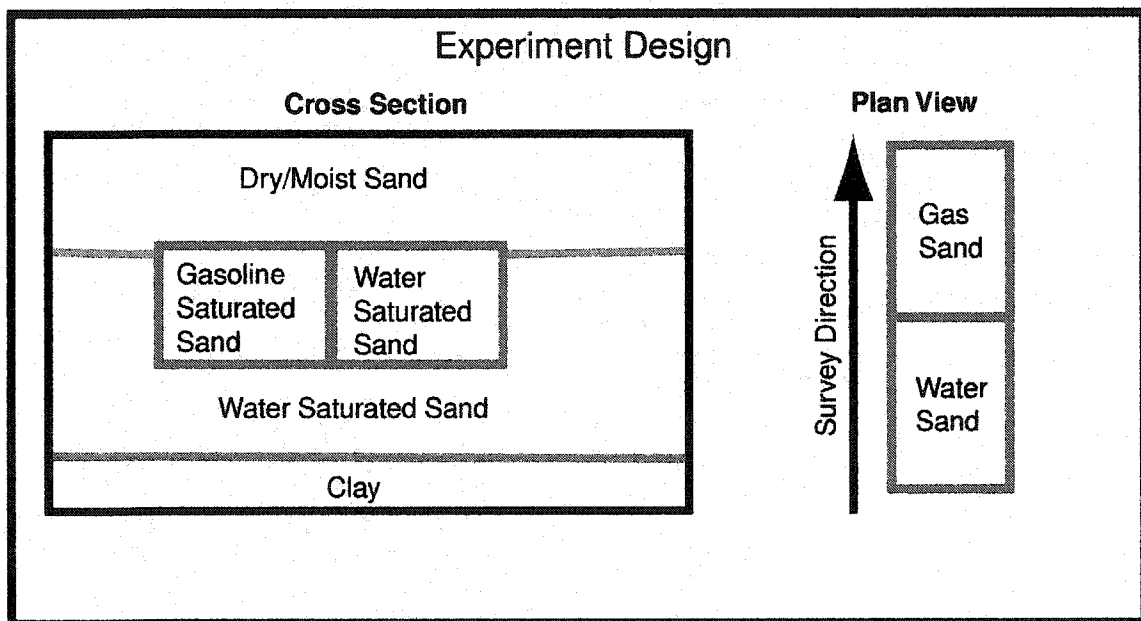


Figure 4.15: Schematic of the LNAPL AVO experiment. The containers are 46 cm x 30 cm x 41 cm and buried at a depth of 0.53 m.

large velocity gradients that are typically present. For the physical model in this discussion, there are very large vertical and lateral velocity contrasts and traditional velocity analysis fails. Under these conditions, accurate imaging requires PSDM velocity analysis and imaging (Kamal, 1989; Lafond and Levander, 1993; Liu, 1997).

In this study, all image processing was carried out with data acquired in the TP configuration. In PSDM processing, we know the velocity model is correct⁴ when all reflections in a common-image-point (CIP) gather (the migrated analog of a CMP gather) are flattened (Kamal, 1989; Lafond and Levander, 1993). I construct a velocity model by first assuming constant velocity above the containers. The data are migrated in the common offset domain with a Kirchhoff PSDM algorithm. PSDM velocity analysis yields an effective interval velocity of 0.139 m/ns for the sand above the containers and 0.058 m/ns for the water saturated sand.

Based on published data (Powers and Olhoeft, 1995), I expect the velocity in the gasoline saturated sand to be close to that for the dry sand. The direct arrival through the sand has a velocity of 0.162 m/ns. PSDM with a velocity block of 0.162 m/ns at the appropriate depth and dimensions for GC, and using the velocities determined above for the water saturated sand and the sand above the containers, yields good results (Figure 4.16). The upper and lower surface of both containers are well resolved and in the correct spatial position (Figure 4.17).

Diffractions from container corners are not entirely collapsed due to migration

⁴PSDM velocities actually represent a sort of mean interval velocity that produces the correct wavefield kinematics within the resolution limits of the data.

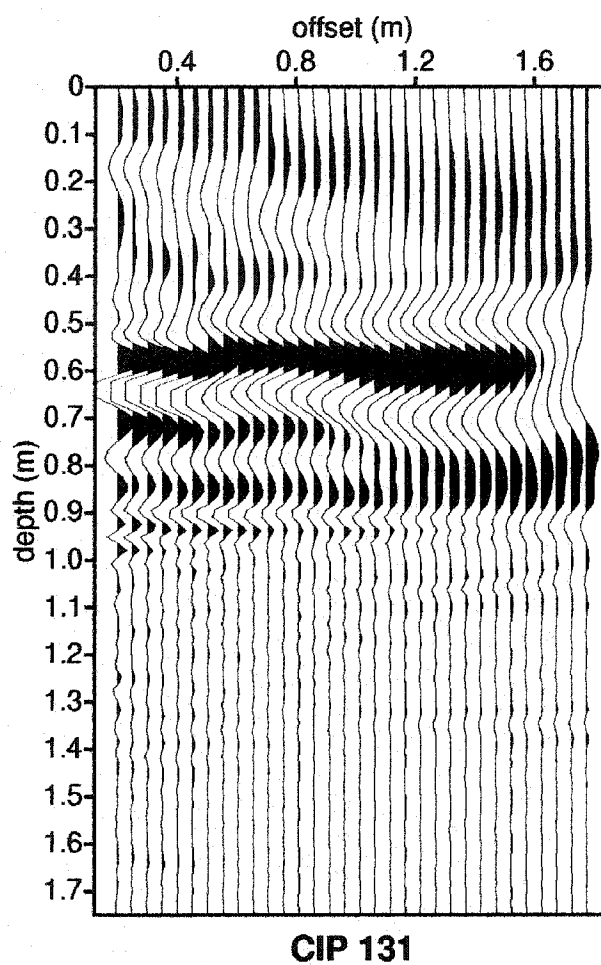


Figure 4.16: Pre-stack depth migrated common-image-point gather (CIP) for the gasoline saturated sand. The reflections from the top and base of the can (.525 and .838 m respectively) are flattened and in the correct depth position indicating that the velocity model is approximately correct.

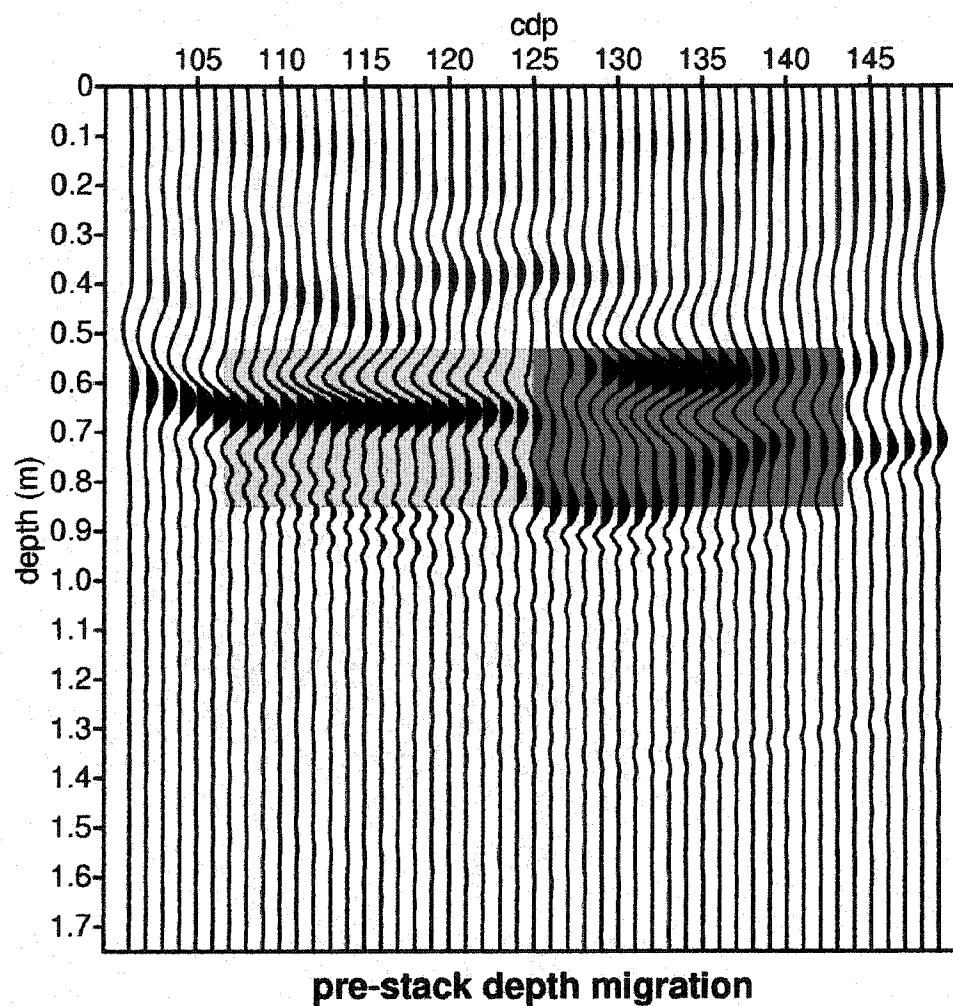


Figure 4.17: Pre-stack depth migrated image of the containers filled with gasoline (red) and water (blue) saturated sand. Colored regions indicate actual positions and dimensions of the containers.

edge effects. The boundaries of GC are not as well defined as those for WC due to the large, sharp velocity contrast from GC to the surrounding formation which degrades the migration response. Surprisingly, there is a weak reflection from the base of WC. This may be due to compaction variation across the container boundary, or to disturbance of the surrounding formation during burial. Reflections from the tops of the containers have opposite polarity as expected.

The wavelength at 450 Mhz in the gasoline saturated sand is about 35 cm which is slightly greater than the thickness of the container (30 cm). Under these conditions, tuning may effect the amplitude of the recorded wavelet, particularly at far offsets where the resolution is lower due travelttime convergence and lower frequency content related to attenuation. The width and length of the containers are also on the order of one wavelength and reverberation within the container may introduce additional tuning effects. These factors must be considered in the AVO analysis. The wavelength in the water saturated sand is about 13 cm which is much smaller than the thickness of the container, and the velocity contrast across the side and bottom boundaries is near zero, so tuning should not be a problem in WC.

Synthetic data generation

Next, I generate synthetic data to model the top-of-can reflections. The Cole-Cole parameters listed in Table 4.1 give a phase velocity (at 450 MHz) of 0.157 m/ns for dry sand, and 0.058 m/ns for wet sand which are quite close to values determined for the sand in our pit so I will use these parameters as a basis for modeling the pit data. Powers

and Olhoeft (1995) also list Cole-Cole parameters for a moist sand. I use the parameters for wet, dry and moist sand to create a lookup table then interpolate to find a phase velocity (at 450 MHz) equivalent to the effective velocity of the pit sand above the containers. This method yields the Cole-Cole parameters listed in Table 4.1 for moist sand.

I generate a CMP for each of the four reflections of interest which I will refer to as water/transverse (WT), gasoline/transverse (GT), water/parallel (WP), and gasoline/parallel (GP). The earth model for each CMP is a two layer model, with moist sand overlying either wet sand or LNAPL sand. I place the reflecting interface at a depth of 0.53 m, and use Cole-Cole parameters as given by Powers and Olhoeft (1995) for the wet sand and LNAPL sand, and parameters for moist sand as determined by interpolation. I generate CMP's with geometry equivalent to the corresponding field data. I do not model the reflection from the base of the containers.

AVO processing

Model comparison. CMP's 112-122, and 132-142 are located directly above the water saturated and gasoline saturated containers respectively (Figure 4.17), and these CMP locations will be used for comparison to the synthetic data. For these comparisons the field data are left in relatively raw form, and only bandpass filtering (50-100-750-1200 Mhz) is applied. No geometric spreading or attenuation corrections are applied so that the raw AVO effects can be compared.

The representative CMP gathers for the field data are supergathers, calculated by

combining adjacent CMP gathers along the water and gasoline reflectors. Supergathers are commonly used in seismic AVO analysis to improve signal to noise ratios. The field AVO curves are extracted from the supergathers with error bars showing the standard deviation for the amplitude curves from the individual gathers. The reflection from the top of the containers has a near offset arrival time of about 9 ns. Qualitatively, the model data match the field data reasonably well (Figures 4.18 and 4.20).

Comparing AVO curves for the synthetic and field data, we find that WT, WP, and GP are relatively well represented by the model (Figures 4.19 and 4.21). However, significant divergence occurs for GT. The model predicts a significant initial increase in amplitude with a maxima at the critical angle of the earth air interface, then a gradual decrease in amplitude. The amplitude of the field data decreases smoothly from the near offset to far offset. The decrease in amplitude is more rapid than that for WT which is opposite the predicted result. I speculate that the decrease in amplitude is primarily due to complex tuning effects related to reverberation within GC. In the case of GP, the AVO response at small θ is dominated by the decrease in amplitude as we approach θ_B , and the divergence of the synthetic and field data is not significant until we reach $\theta > \theta_B$. Additionally, the tuning effect varies with the polarity of the e-field (this is obvious since the non-zero offset reflection coefficient at any given boundary depends on polarity) so I do not expect the same tuning effect for GT and GP.

Recall that I modeled the layer above the containers with a constant, effective velocity. The velocity of the direct arrival through the sand is 0.162 m/ns, but the effective interval velocity of the sand above the containers is 0.139 m/ns. Since there are

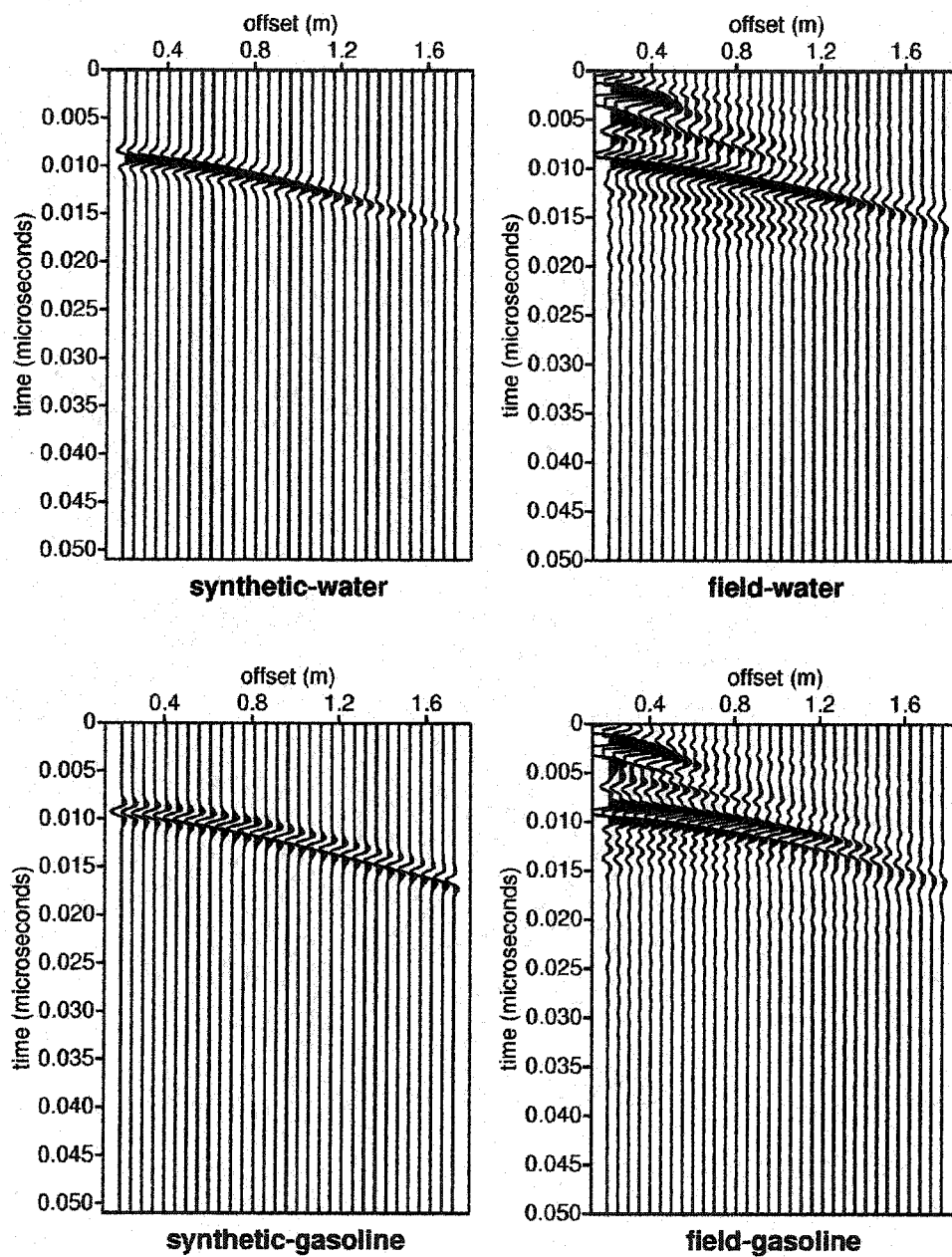


Figure 4.18: Synthetic and field TP response for the LNAPL physical model. The reflections from the water and gasoline saturated sands are centered at about 9 ns.

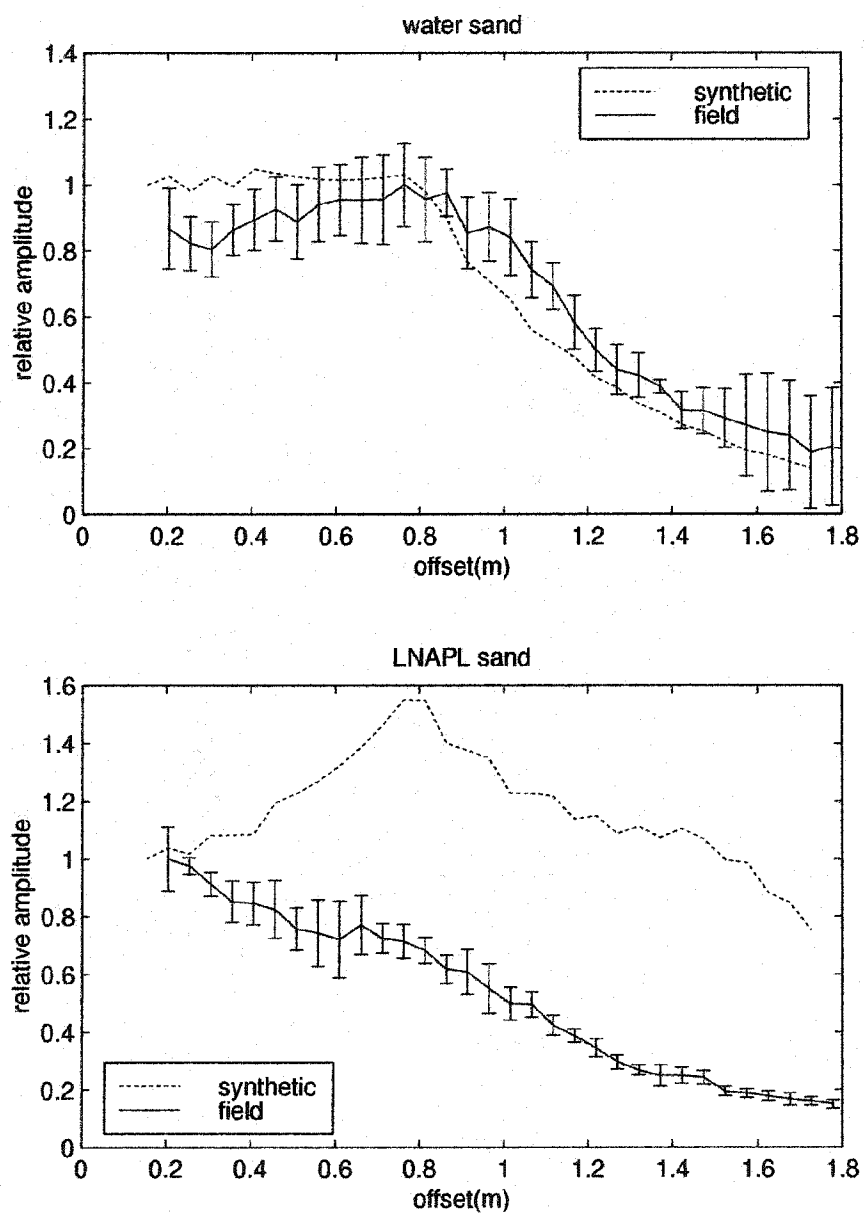


Figure 4.19: TP AVO response for synthetic and field data for the LNAPL physical model. Data are shown in Figure 4.18.

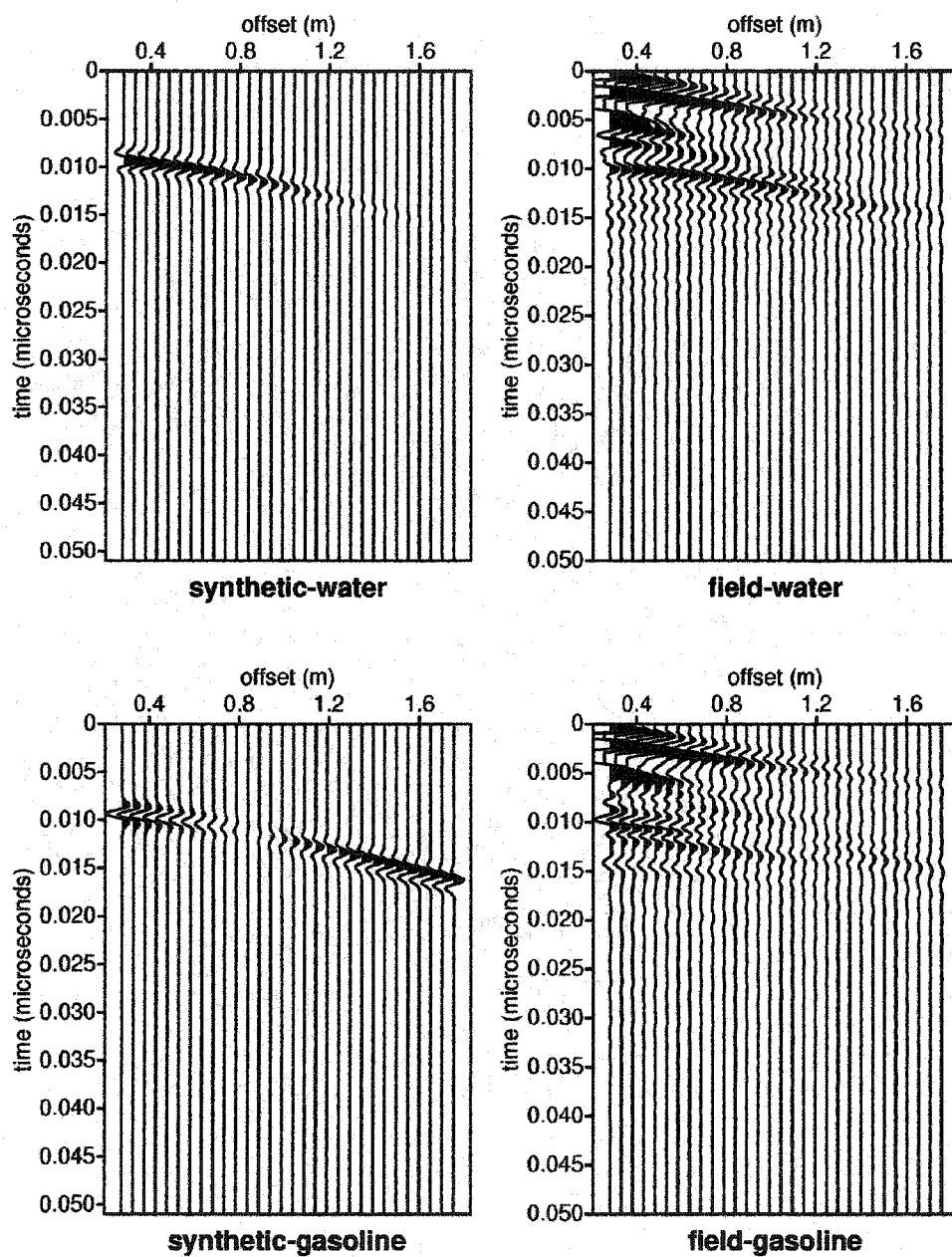


Figure 4.20: Synthetic and field PP data for the LNAPL model. The gasoline and water reflections are centered at about 9ns.

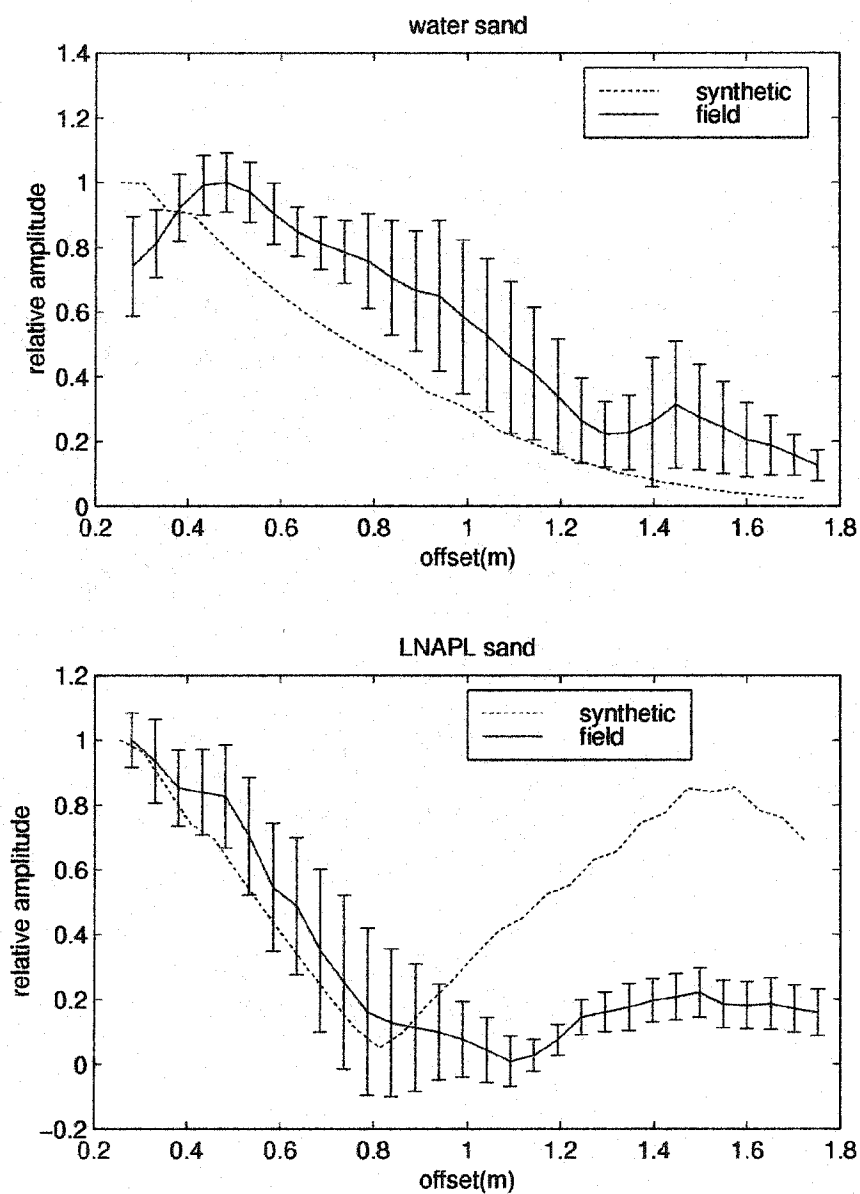


Figure 4.21: PP AVO response for synthetic and field data for the LNAPL physical model. The data are shown in Figure 4.20.

no strong reflections between the surface and the top of the containers, this velocity discrepancy indicates a smooth negative velocity gradient between the surface and the containers. Prior to the introduction of water to the test pit, the velocity of the sand was determined to be a uniform 0.162 m/ns, so the negative velocity gradient is due entirely to a positive moisture gradient with depth. Since there is a large negative velocity gradient, the straight ray approximation is not strictly valid (Figures 4.7 and 4.22), and the accuracy of this approximation decreases at increasing offset. It is more accurate to compare the data in the AVA domain.

Using Zelt and Smith's (1992) ray tracing routine⁵, I compute the angle-of-incidence at the target reflector for the field data using a velocity model with a linear gradient above the containers (Figure 4.7). The velocity at the surface is determined from the direct arrival (0.162 m/ns), and the migration interval velocity (0.139 m/ns) is assumed to be the average velocity between the surface and targets. Based on this assumption, I set the velocity just above the reflectors at 0.116 m/ns. I find that the lengths of the travel paths change very little (justifying the assumption that spherical spreading and attenuation effects are accurately approximated in the straight ray assumption) but the angle-of-incidence at the target changes significantly (Figure 4.22). For the experiment geometry, the straight ray assumption predicts a maximum angle of incidence of about 58°, but the linear gradient model predicts a maximum angle of incidence of only about 43°.

Comparing AVA curves for the synthetic and field data, we find that the synthetic data

⁵Zelt and Smith's algorithm can compute ray paths for piecewise-linear lateral and vertical velocity gradients, but the wavelet modeling portion of the code presented in this paper is not implemented to handle inter-layer gradients in the Cole-Cole parameters.

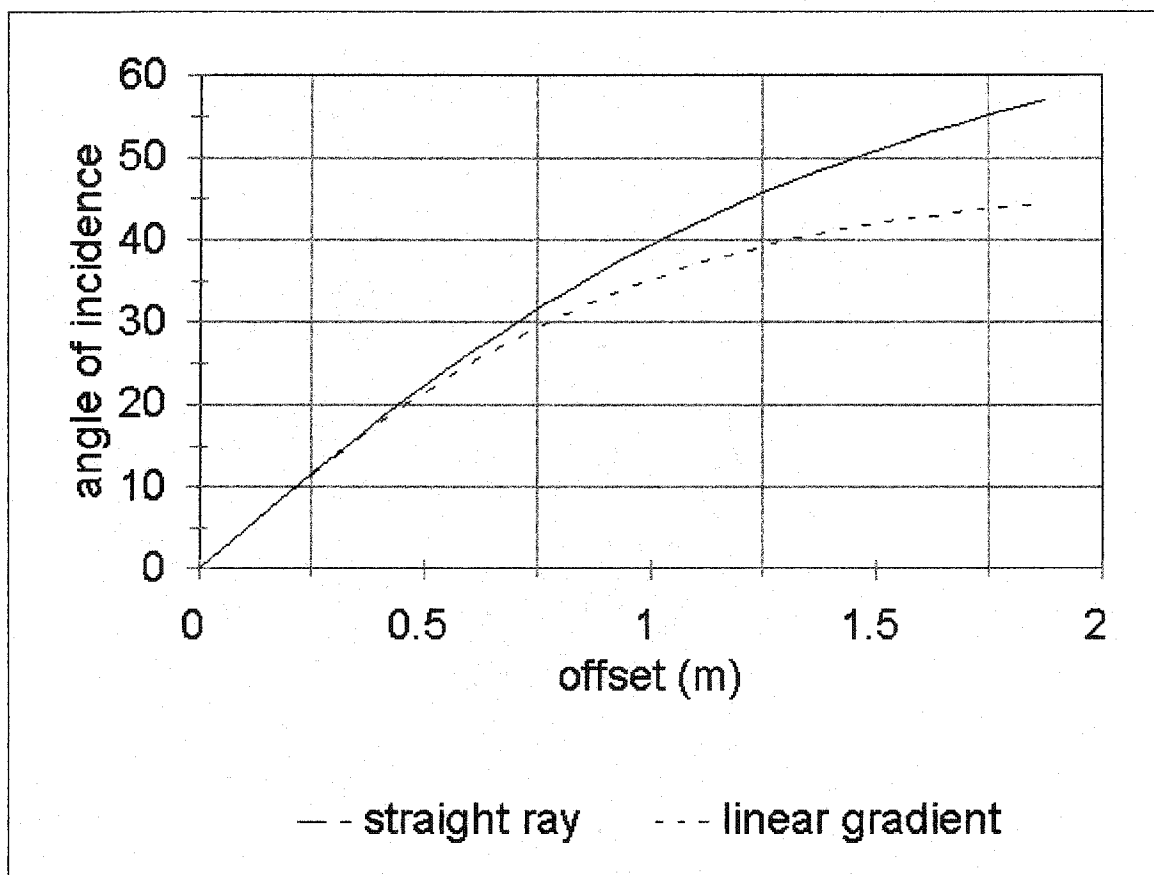


Figure 4.22: Variation in θ vs. offset for the LNAPL physical model assuming straight rays and a linear gradient.

agree with the field data quite well except for the case of WT (Figure's 4.23 and 4.24). The agreement for WP and GP is excellent, and is within roughly one standard deviation across the range of observed θ . I do not expect perfect agreement in the AVA curves since the tuning effects are not modeled, and the upper layer is approximated as homogeneous.

The accuracy of the model prediction is not entirely surprising, given the ideal conditions of the test pit. The comparison serves to verify the validity of the modeling routine for both broadside and end-on acquisition configurations, and suggests that this will be a powerful predictive and analysis tool in field studies. The data also illustrate that tuning effects can cause significant deviation from predicted amplitudes and wave equation based modeling is necessary to properly predict these effects. This example illustrates that AVO analysis is not necessarily straightforward, and requires careful consideration.

LNAPL detection. I first compare the raw AVA curves extracted from the field data for WT and GT, and WP and GP (Figure's 4.25 and 4.26). The TP response for GC diverges significantly from the predicted results, and therefore the LNAPL cannot be detected based on TP AVA attributes without wave equation based modeling of the tuning effects. (Figure 4.25). However, the trend of the PP response for WC and GC is consistent with expected results (Figure 4.26). The AVA gradient is significantly larger for GP, θ_p is clearly observed, and further analysis is warranted.

In trying to identify NAPL's in field data along a profile or in a 3-D volume, it is valuable to have a qualitative interpretive tool that can be used to identify anomalous zones for more detailed study. To do this, I borrow methodologies from the seismic

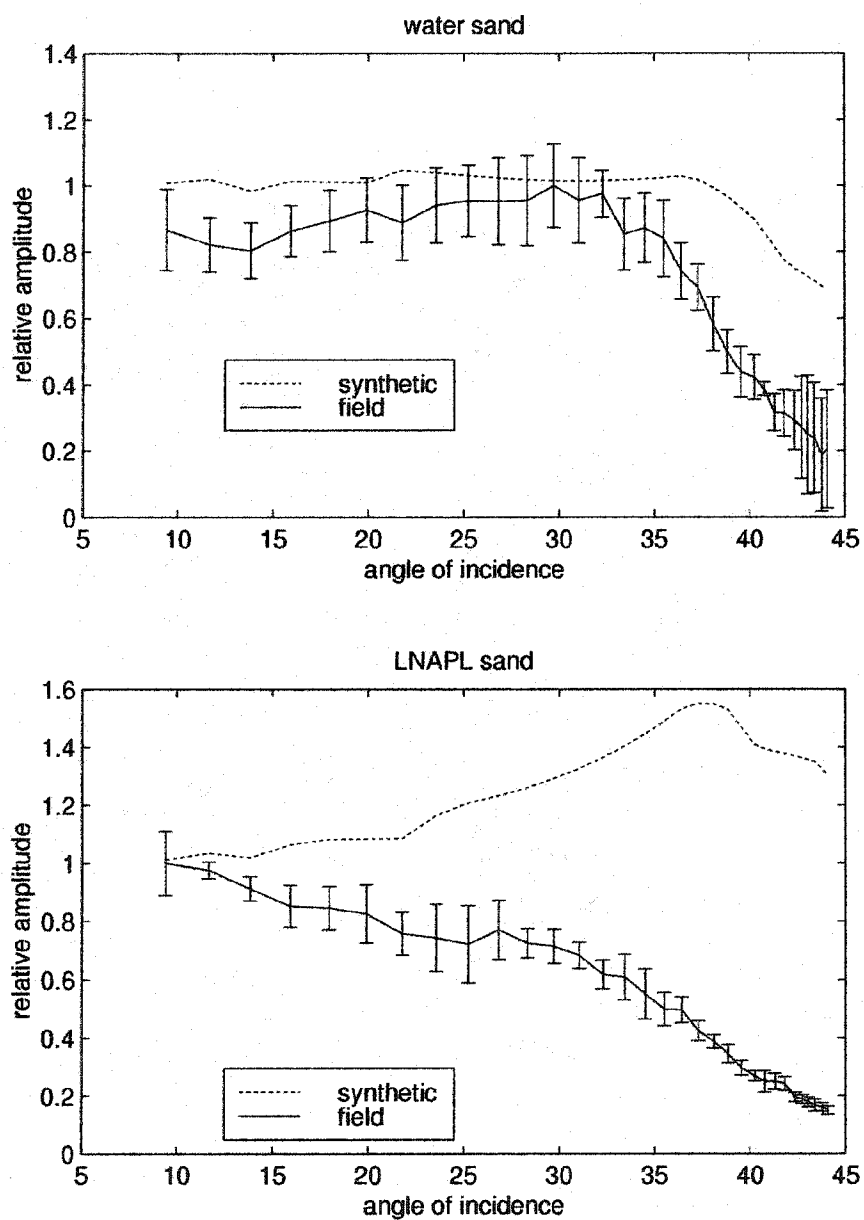


Figure 4.23: Synthetic and field TP AVA curves for the physical model. Data are shown in Figure 4.18.

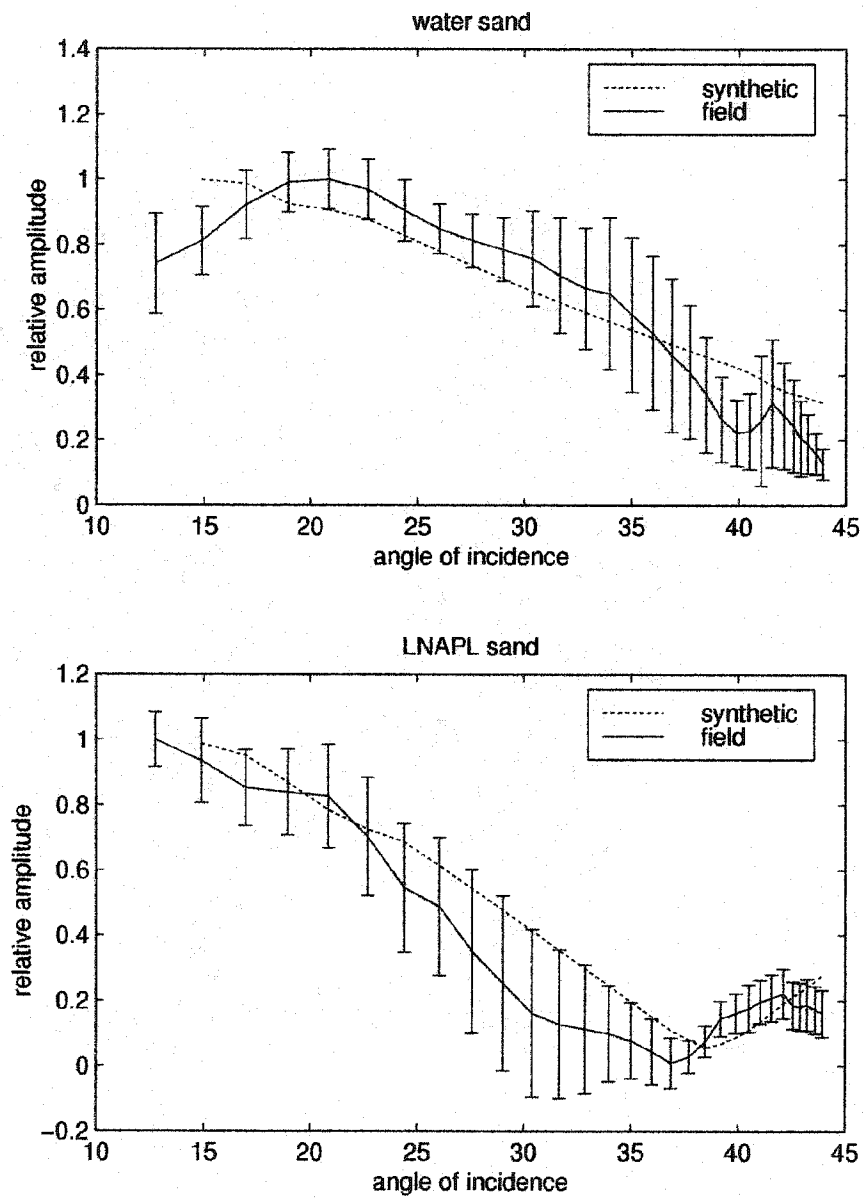


Figure 4.24: Synthetic and field PP AVA curves for the physical model. Data are shown in Figure 4.20.

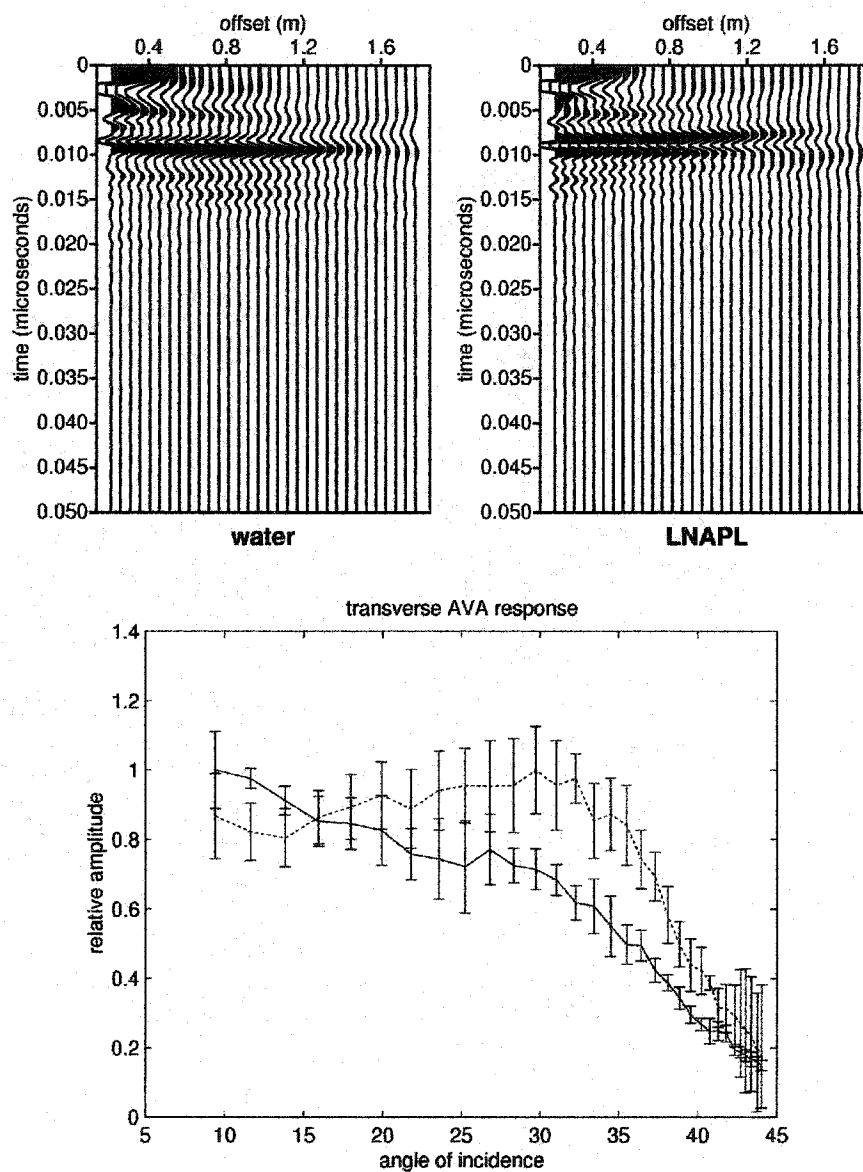


Figure 4.25: NMO corrected TP field data and AVA comparison. The dashed line is the water sand reflection

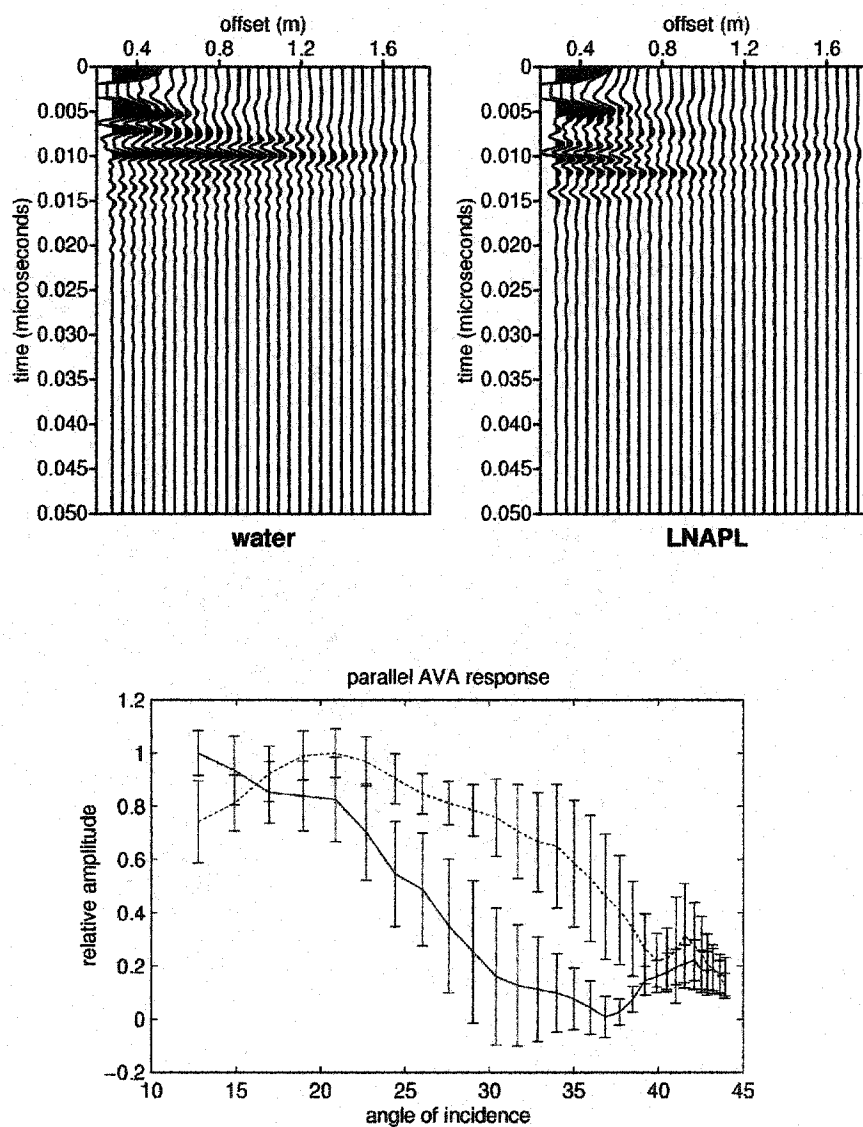


Figure 4.26: NMO corrected PP field gathers and AVA comparison. The dashed line is the water sand reflection amplitudes.

industry, where there are a large number of tools available for interpreting AVO response. While not optimized for GPR data analysis seismic AVO tools are readily available and certain routines can be used for qualitative interpretation. In seismic studies, there is often interest anomalously large AVO gradients. Since this is also the case in GPR NAPL detection, I will use one such tool that is commonly used, and is available with any AVO attribute analysis package. I first estimate the angle of incidence at every point in the CMP gather based on the stacking velocity function (an admittedly rough approximation, but acceptable for qualitative interpretation). The data are then NMO corrected, and a $\sin^2\theta$ function is fit along constant time axes (Figure's 4.25 and 4.26). This yields one intercept (A), gradient (B), and correlation coefficient (C) value at every time sample for each CMP gather. If the data are corrected for geometric spreading, attenuation, and source and receiver directivity the A term represents the zero offset reflection coefficient and the B term is the AVA gradient. These attributes can then be combined in various ways and displayed as times series traces in the same way that the original data are displayed. In seismic studies, the data are generally displayed in A x B plots, and highs may indicate hydrocarbons. In GPR NAPL detection studies, we are interested in large values of B, but there isn't necessarily a large A value, particularly when the target is a diffuse LNAPL plume (Campbell et al., 1995). For this example, I find it useful to display the gradient term weighted by the correlation coefficient (B x C), which I refer to as the gradient attribute. Weighting by C tends to make the analysis less sensitive to noise.

The data are first prepared by applying a spherical spreading correction and exponential gain correction. No attempt is made to correct for source and receiver

directivity (again these are rough approximations, but acceptable for qualitative interpretation). Both the PP and TP data are prestack time migrated in the common offset domain using a true amplitude Kirchhoff algorithm. In this case, prestack migration was necessary in the AVO analysis, since strong diffractions were generated at the corners of the buried containers. Pre-stack migration collapses the diffracted energy which interferes with the AVO analysis. The gradient attribute is extracted from the migrated PP common image point (CIP) gathers, and the migrated TP wiggle trace section is overlain. I display the gradient attribute in a color bias display that shows large values as reds. I overlay the fully processed wiggle trace section so that it is easy to compare the reflection image with the attribute profile (Figure 4.27).

There are strong reflections associated with both the water and gasoline saturated sand, but there is a large value of the gradient attribute for only the reflection from the gasoline (Figure 4.27). The attribute display is a vivid representation, and the LNAPL is easily identified. Once we have identified such anomalous zones throughout the full profile or 3-D volume, we may want to perform a more detailed, quantitative analysis for material property estimation. In GPR studies, it is often appropriate to assume that K is approximately frequency independent (Annan, 1996). The value of θ_B then provides a precise estimate of K_2/K_1 . I consider the LNAPL reflection (Figure 4.26). Extracting the zero crossover angle (θ_B) from CMP's 133 - 140, I find that θ_B occurs at an angle of $36.9 \pm 1.6^\circ$. From Equation 4.6, I find that $K_2/K_1 = 0.56 \pm 0.06$. Migration velocity analysis and assumption of a linear velocity gradient above the target yields a value (at the boundary) of $K_2/K_1 = (0.116 \text{ m/ns} / 0.162 \text{ m/ns})^2 = 0.513$. The two results differ by only

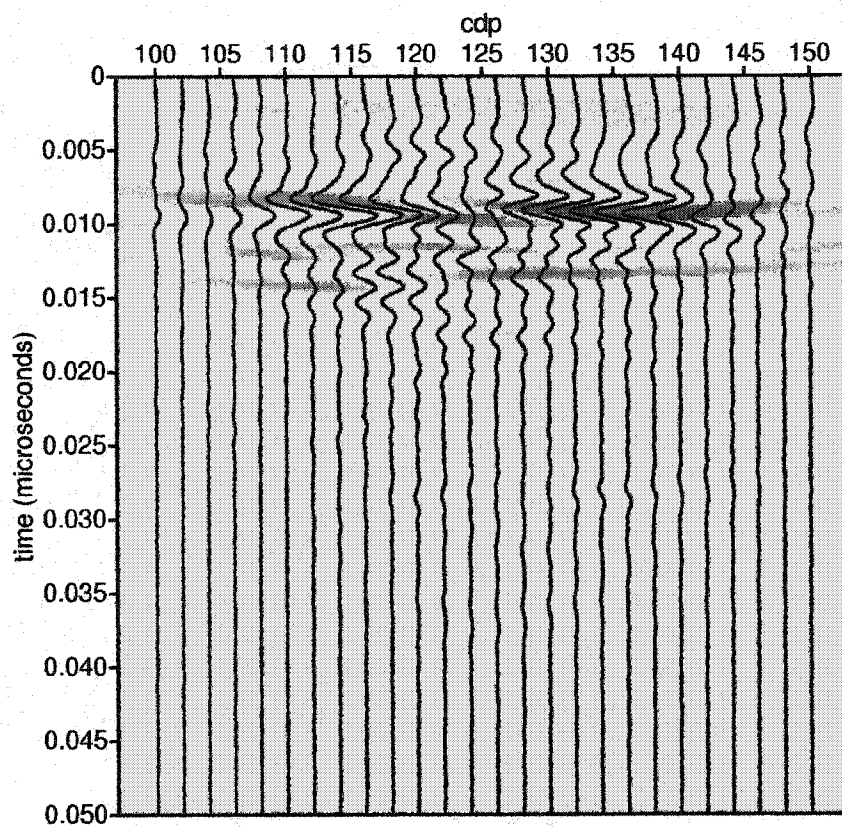


Figure 4.27: AVA attribute image and pre-stack time migrated wiggle trace overlay. Red indicates a large AVA gradient associated with the top-of-LNAPL reflection. Compare with the depth image in Figure 4.17.

8.4% and is within estimated uncertainty. The good correlation serves to support both the velocity and θ_B analyses. The analysis also indicates the robust nature of the PP AVO response when the layer of interest is relatively thin.

Using a physical model, I have demonstrated significant potential to use the PP AVO response as a NAPL indicator. The gradient attribute can be used as an easy to interpret reconnaissance tool, and θ_B can be used to extract precise values of K_2/K_1 . I do not suggest that these are the only attributes of value, nor do I attempt to pursue all possible attributes that may be extracted. There are numerous additional attributes that may be extracted from the AVO curves, and there is much additional work to be done. The attribute extraction algorithms need to be optimized for GPR studies. Most importantly, continued experiments are needed to determine how well the technique works under field conditions where the contaminant boundaries are more diffuse. In the following example I discuss one additional factor that must be considered in field studies; the relationship of the AVO response to potentially severe velocity gradients in the overburden.

LNAPL and DNAPL detection in an aquifer model

To evaluate the effect of the large negative velocity gradient expected above a DNAPL pool below the piezometric surface, I return to the hypothetical aquifer discussed previously (Figure 4.28). Typically, we expect velocities to decrease by a factor of roughly 2 or more as the wave travels from the vadose to water saturated zone. This causes severe ray bending toward the vertical, which will limit the angles of incidence that

can be achieved for reflections below the water table. Fortunately, we expect a strong AVO response for the DNAPL reflection at small angles of incidence (Figure 4.6), which improves the potential for DNAPL detection.

There are essentially four cases to consider in the hypothetical aquifer (Figure 4.28). I construct the velocity model with a 3 m thick vadose zone, 1 m thick LNAPL and DNAPL layers, and a 3 m thick water saturated zone (Figure 4.9). Looking at travel paths for case 3 (Figure 4.29) we see that as the wave is transmitted through the high velocity LNAPL, the travel path bends sharply away from the vertical, then bends sharply back toward the vertical as the wave is transmitted into the slow, water saturated layer. As the wave is transmitted into the high velocity DNAPL sand, the ray again bends sharply away from the vertical. Since the ray is bent toward the vertical across the water table, the angle of incidence for the DNAPL reflection increases slowly as a function of offset relative to the other reflectors (Figure 4.30) and a maximum angle of only 27° is reached at the maximum offset of 12 m. Removing the LNAPL layer (case 1 & 4), we find that θ for the earliest reflection from the base of the aquifer increases more rapidly as a function of offset than when the LNAPL is present (Figure 4.31). Given the amount the θ vs. offset curves vary when $\theta > 15^\circ$ and the very large positive gradient in R for ws/Ds (Figure 4.6) at angles between 15° and 22° , I expect the presence of the LNAPL layer to significantly effect the AVO response.

I generate 4 representative CMP gathers for both TP and PP configurations (Figure's 4.32 and 4.33) to evaluate the AVO response for each of these cases. The data are generated with a Ricker source wavelet with peak frequency of 225 Mhz, offset

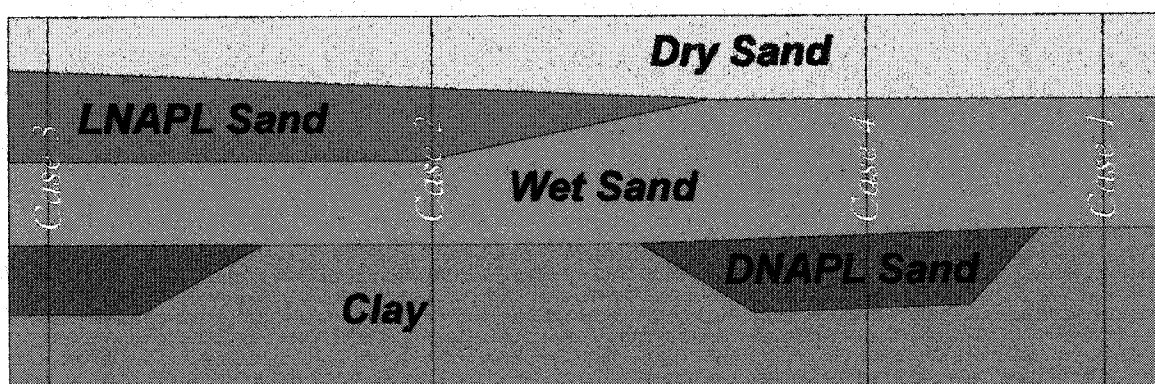


Figure 4.28: Contaminated aquifer model and CMP locations for four cases. Each location has a different velocity profile and reflector configuration.

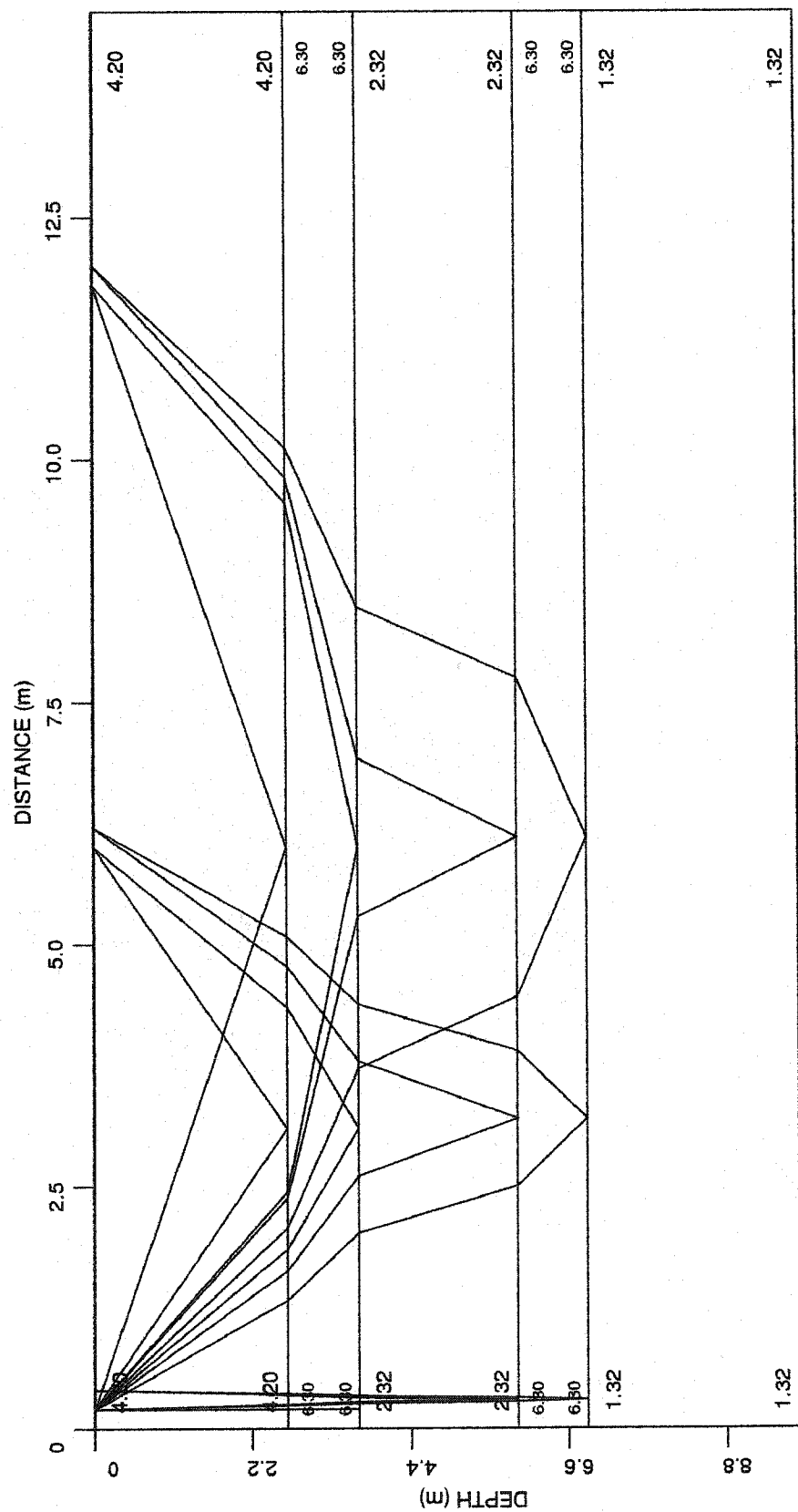


Figure 4.29: Ray paths for case 3 in Figure 4.28. Velocities are given in m/ μ s. Scaling to these units is necessary to use the ray tracing code which is designed primarily for crustal seismology problems.

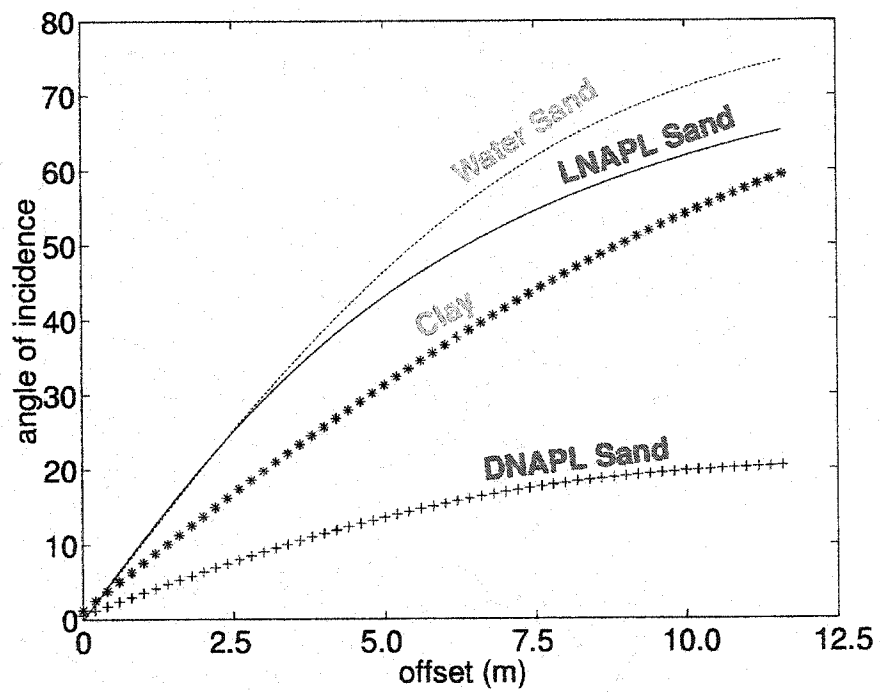


Figure 4.30: θ vs. offset for case 3 (Figure 4.28) reflectors. θ increases much more slowly for the DNAPL reflector due to the large negative velocity contrast from the LNAPL to water saturated zones.

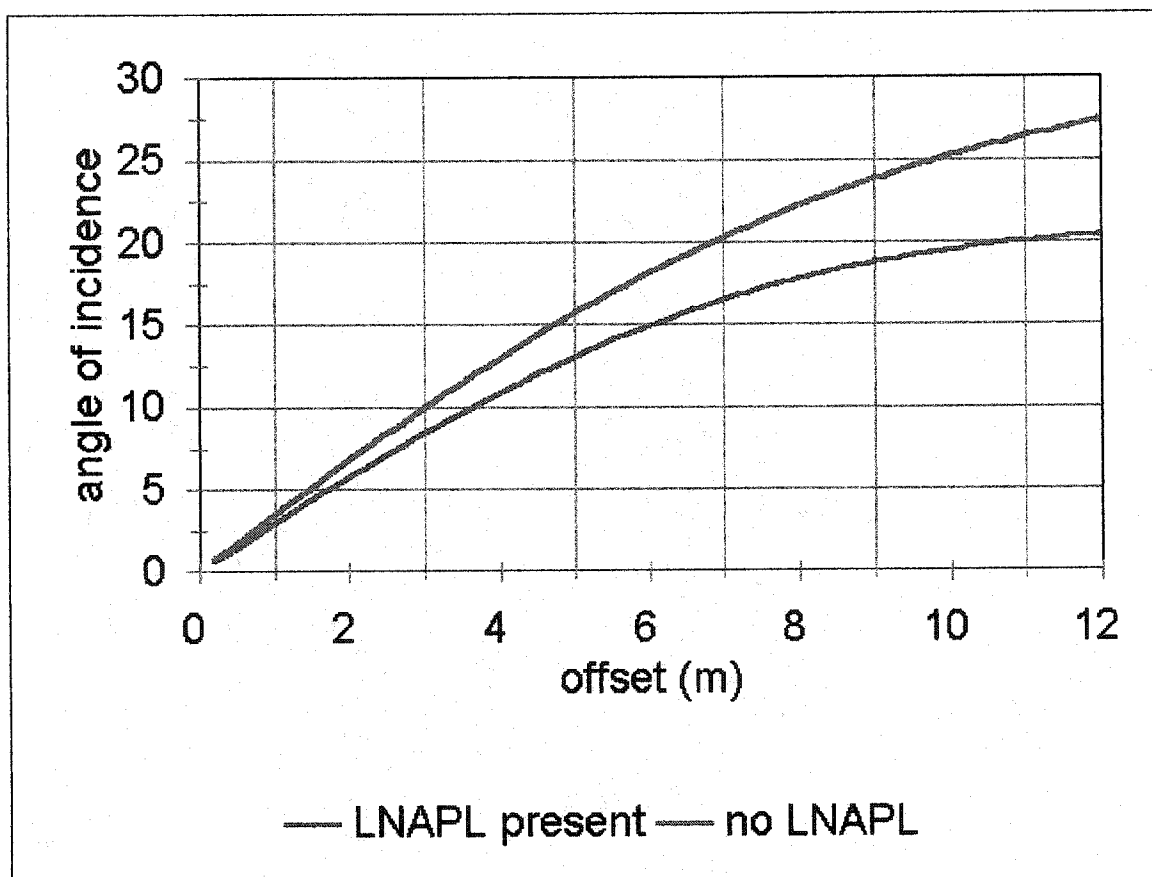


Figure 4.31: Variation in the angle of incidence vs offset at the base of the aquifer with and without a thin LNAPL layer.

interval of 20 cm, and a maximum offset of 12 m, corresponding to twice the depth to the base of the aquifer which is the base of the target zone in this case. The Cole-Cole parameters used to generate the synthetic data are the same as those used previously (Table 4.1) with the exception that the values for moist sand are used rather than those for dry sand. All AVO comparisons are based on the absolute value of the normalized relative amplitudes.

I first consider the earliest reflection from the top of the aquifer which corresponds to a moist sand/water sand (ms/ws) reflection in cases 1 & 4, and a moist sand/LNAPL sand (ms/Ls) reflection in cases 2 & 3. In the end-fire (PP) configuration, we observe Brewster's angle at an offset of 3.68 m and a large AVO gradient for the ms/Ls reflection. θ_B is observed for the ms/ws reflection at much larger offsets where θ approaches 70° (Figures 4.6 and 4.30). Additionally the AVO gradient is significantly smaller for ms/ws (Figure 4.34). In the broadside (TP) configuration, the amplitude of the ms/ws reflection decreases smoothly from a maximum amplitude at zero offset to an amplitude of roughly zero at far offsets, whereas the ms/Ls reflection maintains roughly constant amplitude to an offset of around 4 m then drop sharply and becomes roughly parallel to the ms/ws amplitude curve at an offset of around 8.5 m. The variations in both the TP and PP curves are significant and the potential to detect differences of this magnitude in field data are quite good.

I now consider the earliest reflection from the base of the aquifer which corresponds to a water sand/clay (ws/c) reflection in cases 1 & 2, and a water sand/DNAPL sand (ws/Ds) reflection in cases 3 & 4. I am interested in differences in the

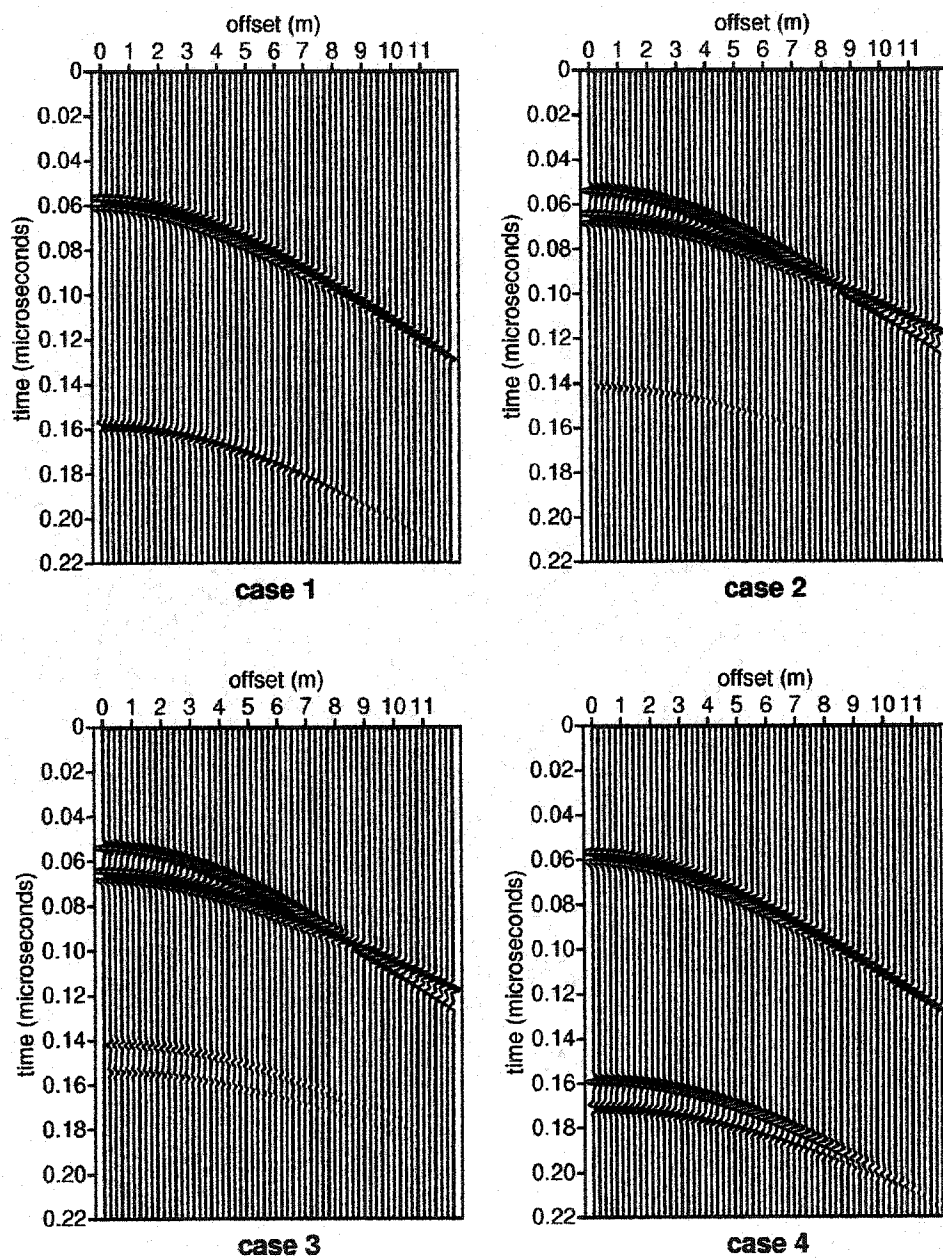


Figure 4.32: TP CMP's for the four cases in Figure 4.28.

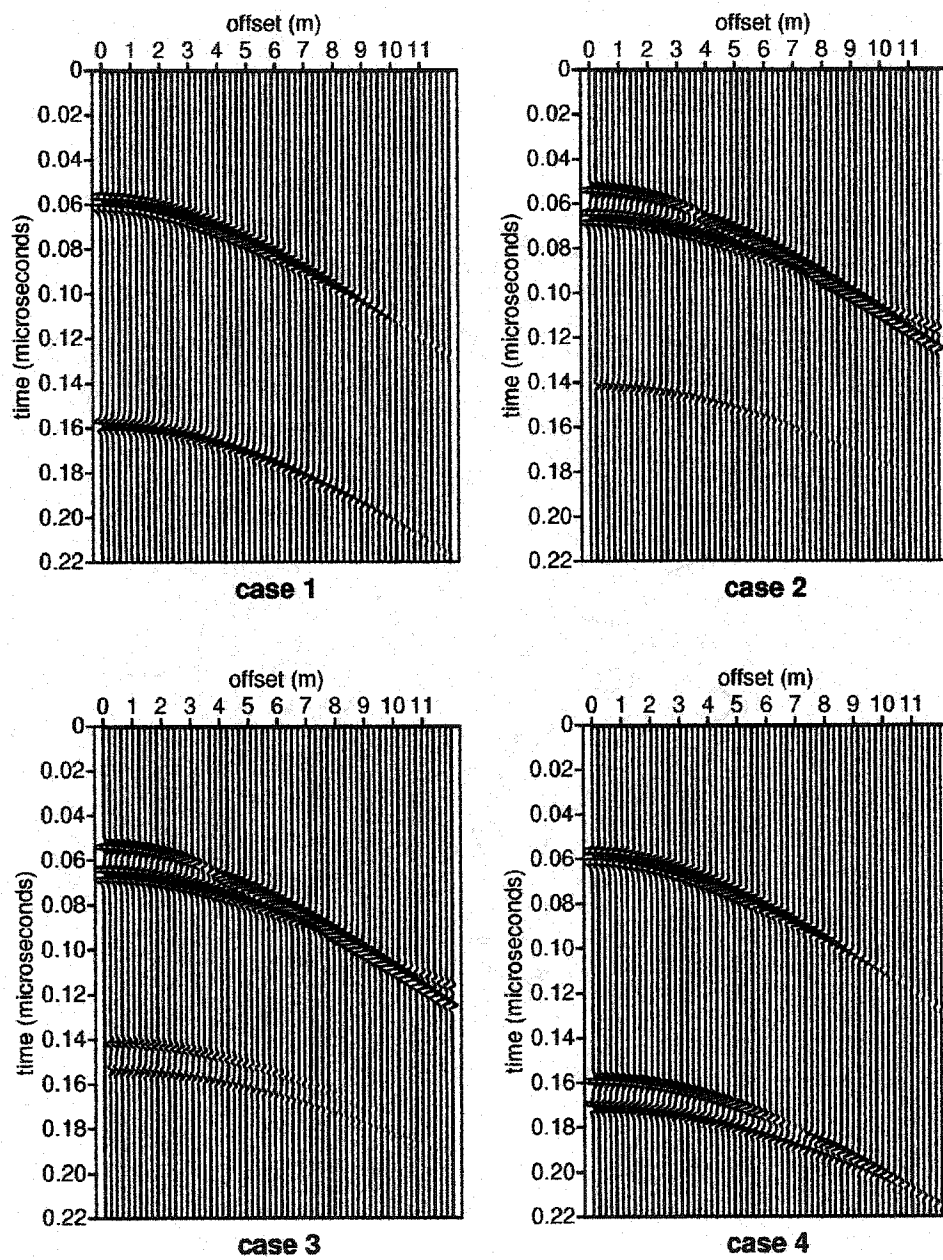


Figure 4.33: PP CMP's for the four cases indicated in Figure 4.28.

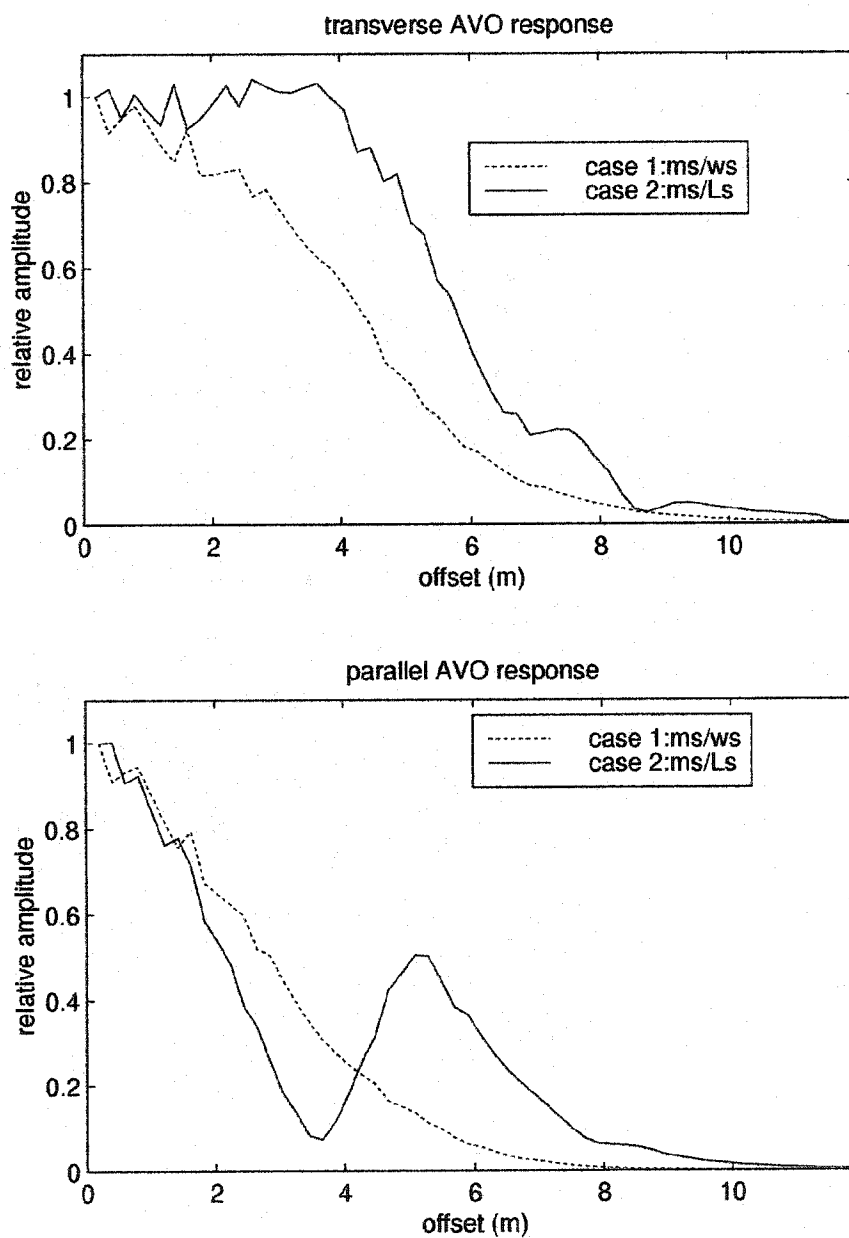


Figure 4.34: TP and PP AVO response for the upper reflectors indicated in Figure's 4.32 and 4.33.

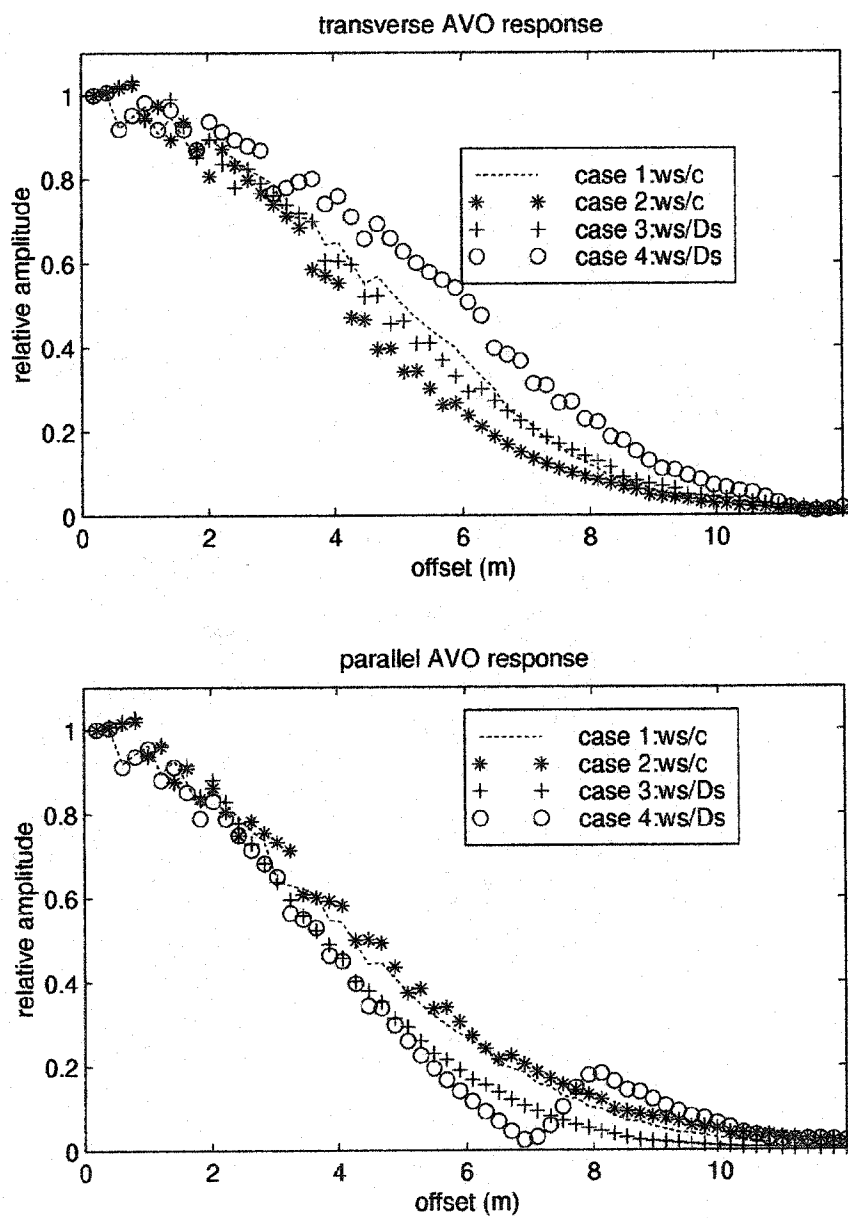


Figure 4.35: TP and PP AVO response for the lower reflectors indicated in Figure's 4.32 and 4.33.

AVO trend of the water sand and DNAPL sand reflections (Figure 4.35). I first compare the ws/Ds and ws/c reflections when the LNAPL is present (cases 2&3). In the TP case, the variation in the amplitude curves is subtle and would likely be difficult to detect in field data. In the PP case, the amplitude for the ws/Ds reflection decreases more sharply than that for the ws/c reflection, but the difference again is relatively subtle. θ_B (19°) is at an offset of 10 m (Figure 4.31) at which point the amplitude has decayed to nearly zero and we cannot clearly observe the increase in amplitude or 180° phase shift within the spread length. When the LNAPL layer is not present (cases 1&4), the TP and PP AVO responses for ws/c and ws/Ds vary significantly. The TP amplitude curve for ws/Ds exhibits roughly linear decay from 2 - 9 m whereas the curve for ws/c decays sharply from 2 - 6 m then decreases more gradually to near zero at 12 m. In the PP case, the curve for ws/Ds decays sharply to 0 at about 7 m. θ_B is clearly observed with a 180° phase change at 7 m and sharply increasing amplitude at greater offsets with a local maxima at about 8 m followed by gradual decay to nearly zero at the maximum offset. The large differences in the AVO curves when the LNAPL is not present could likely be detected and used to differentiate the clay reflection from the DNAPL reflection in field data.

It is interesting to note that the ws/Ds curves vary significantly depending on whether the LNAPL is present or not whereas the curves for ws/c show little dependence on the presence of the LNAPL. Examining the reflection coefficient curves (Figure 4.6), we see that the ws/c reflection coefficient is essentially constant for $\theta < 20^\circ$ so the AVO gradient is not significantly effected by small variations in θ . The reflection coefficient for the ws/Ds curve has a very large gradient from $15^\circ - 22^\circ$ so that small changes in θ have a

significant effect on the amplitude curve.

This example illustrates the need for large offset to depth ratios when trying to detect DNAPL's below the water table. It should be taken as a rule of thumb for survey design, that offsets of at least twice the depth to the target should be acquired when trying to detect contaminants below the water table. If there are no shallow targets, the near offsets can probably be skipped to save time. θ_B is an attribute that is easy to detect, even qualitatively, and for this reason I believe it is the most important attribute in GPR AVO studies. This raises the potential for rapid reconnaissance studies which could identify specific locations within a site for more detailed investigation.

CONCLUSIONS

Amplitude vs offset analysis has been used successfully in the oil and gas industry for direct detection of hydrocarbons. With careful consideration of the physics governing electromagnetic wave propagation these same concepts can be applied to GPR data analysis for direct detection of NAPL contaminants. I have developed a ray-based modeling routine, that accounts for frequency dependent material properties via Cole-Cole parameterization. The model can be used to accurately predict AVO response in field data, although the limitations of ray theory must be considered in the analysis.

Field data were acquired over containers filled with gasoline and water saturated sands. The AVA response in the field data matches the predicted response very well for all but the TP response from the gasoline saturated sand. Divergence from the predicted

amplitude may be due to a complex tuning effect within GC. A dramatic, predictable difference in PP AVO response is observed for the gasoline and water saturated sands, whereas the TP response is less robust. It is important to consider velocity gradients in the analysis, and while interpretation of the AVO response provides a valuable, qualitative reconnaissance tool, the more correct AVA analysis should be used for quantitative analysis. The experiment clearly demonstrates the potential for detecting contaminants based on the parallel polarized AVO response. In nature, the boundaries are more diffuse, however, if a sufficient contrast exists to produce a detectable reflection, AVO analysis can likely be used effectively.

The models presented in this paper were made of discrete layers with sharp material property boundaries. Additional field studies and wave equation based modeling are needed to determine how effectively the AVO response can be used as a contaminant indicator for thin layers with diffuse boundaries which would likely be encountered under in-situ conditions. The physical model presented in this paper indicates that θ_B is a robust AVO attribute when tuning effects are present, but further experiments are needed to determine the limits of the attribute.

Given the potential for a much larger permittivity contrast for a DNAPL pool below the saturated zone, I expect the greatest potential in GPR AVO studies is in the detection of DNAPL's. Of course, problems with signal attenuation across the saturated zone, overburden effects, and limited angles of incidence must be considered. We cannot expect AVO analysis to work well in every situation, but it does give us an additional tool, and will improve subsurface prediction when favorable conditions exist, as is the case for

any geophysical tool. When a reflection originating from the top of a NAPL rich zone can be resolved, AVO analysis is a valuable tool, and has significant potential in direct detection of contaminants.

The robust AVO information obtained from the PP configuration, and improved images acquired from the TP configuration leads to the question of which antenna configuration to use. The obvious conclusion is that if time allows, acquire data in both configurations, if time is limited and imaging is the primary goal of the survey, acquire the data in broadside configuration, if material property extraction is a priority and time is limited, acquire the data in end-fire configuration. Imaging can be accomplished by stacking only the near offset, or with wavelet processing to produce a consistent phase at all offsets along any given reflection.

It should be noted that for these studies, positive control through drilling is required for definitive interpretation, but AVO analysis can dramatically improve subsurface prediction with a minimal number of control points. Additionally, AVO analysis can lead to determination of relatively continuous 3-D distributions of contaminants or other targets of interest. This also raises the possibility of mapping contaminant migration through time or remotely monitoring remediation efforts (4-D studies).

Through theoretical analysis and modeling I have shown the potential for using AVO response as a contaminant indicator, and have demonstrated in field data that the predicted response can be detected. I believe that θ_B and the AVO gradient will be robust contaminant indicators, with gradient analysis valuable as a reconnaissance tool, and θ_B

providing precise estimates of K_2/K_1 . This technology has the potential to become a valuable tool in groundwater remediation studies.

CHAPTER 5. CASE STUDY: SEISMIC AVO ANALYSIS OF LOW VELOCITY, SHALLOW SANDS (<50 m)

INTRODUCTION

Compressional wave velocities (V_p) in shallow, unconsolidated, water-saturated sands, are typically greater than water velocity (1500 m/s). Brandt (1960) presented data showing that V_p decreases as porosity increases, and becomes lower than water velocity only at high porosities (~ 0.65). Typical sand aquifer porosities are on the order of 0.4 (Bedient et al., 1994), so $V_p < 1500$ m/s in saturated sand units should be considered anomalous.

Early theory for wave propagation through a porous medium (Gassman, 1951) indicated that a small gas fraction in the pore fluid reduces V_p by a factor of two or more, while shear velocity (V_s) remains relatively constant (Figure 5.1), resulting in a significant decrease in Poisson's ratio (σ). Several workers have verified this effect experimentally (Brandt, 1960; Domenico, 1977). A large contrast in Poisson's ratio results in anomalous amplitude behavior of the reflected signal with increasing angles of incidence, which is the basis of amplitude vs. offset (AVO) analysis (Castagna, 1993). AVO analysis can help differentiate strong reflections associated with the presence of gas from those associated purely with a change in lithology.

AVO analysis has been developed for hydrocarbon exploration, but is rarely employed at depths appropriate for groundwater or contaminate studies. In this paper, we

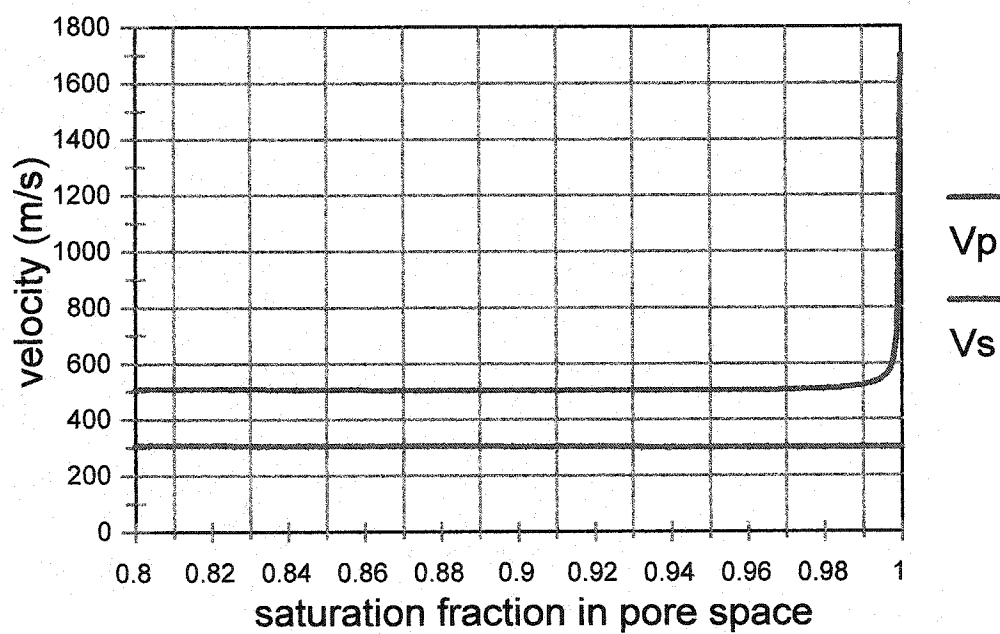


Figure 5.1: P and S velocities for a quartz sand as a function of water saturation. The curves are calculated with Gassman's equations assuming a depth of 10 m.

discuss a case where an AVO response was detected and used to constrain the cause of unexpectedly low V_p values in a 20 m thick sand unit buried at a depth of ~25 m. Our analysis indicates that the low velocity zone is due to partial gas saturation of the pore space.

DATA ACQUISITION

We acquired a 1050 m seismic reflection profile on Bolivar Peninsula, near Galveston, Texas (Figure 5.2). We used Siringan and Anderson's (1993) interpretation of borings acquired by the Army Corps of Engineers to constrain lithology and sedimentary facies (Figure 5.3).

Our objectives were to delineate the stratigraphy of the in-filled, incised valley of the Trinity River. We used a 60 channel seismograph, 28 Hz single geophones, 2 m source and receiver spacing, 30-30 split spread geometry, and a 20 lb. sledge hammer and plate energy source. The hammer and plate provided a good source for the site conditions, and good quality records were obtained with only four shots vertically stacked at each source location (Figure 5.4).

AVO analysis requires rigid control of data consistency (Castagna, 1993). The data were not acquired with the intention of AVO analysis, and measures could have been taken to improve consistency. Channel to channel gain variation (set automatically during acquisition) could not be adequately corrected during processing. It would be more appropriate in AVO studies to use a constant gain for all channels. Crew fatigue and

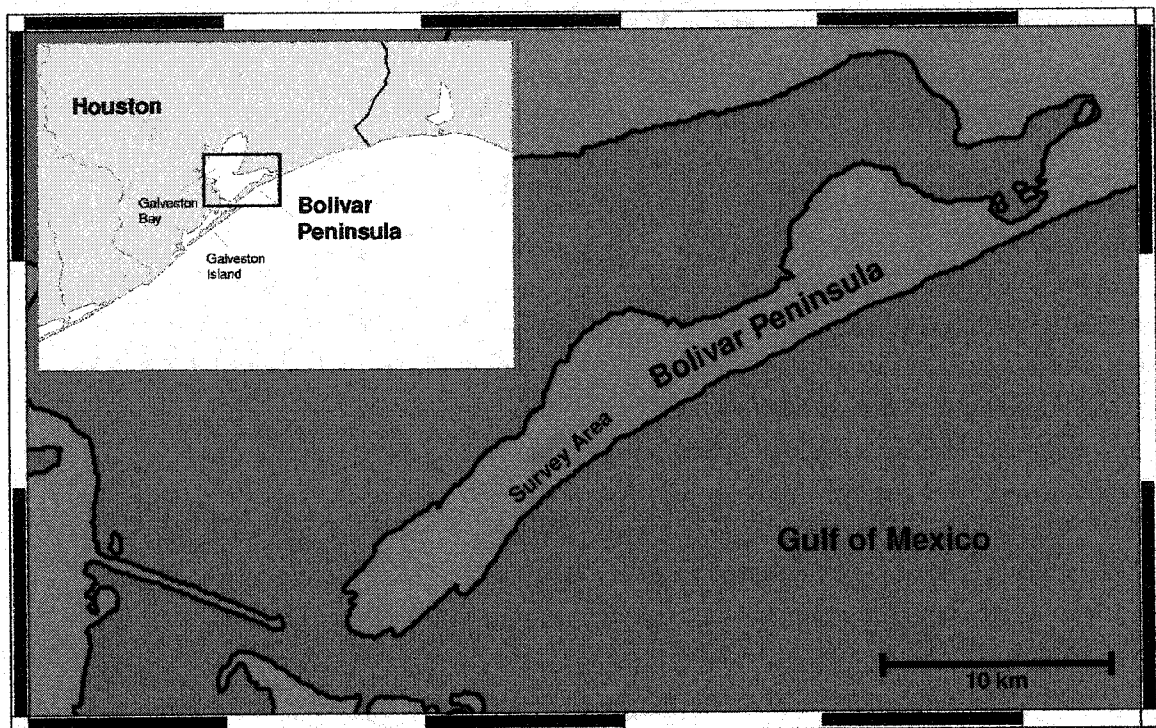


Figure 5.2: Location of field site.

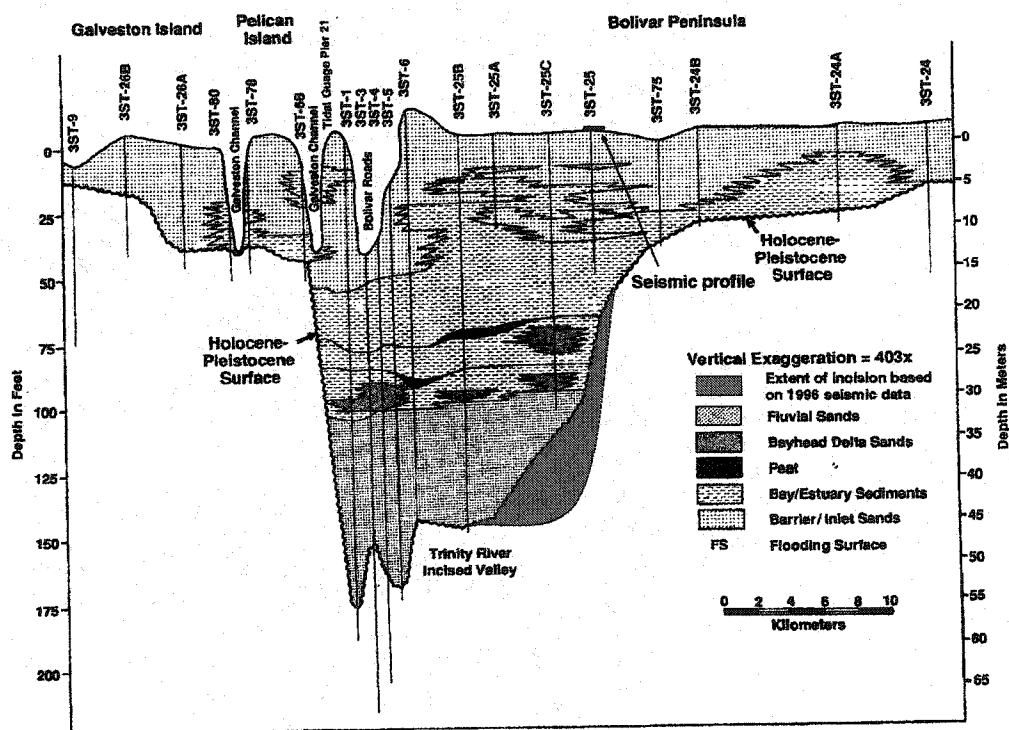


Figure 5.3: Cross section of the Trinity River incised valley. The sediments represent a typical valley fill sequence. (modified from Siringan and Anderson, 1993)

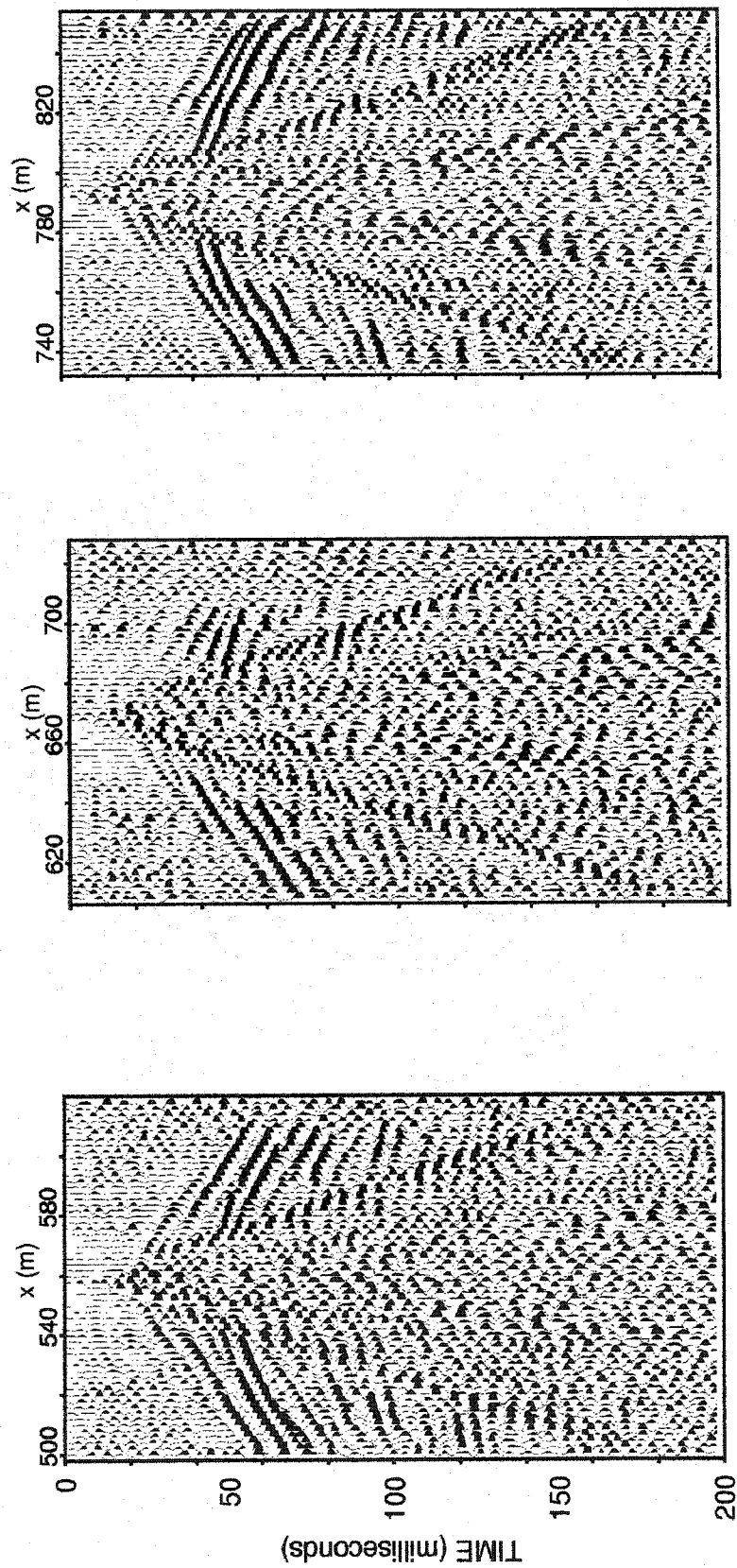


Figure 5.4: Three shots taken from the Bolivar Peninsula line. The top-of-sand reflector has a zero offset arrival time of around 40 -50 ms. Variation along this reflector is obvious in the shot gathers.

different source operators contributed to source inconsistencies. An operator-independent source, such as an automated, accelerated weight drop would be more appropriate for an AVO study. Nonetheless, the data were of sufficient quality to detect an AVO response, and one segment was of sufficient quality to allow a more quantitative AVO gradient analysis.

DATA PROCESSING AND INTERPRETATION

For CMP processing we used a relatively standard processing flow that included spiking deconvolution, spherical spreading and exponential gain corrections, ζ -p trace interpolation, F-K filtering, and residual statics. Dip-moveout was included to improve velocity estimates in areas of dipping reflectors. The processing flow resulted in a high quality stacked profile (Figure 5.5).

Major lithologic boundaries were clearly imaged, and internal stratigraphy within each major unit of the valley fill, up to the base of the barrier, was resolved to about 3 m, with a dominant frequency in the filtered data of about 120 Hz. The most notable feature of the profile is a continuous high-amplitude reflection showing significant topographic relief. The reflection varies from 30 ms to 50 ms across the profile, corresponding to the top of a fluvial sand package at depths ranging from 18 m to 30 m. The bright reflection delineates the top of a low velocity zone (Figure 5.5) with a base that corresponds to a reflection at 90 ms. The reflection at 90 ms is consistent with the base of fluvial incision at a depth of about 50 m.

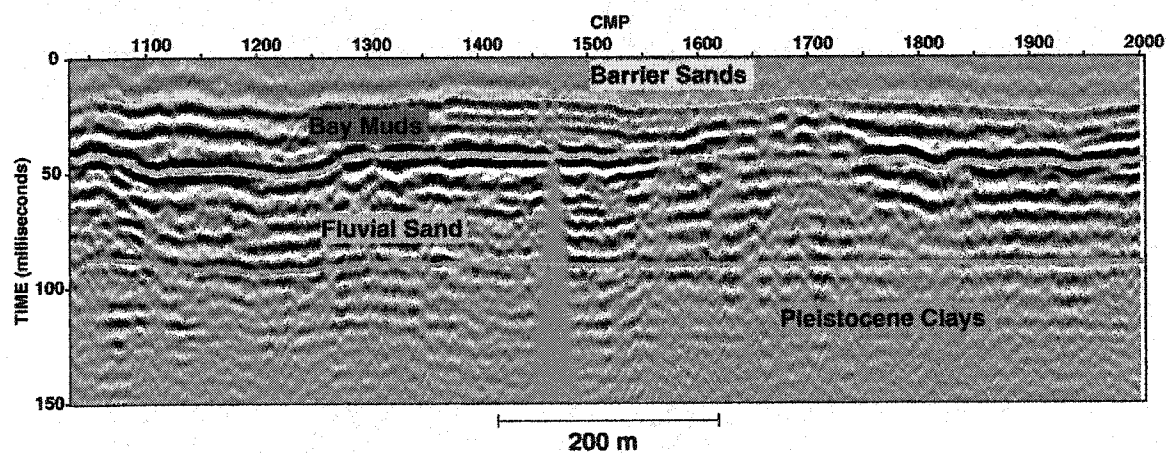


Figure 5.5: Interpreted seismic profile indicting primary unit boundaries. Compare to Figure 5.3. (The data showing the lateral boundary of the incised valley are not included in this study)

Interval velocities derived by smoothed gradient inversion of stacking velocities, range from 900 m/s to 1400 m/s just below the top of sand reflection. This is significantly lower than water velocity and warrants further investigation. Stacking velocities are sometimes unreliable indicators of true interval velocities, and we want to verify the presence of a low velocity zone with an independent method. We use ray tracing with travel time inversion (Zelt and Smith, 1992) to invert for a velocity field based on travel time picks of refractions and reflections from seven shot gathers along the line (Figure 5.6). Ray tracing through the resulting velocity field matches all travel time picks to less than a 1.5 ms RMS misfit. The velocity field corresponds well to interval velocities derived from NMO velocity analysis, including the low velocity zone (Figure 5.7). Velocities in the fluvial sand unit, derived from travel time inversion, range from 920 m/s to 1180 m/s at the top, and from 1120 m/s to 1380 m/s at the base. We consider velocities from the inversion more precise, and use these in the analysis that follows.

AVO ANALYSIS

We suspect that the low values of V_p are caused by the presence of a small amount of biogenic gas trapped in the pore space of the sand, and confined by the overlying bay muds. We first calculate the velocities that could be expected with partial gas saturation (0-10%) for a "typical" sand, with porosities from 0.35 to 0.45, using Gassman's (1951) equations for wave propagation through a porous medium. Castagna et.al. (1993) present the equations in a suitable form for this calculation. We assume a fully water saturated

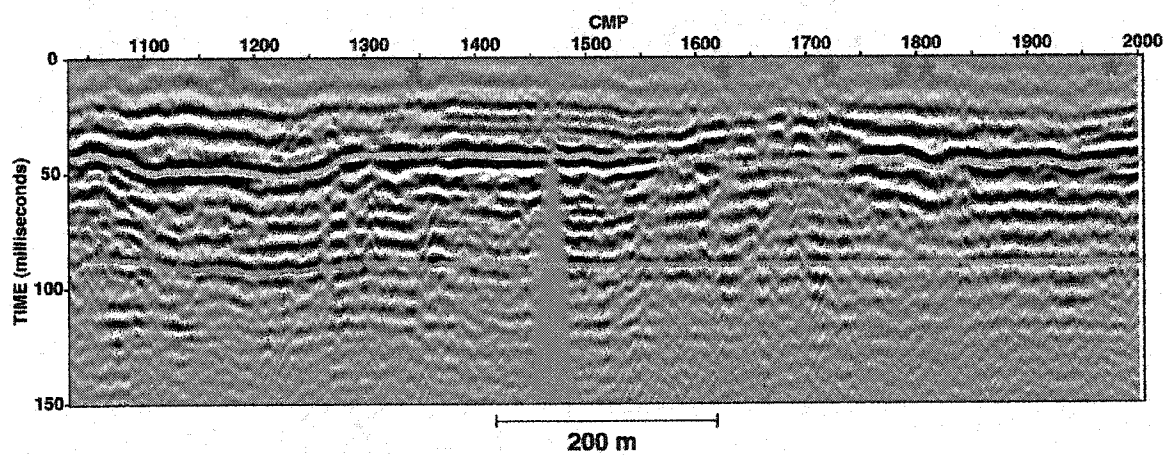


Figure 5.6: Shot point locations used for travel time inversion are shown with red asterisks.

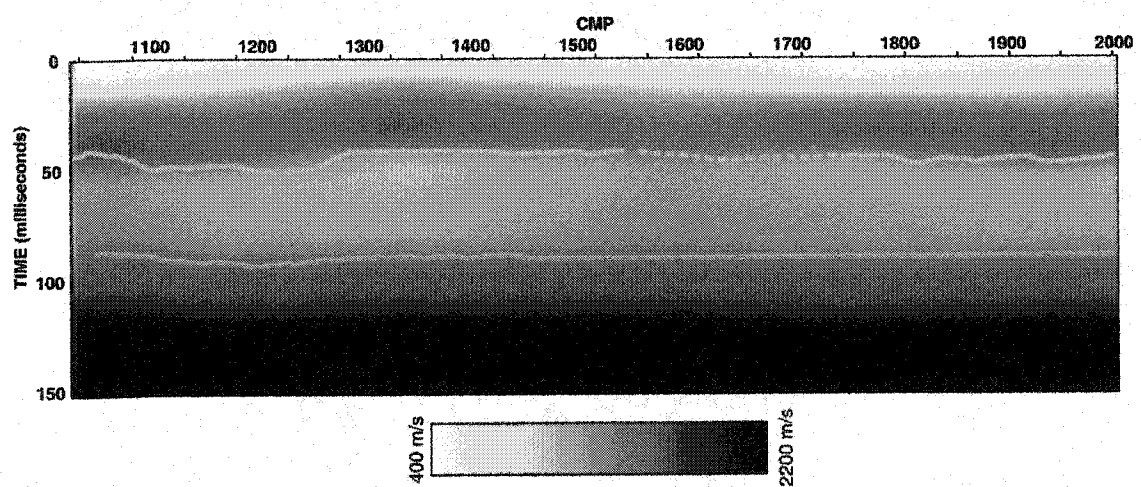


Figure 5.7: Velocity field derived from travel time inversion.

sand V_p of 2000 m/s and $V_s = 500$ m/s (Lankston, 1990). We also assume that the sand grains are comprised of quartz, and that any gas present is pure methane. We find that for partial gas saturation greater than 1%, V_p ranges from 930 m/s to 1300 m/s depending on porosity, and remains relatively constant with increasing gas saturation. This is roughly the same range as the velocities derived for the low velocity zone. Our result verifies that the low measured velocities are consistent with a “typical” sand with partial gas saturation.

Next, we use Aki & Richards (1980) matrix formulation of the Knott-Zoeppritz equations to calculate the variation of V_p reflection coefficients (R_{pp}) with increasing angle of incidence for a P-wave propagating through the overlying bay muds (medium 1) incident on the top of the low velocity sand (medium 2). These equations require six input parameters (V_{p1} , V_{p2} , V_{s1} , V_{s2} , r_1 , and r_2) of which we have only determined two; V_{p1} and V_{p2} . We assume a constant density of 2 g/cm³. A shear velocity of 400 m/s is assumed for the bay muds. We calculate R_{pp} vs. angle of incidence for two cases which correspond to either a low V_p related purely to a lithologic change ($s_2=0.47$) or to partial gas saturation of the sand ($s_2=0.31$) (Table 5.1).

Table 5.1. Parameters used for calculating R_{pp} vs. angle of incidence.

	V_{p1}	V_{s1}	σ_1	V_{p2}	V_{s2}	σ_2	Corresponding CMP	Assumption
case 1	1700 m/s	400 m/s	0.47	950 m/s	500 m/s	0.31	1150	partial gas
case 2	1700 m/s	400 m/s	0.47	950 m/s	250 m/s	0.47	1150	no gas

We find that for these conditions, R_{pp} becomes increasingly negative with

increasing angle of incidence, resulting in an increase in the absolute amplitude (Figure 5.8). The effect is quite significant regardless of gas saturation, however it is more pronounced with gas present in the pore space.

Under these conditions a significant AVO response should be observed regardless of the level of gas saturation. We want to determine if this response can be detected in our dataset. AVO analysis requires special processing considerations, to properly compare trace to trace amplitudes. Castagna (1993) summarized processing flows reported by several authors. In this case, we use processing steps similar to those we described for CMP processing, with the exception that F-K filtering, t-p trace interpolation, and DMO were excluded. Additionally, trace balancing over a window equal to the trace length was applied. This most closely follows the processing steps suggested by Ostrander (1984), and is acceptable for comparing relative amplitudes.

For the analysis, we first compute CMP supergathers in which groups of 5 CMP's and 8 m offset bins are vertically stacked, as recommended by Ostrander (1984). To detect AVO anomalies, we compute the absolute value of the zero-offset reflection coefficient multiplied by the absolute value of the AVO gradient (Castagna, 1993). One trace is computed for each input CMP supergather, and the resulting traces are plotted (Figure 5.9). We will refer to this plot as an ITG (Intercept Times Gradient) display. In the ITG display, a strong zero-offset reflection, having an increasing absolute amplitude with offset, appears as a high, while decreasing absolute amplitude with offset appears as a low.

The ITG display (Figure 5.9) shows an increase in absolute amplitude with offset

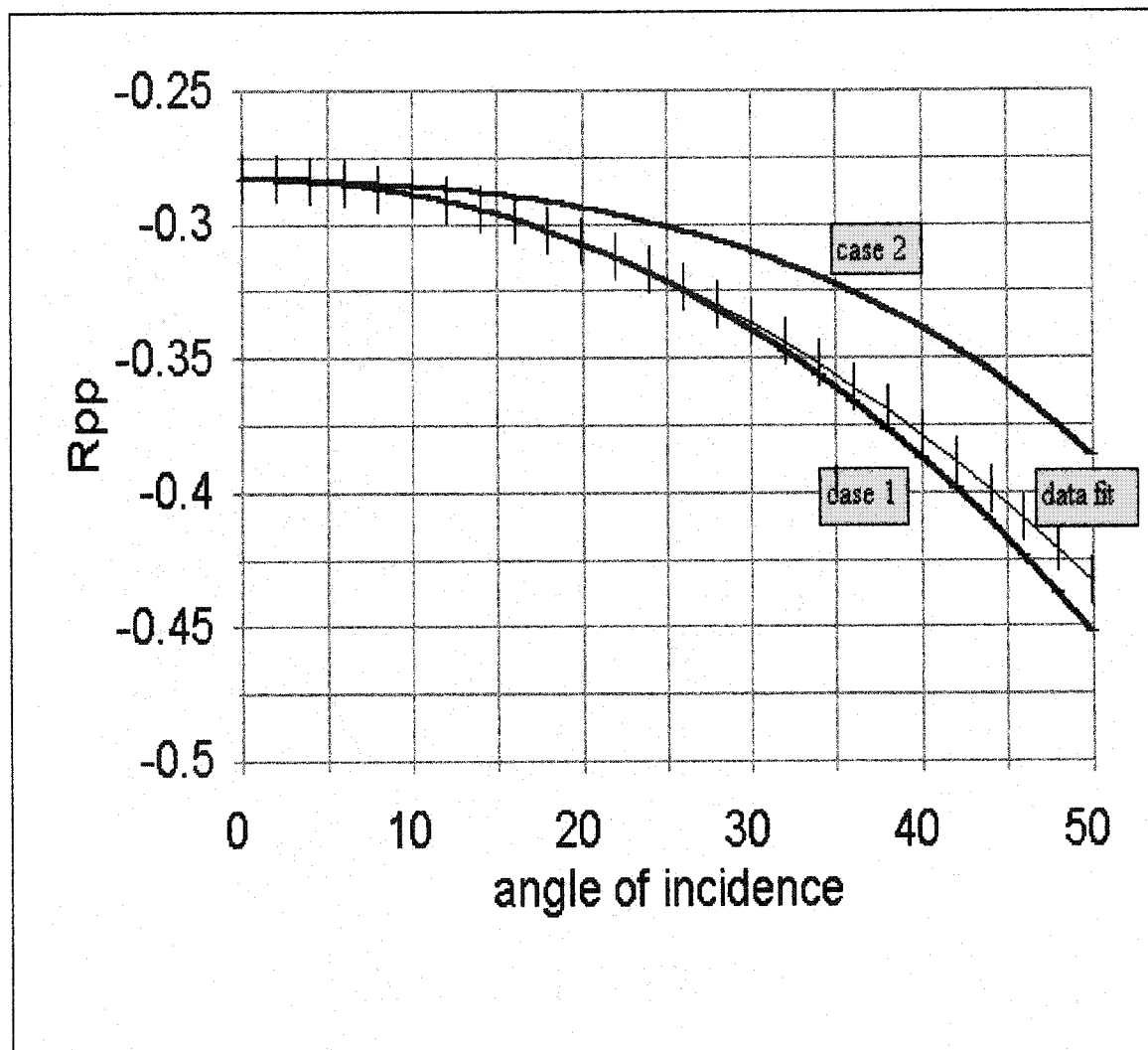


Figure 5.8: Expected and measured AVO response for velocity structure at CMP 1150 for case 1) partial gas saturation, and case 2) no gas present. The measured AVO gradient approaches the curve for partial gas saturation.

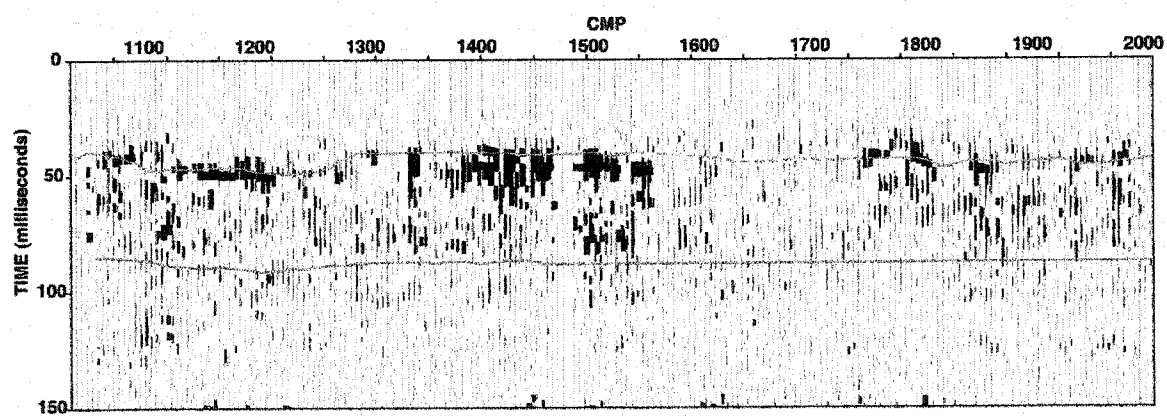


Figure 5.9: ITG display showing the increase in absolute amplitude associated with the top and base of the fluvial sand unit.

that corresponds very well to the top of the sand, as expected. An increase in amplitude with offset is also associated with the base of sand reflection, but is weaker and less consistent across the profile. The obvious lack of AVO response between CMP's 1600 and 1800 is associated with what is interpreted as the lobe of a bayhead delta. Delta sediments are more heterogeneous than the purely fluvial sands they overlie, due to cut and fill erosion, and interbedding of sands and bay muds. Changes in waveform resulting from this increased heterogeneity could account for our inability to detect an AVO response. Other short intermittent gaps in the AVO response from the top of sand reflector which may be related to variations in gas concentration or variable data quality along the profile.

The largest positive ITG deviation is observed between CMP's 1150 and 1200. This is also the area of highest raw data quality. Four CMP supergathers (1127, 1137, 1147, 1152) were chosen from this area for a more quantitative analysis. Increased amplitude with offset, associated with the top of sand reflection is evident (Figure 5.10). For the velocities measured along the profile, an equation of the form: $R_{pp} = a + bq^2$, is a good approximation to the Knott-Zoeppritz equations, where q is the angle of incidence. An equation of this form was fit to the relative amplitude data, and provided a relatively close fit with a standard error of the R_{pp} estimate of $dR_{pp} = 0.019$. We compared the AVO gradient to values calculated for case 1 and case 2 by adjusting the $q = 0$ intercept ($R_{pp}=a$) to equal the zero offset reflection coefficient, estimated from V_{p1} and V_{p2} . The curve is plotted in Figure 5.8. The AVO gradient more closely follows that calculated for a sand with partial gas saturation, than for a sand with total water saturation. This evidence is

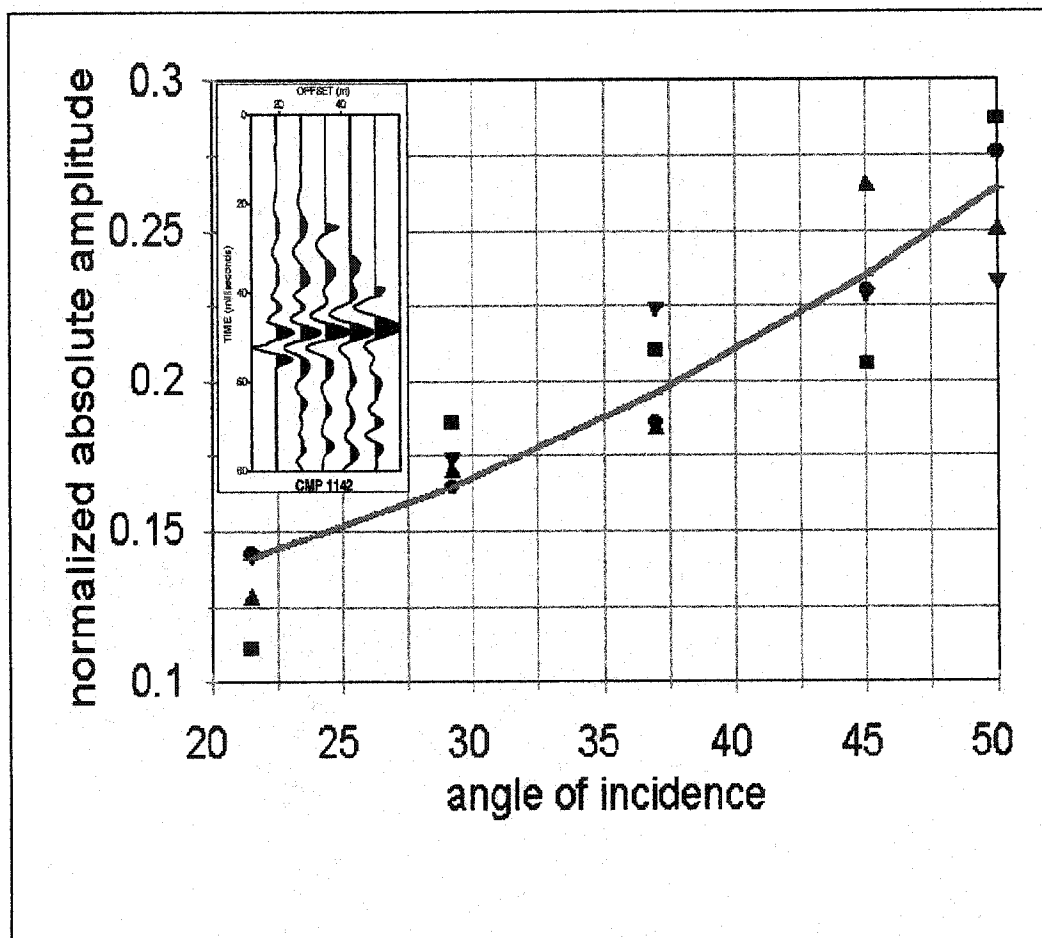


Figure 5.10: Absolute value of normalized amplitudes for the top of sand reflection with increasing angle of incidence, for CMP supergathers 1127, 1137, 1147, and 1157. The increase in amplitude is visibly evident in the representative gather between 40 ms and 55 ms. Angles of incidence were calculated by ray tracing through the velocity model.

not conclusive however, since only the gradient can be compared and several assumptions about the material properties had to be made for the calculation (i.e. shear velocities, and constant density).

CONCLUSIONS

We have shown that a predictable AVO response can be detected in shallow seismic reflection data. The observed values of V_p are consistent with a typical sand with partial gas saturation of the pore space. The measured AVO response is also consistent with partial gas saturation. Based on these results, we favor an interpretation of partial gas saturation, and speculate that the gas is likely biogenic methane. Variations in the AVO response are apparent along the profile and may be related to variations in stratigraphy, gas concentrations or data quality. The favorable results of this preliminary study are encouraging and future AVO research in the shallow environment is warranted.

CHAPTER 6. TIME-FREQUENCY ATTRIBUTE ANALYSIS

INTRODUCTION

Time-frequency (t-f) analysis is a valuable tool for evaluating frequency dependent seismic attributes such as attenuation, dispersion, etc. The windowed Fourier transform and the Wigner distribution are commonly used to obtain the t-f distribution. However, the windowed Fourier transform is time-resolution limited because the window length is fixed, and the Wigner distribution suffers from cross-term interference (Boudreaux-Bartels, 1985). To reduce unwanted cross term interference, signals are commonly decomposed into wavelet atoms that are used to construct a t-f distribution (Daubechies, 1991).

We present a method of calculating the t-f distribution, based on a matching pursuit algorithm (Mallat and Zhang, 1992), in which a band-limited seismic signal is decomposed into a linear combination of complex Ricker wavelets. In each iteration, the location, phase, amplitude, and dominant frequency of each significant event are estimated based on the envelope and phase functions of the signal. Each event is then represented by a complex Ricker wavelet and subtracted from the signal. Iterations are continued until the residual energy of the trace is below a specified threshold value.

We then construct 2D, t-f atoms by mapping the complex spectrum of each complex Ricker wavelet to the t-f plane using an adaptive Gaussian window function. The t-f distribution is then the 2D amplitude spectra of a linear summation of the complex t-f

atoms. This method provides a more accurate spectral representation than summation of the auto-contribution of each wavelet to the Wigner distribution, and avoids unwanted cross-term interference. Our distribution can be shown to be related to the Wigner distribution. We present the relationship of our t-f distribution to the Wigner distribution of both the real and analytic trace.

It is well known that hydrocarbon bearing zones can strongly attenuate the seismic signal, and if the attenuation can be quantified, this information can potentially be used as a direct hydrocarbon indicator (DHI). Based on our t-f distribution, we have developed method of estimating attenuation from seismic reflection data using a spectral ratio method. Effects other than intrinsic attenuation, such as the presence of thin beds, can lead to frequency dependent losses, and an *apparent* attenuation. With this in mind, we consider our attenuation estimate the apparent or relative attenuation and refer to it as the attenuation attribute. We are investigating the potential for using anomalous values of the attenuation attribute as a DHI.

Propagating electromagnetic waves are also subject to frequency dependent attenuation which depends primarily on conductivity. Typically, over the bandwidth of a ground-penetrating-radar (GPR) pulse, the attenuation can be approximated with a frequency independent quality factor (Q), analogous to propagating acoustic waves. Therefore, attenuation analysis has potentially valuable application in GPR studies, and our attenuation estimation algorithm can be applied directly to GPR data. One particularly important application is direct detection of non-aqueous phase liquid (NAPL) contaminants in shallow aquifers. NAPL's typically have much lower conductivity than

water or earth materials, and therefore soils containing NAPL do not attenuate a propagating GPR signal as strongly as the surrounding formation (Powers and Olhoeft, 1995). By extracting an attenuation profile, we can identify zones of anomalously low attenuation as potential NAPL rich zones.

Initially we applied the attenuation attribute algorithm to post-stack data, and found that the attribute is relatively sensitive to random noise. Additionally, the stacking process effects the spectrum of the data through NMO stretch, and the attenuation estimate can be adversely affected. In any case, it is desirable to use the spectral values of data with minimal manipulation. This leads directly to applying the attenuation algorithm to pre-stack data, with minimal pre-processing. The effects of random noise can be minimized by stacking the attenuation attribute across CMP gathers, and the spectral values are more representative of material properties. We present several examples, both field and synthetic, of the wavelet decomposition, t-f distribution, and attenuation attribute estimation. Our initial tests indicate that pre-stack estimation of the attenuation attribute, followed by NMO and stacking, is a more robust analysis.

THE WAVELET TRANSFORM AND A NEW TIME-FREQUENCY REPRESENTATION

It is well known that earth materials produce frequency dependent attenuation of both propagating seismic and GPR signals. The focus of this study is to determine if the attenuation can be quantified consistently, and used to identify material properties. Since

intrinsic attenuation is frequency dependent, it is valuable to analyze spectral variation of the seismic signal through time, which is the basis of time-frequency (t-f) analysis.

Traditional methods of t-f analysis are the windowed Fourier transform (WFT) and the Wigner Distribution (WD) (Boudreaux-Bartels, 1985). The WFT provides a good spectral representation, but has poor time localization properties. The WD, which is the Fourier transform of the instantaneous autocorrelation, has both time and frequency localization, but suffers from cross-term interference. Wavelet methods have good localization in both time and frequency domains, and do not suffer from cross term interference associated with the WD. This paper will focus on a new wavelet transform and t-f distribution, developed for applications in seismic and GPR attenuation analysis.

The continuous wavelet transform is given by (Daubechies, 1991)

$$WT[S(t)](a,b)=|a|^{-1/2}\int S(t)\psi\left(\frac{t-b}{a}\right)dt \quad 6.1$$

Where ψ is the wavelet basis. The wavelet basis is a function that is well defined in both the time and frequency domains, and is parameterized by b , which is the translation along the time axis, and a , which is the scale and is related to the dominant frequency of the wavelet. The wavelet must satisfy the condition:

$$\int \psi(t)dt=0 \quad 6.2$$

The t-f domain is non-unique, and therefore it is best to choose a wavelet basis that is a good representation of the signal of interest. The second derivative of a Gaussian, or

Ricker wavelet satisfies Equation 6.2 and is given by

$$R(t) = \frac{\delta^2 e^{-\lambda t^2}}{\delta t^2} = 2\lambda e^{-\lambda(t-t_0)^2} (2\lambda(t-t_0)^2 - 1) \quad 6.3$$

We see that $b=t_0$, and $a=1/\lambda$, where $\lambda = \pi^2 f_0^2$. The Ricker wavelet basis is useful in seismic signal analysis because it is discrete, and either the Ricker wavelet, or a phase variant form, provides a good representation of many seismic signals (Dobrin and Savit, 1988). We obtain a semi-continuous wavelet transform using a matching pursuit, or wavelet matching algorithm similar to that developed by Mallat and Zhang (1992). We use the term “semi-continuous” since the signal is necessarily discretized in time, with a sampling rate Δt_s , but the transform is continuous in the frequency domain. We assume that the seismic signal, $S(t)$, is band-limited, and can be represented by linear summation of wavelet atoms, which are specified by four parameters

$$S(t) = \sum R_i(A, \omega, t_0, \phi) \quad (4)$$

where A is the amplitude, ω is the dominant frequency, t_0 is the time dilation, and ϕ is the phase angle. The amplitude and time of each significant seismic event is estimated by locating the local maxima in the envelope function (absolute value of the complex trace). The phase angle and dominant frequency are then estimated at t_0 from the phase function and its derivative, respectively. The wavelet atom is then subtracted from the original trace. This process is continued until the energy of the residue is lower than some specified threshold value (Figure 6.1).

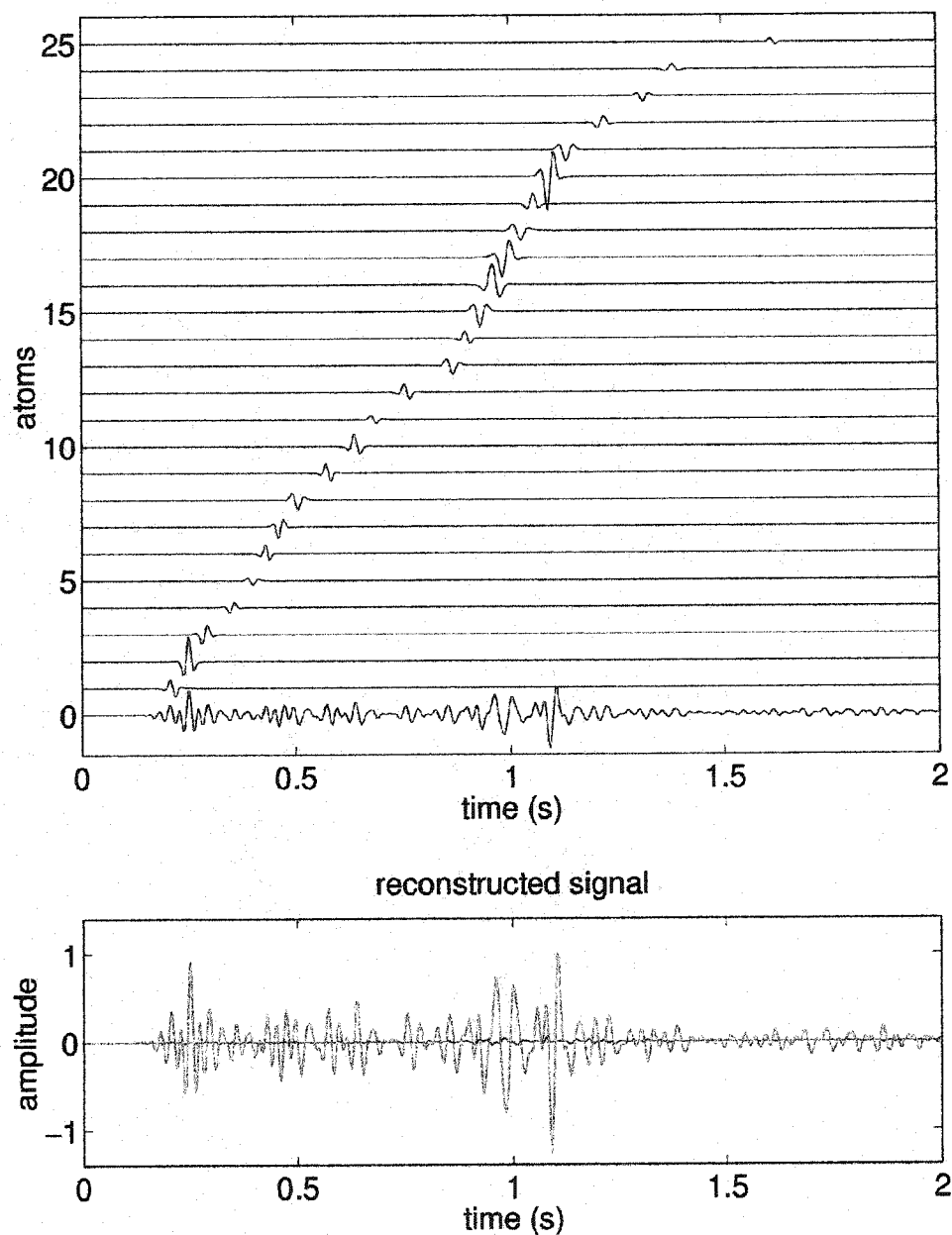


Figure 6.1: In the upper figure, a seismic trace is plotted along with the first 25 atoms of the decomposition. The reconstructed trace (green) is plotted with the residual (blue) in the lower figure. The energy of the residual, E_r , is less than $0.001 E_0$. The reconstructed trace is a linear summation of 96 wavelets which were extracted in three iterations.

The time extent of the Ricker wavelet is well defined by the Gaussian window function, $G(t)=\exp(-\lambda t^2)$. As we will show later, $G(t)$ also appears in the Wigner distribution. Two-dimensional, t-f atoms are constructed by mapping the complex Fourier spectra of each Ricker wavelet to the t-f plane using the windowing function $G(t)$. The t-f distribution (Figure 6.2), $TF(S)$, is then the linear summation of complex t-f atoms

$$TF(S) = \sum G_i(t) \tilde{F}(R_i) \quad 6.5$$

where

$$G_i(t) \tilde{F}(R_i) = K_i A_i e^{-\lambda_i(t-t_{0i})^2} \omega_i^2 e^{\frac{-\omega_i^2}{4\lambda_i}} e^{j\omega_i t_{0i} + \phi_i} \quad 6.6$$

where K is a normalization constant.

Since we preserve phase information through the mapping to the t-f plane, the spectra of a multi component signal is correctly reconstructed in the t-f domain and our distribution has the following properties

$$F(S) = \int TF(S) dt \quad 6.7$$

which leads to

$$PS(S) = \left(\int TF(S) dt \right)^* \left(\int TF(S) dt \right) \quad 6.8$$

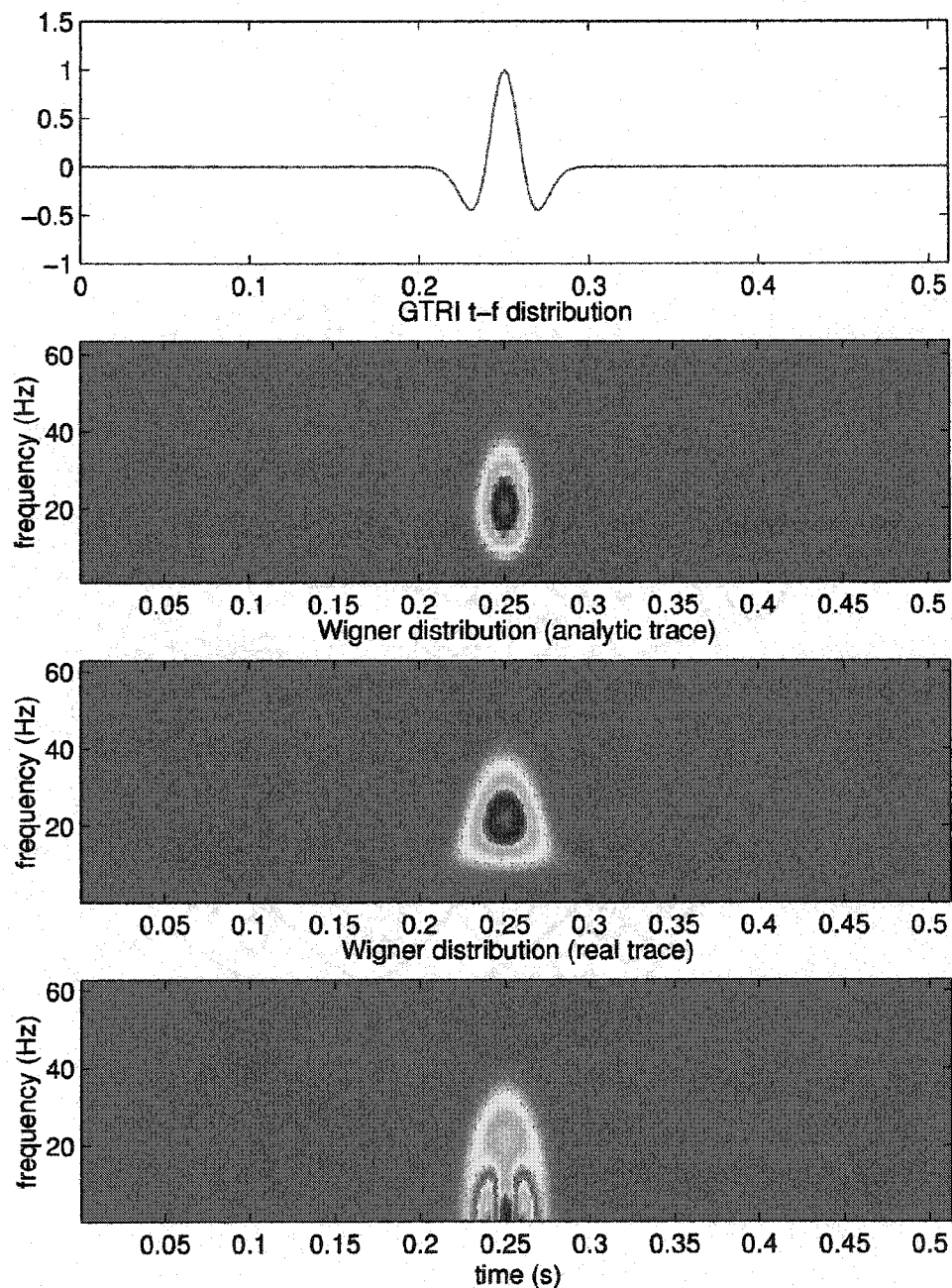


Figure 6.2: Different t-f representations of a 20 Hz Ricker wavelet. The WD of the analytic wavelet is similar to our t-f distribution. The WD of the real wavelet has a large DC component. Note that these are the absolute values of the distributions, and that the WD has negative terms for both the real and analytic cases.

Where $PS(S)$ is the power spectra of the signal (S) and $F(S)$ is the Fourier transform of S . It is useful to look at the phase independent form ($|TF|^2$) of our distribution for comparison to the WD, since the WD is always real valued and proportional to the power spectra of the signal. We first consider a single Ricker wavelet, with t-f distribution given by

$$|TF|^2 = K e^{-2\lambda(t-t_0)^2} e^{-\frac{\omega^2}{2\lambda}} \omega^4 \quad 6.9$$

Which is directly proportional to the power spectra. The WD for $R(t-t_0)$ is given by (Appendix A):

$$WD(S) = F \left[R(t + \frac{\tau}{2}) R(t - \frac{\tau}{2}) \right] = K_w e^{-2\lambda(t-t_0)^2} e^{-\frac{\omega^2}{2\lambda}} \left[\frac{\omega^4}{4\lambda^2} + \left(2(t-t_0)^2 - \frac{1}{2\lambda} \right) \omega^2 + 4\lambda^2(t-t_0)^4 - 6\lambda(t-t_0)^2 + 3/4 \right] \quad 6.10$$

We see that our distribution is directly proportional to the ω^4 term in the WD. As mentioned earlier, we see that the WD contains the window $G_1^2(t)$. It is interesting to note that the WD has a significant DC component ($WD \neq 0 @ \omega=0$) (Figure 6.2). This is surprising since $F(R(t))=0$ at $\omega=0$. The DC component arises from the instantaneous autocorrelation since $R(t)$ is symmetric about $t=t_0$. For attenuation analysis, we need a TF representation that is locally proportional to the power spectra of the seismic wavelet. The DC component makes $WD[R(t)]$ undesirable for attenuation analysis. If we take the WD of the complex representation of $R(t)$, we find that the DC terms are suppressed and the WD of the analytic signal is directly proportional to $|TF|^2 @ t=t_0$ (Figure 6.3).

If we consider a multi-component signal, we find that the WD of the complex trace

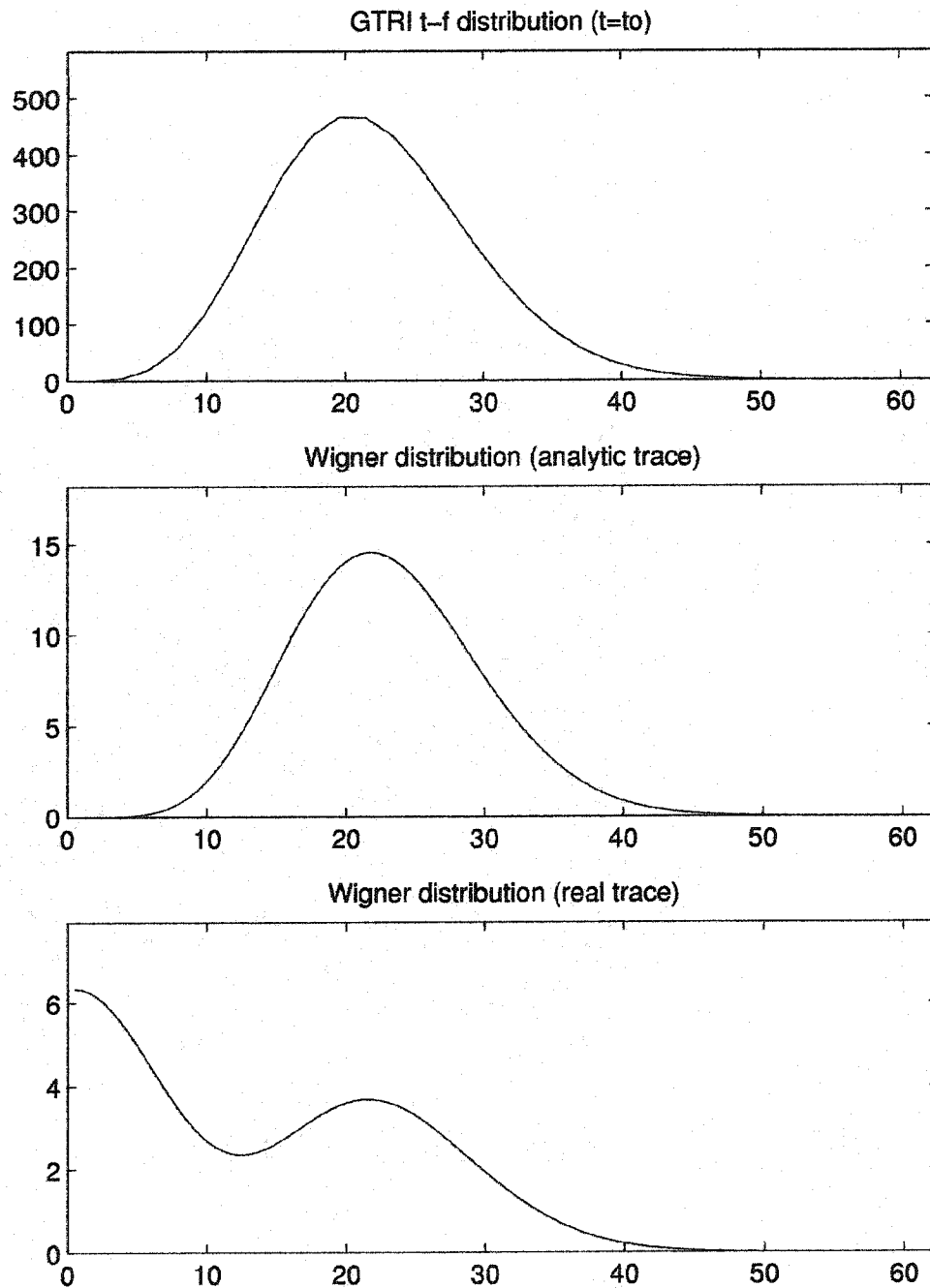


Figure 6.3: Cross sections through the t-f distributions at $t=t_0$. In this comparison, we are interested in the shapes of the distributions, not the amplitude scaling. Horizontal labels are frequencies in Hz. The WD of the analytic trace has essentially the same shape as our distribution. The WD of the real trace has a large DC component, but is similar at high frequencies where the ω^4 term dominates.

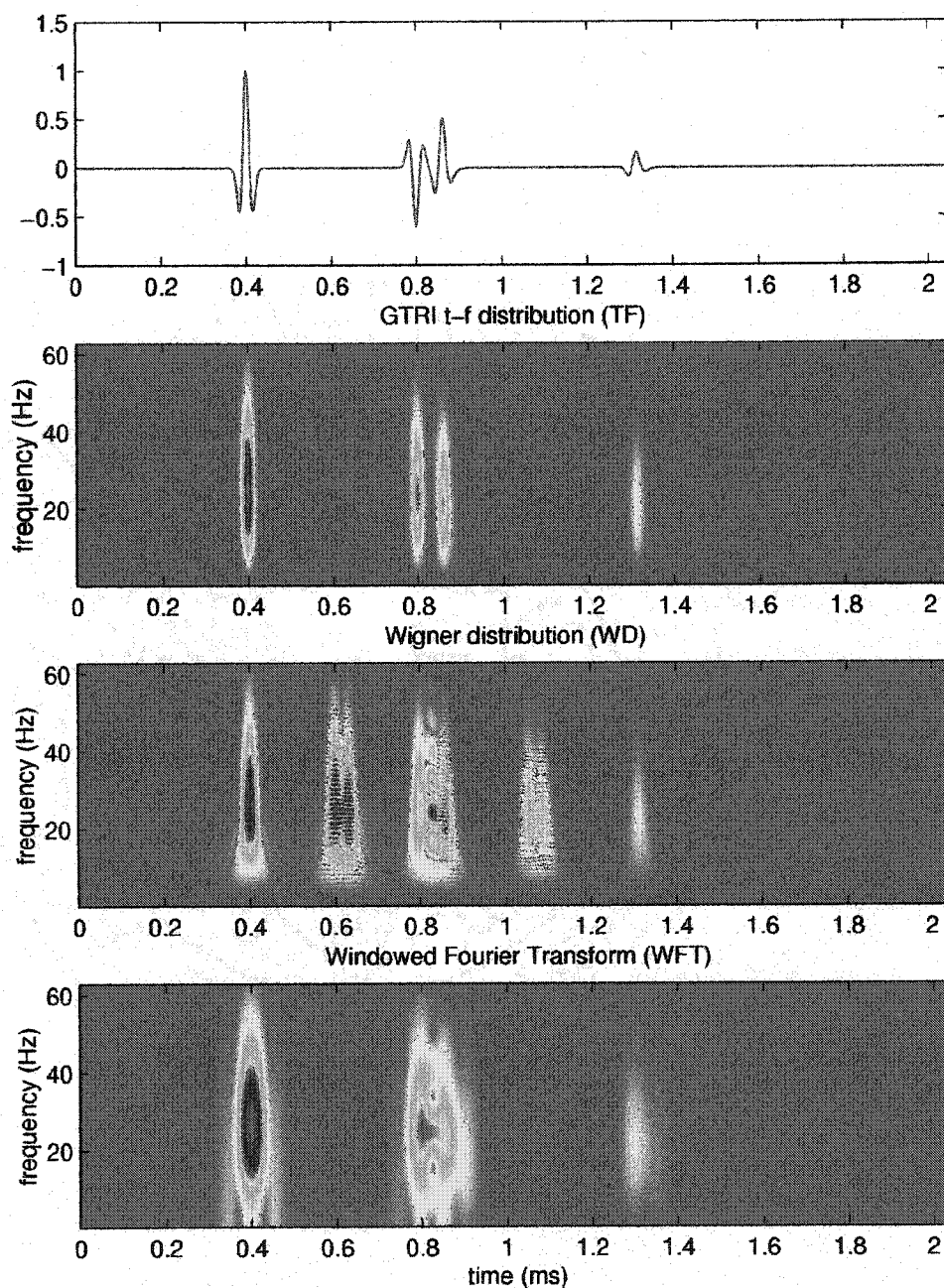


Figure 6.4: A multi-component signal, and t-f representations via 1) our distribution, TF; 2) the WD of the analytic trace; and 3) the WFT. The WD has severe cross-term interference which has amplitudes near that of the desired signal. The WFT has no cross-term problems, but provides relatively poor time resolution.

produces strong cross term interference which also makes this distribution undesirable for attenuation analysis (Figure 6.4). The windowed Fourier transform does not suffer from cross-term interference, but has poor time resolution properties (Figure 6.4). Our distribution, TF, has good time localization properties, and no cross term interference. Additionally, $|TF|$ is locally proportional to the amplitude spectra of the zero-phase wavelet and $|TF|^2$ is locally proportional to the power spectra. We conclude that TF is well suited to time-frequency analysis of seismic signals.

MODELING THE ATTENUATION AND DISPERSION EFFECTS IN 2-D

It can be shown that, given a frequency independent $Q(z)$, in a layered earth model, the amplitude spectra varies according to the following equation (Appendix B)

$$A_n(f) = A_0(f) e^{\frac{-\pi f t_n}{Q_{eff_n}}} K_n \quad (11)$$

where f is the frequency, K_n is a constant at any specified time which accounts for geometric spreading, transmission, and reflection losses (this of course assumes that these parameters are frequency independent), A_0 is the source spectrum or reference spectrum, and t_n is the travelttime to the base of the layer of interest. Q_{eff} is an effective Q value which accounts for the cumulate intrinsic attenuation of all layers above the time of interest, and is given by

$$\frac{1}{Q_{eff_n}} = \frac{\sum (\Delta t_i / Q_i)}{t_n} \quad 6.12$$

where Δt_i and Q_i are the interval traveltimes and Q for each layer, and t_n is the total traveltimes.

Aki and Richards (1980) showed that the dispersion effect due to attenuation can be estimated by the following equation

$$c(f) = c(f_{ref}) \left[1 + \frac{1}{\pi Q_{eff}} \ln \left(\frac{f}{f_{ref}} \right) \right] \quad 6.13$$

where c is the frequency dependent velocity, f is frequency, and f_{ref} is a specified reference frequency at which c is known.

Given the need to investigate attenuation analysis in the pre-stack domain, we have developed a 2-D visco-acoustic, ray based modeling code. We find it useful to use ray-based methods initially for this study since it is fast for simple models, and we can compute the exact waveform after propagation through our model, thereby minimizing numerical error that may be associated with finite difference or pseudo spectral methods. Ray based methodology is not valid for modeling frequency dependent effects related purely to geometry such as thin beds. In general, we assume that modeling will be accurate as long as the layer thickness is greater than one wavelength (Mukerji et al., 1993).

Travel time computation

For travel time computation, I use Zelt & Smiths ray tracing code (Zelt and Smith, 1992). The earth model is parameterized using discrete blocks of constant velocity, density, and Q . This allows for discrete lateral and vertical material property variation. The velocity within each block is specified as the phase velocity at the peak frequency of the source wavelet $[c(f_{ref})]$. Two-point ray tracing is performed from the source to receiver and the length of each straight ray segment is stored in a table. The length of each segment is assumed frequency independent, which is only approximate for a dispersive media. Spatial dispersion due to frequency dependent travel paths can be thought of as small perturbations along a single, frequency independent travel path and can safely be ignored in most cases .

Wavelet modeling

Several factors must be considered when modeling the amplitude, attenuation, and dispersion along a given travel path. These include source and receiver directivity, geometrical spreading, G , the reflection coefficient, R , transmission losses, T , attenuation, Q , and dispersion. I calculate the amplitude and phase shift of each frequency component in the frequency domain. The wavelet for ray n , $S_n(t)$, is then the real part of the inverse Fourier transform, given by

$$S_n(t) = \text{Re} \left[\text{IFFT} \left(S_n(\omega) = R_n(\theta_n) G_n \prod [T_i(\theta_i) e^{i\omega \Delta t_i(\omega)}] A_n(\omega) \right) \right] \quad 6.14$$

where we have assumed spherical response for the source and receiver. R_n is the reflection coefficient at layer n , T_i is the transmission coefficient (up or downward traveling) at the i th layer, θ is the angle of incidence, G_n is the geometric spreading term, and A_n is calculated using Equation 6.11. The frequency dependent traveltime for each ray segment, $\Delta t_i(\omega)$, is calculated from Equation 6.13.

The source pulse is a causal Ricker wavelet, and is parameterized by specifying the dominant frequency and time delay, t_0 . Reflection and transmission coefficients are calculated according to the Knott-Zoepritz equations (Aki and Richards, 1980), and are allowed to be complex so that the phase of wide-angle reflections is properly computed.

CALCULATING THE ATTENUATION ATTRIBUTE

The spectral ratio method is commonly used for estimating Q values in laboratory measurements or sonic logs, but can also be applied to seismic reflection data, given an accurate t - f distribution. It is an attractive method because, ideally, it allows one to separate frequency dependent attenuation due to viscous effects (intrinsic attenuation) from attenuation due to reflection and transmission losses, spherical spreading and source and receiver effects, which are assumed frequency independent. Taking the natural log of both sides of Equation 6.11, we derive the following equation:

$$\ln \frac{A_0(f)}{A_n(f)} = \frac{\pi t_n}{Q_{eff_n}} f - \ln(K_n) \quad 6.15$$

Q_{eff} can then be estimated from the slope of a plot of $\ln(A_0/A_n)$ vs. f . Given Q_{eff} , the interval Q value can be estimated from the following equation (Appendix B)

$$\frac{1}{Q_n} = \left(\frac{t_n}{Q_{\text{eff}_n}} - \frac{t_{n-1}}{Q_{\text{eff}_{n-1}}} \right) \frac{1}{\Delta t_n} \quad 6.16$$

We see from Equation 6.16 that our estimate of $1/Q_n$ is most sensitive to small values of Q_{eff} or alternatively from Equation 6.12, that Q_{eff} is sensitive to small interval Q values. It is apparent from this observation that $1/Q_n$ is most sensitive to zones of high attenuation (low Q). As will be shown, this becomes a problem in GPR NAPL detection studies where we are primarily concerned with zones of low attenuation.

In field data, it is often difficult to estimate the source spectra and certain assumptions such as frequency independent reflection and transmission may not be valid. In this case, extracting the true Q value may be difficult, or even impossible. However, as with other attributes, we are searching for anomalies, and is not necessary to determine the absolute value. With this in mind, we will refer to $1/Q_n$ as the high attenuation attribute (HA), with the caveat that, in practice, we are calculating only a relative attenuation parameter.

Practical considerations

To extract Q_{eff} from field data we must first choose a reference spectrum $A_0(f)$. Ideally, we would always use the source spectrum, but this is not always trivial in field data. From Equation 6.15, we see that the spectrum of any wavelet along the trace will

produce the correct result. We typically choose the first clean event that is laterally coherent and is isolated in time. This may be the direct arrival, water bottom reflection, or a water table reflection in the case of shallow seismic studies. If the signal wavelet can be approximated by a synthetic wavelet such as the Ricker or Klauder wavelet, this will provide acceptable results. GPR data typically have a very consistent, high amplitude direct wave that can be isolated and used as the reference wavelet. However, this event typically contains a low frequency induction component that decays quickly. With the Sensor's and SoftwareTM system, we find that a Ricker source wavelet, with peak frequency corresponding to the dominant frequency of the antenna produces good results.

Secondly, we must choose which events to use for attenuation analysis. We cannot simply carry out the analysis at every time sample, since there will only be noise or no data at some locations, which would produce erroneous results. Thresholding is one method (i.e. every event with amplitude above a certain threshold are deemed significant and used in the analysis). But this method is quite sensitive to noise even in good quality data. We currently interpret significant events manually. A time gate is chosen that spans the event of interest. The maximum amplitude of the envelope function within this gate is specified as t_0 for the corresponding event. Choosing amplitudes from the envelope function avoids the problem of incorrect placement of t_0 due to phase rotation.

Estimating the attenuation attribute in synthetic and field data

Application to hydrocarbon exploration. We extracted t-f distributions of several representative traces from a seismic profile located over a known hydrocarbon deposit

(Figure 6.5). The data have been fully processed, including stacking, deconvolution, and migration. Comparing the t-f distribution along trace 10 (away from the known deposit) with the t-f distribution along trace 76 (Figure 6.6), we find that the t-f response does not meet our expectations. In fact the frequency content increases just below the bright reflector associated with the top of the hydrocarbon bearing zone. This could be due to geometric tuning of the signal, however, we know that the processing that has been applied has a significant effect on the spectral qualities of the data. Therefore, we do not think the post-stack t-f decomposition is very reliable, particularly with the heavy processing carried out prior to our receiving the data. This example illustrates the need for pre-stack t-f processing.

Figure 6.7 is a 2D attenuation model, superimposed on a 1-D velocity model with parameters listed in Table 6.1 (density is held constant).

Table 6.1. Parameters for velocity model.

<i>Layer #</i>	<i>v_p (m/s)</i>	<i>v_s (m/s)</i>	<i>thickness (m)</i>
1	1500	0	300
2	2000	1100	400
3	1600	1100	60
4	2200	1210	500
5	2500	1375	400

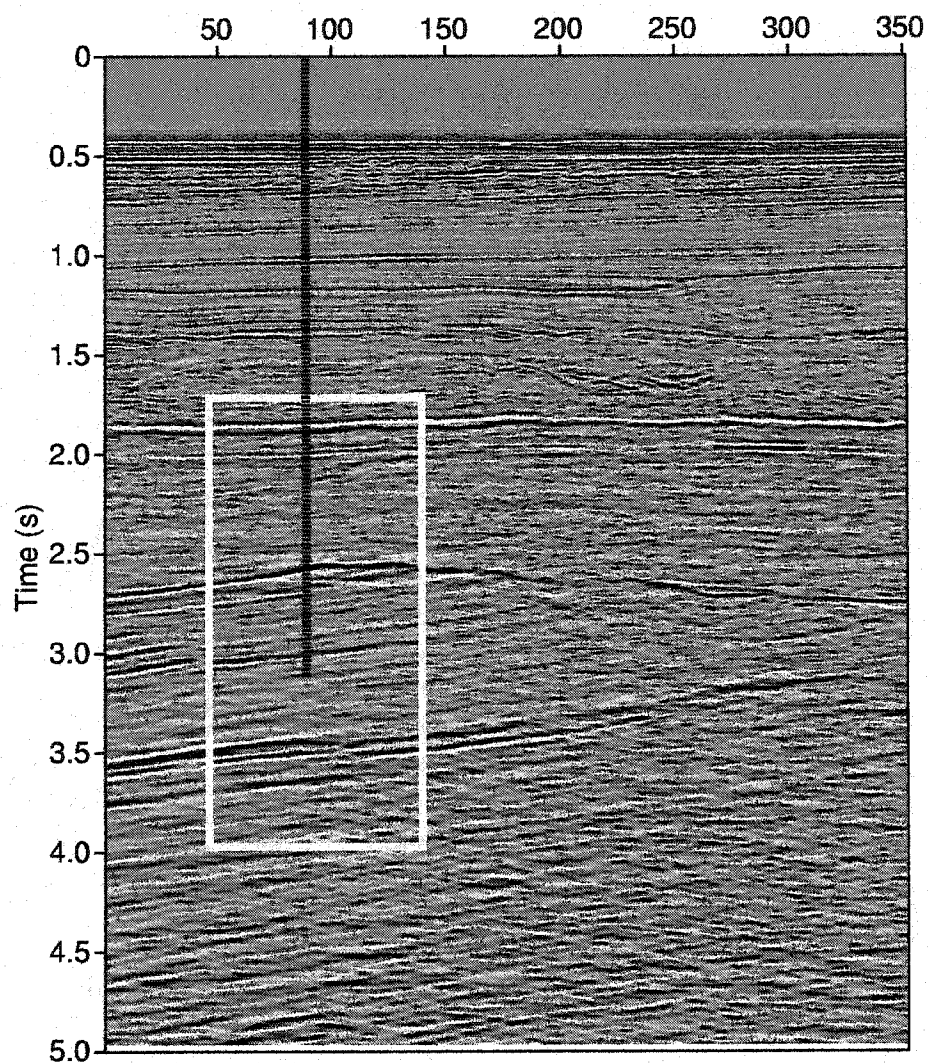


Figure 6.5: Seismic profile over a known hydrocarbon deposit. The well location is shown with a dashed line. The strong reflection at the high in the discontinuity is associated with hydrocarbon accumulation.

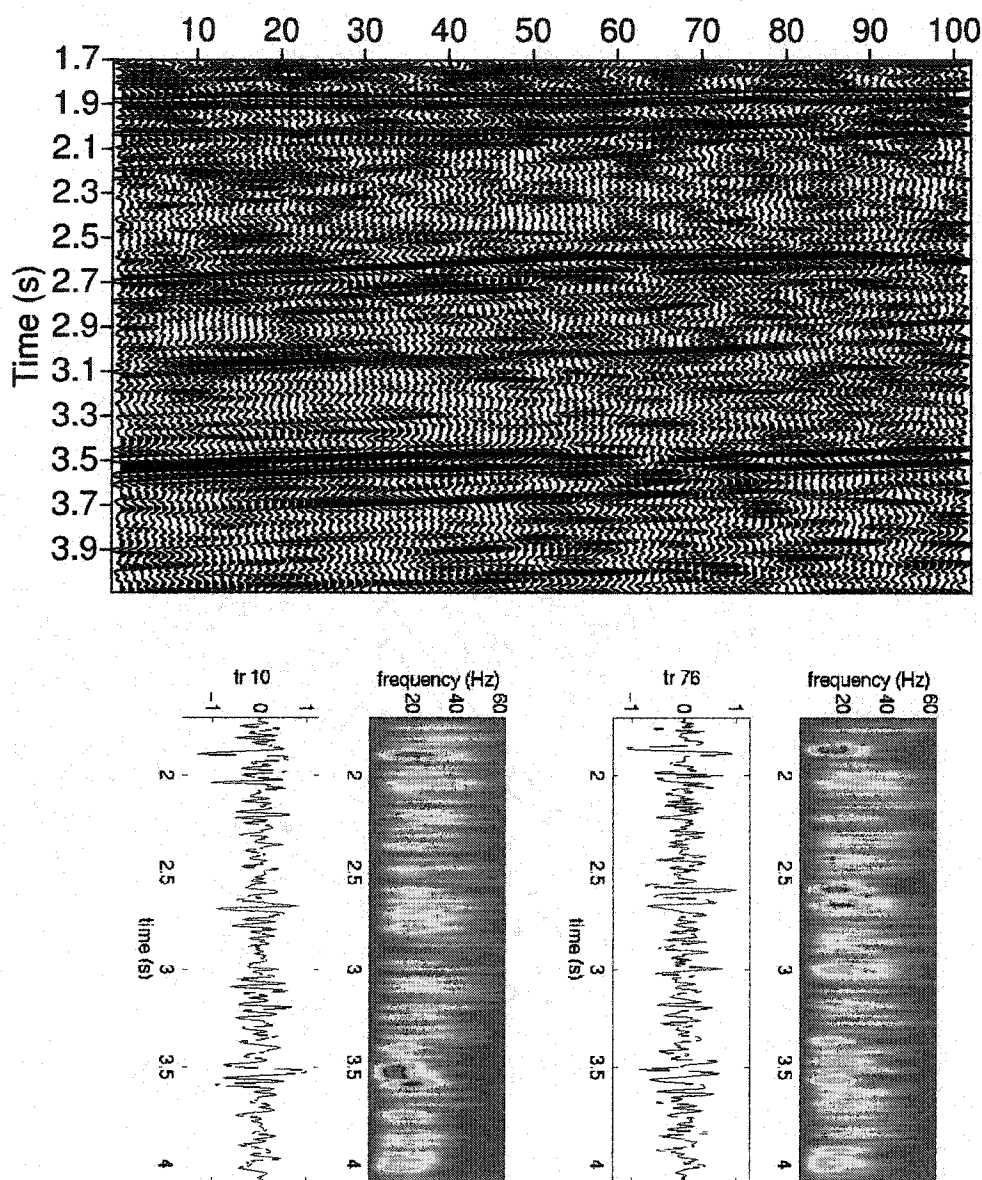


Figure 6.6: Seismic profile taken from the windowed area in Figure 6.5. The hydrocarbon accumulation is between traces 30 and 100 and from 2.5 - 2.9s. The spectral trend is essentially the same at both trace 10 and trace 76, which is not what we suspect. This is not too surprising given the heavy processing applied prior to attenuation analysis, and spectral estimates may be indicative of processing artifacts. This example illustrates the need for pre-stack analysis, with minimal data manipulation.

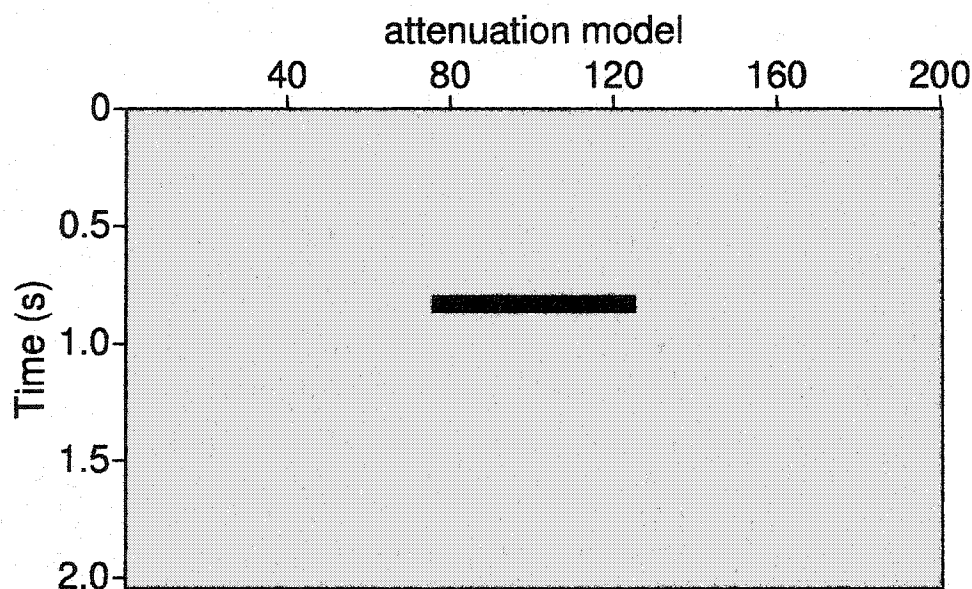


Figure 6.7: Attenuation model used to generate multi-offset synthetic seismograms. The black box corresponds to a zone of high attenuation with $Q=10$.

We generate a 30-fold CMP profile with a 25 Hz Ricker wavelet as the source pulse. The source and receiver spacing are set at 20 m, with a 0 m source-near receiver gap. We then add broadband noise to the data. The level of the noise is set such that the signal to noise ratio is approximately equal to 1 around the deepest reflector. In the zero-offset section the low Q interval is clearly evident as a high in HA (Figure 6.8) starting at a time of about 0.8s. The 60 m thick, low Q interval is slightly less than one wavelength. The Q estimation is effected by the addition of random noise which is evident by the banded pattern. Not surprisingly, the effect of random noise becomes more significant deeper in the section where the signal to noise ratio approaches 1.

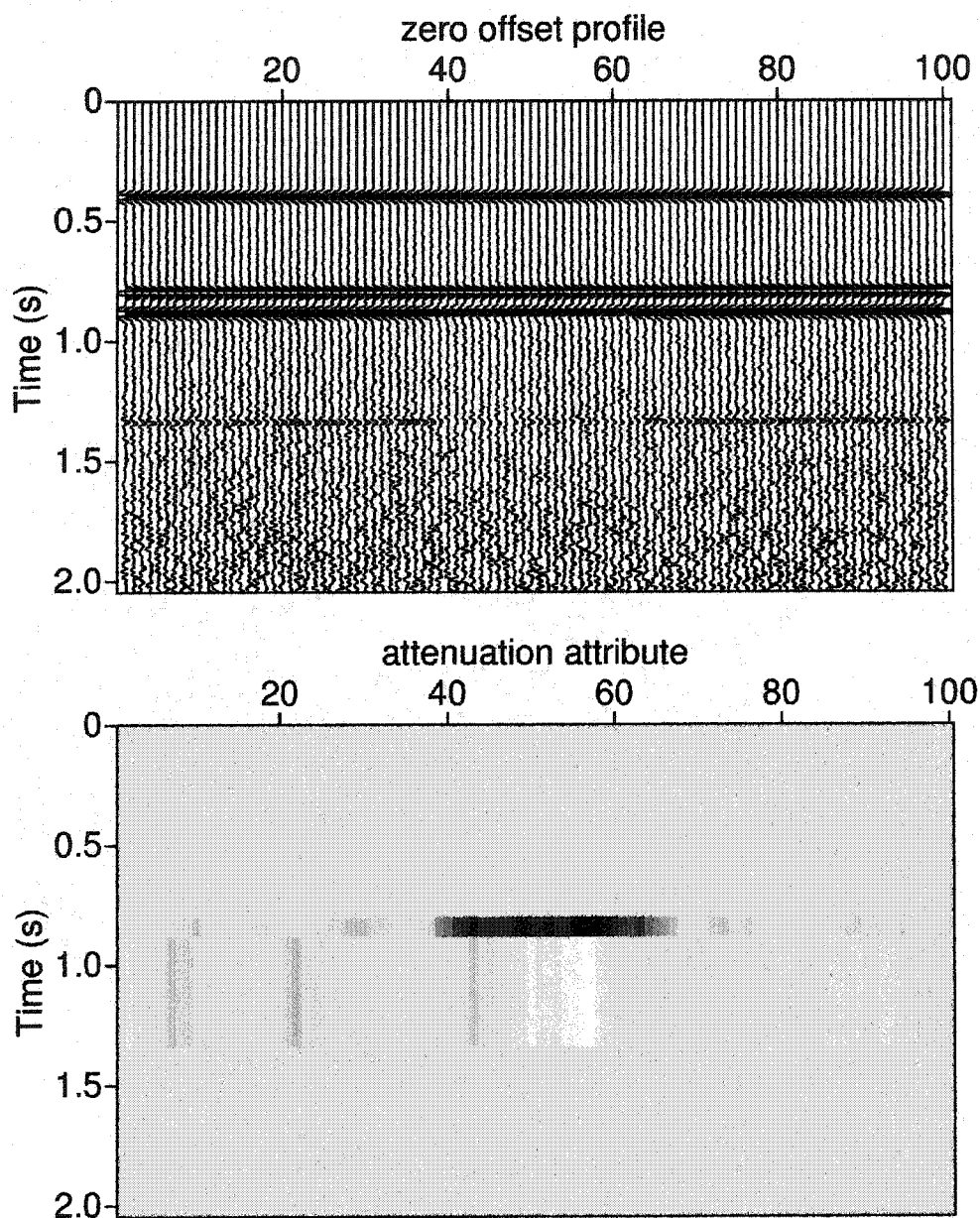


Figure 6.8: A zero-offset section generated using the attenuation model in Figure 6.7. Band-limited noise was added to the data. The zone of high attenuation is delineated. The banding is related to random noise and becomes more prominent deeper in the section where the signal to noise ratio approaches 1.

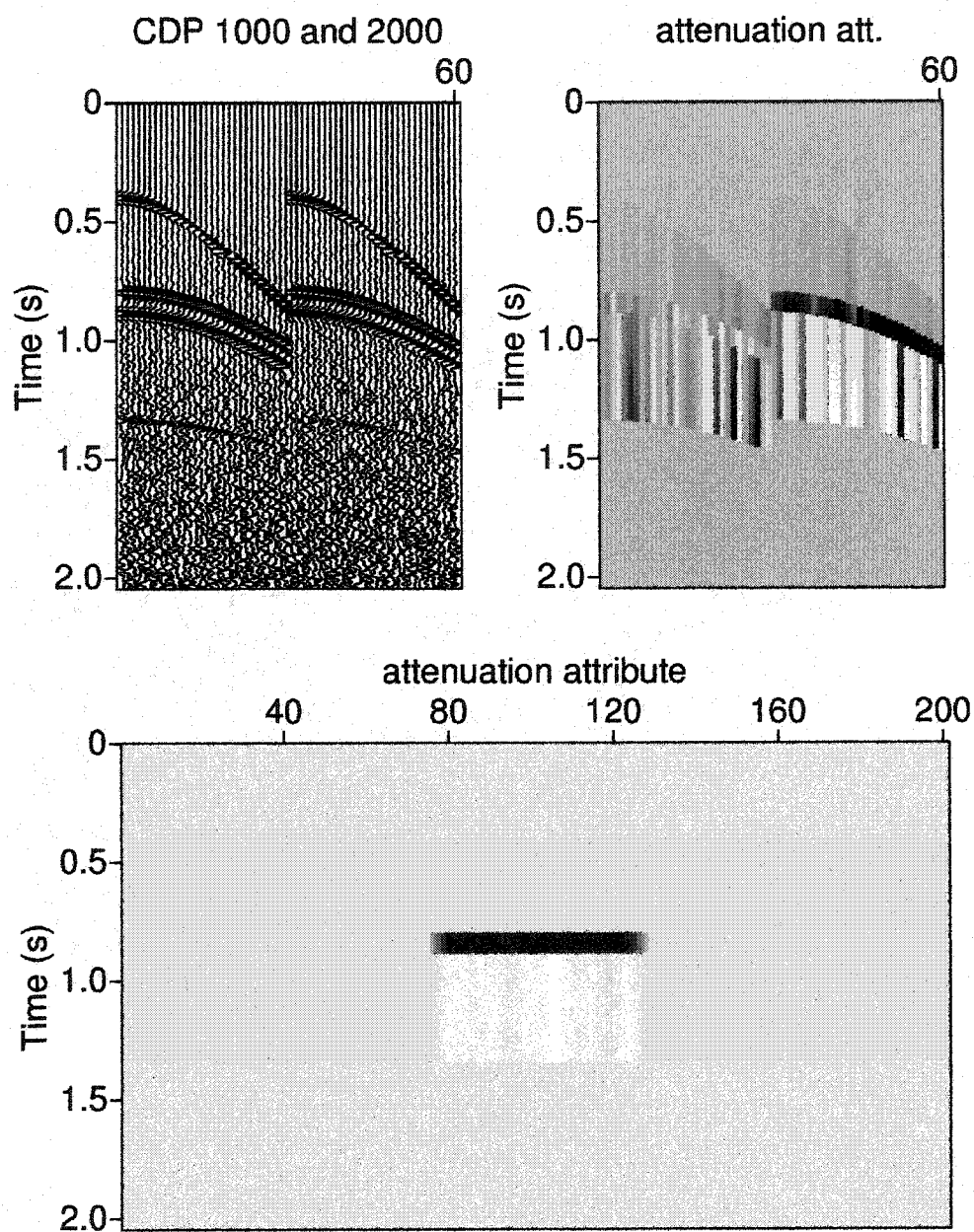


Figure 6.9: CMP gathers of the data generated using the model in Figure 6.7, and CMP gathers of the attenuation attribute. The attribute stack is a significant improvement over Figure 6.8.

The attenuation attribute stack (Figure 6.9) is a much improved attribute profile. The banding observed in the zero offset section has been strongly attenuated, and with the exception of the zone just below the low Q region, the extracted attribute is accurate to about 5%. Just below the low Q zone is a zone of negative apparent Q. This arises because the center frequency of the noise is higher than the peak frequency of the source wavelet, and the signal to noise ratio is close to 1 at the deep reflector. This creates an apparent increase in frequency content between the bottom of the low Q zone and the deepest reflector leading to a negative Q value. This effect is most evident below the low Q zone since the amplitude along the deepest reflector is about $\frac{1}{2}$ its value away from the low Q zone, so the signal to noise ratio is much lower.

Application to GPR: DNAPL detection. Propagating electromagnetic waves are also subject to frequency dependent attenuation which depends primarily on conductivity. Typically, over the bandwidth of a ground-penetrating-radar (GPR) pulse, the attenuation can be approximated with a frequency independent quality factor (Q), analogous to propagating acoustic waves (Turner and Siggins, 1994). Therefore, our attenuation estimation algorithm can be applied directly to GPR data. NAPL's typically have much lower conductivity than water or earth materials, and therefore soils containing NAPL do not attenuate a propagating GPR signal as strongly as the surrounding formation (Powers and Olhoeft, 1995). By extracting an attenuation profile, we can identify zones of anomalously low attenuation as potential NAPL rich zones.

For attenuation analysis it is acceptable to use our visco-acoustic model to simulate GPR wave propagation since we are interested only in spectral changes and

kinematic effects which are appropriately treated with a frequency independent Q , visco-acoustic model. Amplitude of the zero offset reflection coefficients are accurate, but the AVO effects are not correct. This has no effect on our attenuation estimate since we use the spectral ratio method (Equation 6.15). We construct a 2-D aquifer model (Table 6.2, Figure 6.10) contaminated with dense, non-aqueous phase liquid (DNAPL).

Table 6.2. Aquifer model parameters for GPR simulation

<i>Layer no.</i>	<i>v (m/ns)</i>	<i>Q</i>			<i>thickness (m)</i>
1	0.11	150 (0-9m)	300 (9-11m)	150 (11-13m)	3
2	0.058	30 (0-7m)	100 (7-11m)	30 (11-13m)	3
3	0.16	1000 (0-3m)	300 (3-7m)	na	1
4	0.034	10			3

Density and shear velocity are not applicable parameters and were held constant at 1 and 0 respectively. The velocities are representative of 1) moist sand, 2) water saturated sand, 3) sand saturated with perchloroethylene (PCE), a common DNAPL, and 4) water saturated clay. The values are based on data presented by Power's and Olhoeft (1995).

The aquifer model can be used to illustrate a common DNAPL remediation problem (Figure 6.10). DNAPL's tend to migrate through the permeable vadose and saturated zones until they reach an impermeable layer (Bedient et al., 1994). Upon reaching the impermeable layer, the DNAPL flows in the direction groundwater flow, then pools in topographic lows of the aquifer/aquiclude boundary. Some residual DNAPL remains trapped in the pore space along the migration route. Where the DNAPL pools, it may completely displace the water in the pore space, and the sediments become DNAPL

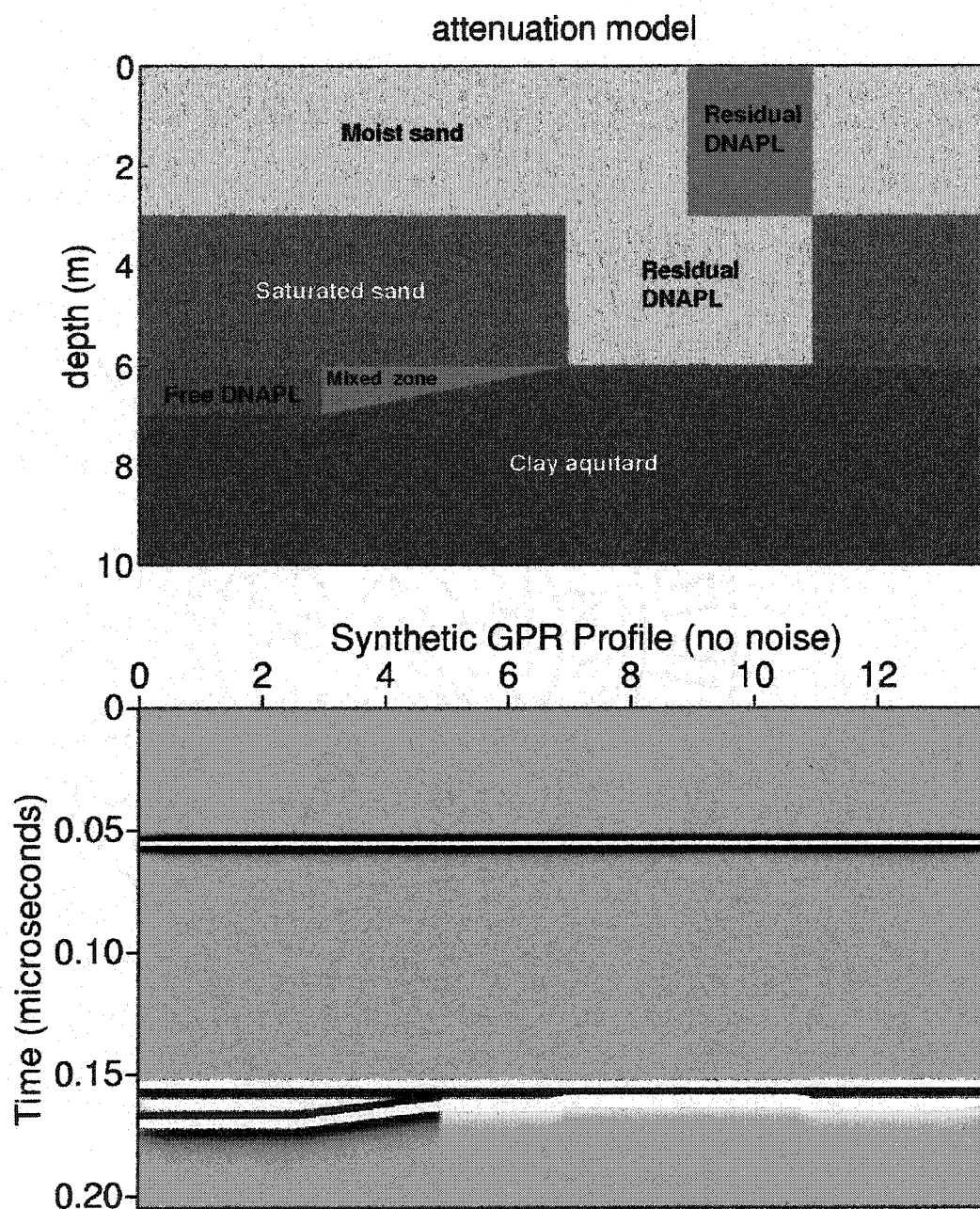


Figure 6.10: Attenuation model for an aquifer contaminated with DNAPL, and 6-fold stack of synthetic data.

saturated. In remediation studies it is necessary to identify both the DNAPL saturated and DNAPL residual zones. The boundaries of the DNAPL zone produce a sharp contrast in electrical properties and a strong reflection is generated at the upper and lower boundaries (Annan et al., 1992; Daniels et al., 1995). The boundaries of the residual zone are more diffuse, and the contrast in electrical properties is less distinct. A reflection may not be generated directly from the residual zone, and we must resort to indirect detection of the DNAPL. If we record any reflection above and below the residual zone we can potentially use attenuation analysis to detect the DNAPL. Success depends on the reflections extending beyond the bounds of the DNAPL rich zone so that the contaminated region appears as a zone of anomalously low attenuation.

In our model, we include a laterally variable zone of residual DNAPL that extends from the surface to the clay layer, and a laterally variable DNAPL saturated zone at the base of the aquifer. The velocities used in the model are appropriate for the corresponding materials (Powers and Olhoeft, 1995), but the attenuation model is somewhat artificial. The Q values listed in Table 6.1 are at the high end of the range that would likely exist under field conditions (Turner and Siggins, 1994). We use these values because, as previously noted, the attenuation attribute is most sensitive to low Q values, but in NAPL detection we are interested in high Q values; our model is designed to test the limits of the attenuation attribute. Additionally, the values for the residual DNAPL (three-phase and four phase) zones are set somewhat arbitrarily at an intermediate value since no predictive model is available (Powers and Olhoeft, 1995).

We generate 130 shots with a 225 MHz source pulse, source spacing of 10 cm,

receiver spacing of 5 cm, and a source-near receiver gap of 0 cm. This geometry results in a 6-fold profile with 2.5 cm CMP spacing. Attenuation attributes are extracted in the pre-stack domain, then NMO corrected and stacked to produce the final profiles. The attribute profiles are displayed as $1/Q_n$ rather than HA which is used in the seismic case. Plotting in this manner will tend to highlight high values of Q_n (low attenuation). After adding band-limited noise, attenuation analysis yields some interesting results. The zones of residual DNAPL are relatively well represented, however the thin DNAPL saturated zone is not well detected (Figure 6.11). In fact the values of the attenuation attribute jump randomly from positive to negative values. This occurs because Q is very high and the time interval is very small, therefore Q_{eff} changes very little across DNAPL sand according to Equation 6.12. Random noise will cause small random variation ($\pm \Delta Q_{eff}$) in our estimate, and since the actual Q_{eff} changes very little, we see from Equation 6.16 that changing our estimate by a small $\pm \Delta Q_{eff}$ can cause our estimate of Q_n to fluctuate about 0 (although there should be some bias towards the correct positive value of Q).

To avoid this problem, I define a new attribute that is sensitive to zones of low attenuation and has the following form

$$LA = \frac{Q_{eff_n} t_n - Q_{eff_{n-1}} t_{n-1}}{Q_{eff_n} (t_n - t_{n-1})} - 1 \quad 6.17$$

Unlike HA , which depends only on $1/Q_n$, LA is strongly dependent on $1/Q_n$, and weakly dependent on t_{n-1}/t_n , and $Q_{eff_{n-1}}$, so interpretation should be treated carefully. It is well suited to the specific application of identifying thin layers of very low attenuation that lie

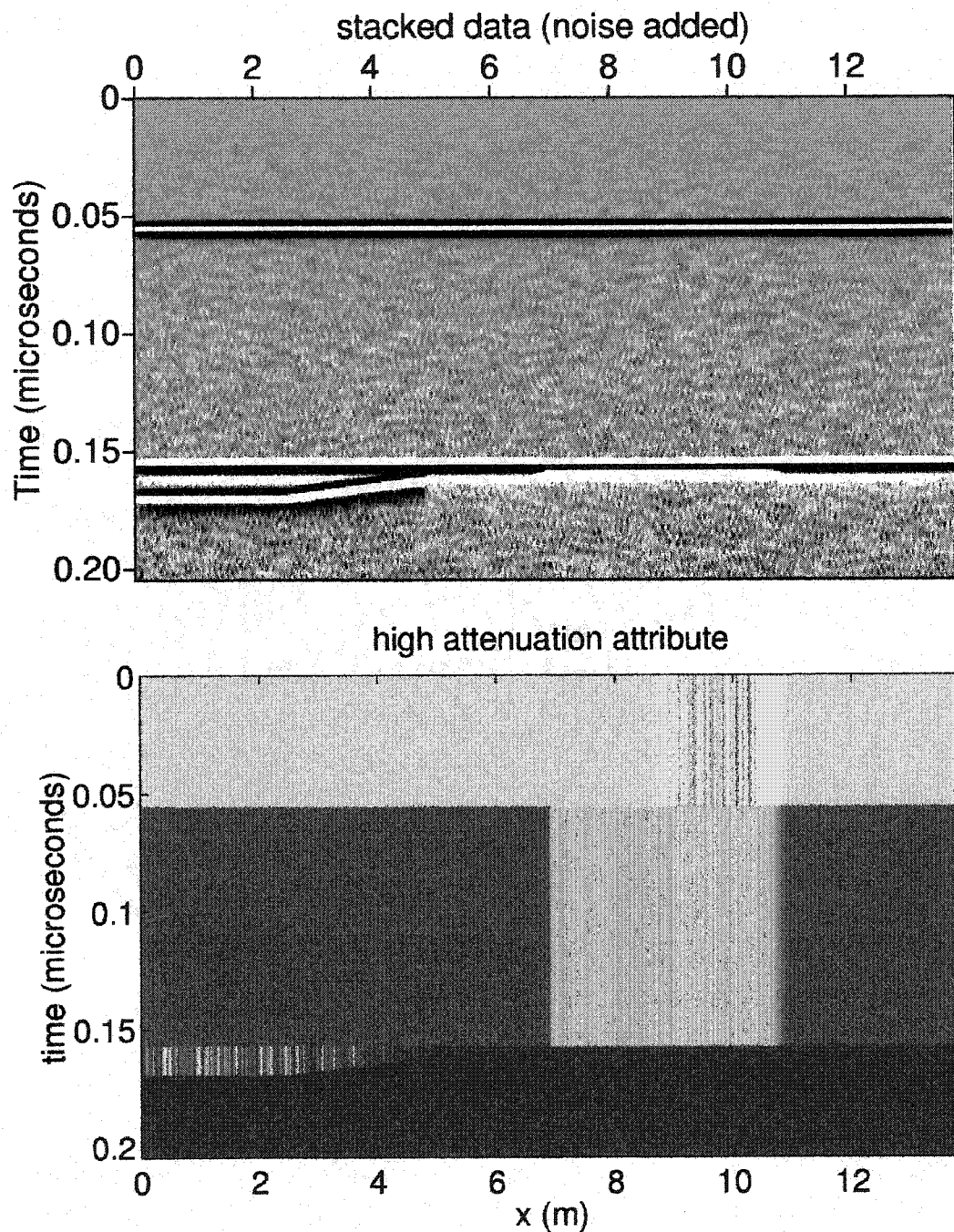


Figure 6.11: Stacked data after adding band-limited noise and the $1/HA$ attribute. The zones of residual DNAPL are clearly delineated as anomalous regions, but the response across the free DNAPL at the base of the aquifer is essentially random.

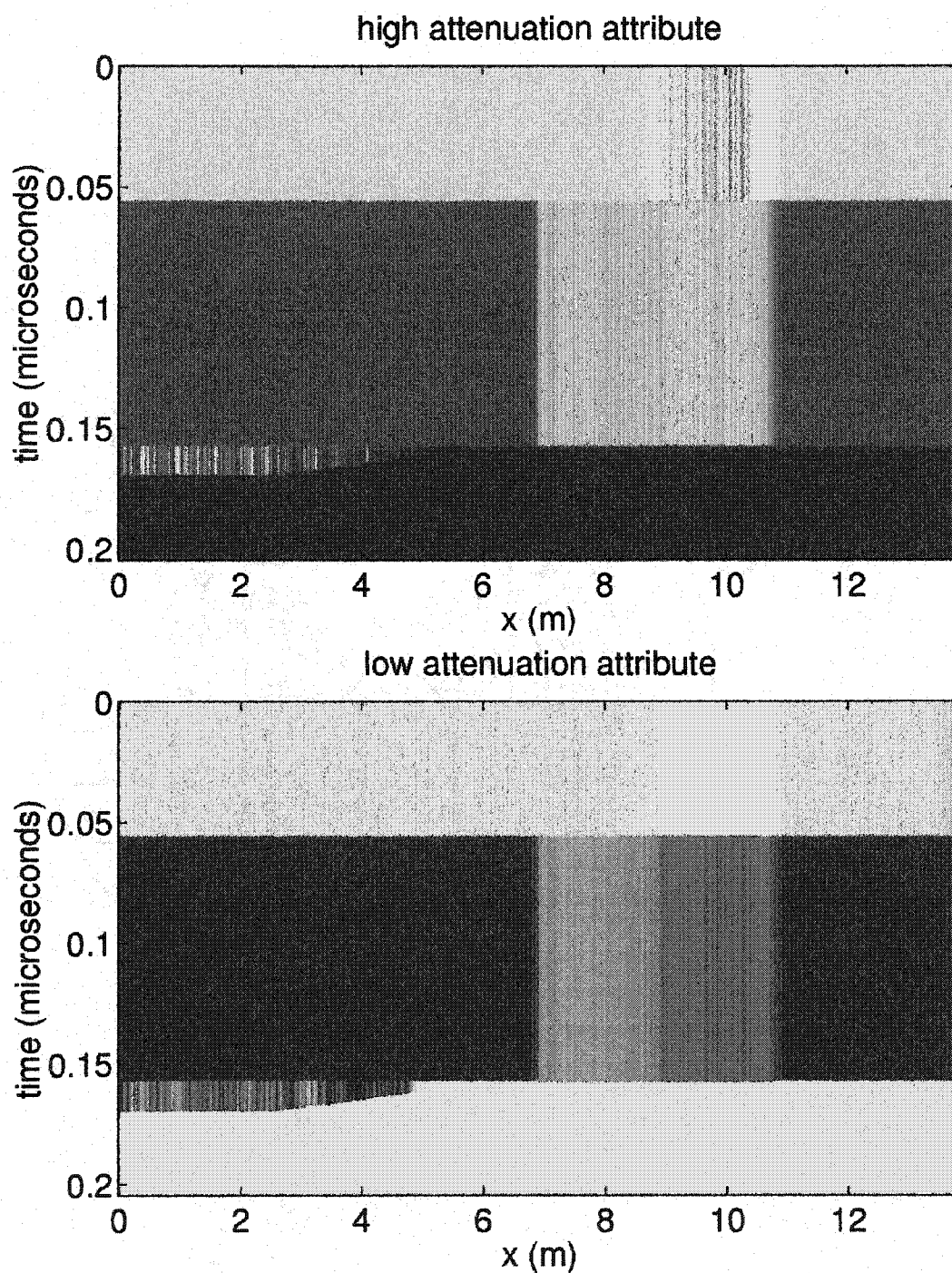


Figure 6.12: Comparison of $1/HA$ (high attenuation attribute) and LA (low attenuation attribute). A zone of low attenuation associated with the free DNAPL is consistently and definitively resolved with LA.

below zones of high attenuation. When $Q_{eff_n} < Q_{eff_{n-1}}$ (n is a high attenuation layer), LA is less than 0, when $Q_{eff_n} = Q_{eff_{n-1}}$ (the homogeneous case) $LA = 0$, and when $Q_{eff_n} > Q_{eff_{n-1}}$ (n is a low attenuation layer) $LA > 0$. LA is valuable as a qualitative interpretation tool used to identify zones of low attenuation. Extracting LA from the synthetic dataset, and comparing to HA , we find that LA indicates a distinct anomaly associated with the residual DNAPL zones, and a distinct, consistent anomaly is indicated for the saturated DNAPL zone (Figure 6.12). This is in contrast to the random response associated with $1/HA$ for the saturated DNAPL zone. I conclude that LA is a value attribute, but is not unique and depends on the overburden. $1/HA$ does not depend on the overburden, and the interpretations should be drawn from both $1/HA$ and LA . In this synthetic example, both the residual and saturated DNAPL zones are clearly isolated as zones of low attenuation, even in the presence of significant random noise.

GPR application: Lithology identification. Extracting an attenuation profile can also aid in differentiating lithologies. For example, clay content typically increases electric conductivity. The GPR signal will be more strongly attenuated in a clay rich sand than a clean sand. In hydrologic studies, we may want to identify zones of low hydraulic conductivity, which would also be associated with high clay content. The following example illustrates lithology differentiation based on the attenuation response and demonstrates problems that can be encountered in field data.

The GPR test pit at the Houston Advanced Research Center contains two types of sand (Loughridge, 1998). The lower sand unit is comprised of a medium grained sand (CS) with roughly 10% clay content. The upper sand is a washed, coarse grained quartz

sand (QS). The pit is bounded at the base and four sides by a dense clay unit (CL). There is significant topographic variation along the boundary of the two sands (Figure 6.14). In a 2-D zero-offset profile, acquired with 450 MHz antennas, we can clearly identify reflections from the QS/CS boundary and from the CS/CL boundary at the base of the pit.

Extracting an attenuation profile, we find that HA indicates a zone of high attenuation associated with the wedge of CS that thickens towards the right (Figure 6.14). This is consistent with expectations, however there are some problems with the HA profile that we need to consider. In general, HA indicates high attenuation associated with CS, however there are significant inconsistencies in the response in two locations. The wedge of CS becomes very thin from traces 48 - 60. In this case, tuning effects the spectrum and the attenuation extraction is not reliable. The second problem is observed from traces 28 - 40 where scatter from a buried pipe to the right of the profile interferes with the reflection

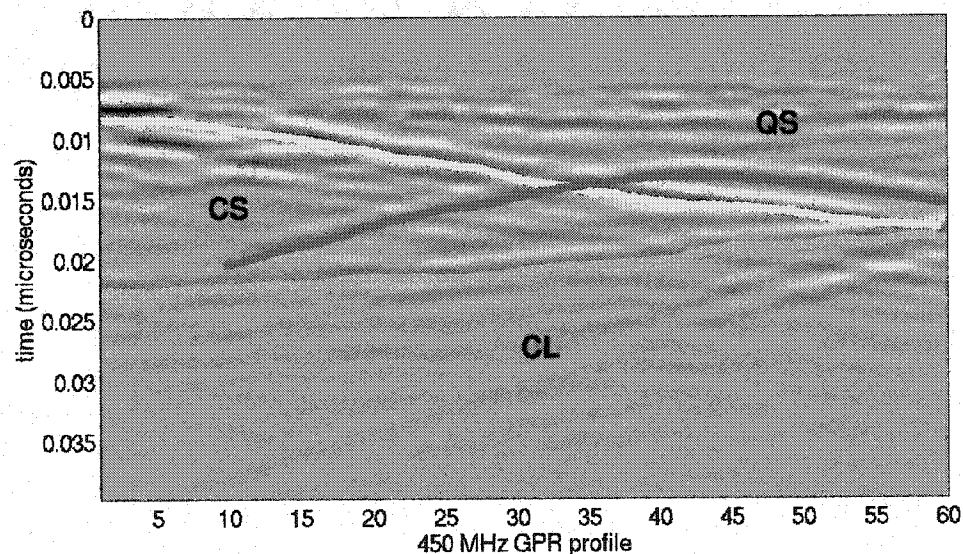


Figure 6.13: Zero offset GPR profile from the test pit at HARC. Note reflections from the QS/CS boundary (yellow), CS/CL boundary (green), and a diffraction from a buried PVC pipe (red).

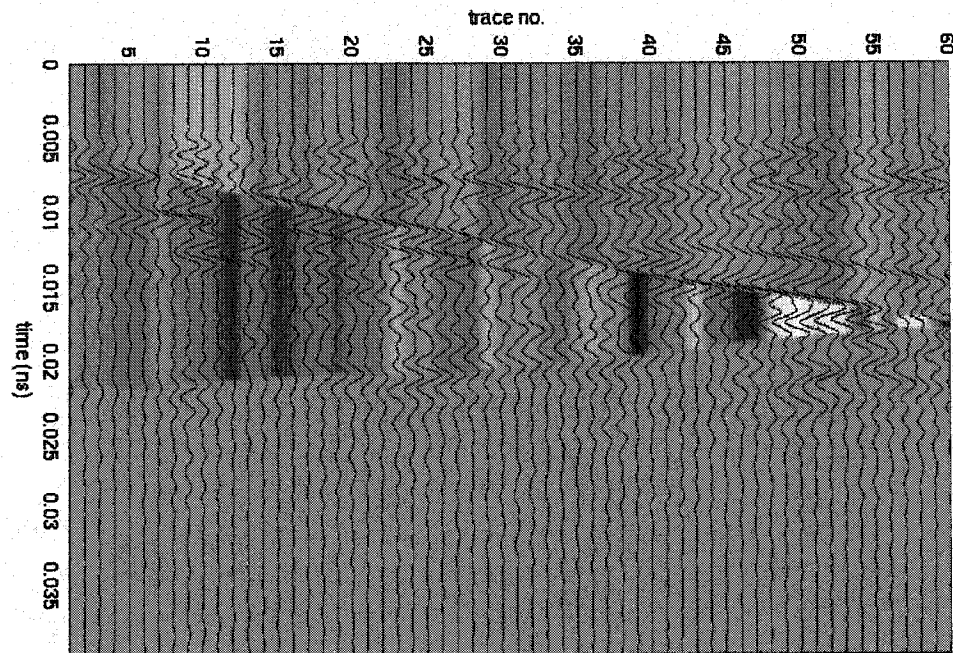


Figure 6.14: HA attribute with wiggle traces overlain for the GPR profile shown in Figure 6.14. The interference from the pipe diffraction, tuning as the wedge pinches out, and random noise effect the consistency of HA. Overall, the wedge of CS appears darker than the overlying material indication high relative attenuation. This is consistent with our expectations.

from the QS/CS boundary and interferes with the spectrum. This problem indicates the need for migration routines that preserve spectral qualities. Overall the attenuation profile is consistent with our expectations, but problems with tuning, random noise, and scatter from shallow events must be considered.

SUMMARY

We have developed a wavelet transform and time-frequency representation of time

series based on a matching pursuit algorithm. The algorithm was designed for the specific purpose of extracting attenuation profiles from seismic data. The new t-f distribution is more appropriate for attenuation analysis than existing methods, and the wavelet decomposition may prove valuable in other applications such as de-noising and phase deconvolution. A seismic modeling code has been developed that accounts for attenuation and dispersion effects in a 2D medium. A method of extracting an attenuation attribute (HA) has been developed based on a method of spectral ratios. HA is particularly sensitive to zones of high attenuation. A second attribute, LA, is defined, and is well suited to identifying thin layers of very low attenuation, that lie below zones of high attenuation. We have successfully delineated low Q zones in synthetic seismic data, and high Q zones in GPR data.

It is clear that it will be important to extract attenuation attributes in the pre-stack domain. Post-stack attribute extraction may prove viable if minimal preprocessing is done. Much additional work is needed. Primarily, rigorous testing with numerous field datasets in both the pre- and post-stack domain is necessary to determine if material properties (relative or absolute) can be determined consistently. This must be done with data for which detailed control is available in the form of well logs. Additional research in t-f attribute extraction would be valuable. Many attributes may be extracted from the t-f distribution, and some may prove to be more robust than HA or LA. Additionally, some method of picking events that eliminates the need for user interpretation would be valuable. An approach that uses a combination of amplitude thresholding and lateral coherence testing may be appropriate. The initial results are promising and warrant

continued research.

REFERENCES

- Aki, K., and Richards, P.G., 1980, Quantitative seismology: Theory and methods: New York, W.H. Freeman and Co., 557 p.
- Al-Chalabi, M., 1974, An analysis of stacking, RMS, average, and interval velocities over a horizontally layered ground: *Geophysical Prospecting*, v. 22, p. 458-475.
- Allen, J.L., and Peddy, C.P., 1993, Amplitude variation with offset: Gulf Coast case studies, *Geophys. Dev. Ser.*, Volume 4: Tulsa, Soc. Expl. Geophys.
- Annan, A.P., 1996, Transmission dispersion and GPR: *J. Env. Eng. Geophys.*, v. 0, p. 125-136.
- Annan, A.P., Brewster, M.L., Greenhouse, J.P., Redman, J.D., and Schneider, G.W., 1992, Geophysical monitoring of DNAPL migration in a sandy aquifer, 62nd Ann. Internat. Mtg.: Expanded abstracts, Soc. Expl. Geophys., p. 344-347.
- Annan, A.P., Waller, W.M., Strangway, D.W., Rossiter, J.R., Redman, J.D., and Watts, R.D., 1975, The electromagnetic response of a low-loss, 2-layer, dielectric earth for horizontal electric dipole excitation: *Geophysics*, v. 40, p. 285-298.
- Bachrach, R., Dvorkin, J., and Nur, A., 1998, High-resolution shallow-seismic experiments in sand, Part II: Velocities in shallow unconsolidated sand: *Geophysics*, v. 63, p. 1234-1240.
- Bachrach, R., and Nur, A., 1998, High-resolution shallow-seismic experiments in sand, Part I: Water table, fluid flow, and saturation: *Geophysics*, v. 63, p. 1225-1233.
- Baker, G.S., 1998, Applying AVO analysis to GPR data: *Geophys. Res. Let.*, v. 25, p.

397-400.

Baker, G.S., Steeples, D.W., and Drake, M., 1998, Muting the noise cone in near-surface reflection data: An example from southeastern Kansas: *Geophysics*, v. 63, p. 1332-1338.

Bedient, P.B., Rifai, H.S., and Newell, C.J., 1994, Ground water contamination: Transport and remediation: Englewood Cliffs, NJ, Prentice-Hall, Inc., 541 p.

Bergmann, T., Robertsson, J.O.A., and Holliger, K., 1998, Finite-difference modeling of electromagnetic wave propagation in dispersive and attenuating media: *Geophysics*, v. 63, p. 856-867.

Boudreaux-Bartels, G.F., 1985, Time-varying signal processing using the Wigner-Distribution time-frequency signal representation, *Advances in geophysical data processing*, Volume 2, JAI Press Inc., p. 33-79.

Bradford, J., Ramaswami, M., and Peddy, C., 1995, Imaging PVC gas pipes using 3-D GPR, *SAGEEP '95: Expanded abstracts*: Keystone, CO, Soc. Appl. Geophys. Env. Eng., p. 519-524.

Bradford, J.H., Sawyer, D.S., and Zelt, C.A., 1997, AVO analysis of low-velocity, shallow sands (<50m), *Society of Exploration Geophysicists international exposition and 67th annual meeting*, Volume 1: Dallas, TX, p. 158-162.

Bradford, J.H., Sawyer, D.S., Zelt, C.A., and Oldow, J.S., 1998, Imaging a shallow aquifer in temperate glacial sediments using seismic reflection profiling with DMO processing: *Geophysics*, v. 63, p. 1248-1256.

Bradford, J.H., and Wu, Y., 1997, Time-frequency representation of seismic signals via

- matching pursuit decomposition with complex Ricker wavelets, AGU Fall meeting, Volume 78: EOS Supplement: San Francisco, American Geophysical Union, p. 33.
- Brandt, H., 1960, Factors affecting compressional wave velocity in unconsolidated marine sand sediments: *J. Acoust. Soc. Am.*, v. 32, p. 171-179.
- Cai, J., and McMechan, G.A., 1995, Ray-based synthesis of bistatic ground-penetrating radar profiles: *Geophysics*, v. 60, p. 87-96.
- Campbell, D.L., Lucious, J.E., Ellefson, K.J., and Deszcz-Pan, M., 1995, Monitoring of a controlled LNAPL spill using ground-penetrating radar, SAGEEP '95: Expanded abstracts: Keystone, CO, Soc. Appl. Geophys. Env. Eng., p. 511-517.
- Carcione, J.M., 1996, Ground-penetrating radar: Wave theory and numerical simulation in lossy anisotropic media: *Geophysics*, v. 61, p. 1664-1677.
- Casper, D.A., and Kung, K.-J.S., 1996, Simulation of ground-penetrating radar waves in a 2-D soil model: *Geophysics*, v. 61, p. 1034-1049.
- Castagna, J.P., 1993, AVO Analysis - Tutorial and review, *in* Castagna, J.P., and Backus, M.M., eds., Offset-dependent reflectivity - Theory and practice of AVO analysis, Volume 8: Investigations in Geophysics: Tulsa, Soc. Expl. Geophys., p. 3-36.
- Castagna, J.P., Batzle, M.L., and Kan, T.K., 1993, Rock physics - the link between rock properties and AVO response, *in* Castagna, J.P., and Backus, M.M., eds., Offset - dependent reflectivity - theory and practice, Volume 8: Investigations in geophysics series: Tulsa, Soc. Expl. Geophys., p. 135-171.
- Cole, K.S., and Cole, R.S., 1941, Dispersion and absorption in dielectrics, I, alternating current characteristics: *J. Chem. Phys.*, v. 9, p. 341-351.

- Daniels, J.J., Robert, R., and Vendl, M., 1995, Ground penetrating radar for the detection of liquid contaminants: *J. Appl. Geophys.*, v. 33, p. 195-207.
- Daubechies, I., 1991, Ten lectures on wavelets, SIAM.
- Deregowski, S.M., 1986, What is DMO?: *First Break*, v. 4, p. 7-24.
- Dix, C.H., 1955, Seismic velocities from surface measurements: *Geophysics*, v. 34, p. 180-195.
- Dobrin, M.B., and Savit, C.H., 1988, Introduction to geophysical prospecting: New York, McGraw-Hill, 867 p.
- Domack, E.W., 1982, Facies of late Pleistocene glacial marine sediments on Whidbey Island, Washington [Ph.D. thesis]: Houston, Rice University.
- Domenico, S.N., 1977, Elastic properties of unconsolidated porous sand reservoirs: *Geophysics*, v. 42, p. 1339-1368.
- Edwards, M., 1986, Glacial Environments, *in* Reading, H.D., ed., Sedimentary environments and facies, Blackwell Scientific Publications.
- Evans, B.J., 1997, A handbook for seismic data acquisition: Tulsa, Soc. Expl. Geophys., 305 p.
- Evans, B.J., Cocker, J., and Urosevic, M., 1996, Recording seismic reflections beneath high velocity layers, 66th Ann. Internat. Mtg., Soc. Expl. Geophys., p. 194-197.
- Fisher, E., McMechan, G.A., and Annan, A.P., 1992a, Acquisition and processing of wide-aperture ground-penetrating radar data: *Geophysics*, v. 57, p. 495-504.
- Fisher, E., McMechan, G.A., Annan, A.P., and Cosway, S.W., 1992b, Examples of reverse-time migration of single channel ground-penetrating radar profiles:

- Geophysics, v. 57, p. 577-586.
- Gassman, F., 1951, Elastic waves through a packing of spheres: Geophysics, v. 16, p. 673-685.
- Griffiths, D.J., 1989, Introduction to electrodynamics: Englewood Cliffs, NJ, Prentice-Hall, 532 p.
- Haeni, F.P., 1986, Application of seismic refraction methods in groundwater modeling studies in New England: Geophysics, v. 51, p. 236-249.
- Hale, D., 1991, Dip moveout processing: Tulsa, Soc. Expl. Geophys.
- Henstock, T.J., and Levander, A., in preparation, Effect of changes in vertical wavenumber: Geophysics.
- Hunter, J.A., Pullan, S.E., Burns, R.A., Gagne, R.M., and Good, R.S., 1984, Shallow seismic reflection mapping of the overburden-bedrock interface with the engineering seismograph - some simple techniques: Geophysics, v. 49, p. 1381-1385.
- Jakubowicz, H., 1995, A simple efficient method of dip-moveout correction: Geophys. Prosp., v. 38, p. 221-245.
- Kahle, X., and Olsen, Y., 1995, Hydrogeology and quality of ground water on Guemes Island, Skagit County, Washington, U.S. Geol. Surv.
- Kamal, A., 1989, Velocity analysis by iterative profile migration: Geophysics, v. 54, p. 718-729.
- Keiswetter, D., Black, R., and Steeples, D., 1994, Mapping bedrock beneath glacial till using CDP seismic reflection methods: Geophys. Res. Lett., v. 21, p. 453-456.

- Kelly, K.R., and Marfurt, K.J., 1990, Numerical modeling of seismic wave propagation, *in* Levin, F.K., ed., Geophysics reprint series, Volume 13: Tulsa, Soc. Expl. Geophys.
- Kong, J.A., 1972, Electromagnetic fields due to dipole antennas over stratified anisotropic media: Geophysics, v. 37, p. 985-996.
- Lafond, C.F., and Levander, A.R., 1993, Migration moveout analysis and depth focusing: Geophysics, v. 58, p. 91-100.
- Lankston, R.W., 1990, High-resolution refraction seismic data acquisition and interpretation, *in* Ward, S.H., ed., Geotechnical and environmental geophysics, Volume 1: Investigations in Geophysics: Tulsa, Soc. Expl. Geophys., p. 45-73.
- Lanz, E., Pugin, A., Green, A., and Horstmeyer, H., 1996, Results of 2- and 3-D high-resolution seismic reflection surveying of surficial sediments: Geophys. Res. Lett., v. 23, p. 491-494.
- Lehmann, F., 1996, Fresnel equations for reflection and transmission at boudnaries between conductive media, with applications to georadar problems, 6th Internat. Conf. GPR (GPR'96): Expanded abstracts.
- Li, X., and Ulrych, T.J., 1996, Multi-scale attribute analysis and trace decomposition, 66th Ann. Internat. Mtg.: Expanded abstracts, Soc. Expl. Geophys., p. 1634-1637.
- Liu, Z., 1997, An analytical approach to migration velocity analysis: Geophysics, v. 62, p. 1238-1249.
- Loughridge, J., 1998, Application of seismic tools and techniques to ground-penetrating radar (GPR) studies [M.A. thesis]: Houston, Rice University.

- Mallat, S., and Zhang, Z., 1992, Matching pursuit with time-frequency dictionaries: Technical Report 619, IEEE transactions in signal processing.
- Miller, R.D., and Xia, J., 1998, Large near-surface velocity gradients on shallow seismic reflection data: *Geophysics*, v. 63, p. 1348-1356.
- Mukerji, T., Mavko, and Marion, D., 1993, Velocity dispersion and scale effects in layered media: Modeling of experimental results, Stanford rock physics and borehole geophysics project, Volume 53, p. A:1-A:12.
- Olhoeft, G.R., 1986, Direct detection of hydrocarbon and organic chemicals with ground-penetrating radar and complex resistivity, NWWA/API Conference on petroleum and hydrocarbons and organic chemicals in groundwater -- Prevention, detection, and restoration: Houston, NWWA, p. 284-305.
- Olhoeft, G.R., and Capron, D.E., 1994, Petrophysical causes of electromagnetic dispersion, 5th Internat. Conf. GPR: Proceedings: Kitchener, Ontario, Canada, p. 145-152.
- Olhoeft, G.R., and Strangway, D.W., 1974, Magnetic relaxation and the electromagnetic response parameter: *Geophysics*, v. 39, p. 302-311.
- Ostrander, W.J., 1984, Plane-wave reflection coefficients for gas sands at nonnormal angles of incidence: *Geophysics*, v. 49, p. 1637-1648.
- Papas, C.H., and Engheta, 1982, Radiation patterns of interfacial dipole antennas: *Radio Science*, v. 17, p. 1557-1566.
- Pasasa, L., Wenzel, F., and Zhao, P., 1998, Prestack Kirchhoff depth migration of shallow seismic data: *Geophysics*, v. 63, p. 1241-1247.

- Powers, M.H., and Olhoeft, G.R., 1995, Modeling the response of leaking, buried pipes, SAGEEP '95: Expanded abstracts: Keystone, CO, Soc. Appl. Geophys. Env. Eng., p. 525-534.
- Roberts, R.L., and Daniels, J.J., 1992, 3-D data collection and analysis for high-resolution GPR studies, 62nd Ann. Internat. Mtg.: Expanded abstracts, Soc. Expl. Geophys., p. 360-363.
- Roberts, R.L., and Daniels, J.J., 1997, Modeling near-field GPR in three dimensions using the FDTD method: Geophysics, v. 62, p. 1114-1126.
- Robertsson, J.O.A., Holliger, K., Green, A.G., Pugin, A., and De Iaco, R., 1996, Effects of near-surface waveguides on shallow high-resolution seismic refraction and reflection data: Geophys. Res. Lett., v. 23, p. 495-498.
- Sananikone, K., and Everett, M.E., 1997, Characterization of the electrical structure of an agricultural field in Burleson County, TX, Symposium on the Application of Geophysics to Engineering and Environmental Problems: Reno, NV.
- Siahkoohi, H.R., and West, G.F., 1996, 3-D seismic imaging of complex structures in glacial deposits, 66th Ann. Internat. Mtg., Soc. Expl. Geophys., p. 873-876.
- Siringan, F.P., and Anderson, J.B., 1993, Seismic facies, architecture, and evolution of the Bolivar Roads tidal inlet/delta complex, East Texas Gulf Coast: J. Sed. Petrol., v. 63, p. 794-808.
- Smith, G.S., 1984, Directive properties of antennas for transmission into a material half-space: IEEE transactions on antennas and propagation, v. AP-32, p. 232-246.
- Steeple, D.W., 1998, Shallow seismic reflection section - Introduction: Geophysics, v.

63, p. 1210-1212.

Steeple, D.W., and Miller, R.D., 1990, Seismic reflection methods applied to engineering, environmental, and groundwater problems, *in* Ward, S.H., ed., Geotechnical and environmental geophysics, Volume 5: Investigations in geophysics: Tulsa, Soc. Expl. Geophys., p. 1-30.

Steeple, D.W., and Miller, R.D., 1998, Avoiding pitfalls in shallow seismic reflection surveys: *Geophysics*, v. 63, p. 1213-1224.

Szarancic, E., 1976, Fundamental functions for horizontally stratified earth: *Geophysical Prospecting*, v. 24, p. 528-548.

Szarancic, E., 1979, Towards unification of geophysical problems for horizontally stratified media: *Geophysical Prospecting*, v. 27, p. 576-583.

Taner, M.T., and Koehler, F., 1969, Velocity spectra - Digital computer derivations and applications of velocity functions: *Geophysics*, v. 34, p. 859-881.

Tsang, L., and Kong, J.A., 1973, Interference patterns of a horizontal electric dipole over layered dielectric media: *J. Geophys. Res.*, v. 78, p. 3287-3300.

Turner, G., and Siggins, A.F., 1994, Constant Q attenuation of subsurface radar pulses: *Geophysics*, v. 59, p. 1192-1200.

Ursin, B., 1983, Review of elastic and electromagnetic wave propagation in horizontally layered media: *Geophysics*, v. 48, p. 1063-1081.

Wang, T., and Tripp, A.C., 1996, FDTD simulation of EM wave propagation in 3-D media: *Geophysics*, v. 61, p. 110-120.

Xu, T., and McMechan, G.A., 1997, GPR attenuation and its numerical simulation in 2.5

dimensions: *Geophysics*, v. 62, p. 403-414.

Zelt, C.A., and Smith, R.B., 1992, Seismic traveltime inversion for 2-D crustal velocity structure: *Geophysical Journal International*, v. 108, p. 16-34.

Zeng, X., McMechan, G.A., Cai, J., and Chens, H.-W., 1995, Comparison of ray and Fourier methods for modeling monostatic ground-penetrating radar profiles: *Geophysics*, v. 60, p. 1727-1734.

Zeng, X., McMechan, G.A., and Xu, T., in review, GPR AVO: *Geophysics*.

APPENDIX A: DERIVATION OF THE WIGNER DISTRIBUTION FOR A RICKER WAVELET

The Wigner distribution is given by the Fourier transform of the instantaneous autocorrelation

$$W(S(t)) = F_{\tau} \left[S \left(t + \frac{\tau}{2} \right) S \left(t - \frac{\tau}{2} \right) \right] \quad \text{A.1}$$

Where S is an arbitrary time series, t is time, and τ is the time lag variable. F_{τ} indicates the Fourier transform over τ . The Ricker wavelet is given by

$$R(t) = \frac{\delta^2 e^{-\lambda t^2}}{\delta t^2} \quad \text{A.2}$$

Taking the derivatives and inserting the time lag variable we find

$$R \left(t + \frac{\tau}{2} \right) R \left(t - \frac{\tau}{2} \right) = R^2(t) e^{-\frac{\lambda}{2}\tau^2} + e^{-2\lambda t^2} e^{-\frac{\lambda}{2}\tau^2} \left[\frac{\lambda^2 \tau^4}{4} - \lambda(1 + 2\lambda t^2)\tau^2 \right] \quad \text{A.3}$$

To take the Fourier transform I break Equation A.3 into three terms

$$\begin{aligned}
F_{\tau} \left[R \left(t + \frac{\tau}{2} \right) R \left(t - \frac{\tau}{2} \right) \right] &= R^2(t) F_{\tau} \left(e^{-\frac{\lambda}{2} \tau^2} \right) + \\
&e^{-2\lambda t^2} F_{\tau} \left(\frac{\lambda^2}{4} \tau^4 e^{-\frac{\lambda}{2} \tau^2} \right) + \\
&e^{-2\lambda t^2} F_{\tau} \left(-\lambda(1 + 2\lambda t^2) \tau^2 e^{-\frac{\lambda}{2} \tau^2} \right)
\end{aligned} \tag{A.4}$$

To solve this equation we the Fourier transforms of the following form

$$\begin{aligned}
\text{Transform 1: } &F_{\lambda}(e^{-\lambda t^2}) \\
\text{Transform 2: } &F_{\lambda}(t^2 e^{-\lambda t^2}) \\
\text{Transform 3: } &F_{\lambda}(t^4 e^{-\lambda t^2})
\end{aligned} \tag{A.5}$$

Transform 1 can be found in the math tables but transforms 2 and 3 are not generally tabulated in standard math tables. We can find the transforms based on our knowledge of the transform of the Ricker wavelet

$$\begin{aligned}
F_t[R(t)] &= F_t \left(\frac{\delta^2 e^{-\lambda t^2}}{\delta t^2} \right) \\
&= \omega^2 F_t(e^{-\lambda t^2})
\end{aligned} \tag{A.6}$$

which comes from the properties of the Fourier transform. We then find

$$R(t) = 2\lambda e^{-\lambda t^2} (2\lambda t^2 - 1) \tag{A.7}$$

and from Equations A.7 and A.6 we find

$$\begin{aligned}
 F_t[2\lambda e^{-\lambda t^2}(2\lambda t^2 - 1)] &= 2\lambda \left[F_t(2\lambda t^2 e^{-\lambda t^2}) - F_t(e^{-\lambda t^2}) \right] \\
 &= -\frac{\omega^2}{\sqrt{2\lambda}} e^{-\frac{\omega^2}{4\lambda}}
 \end{aligned}
 \tag{A.8}$$

taking the appropriate transform and rearranging we see that

$$F_t(t^2 e^{-\lambda t^2}) = \frac{1}{4\lambda^2 \sqrt{2\lambda}} e^{-\frac{\omega^2}{4\lambda}} (1 - \omega^2) \tag{A.9}$$

Now that we have Transform 2, we can find Transform 3 in a similar way from the 4th derivative of the Gaussian, and after a lot of algebra we find

$$F_t(t^4 e^{-\lambda t^2}) = \frac{1}{16\lambda^4 \sqrt{2\lambda}} e^{-\frac{\omega^2}{4\lambda}} (\omega^4 + 12\lambda\omega^2 + 12\lambda^2) \tag{A.10}$$

With Transforms 1 - 3 we can now find the transforms for the three terms on the right side of Equation A.4. After combining the terms and a lot more algebra we find

$$\begin{aligned}
 WD(S) &= F \left[R(t + \frac{\tau}{2}) R(t - \frac{\tau}{2}) \right] = \\
 &K_w e^{-2\lambda(t-t_0)^2} e^{-\frac{\omega^2}{2\lambda}} \left[\frac{\omega^4}{4\lambda^2} + \left(2(t-t_0)^2 - \frac{1}{2\lambda} \right) \omega^2 + 4\lambda^2(t-t_0)^4 - 6\lambda(t-t_0)^2 + 3/4 \right]
 \end{aligned}
 \tag{A.11}$$

APPENDIX B: DERIVATION OF EQUATIONS FOR ATTENUATION ATTRIBUTE CALCULATIONS

Given the assumption of a frequency independent quality factor, Q , the amplitude decay of a monochromatic wave due to intrinsic attenuation, after propagation through a homogeneous medium for some time t , is given by

$$A = A_0 e^{-\pi f \frac{t}{Q}} \quad \text{B.1}$$

where A_0 is the initial amplitude, A is the amplitude at time t , Q is the quality factor, and f is the frequency. Now consider propagation through a discretely layered media. The amplitude at the base of layer n is now given by

$$\begin{aligned} A_n &= A_0 \prod_{i=1}^n e^{-\pi f \frac{\Delta t_i}{Q_i}} \\ &= A_0 e^{-\pi f \sum_{i=1}^n \frac{\Delta t_i}{Q_i}} \end{aligned} \quad \text{B.2}$$

where Δt_i and Q_i are the travel time and Q value in the i th layer respectively. I now define the effective Q value at the base of layer n

$$\frac{t_n}{Q_{eff_n}} = \sum_{i=1}^n \frac{\Delta t_i}{Q_i} \quad \text{B.3}$$

where t_n is the total travel time to the base of layer n ($t_n = \sum \Delta t_i$) and

$$\frac{1}{Q_{eff_n}} = \frac{\sum_{i=1}^n \frac{\Delta t_i}{Q_i}}{t_n} \quad \text{B.4}$$

I now derive the expression to extract the interval Q value from a series of effective Q values. From Equation B.4 we see that

$$\frac{1}{Q_{eff_n}} = \frac{\frac{\Delta t_n}{Q_n} + \sum_{i=1}^{n-1} \frac{\Delta t_i}{Q_i}}{t_n} \quad \text{B.5}$$

rearranging and multiplying both sides by $1/\Delta t_{n-1}$ we derive the following

$$\begin{aligned} \frac{t_n}{t_{n-1}} \frac{1}{Q_{eff_n}} &= \frac{\Delta t_n}{t_{n-1}} \frac{1}{Q_n} + \frac{\sum_{i=1}^{n-1} \frac{\Delta t_i}{Q_i}}{t_{n-1}} \\ &= \frac{\Delta t_n}{t_{n-1}} \frac{1}{Q_n} + \frac{1}{Q_{eff_{n-1}}} \end{aligned} \quad \text{B.6}$$

solving for $1/Q_n$ we find

$$\frac{1}{Q_n} = \left(\frac{t_n}{Q_{eff_n}} - \frac{t_{n-1}}{Q_{eff_{n-1}}} \right) \frac{1}{\Delta t_n} \quad \text{B.7}$$

It is interesting to note that Q_n depends only on the effective Q values bounding the layers, and the travel time difference between the two layers. This is similar to Dix inversion for interval velocities.